THE UNIVERSITY OF SOUTHAMPTON

AN INVESTIGATION INTO THE ELECTROSTATIC AGGLOMERATION OF FLY-ASH

A THESIS SUBMITTED FOR THE DEGREE
OF MASTER OF PHILOSOPHY

BY

GILES ADRIAN CARTWRIGHT

JULY 1992

TO

J.B. & H.J.

For all their 'uplifting' moments.

ACKNOWLEDGEMENTS

I would like to thank Professor John F. Hughes, of the department of Electrical Engineering at Southampton University, for all his valuable advice, interest and encouragement given in the supervision of this project.

My grateful thanks are also extended to all those at what was the Central Electricity Research Laboratories at Leatherhead*, the co-operating and funding body of this project. Particular thanks goes to Dr. John Horrocks and Dr. Rob Corbin, for all their support and encouragement throughout the research program.

I would also like to express my appreciation for all the valuable help and assistance received from all my colleagues within the Applied Electrostatics Research Group at the University of Southampton. Special recognition must go to Mr. Ian Parker for all his help and guidance given in the laboratory and also to Mr. Harvey Green for all his time spent in the construction of the experimental equipment.

I would also like to thank my parents for their support and help, especially to my father who proof read this work.

Finally not forgetting all my friends for putting up with me working all the time and not coming out to play!

*(Now The National Power Company)

CONTENTS

CHAPTER SEVEN 210

BI-POLAR CHARGER 210

LIST OF FIGURES

LIST OF PLATES

PRINCIPLE NOTATION

The following notation is used throughout this document, other terms are used less frequently and are defined where they occur.

A	The Hamaker constant.
a	Radius.
b	Ion mobility.
C	Capacitance.
Cc	Slip correction factor.
D	Equivalent duct diameter.
d	Distance.
E	Electric field strength.
E_b	The Breakdown field strength of air.
e^-	The charge on an electron.
F	Force.
F_c	Centrifugal force.
F_d	Drag force.
F_g	Gravitational force.
g	Gravitational field strength ≈ 9.81 N/m.
I	Current.
J	Current density.
k	Boltzman's constant (1.38×10^{-23})
kE	Kinetic energy.
m	Mass.
N_o	Ion density.
pH	Acidity level.
Q	Charge.
Q_v	Volume charge density.
q_{ga}	Gaussian limit charge.
q_{pa}	Pauthenier limit charge.
R	Resistance.
R_e	The Reynolds number.
U	Energy

u	Velocity.
ui	Ion velocity.
V	Potential difference.
Y	Young's modulus.

β	Mobility
ε_o	The permittivity of free space.
ε_r	The relative permittivity.
η	Viscosity.
λ	Wavelength.
ρ	Resistivity.
ρ	Density.
τ	Time constant.
υ	Poisson's ratio.
ψ	Euler's constant (0.577)
Ω	Ohms.
$\mho$	Siemens.

UNIVERSITY OF SOUTHAMPTON

ABSTRACT

FACULTY OF ENGINEERING AND APPLIED SCIENCE
ELECTRICAL ENGINEERING DEPARTMENT

Master of Philosophy

AN INVESTIGATION INTO THE ELECTROSTATIC AGGLOMERATION OF FLY-ASH

By Giles Adrian Cartwright

The removal of solid particulate matter from industrial gasses is of considerable economic and environmental importance. Not least, in the removal of ash particles from the exhaust gasses of electrical power generation plant, reported to be responsible for 47.9% of all solid airborne pollution.

Electrostatic precipitation is the most widely used process for flue gas cleaning in the power generation industries. In coal burning power stations figures of up to 98% volume capture efficiency are not unusual. However, the collection efficiency is very dependent on the particle size and it is known that the smallest of the ash particles evade capture altogether. Ironically it is these smallest particles that can cause the greatest environmental damage as they can drift up into the upper atmosphere, sometimes as far as the troposphere (up to 20km), where they can be transported by air currents for many hundreds of miles. In the lower atmosphere these fine particles will act as nuclei for the condensation of water droplets within rain clouds and any acidity absorbed onto the surface of the particles will dissolve into the water and eventually fall as 'acid rain'.

This thesis is concerned with the study of the electrostatic agglomeration of fly-ash as a pre-precipitation collection efficiency enhancement stage for fossil fuel burning power stations. The principle behind the agglomeration process is to cause the attachment of the finest ash particles to other larger ash particles by electrostatic attraction prior to the ash laden gas stream entering the electrostatic precipitator. Thus shifting the entire particle size distribution of the ash to within the capture size range of the precipitator.

A test rig was constructed that allowed for various electrical and physical parameters to be monitored during the agglomeration process. These included the charge to mass ratio and the dynamic particle size distribution of the ash cloud, both important parameters for monitoring the particle charging and the agglomeration process. A bi-polar charger has also been developed, designed to produce two maximumly charged ash clouds of opposite polarity. Measurements of the mass and charge of precipitated ash particles were able to show some evidence of agglomeration. The degree of agglomeration was also assessed by using the dynamic particle sizing techniques developed in this study.

CHAPTER ONE

INDUSTRIAL GAS CLEANING

Ever since the massive industrial development seen in this country in the latter part of the nineteenth century, control of dust laden emissions from large-scale industrial processes has been of increasing concern.

Although the highest profile use of gas cleaning is for the removal of these unwanted and often hazardous materials from gasses being discharged into the atmosphere, there are several other important industrial considerations.

1.1 RECLAMATION OF INDUSTRIAL MATERIALS

1.1.1 ECONOMIC CONSIDERATIONS

Of particular note here would be the production of silver in smelting plants, where the silver salts in the waste gasses can be captured and the silver re-claimed by an electrolysis process. Other processes such as the refinement of crude oil into petroleum use catalysts that can be re-cycled back into the process. However, the relatively low cost of the catalyst does not always justify the high cost of the highly efficient dust collection equipment that is required[ref 1.1].

1.1.2 THE REMOVAL OF DUSTS FROM AIR STREAMS

Abrasive dusts and other particulate matter will often require removal from the gas streams entering industrial and chemical processes, in order to

reduce the wear on mechanical components further down stream. Even the indoor air quality for certain types of industrial processes is required to be almost purged of all solid matter. Particularly in the micro-electronics industry, where extreme air purities are needed as any dust settling on a micro chip wafer during its construction can completely destroy the electronic device being fabricated[ref 1.2].

1.2 ENVIRONMENTAL CONSIDERATIONS

1.2.1 POLLUTION SOURCES

The sources of air pollution are diverse, coming from both industrial plant and domestic users. As such, it is often difficult to distinguish the exact source of any pollutant as many potential sources are often located together. Factories tend to locate close to one another, in order to be near to their sources of raw materials, power supply, labour force and market. So the result is the close physical proximity of mines, factories, power stations, transport networks and centres of population. So distinguishing the exact source of any atmospheric pollution is not always easy. Table (1.2.1) shows the approximate proportions of the different types of pollution that are caused by various activities, no distinction has been made between the domestic and industrial user. These figures are based on air pollution measurements for the U.S.A..

1.2.2 AESTHETICS

The aesthetic reasons for fine particle capture is simply a case of 'stack visibility'. Finer particles especially in the range 0.2 μm to 2 μm in diameter contribute greatly to the visibility of particle clouds, as they scatter light at a greater angle than the larger particles.

OPERATION	SOLIDS	SULPHUR DIOXIDE	NITROGEN OXIDES	CARBON MONOXIDE
	(%)	(%)	(%)	(%)
HEAT AND POWER GENERATION	47.9	74.9	53.2	2.2
TRANSPORT	6.5	2.3	42.7	76.7
REFUSE DISPOSAL	5.3	0.3	2.9	9.4
OTHER OPERATIONS	40.2	22.4	1.1	11.7

TABLE 1.2.1 SOURCES OF AIRBORNE POLLUTION

1.2.3 HEALTH ASPECTS

A great deal of work has been carried out, by many researchers, into the damage caused by the inhalation of particulate matter into the human respiratory system. Early studies into the retention of such solid matter showed that particles larger than 10 μm in diameter were either not inhaled or if inhaled were captured in the upper respiratory system from where they would be removed by the normal wafting action of the cilia. Also it was noted that particles with a diameter of less than 1 μm in diameter were not effectively retained by the lungs[ref 1.1]. So initially the size range of 1 μm to 10 μm was considered to be of greatest importance with regard to human health.

More recent work has shown that the deposition of particles within the lung of a diameter of less than 1 μm is also significant, especially if the particles are either charged or contain absorbed toxins / irritants. It has been shown that particles as small as 0.01 μm in diameter are in fact inhaled and deposited within

the deepest regions of the lung[ref 1.3].

1.2.4 ACID RAIN

Acid rain has been considered responsible for the destruction of thousands of acres of forestry in many continents of the world, along with the poisoning of many lakes and rivers. Some of the worst cases of this pollution can be seen in Canada, where the industrial waste gasses from the east coast of the U.S.A. are reputed to be the cause of acidic rain water. Also extreme pollution in north eastern Europe caused through acidic rain has been blamed on the industrial exhaust from the U.K.

1.2.4.1 AIR POLLUTION FROM POWER STATIONS

The burning of fossil fuels for heat and power generation contribute greatly to the emissions of particulate matter, sulphur dioxide and nitrogen oxides as well as other pollutants. As was shown in Table (1.2.1). These oxides will either be emitted in the gas phase or will be adsorbed onto the surface of the particulate matter. However, the burning of different fossil fuels will produce different proportions of the pollutants, even the same fuel type mined from a different location will produce different proportions of the pollutants. Table (1.2.2) shows the ranges of the pollutants that can be measured in power plant stack emissions, from power stations that have not been retrofitted with desulphurization or denitrification units[ref 1.4].

1.2.4.2 DISPERSION

More than 90 % of the man made emissions of sulphur dioxide come from the industrial and urbanised areas of Europe, North America, India and the Far East. The majority of these emissions are made through tall stacks, up to 100 meters tall, injecting the pollutant way up into the troposphere. The emissions will then rise to a height, (up to 20 km) depending on the prevailing conditions, until the temperature of the rapidly cooling gasses and the surrounding air are equal. A discreet plume will then be carried away at that

level. Exactly what then happens to the plume will again be dependent on the prevailing weather conditions.

POLLUTANTS	FOSSIL FUEL			
	COAL	OIL	GAS	PEAT
	(ppmv)	(ppmv)	(ppmv)	(ppmv)
SO_2	400-3000	500-3000	-	100-1000
NO	300-1300	250-1300	200-500	100-1000
NO_2	10-40	10-40	10-30	3-30
CO	-	-	100	2000-5000
HYDROCARBONS	10-60	100-2000	100-2000	30
HCl	80	-	-	-

(ppmv) = parts per million by volume

TABLE 1.2.2 LEVELS OF POLLUTION MEASURED IN STACK EMISSIONS FROM POWER PLANT

1.2.4.3 DEPOSITION OF THE POLLUTANTS

The pollution will eventually return to the ground. This may be after a very short period through dry-deposition, or the plume may be carried many hundreds of kilometres away in the prevailing air current and eventually fall as an acidic rain. The drawing in Figure (1.2.1) shows these deposition processes[ref 1.5].

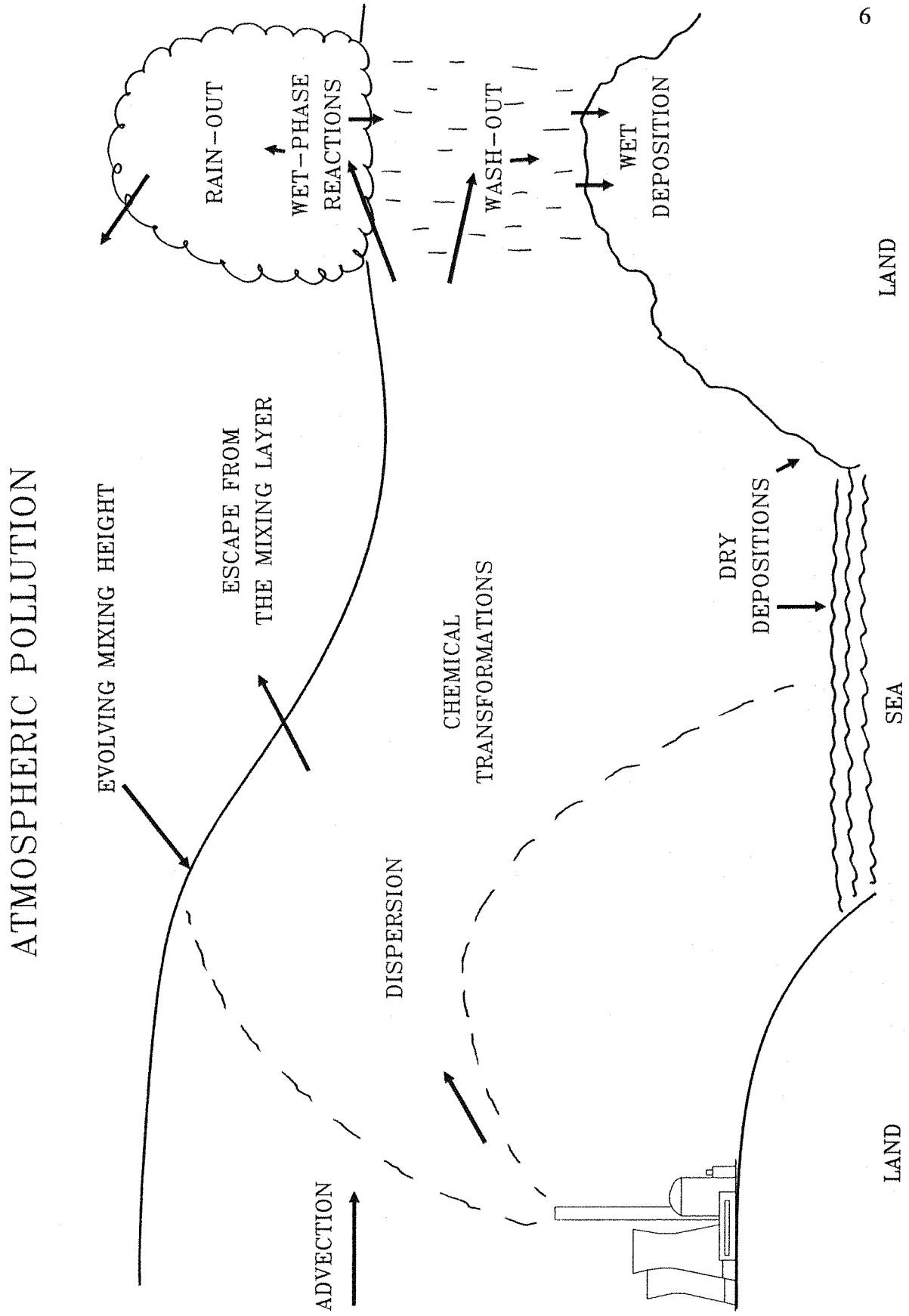

FIGURE 1.2.1 PROCESSES INVOLVED IN THE DISPERSION AND DEPOSITION OF AIR-BORNE POLLUTION

1.2.4.3.1 DRY DEPOSITION

The particulate matter, along with the adsorbed oxides of sulphur and nitrogen, may simply fall to the ground through the process of gravitational settlement. This is known as 'dry-deposition' and will occur within a few days of the original dispersion and hence will be close to the original pollution source. Once on the ground the oxides can react with the ground water to produce acidity. However, this acidity is not a major cause for concern, as these acids will react with the natural buffer systems within the soil to produce neutral salts. Table (1.2.3) gives a list of the naturally occurring acidity buffers, along with the range of pH they can counter[ref 1.4].

BUFFER SYSTEM	BUFFER RANGE (pH)
Calcium carbonate - bicarbonate	8 → 6.2
Silicate - bicarbonate exchange	6.2 → 5
Cation exchange systems	5 → 4.2
Hydrated aluminium hydroxide exchange	4.5 → 2.8
Iron exchange	3.8 → 2.4

TABLE 1.2.3 SOIL ACIDITY BUFFER SYSTEMS

1.2.4.3.2 WET DEPOSITION (ACID RAIN)

The term 'Acid Rain' was first used by Robert Angus Smith in 1872 to describe the acidic nature of the rain falling around Manchester in one of his early reports as the first 'Chief Alkali Inspector' of the U.K.

The processes that involve a water phase reaction within the atmosphere which then cause the pollutant to reach the ground by precipitation are collectively known as 'wet-deposition' and include the acid producing reactions giving rise to 'acid rain'. These process are also summarised in Figure (1.2.1).

1.2.4.4 RAIN DROP FORMATION

The very fine particulate matter within the plume will act as nuclei for the condensation of water droplets within a rain cloud. The water will then collect and react with the oxides adsorbed onto the surface of the particle in a very efficient process known as 'rain-out' also shown in Figure (1.2.1). Of a lesser importance is the process of 'wash-out', this is the mechanism whereby the falling precipitation becomes attached to the particulate and gaseous pollutants within the plume, causing them to deposit on the ground. This wash out process is not significant in the production of acid rain, as the time available for the pollutants to react with the water is very short and on reaching the ground the oxides will react with the natural buffers within the soil producing neutral salts, as listed in Table (1.2.3).

1.2.4.5 CHEMICAL REACTIONS

1.2.4.5.1 NATURAL ACIDITY

Not all the acidity within rain water is caused by industrial or domestic pollution, some is naturally occurring.

The source of this natural acidity is carbon dioxide reacting with water, both of which occur naturally within the atmosphere. The aqueous reactions of carbon dioxide, to produce a carbonate and a bicarbonate are as shown in reactions (1.2.1) to (1.2.3). Both the carbonate and the bicarbonate will readily reduce to donate a proton, hence the rain water will be acidic.

$$CO_2 + H_2O \rightleftharpoons H_2CO_3 \qquad \textbf{Reaction (1.2.1)}$$

$$H_2CO_3 \rightleftharpoons HCO_3^- + H^+ \qquad \textbf{Reaction (1.2.2)}$$

$$HCO_3^- \rightleftharpoons CO_3^{2-} + H^+$$ **Reaction (1.2.3)**

Calculations of this natural acidity have been made in order to asses the contribution to measured acidity of the pollutants. These show that the cloud water would naturally range between pH 4.5 and pH 5.6

1.2.4.5.2 MAN MADE ACIDITY

The pollutants absorbed into the water droplets during the rain-out process now react with the water to create acid solutions. These reactions are known as 'wet-phase' reactions.

Table (1.2.2) showed the pollution from burning fossil fuels to consist of mainly the oxides of sulphur and nitrogen. These now react with the atmospheric water to produce sulphuric and nitric acid, both of which contribute to the acidity that is found in acid rain water.

SULPHURIC ACID FORMATION

Reaction (1.2.4) shows the reaction of the dissolved sulphur dioxide gas with the water to produce sulphuric acid. The sulphuric acid will then reduce to a bisulphite ion and 'donate a proton' (a +Ve hydrogen ion), reaction (1.2.5).

$$SO_2 + H_2O \rightleftharpoons H_2SO_3$$ **Reaction (1.2.4)**

$$H_2SO_3 \rightleftharpoons H^+ + HSO_3^-$$ **Reaction (1.2.5)**

A further proton can be generated by the further reduction of the bisulphite ion, shown in reaction (1.2.6). However, this reaction will not be seen in cloud water, as the equilibrium of the reaction would not allow the sulphite ion to exist. If it were to form it would be instantly oxidised back to the bisulphite form.

$$HSO_3^- \rightleftharpoons H^+ + SO_3^{2-}$$ **Reaction (1.2.6)**

The level of acidity in rain water that would be caused by reactions (1.2.4) and (1.2.5) when considered with the acidity produced naturally from the reaction of the carbon dioxide with water, would produce an acidity of only pH 4.9. However, higher levels than this can be recorded in rain drops, so other mechanisms beyond the simple dissolution of sulphur dioxide must therefore be involved in the formation of the acidity from sulphur dioxide.

This process is the acidification through oxidation of the dissolved bisulphate ions by oxidising agents such as ozone, hydrogen peroxide, peroxyacylnitrates or other free radicals. These reactions are shown in reactions (1.2.7) and (1.2.8).

$$O_3 + HSO_3^- \rightarrow HSO_4^- + O_2$$ **Reaction (1.2.7)**

$$H_2O_2 + HSO_3^- \rightarrow HSO_4^- + H_2O$$ **Reaction (1.2.8)**

The sulphate ions produced are acidic and can reduce to donate a proton, as shown in reaction (1.2.9).

$$HSO_3^- \rightleftharpoons H^+ + SO_4^{2-}$$ **Reaction (1.2.9)**

NITRIC ACID FORMATION

The nitric acid is formed from the nitrogen oxides produced in the combustion process. These reactions take place partly in the dry-phase and partly in the wet-phase. Reactions (1.2.10) and (1.2.11) are the gas-phase reactions which produce nitrogen peroxide. While the formation of the nitric acid occurs in the wet-phase as soon as the nitrogen peroxide comes into contact with

the water, this is shown in reaction (1.2.12).

$$O_3 + NO_2 \rightarrow NO_3 + O_2 \qquad \textbf{Reaction (1.2.10)}$$

$$NO_3 + NO_2 \rightarrow N_2O_5 \qquad \textbf{Reaction (1.2.11)}$$

$$N_2O_5 + H_2O \rightarrow 2HONO_2 \qquad \textbf{Reaction (1.2.12)}$$

The nitric acid produced can now reduce to provide a proton, as shown in reaction (1.2.13).

$$HONO_2 \rightleftharpoons H^+ + NO_3^- \qquad \textbf{Reaction (1.2.13)}$$

1.2.4.6 OTHER DEPOSITION MECHANISMS

Some of the pollutants can escape above the mixing layer, as can be seen in Figure (1.2.1), these tend to be the very finest of the particulate matter known as 'Aitken nuclei' (0.005 μm to 0.1 μm). These can then remain suspended in the atmosphere for many years and only return to ground level, through the processes already described, after forming clumps with other fine particles.

1.2.4.7 ACID RAIN PRECIPITATION

The pollutants may be dispersed by turbulent eddying. However, they may also accumulate if the weather conditions remain constant. Slow moving high pressure areas with low advection and dispersion rates will concentrate pollutants. When these eventually meet an advancing low pressure system, all the wet deposition mechanisms occur, and the pollutants will fall as acid rain. This may often be several hundreds of kilometres away from the original source of

the pollution.

Such conditions occur over northern Europe and eastern U.S.A., where extremely high levels of acidic precipitation can be measured. The map in Figure (1.2.2) shows the mean rain water pH measured during the late 1970^{s} [ref 1.6]. Large areas of northern Asia and America show acidity values between pH 5 and pH 5.5 which lie within the range of calculated natural acidity of rain water from the naturally occurring carbon dioxide within the atmosphere. However, there are large areas shown to receive rainfall with acidity levels over ten times the natural level, with a pH figure of less than pH 4.5, these areas are the east coast of the U.S.A. and parts of northern Europe. The most acidic conditions are found in Denmark, southern Sweden and the north of New York state U.S.A., where acidity levels as high as pH 4, nearly 40 times the naturally occurring level can be recorded.

If the map in Figure (1.2.2) were to be superimposed onto a map showing the prevailing wind directions and strengths, it is possible to draw some conclusions as to the sources of this global acidity. The prevailing wind over northern Europe is a westerly.

1.2.4.8 THE CONSEQUENCES OF ACID RAIN ON PLANTS

The range of acidity found within acid rains falling directly onto the ground can be adequately dealt with by the naturally occurring buffer systems within the soil. These buffers were listed in Table (1.2.3).

1.2.4.8.1 DIRECT FOLIAGE INJURY BY ACIDITY

There is no real evidence that the wet deposition of acidic rain waters onto the leaves of plants causes any direct injury to the foliage. However, this wet deposition should not be ignored as a stress causing factor, which could result in the long term reduction in plant growth and reproduction.

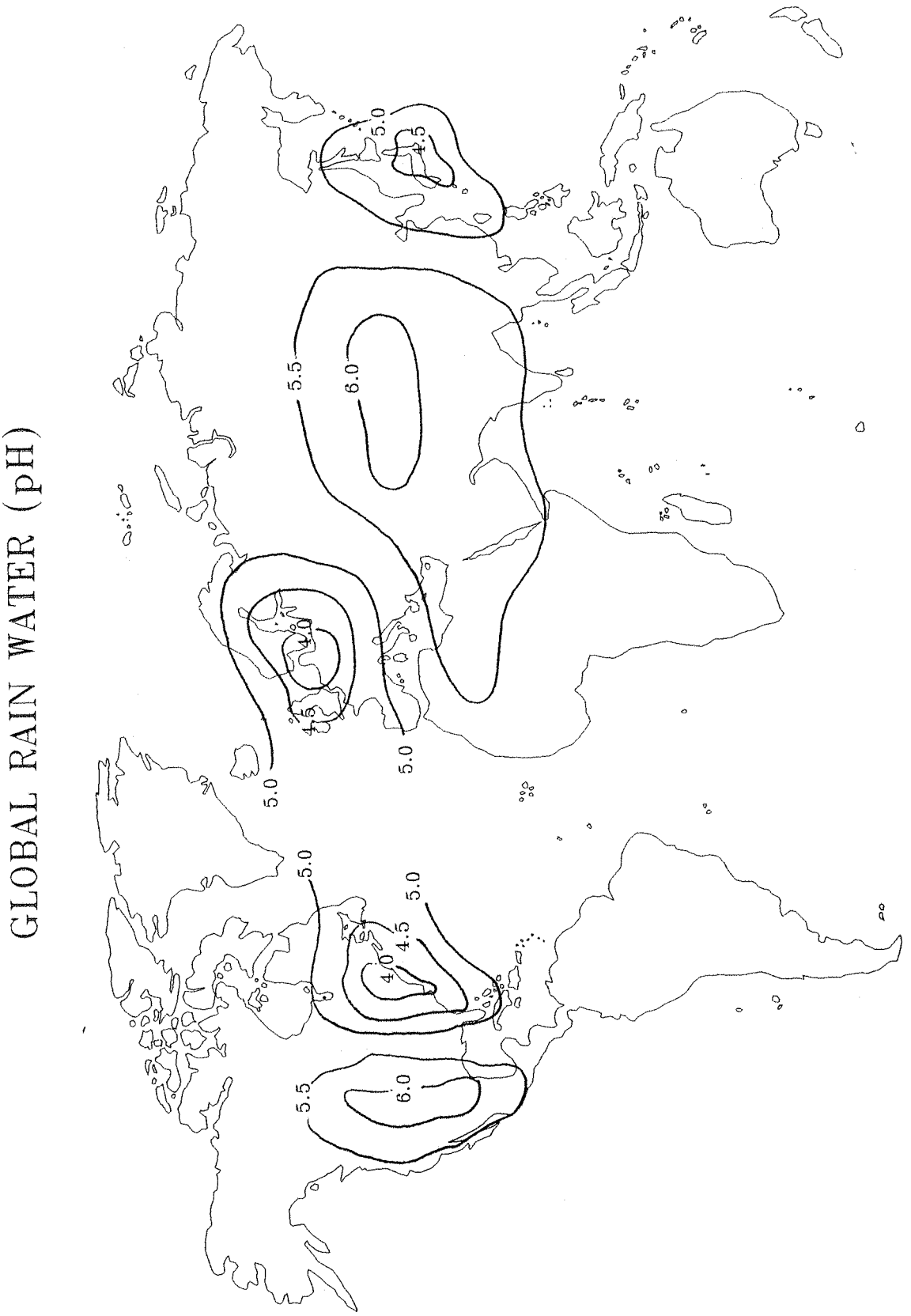

FIGURE 1.2.2 MAP OF GLOBAL RAINFALL ACIDITY

1.2.4.8.2 FOLIA LEACHING OF CATIONS

Acidic rain can cause the leaching of cations such as potassium, calcium and magnesium from the leaves of many plants species. However, these cations may then accumulate in the soil at the base of the plant, where an increased uptake by the roots should balance the depletion from the leafs.

So within the range of acidification expected from acid rain it is unclear why plant life especially evergreen forestry is seen to suffer. The only conclusion that can be drawn is that the effect is the result of stress caused by the combination of more than one factor.

1.2.4.9 THE CONSEQUENCES OF ACID RAIN ON ANIMALS

A major concern of acidic precipitation is the effect the acidity is having is having on animal life, both in the wild and in captivity. This is of particular concern for aquatic species, as acidity levels in wet habitats can accumulate to a very low pH value.

1.2.4.9.1 FISH

The graph in Figure (1.2.3) shows how the acidity levels of eighty-seven lakes in southern Norway has changed over a 40 year period from the late 30^{s} to the early 70^{s}[ref 1.7].

The short term effects of this acidity on the fish that live in these acidic environments has been studied by Alabaster and Lloyd[ref 1.8] and are summarised in Table (1.2.4). These are only a rough guide as there are considerable differences in the effects seen in different species of fish as well as considerable differences in the effect seen on the same species at different stages of their life cycle.

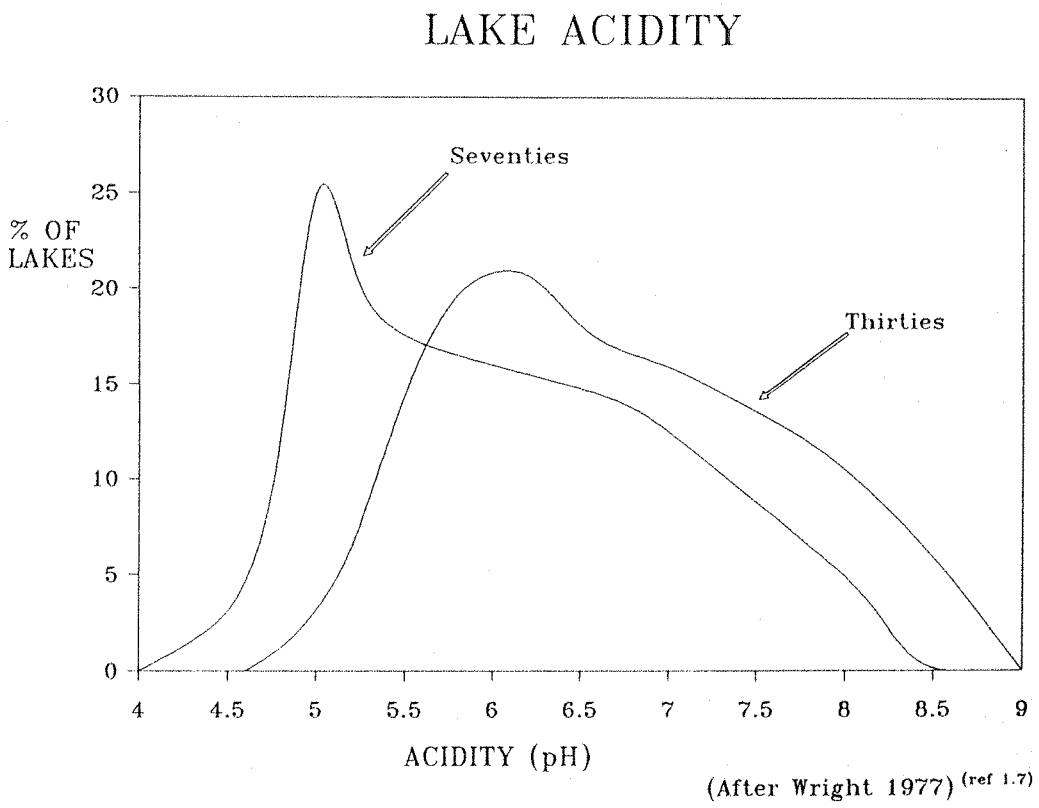

FIGURE 1.2.3 ACIDITY LEVEL INCREASE IN NORWEGIAN LAKES

The main cause of fish death in acidic waters is the loss of essential ions such as sodium and chloride. When the levels of sodium and chloride ions within the blood plasma fall to about a third of their usual value, the body cells swell and the extracellular fluids become too concentrated. Losses of potassium from the cells partially compensates for these losses. However, the loss of potassium will cause a depolarisation of the nerve and muscle cells causing uncontrollable twitching.

1.2.4.9.2 MAMMALS

There are no proven direct effects of the precipitation of acid rain onto mammals. Any indirect effects are due mainly to the quality of drinking water but are also limited. However, some wild animals are suffering as the numbers of other species further down their food chain become depleted, such as fresh water invertebrates and fish.

It has been considered that the greatest risk to humans of acid rain is a general increase in the level of aluminium found in water supplies due to the leaching in the soils of the rain water catchment areas.

ACIDITY LEVEL (pH)	SHORT TERM EFFECTS OF ACIDITY ON FRESH WATER FISH
9 → 6.5	No effect
6.4 → 6.0	Unlikely to be harmful except when carbon dioxide levels are very high (>1000 mg/l).
5.9 → 5.0	Not especially harmful except when carbon dioxide levels are high (>20 mg/l) or ferric ions are present.
4.9 → 4.5	Harmful to the eggs of salmon and trout species (salmonids) and to the adult fish when levels of Ca^{2+}, Na^{+} and Cl^{-} ions are low.
4.4 → 4.0	Harmful to the adult fish of many species which have not been progressively acclimatized to the low pH.
3.9 → 3.5	Lethal to salmonids, although acclimatized roach can survive for longer.
3.4 → 3	Most fish are killed within hours at these levels.

(After Alabaster and Lloyd 1990)[ref 1.8]

TABLE 1.2.4 SHORT TERM EFFECTS OF ACIDITY ON FISH

1.2.4.9.3 BIRDS AND INVERTEBRATES

Most species of mayflies, caddisflies, freshwater shrimps, limpets, snails and beetle larvae are absent from acidic waters at a pH of 5.4 and below. This has a very significant effect on the wildlife that feed on these invertebrates, especially birds. Also the increased levels of aluminium in the diet of the birds can cause imperfect calcification of their eggs, which will then fail to produce live fledglings.

1.3 GOVERNMENT LEGISLATION

1.3.1 HISTORICAL ACTION

The environmental considerations for the removal of particulate matter from industrially generated gaseous exhausts has in recent years become a public concern, which in turn has forced it to become a political issue. However, the condition of the air we breath and legislation are no new companions, first coming together in June 1858, when members of parliament were 'seen racing through the Palace of Westminster holding handkerchiefs to their faces'. The cause of this air-borne stench, later known as the 'great stink' was the pollution in the river Thames to react on an unusually hot day and then waft foul odours through the windows of the Commons. The effect was that within a fortnight Disraeli himself was seen to introduce a bill aimed to curb industrial environmental pollution[ref 1.9]. However, it was not until 1954/55 that government finally passed the clean air act and at last put pressure on industry to clean up its gaseous emissions.

1.3.2 CURRENT OBJECTIVES

Legislation on the control of industrial waste gasses has now become a concern not just of national government, but also international government. In 1988 The Council of European Community Environment Ministers decreed that sulphur dioxide emissions, from existing large combustion plants, should be reduced by 60% on the 1980 levels. It was decided that this should be carried out in three stages; 20% by 1993, 40% by 1998 and 60% by 2003. Agreement was also reached to reduce nitrogen oxide levels by 15% by 1993 and 30% by 1998[ref 1.10].

CHAPTER TWO

GAS CLEANING SYSTEMS

2.1 BASIC GAS CLEANING SYSTEMS

The industrial techniques used in gas cleaning have been reviewed by many workers including Strauss[ref 2.1] and Stairmand[ref 2.2].

The removal of small particles and droplets from a gas stream is a very complex process, especially if high cleaning efficiencies are required from the system involved. The basic mechanisms of particle capture are listed below. However, the actual process of capture may in fact consist of a combination of these mechanisms.

PARTICLE CAPTURE MECHANISMS

1/ Gravitational Separation
2/ Centrifugal Separation
3/ Inertial Impaction
4/ Direct Interception
5/ Brownian Diffusion
6/ Eddy Diffusion
7/ Thermal Precipitation
8/ Electrostatic Attraction
9/ Magnetic Attraction
10/ Brownian Agglomeration
11/ Sonic Agglomeration

2.1.1 SIMPLE SEPARATORS

2.1.1.1 GRAVITY SEPARATION

As stated above, several of these mechanisms will be combined to form the actual process used in the industrial application. The simplest of which is the settlement of dust under the influence of gravity. In this case the dust laden gas stream is passed into a large chamber and the solid particles allowed to fall under the influence of gravity as the gas velocity reduces. A simple gravitational separator is shown in Figure (2.1.1). These settlement chambers tend to be very large and have a very low efficiency, as the gravitational force acting on the individual particles is very low. The gravitational force is also dependent on the particle mass, by equation (2.1.1), So the larger particles will preferentially settle, leaving the finer particles still entrained in the gas stream.

$$F_g = m \times g \qquad \textbf{Equation (2.1.1)}$$

Where: Fg = The force on the particle due to gravity.
m = The mass of the particle.
g = The gravitational field strength.

In a practical situation, a gravitational settlement chamber will only be effective in the removal of particles with a diameter greater than 100μm. The capture of particles smaller than this would require excessively long settlement chambers, as the rate of settlement is proportional to the square of the particle radius, (Stokes's law).

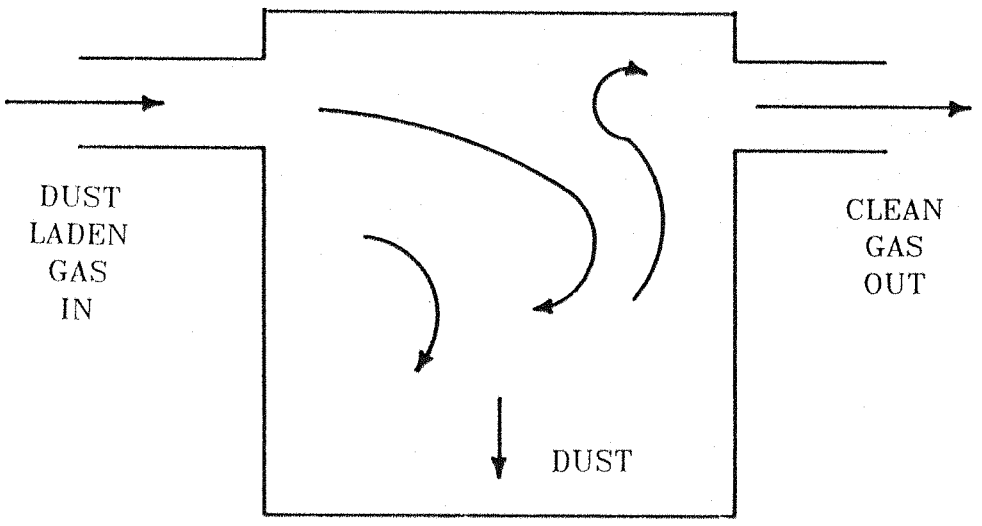

FIGURE 2.1.1 GRAVITATIONAL SETTLEMENT CHAMBER

2.1.1.2 MOMENTUM SEPARATION

The efficiency of the simple settlement chamber, such as the one shown above, can be improved and its size reduced by giving the solid particles a downward momentum as they enter the chamber. This force then combines with the gravitational force to increase the system efficiency. Four different versions of this type of device are shown in Figure (2.1.2).

By giving the particles an initial momentum in the direction of the collection and then turning the gas flow through a fast corner, a greater efficiency of collection of the suspended solids is achieved than by the settlement process alone. However, the very finest particles will still simply follow the air flow back out of the separator.

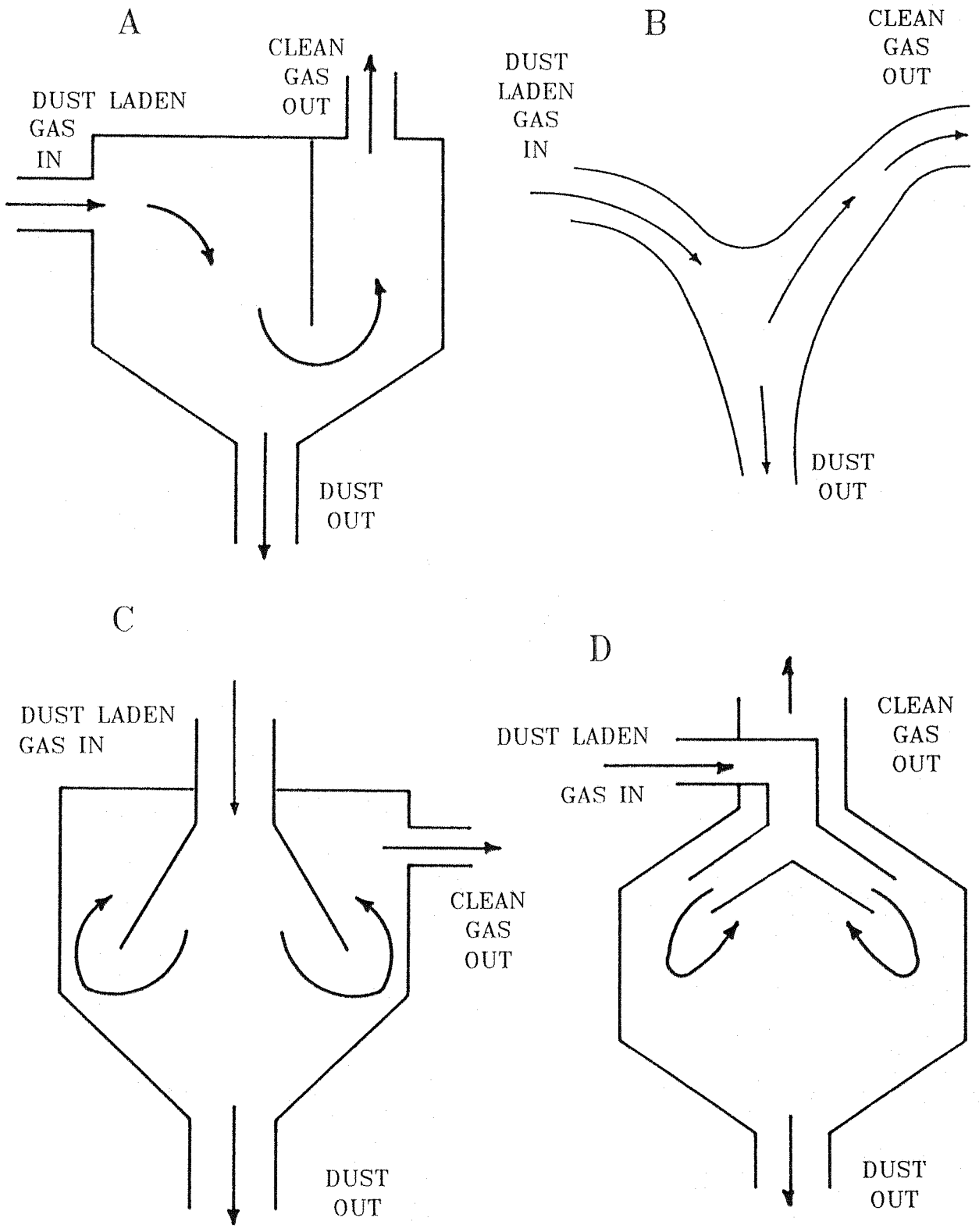

FIGURE 2.1.2 **MOMENTUM SEPARATORS**

A/ Simple baffle type. B/ Rounded inertial type.

C/ Downward facing entry. D/ Accelerated settling chamber.

2.1.2 CENTRIFUGAL SEPARATOR

The next step up from the gravitational and momentum settlement chambers is centrifugal separation. In this case the gas is passed into a cylindrical sectioned vessel and caused to rotate. Solid particles entrained within the gas stream will have a centrifugal force acting upon them. This force will be normal to the tangent of the arc, i.e. at 90° to the flow of the gas. This separation system is illustrated in Figure (2.1.3) and defined by equation (2.1.2).

$$F_C = m \frac{U_T^2}{R} \qquad \textbf{Equation (2.1.2)}$$

Where: F_c = The centrifugal force.
m = The mass of the particle.
U_T = The tangential component of the gas velocity.
R = The radius of the arc.

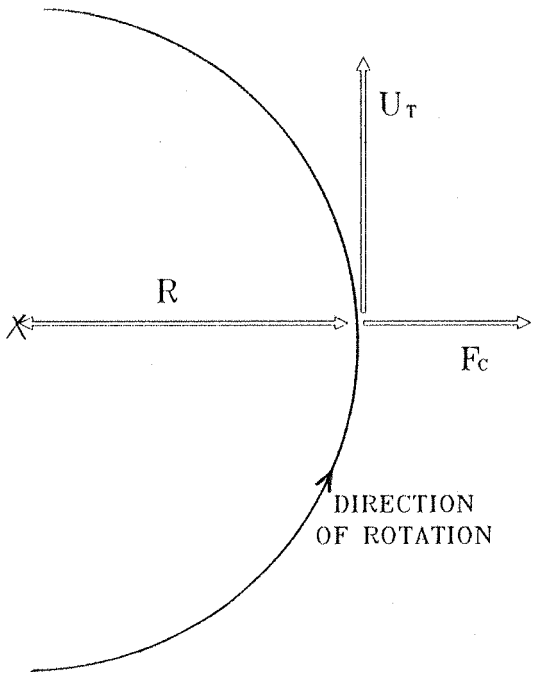

FIGURE 2.1.3 CENTRIFUGAL FORCE

The rotating gas will form a vortex along the outer wall of the separator, extending along the entire length of the unit. The velocity of the gas within this vortex increases towards the base of the unit, where the bulk flow of the gas changes direction and the gas vortex returns up the centre and out of the gas outlet. The particles within the gas will be forced to the outer edge of the unit, where they will work their way down the walls to the dust hopper at the base. Any fine particles that remain suspended in the vortex by the time it reaches the base of the unit will be expelled from the gas as it changes direction. A diagram of a cyclone centrifugal separator is included in Figure (2.1.4).

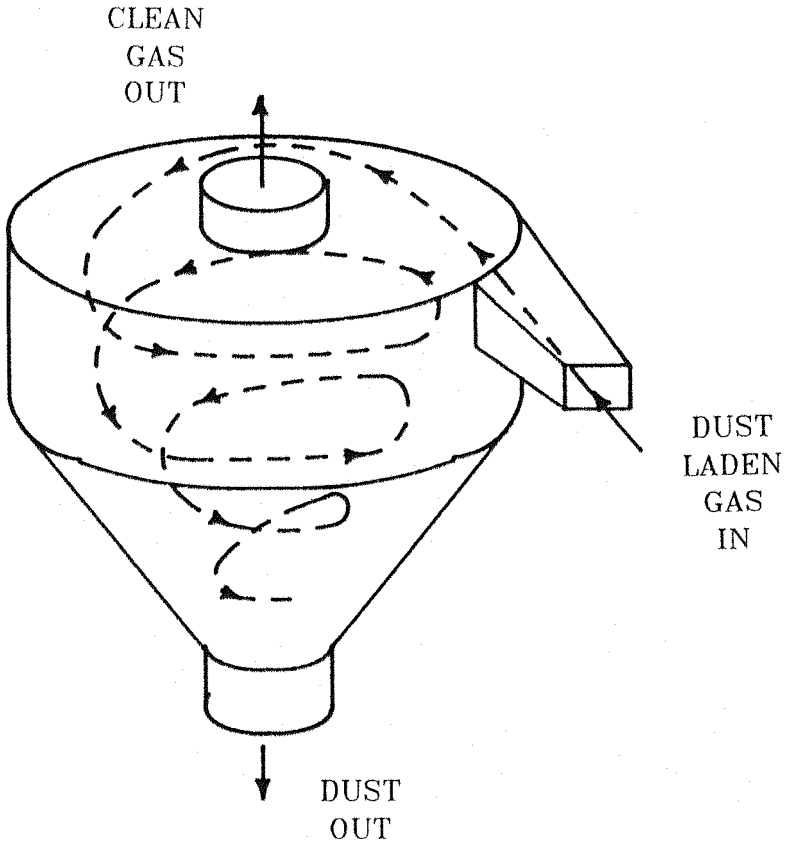

FIGURE 2.1.4 CYCLONE TYPE CENTRIFUGAL SEPARATOR

The time taken for the particles to migrate out of the gas stream and hence the efficiency of the separation is going to be proportional to the centrifugal force F_c. From equation (2.1.2) we can see that this force will be proportional to the mass of the particle, which is proportional to the cube of the

particle diameter. So again the finer particles will be harder to capture. The efficiency of a cyclone separator is also inversely proportional to the gas flow throughput, as there will be less time for the particles to migrate out of the flow in a faster system.

Cyclones are in fact most useful in removing particles down to 10μm in diameter, after which point their efficiency falls off very quickly with the reduction of particle size[ref 2.3].

2.1.3 FILTERS

In simple terms a filter works in exactly the same way as a domestic vacuum cleaner. The dust laden gas if forced to flow through a fabric mesh and the dust is removed from the gas by becoming attached to the bag. The actual mechanisms involved in the capture of the particles are quite complex and efficiencies of dust retention exceed the simple sieving theory, as particles with diameters far smaller than the gaps between the fibres are captured.

The basic building block of a fabric filter is the fibre. These are far bigger than the particles which they capture and are woven into a mesh. There are four basic mechanisms of particle capture, these are shown in the diagram in Figure (2.1.5) and are summarised below:

1/ Direct Interception

A particles will be captured if the streamline it is following passes within half a particle diameter of the fibre, in which case the particle will collide with the fibre and be retained.

2/ Inertial Impaction

When the streamline a particle is following is deflected so that it passes the fibre at a distance greater than half the particle diameter, the particle can still become attached to the fibre if it has enough inertia to leave the streamline and stay on a collision course with the fibre.

3/ Brownian Motion

Particles of a very small diameter come into contact with the fibre due to their own random motion. This motion known as 'Brownian motion' and can even be against the nett flow, as is shown in Figure (2.1.5).

4/ Electrostatic Attraction

Particles which are not on a collision course to the fibre nor whose streamline would pass within half a diameter of the fibre, may still become attached to the fibre if there is an electrostatic force of attraction between the particle and the fibre.

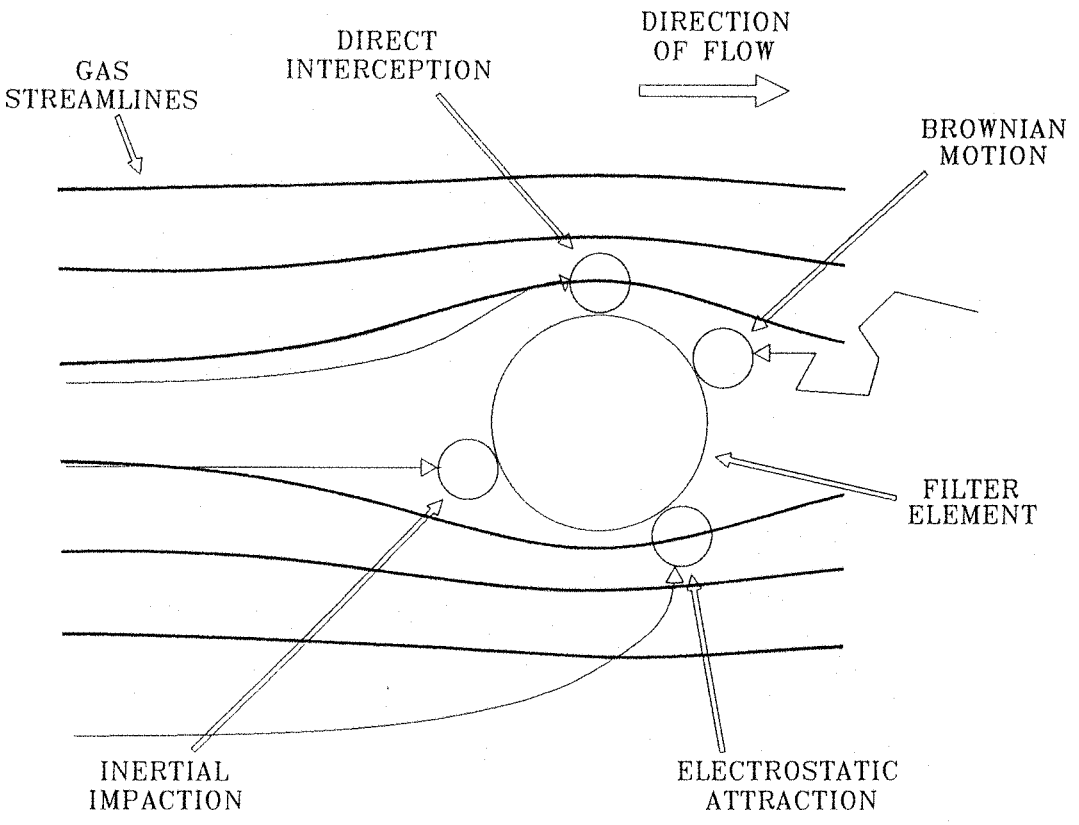

FIGURE 2.1.5 FILTER FIBRE SHOWING THE MECHANISMS OF PARTICLE CAPTURE

A layer of captured particles will build up on the surface of the filter. This will increase the capture efficiency of the filter but at the expense of an

increased pressure drop across the filter.

The efficiency of a filter can actually be increased without having to pay the penalty of an increased pressure drop across it. By enhancing the electrostatic force of attraction between the filter fibres and the particles through either charging the particles or the filter or both.

2.1.4 WET SCRUBBERS

A dust laden gas stream may also be cleaned by the use of a wet scrubber, in which the mass of the solid particles is increased through their impingement with water droplets in the form of a fine spray. The solid is then collected in a wet slurry, which usually requires further treatment. A simple wet scrubber is shown in Figure (2.1.6), where the dust laden gas passes through a fine water spray. This type of device is only really effective for larger particles. However, it is often used as a pre-cleaner stage, particularly where the removal of the bulk of the material and an increase in humidity with a lower gas temperature would increase the efficiency of the subsequent stage, as is the case with electrostatic precipitation.

The wet scrubber is effective for the capture of particles down to a few micrometres. The particle size capture range can be further increased by electrostatically charging the aerosol and the dust laden gas stream in opposite polarities. In this case high collection efficiencies are achievable for dust particles with diameters of a fraction of a micrometre[ref 2.3].

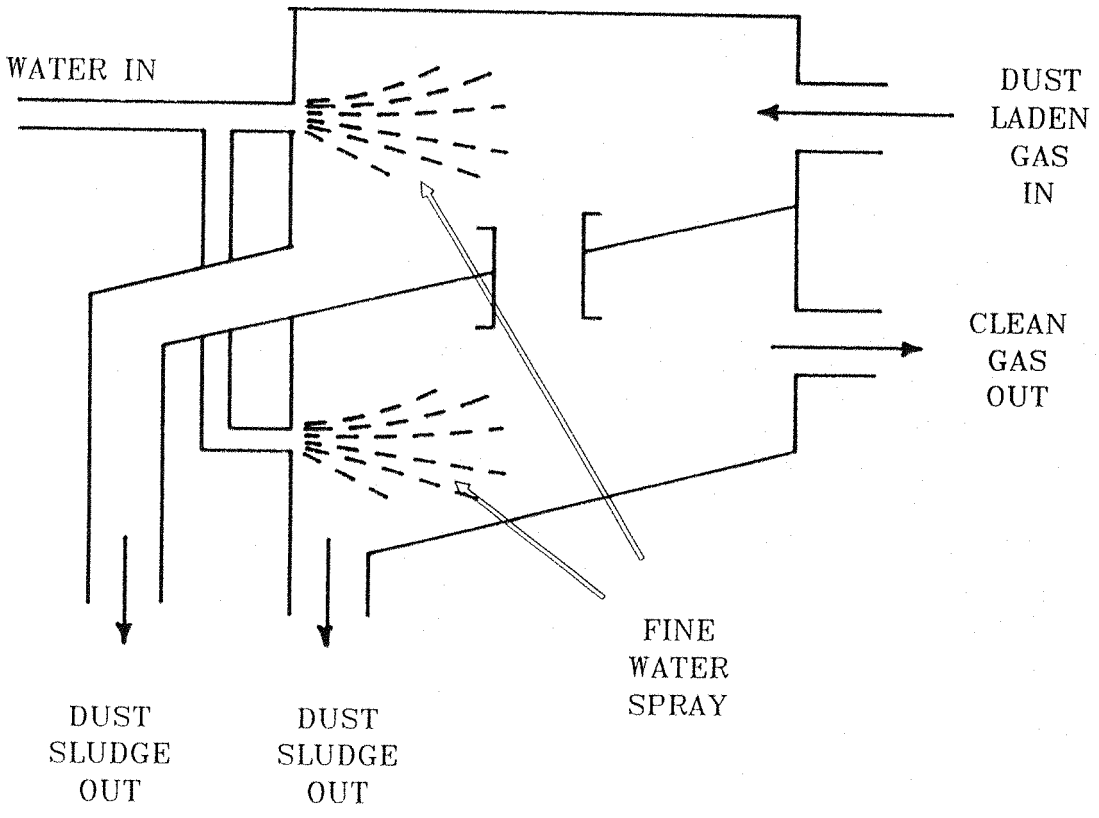

FIGURE 2.1.6 SIMPLE WET SCRUBBER

2.2 ELECTROSTATIC GAS CLEANING SYSTEMS

Many of the disadvantages discussed above for these simple separator systems are overcome by the use of an electrostatic precipitation system. In an electrostatic precipitator (E.S.P.) the solid particles are given an electrical charge and then collected by their attraction towards a plate with the opposite charge. In theory very high collecting efficiencies are possible over the entire range of particle sizes, with very little adverse effect on the gas flow.

2.2.1 HISTORICAL DEVELOPMENT

The first recorded observations of electrostatic phenomena are credited to the early Greek philosophers, with workers such as Thales (640 - 548 BC)[ref

[2.4] who reported on the attractive properties of amber spindles which had become charged in the silk spinning process. We can still find references to this early greek work in our language, one example being the word electrical or electron which comes from the greek word for amber 'ελεκτρου'.

Little progress was then seen for the next 2000 years until the English scientist, William Gilbert (1540 - 1603), physician to Queen Elizabeth I, discovered that materials other than amber could be made to exhibit electrostatic attraction. He is also credited with the classification of materials into '*electrics*' and '*non-electrics*'; electrics being materials that could be frictionally charged and non-electrics being materials that would not charge.

William Gilbert also wrote that a rubbed '*electric*' would 'entice smoke sent out by an extinguished light'[ref 2.5]. This is the first recorded reference to the use of electrostatic phenomena for gas cleaning.

Gilberts '*electric*' and '*non-electric*' model was then not modified until the next century when in 1733 DuFay stipulated that there were two different forms of electricity[ref 1.1]. The first he called '*resinous*' and was found by rubbing materials such as amber, thread and paper. The second was '*vitreous*' which was found in materials like glass, rock crystals and precious stones. He also noted that bodies charged with the same type of electricity were found to repel one another whilst bodies of the opposite electricity were found to be attracted to one another. DuFay also stipulated that these two types of electricity were weightless fluids. This two fluid theory of DuFay's was at that time opposed by Benjamin Franklin's one fluid theory[ref 1.1], where '*vitreous*' electricity was conceived to be an excess of fluid, (i.e. a positive quantity of fluid) and '*resinous*' electricity being a lack of fluid, (i.e. a negative quantity of fluid). Although we now know that there are two types of charge, we have dropped the words vitreous and resinous in favour of positive and negative.

Work in electrostatics then continued in a qualitative manner until the end of the 18th century, when a quantitative study of electric phenomena was undertaken by Charles de Coulomb in the years 1785 - 1789[ref 2.6]. This work of Coulomb's defined the now well known inverse square law for electrostatic forces.

i.e. The force 'F' between two equally charged bodies with charge 'q' and a separation 'd' is defined by:-

$$F = C \frac{q^2}{d^2} \qquad \textbf{Equation (2.2.1)}$$

Where: C is the constant $\dfrac{1}{4\pi\ \varepsilon_o\ \varepsilon_r}$ **Equation (2.2.2)**

Where: ε_o = The permittivity of free space.
ε_r = The relative permittivity.

Over two hundred years after William Gilbert demonstrated the enticement of smoke, M. Hohfield built in 1824[ref 2.7] a laboratory device to demonstrate the removal of smoke contained in a bottle, using an electric spark. This work was also repeated in 1858 by C. F. Guitard[ref 1.1] but in this case using a silent Corona discharge.

In 1883 Sir Oliver Lodge[ref 2.8], the British Physicist, proposed in an article in 'Nature' that smog and smoke pollution could be removed from the air in cities by some form of electrostatic precipitation. Two years later in 1885 Walker and Hutchings[ref 1.1], working under the guidance of Sir Oliver Lodge produced the first commercial electrostatic precipitator. This unit designed for a lead smelting works in Bagellt, North Wales was however of very limited success. The unit was powered by the then only type of high voltage generator available, the Wimshurst machine. These generators were found to be unreliable and particularly dependent on the ambient conditions in which they were working. The choice of a lead smelting plant was also unfortunate for a first precipitator, as lead oxide forms a particularly fine dust with a very high resistivity, both of which render electrostatic precipitation difficult.

Other scientists working on electrostatic precipitators at this time include Karl Moeller[ref 1.1] who, working independently in Brockwede, Germany, developed his own precipitator and was awarded a patent for his machine in 1884. There is however no record of the commercialization of this machine.

Work on electrostatic precipitators again seemed to come to a halt and it was not until 1907 when Frederick G. Cotterell[ref 2.9 & ref 2.10], professor of chemistry at the university of California revived the technique and successfully used it for industrial gas cleaning. Cotterell used the methods described by Hohlfeld and Guitard to collect the acidic mist emitted by a sulphuric acid plant. Cotterell was able to overcome the previous power supply problems of Lodge, by utilising the recently developed synchronous mechanical rectifier[ref 2.11]. The use of such machines as a means of powering precipitators has remained with us as the primary type of power supply up until the 1940's.

The success of Cotterells precipitator in controlling acid fumes led to a vast and rapid expansion in the use of such devices in other areas of industrial air purification. The most important of which was the electrical power generation industries, where precipitators are used to remove the ash particles from the flue gasses of fossil fuel fired power stations. The volume of ash captured from a modern coal burning power station can amount to thousand of tons every day.

From the production of the first Cotterell machine, up until the present day the systems of particle charge and capture have been studied and documented by many scientists, although there has been no major change to the basic design philosophy.

2.2.2 BASIC PRINCIPLE OF OPERATION

In an electrostatic precipitator a dust laden gas stream is fed past an electrode system consisting of sharply pointed discharge electrodes and flat collector electrodes.

The sharp electrodes are energised into a corona discharge and as the dust laden gas passes through the precipitator the particles become charged by the gaseous ions from the corona discharge. The charged particles then migrate under the influence of the electric field to the flat plate electrodes. The collected layer of ash can then be removed, usually by rapping the collector electrodes. This much simplified model of an electrostatic precipitator is illustrated in Figure (2.2.1). A block diagram of the different steps of the electrostatic precipitation process is given in Figure (2.2.2).

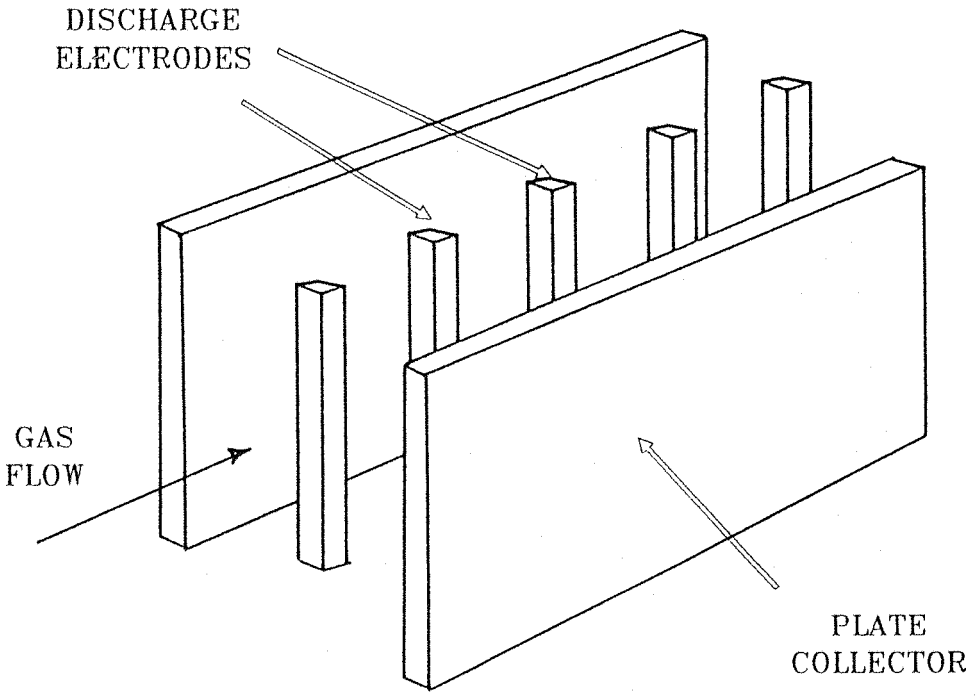

FIGURE 2.2.1 SIMPLE ELECTROSTATIC PRECIPITATOR

Commercial units would typically have more than one charging/collection stage, three stages being most common. These units would also have a very large number of high voltage electrodes and hence corona generation points.

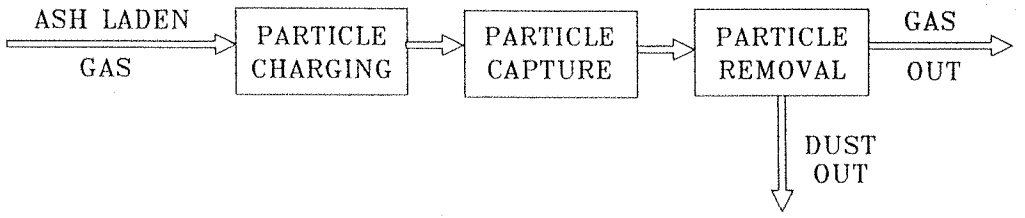

FIGURE 2.2.2 BLOCK DIAGRAM OF AN ELECTROSTATIC PRECIPITATOR SYSTEM

2.3 AGGLOMERATION

Electrostatic precipitation of solid matter from a gas stream is very efficient. In coal burning power stations a figure of 98% collection efficiency for fly-ash is not unusual. However, the collection efficiency is very dependent on the particle size of the ash. It is known that the very smallest of the particles still evade capture from this simple precipitator system. This deficiency in the range of particle sizes that can be caught may be solved by causing the finer particles to form clumps of agglomerates

The principle behind the agglomeration process is to somehow attach the finer particles to one another or to larger particles prior to passing the ash laden gas stream through the precipitation system. Thus shifting the entire particle size range of the solids to within the capture range of the electrostatic precipitator. The block diagram in Figure (2.2.2) can now be modified to show the addition of the agglomeration unit. This new block diagram can be seen in Figure (2.3.1).

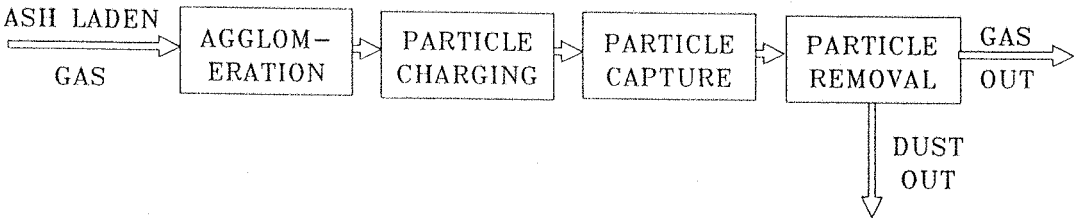

FIGURE 2.3.1 BLOCK DIAGRAM OF AN ELECTROSTATIC PRECIPITATOR SHOWING THE LOCATION OF THE ADDITIONAL AGGLOMERATION STAGE

It is intended to form this agglomeration of the ash particles by producing an electrostatic force of attraction between the particles. This should form a bond between the particles strong enough to allow electrostatic precipitation without breaking the agglomerate. To create this force of attraction opposite charges will have to be induced on the ash particles. So the gas stream will have

to be split and one half charged positively while the other half is charged negatively. The two streams will then have to be rejoined and mixed in such a way as to allow particles with opposite charges to become within an adequately close proximity to have a significant attractive force acting between them. This mixed stream will then have to be allowed a time of minimum turbulence for the particle migration to occur and the bonds to form. Thus the block diagram for the agglomeration stage can now be drawn as in Figure (2.3.2).

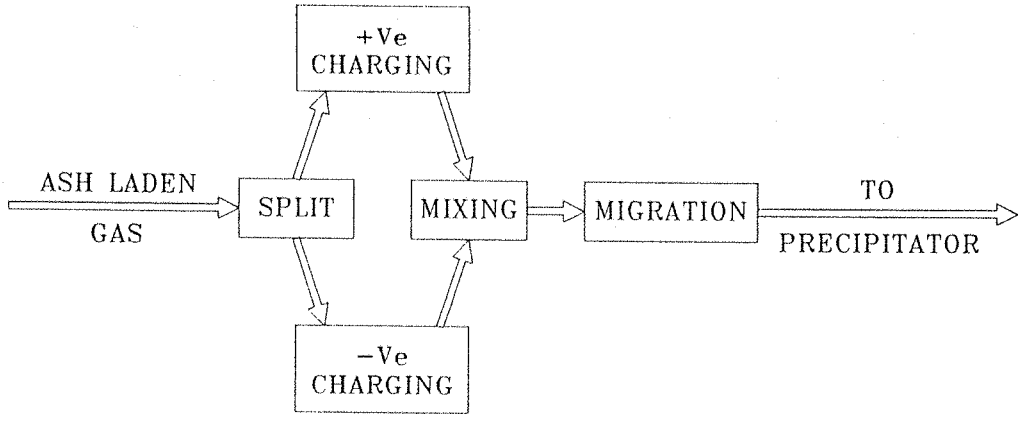

FIGURE 2.3.2 BLOCK DIAGRAM OF THE AGGLOMERATION STAGE

CHAPTER THREE

THEORETICAL CONSIDERATIONS

3.1 CHARGING MECHANISMS

We have seen in the previous chapter that the first stage of the agglomeration process is to split and then bi-polarly charge the ash laden gas stream. Splitting the flow is relatively straight-forward and can be done quite simply by fabricating a central 'barrier' within the exhaust duct from the furnace. However, the charging of the two ash streams is more complex.

In the charging of solid particulate matter, which is what we have in the case of fly-ash, several charging mechanisms are possible. These include Contact charging, Frictional charging (otherwise known as tribo electrification), Induction charging and Corona charging.

The method of charging to be considered in this study is the Corona. Corona charging has been chosen as historically no other method of exhaust particle charging has been found to be satisfactory[ref 3.1]. Also, the process is less dependent on the ambient conditions than other mechanisms, although it is the least power efficient of all the methods available.

3.1.1 CORONA DISCHARGE

The mechanisms of the Corona discharge have been investigated extensively by many researchers since the production of the first precipitator. This work was started by Townsend[ref 3.1] in the early 1900^s but it was Loeb working at the University of California[ref 3.2] who is credited with developing the fundamental theories of the corona discharge. His work started in 1930 and continued into the 1970^s. Other notable researchers working in this field at the

same time were Von Engel working at Oxford University[ref 3.3] and Goldman[ref 3.4]. All of these studies have contributed greatly to the understanding of the fundamental theories of the corona generation and the development of the current / voltage relationship and electrical field equations that form the basis of the present precipitator technology.

A corona discharge is produced when a high voltage is applied between two electrodes, one of which has a small radius of curvature. This non-uniform field causes an electrical discharge near to the sharp electrode, at voltages well below the spark breakdown voltage of the electrode system. A typical electric field plot for this configuration is illustrated in Figure (3.1.1).

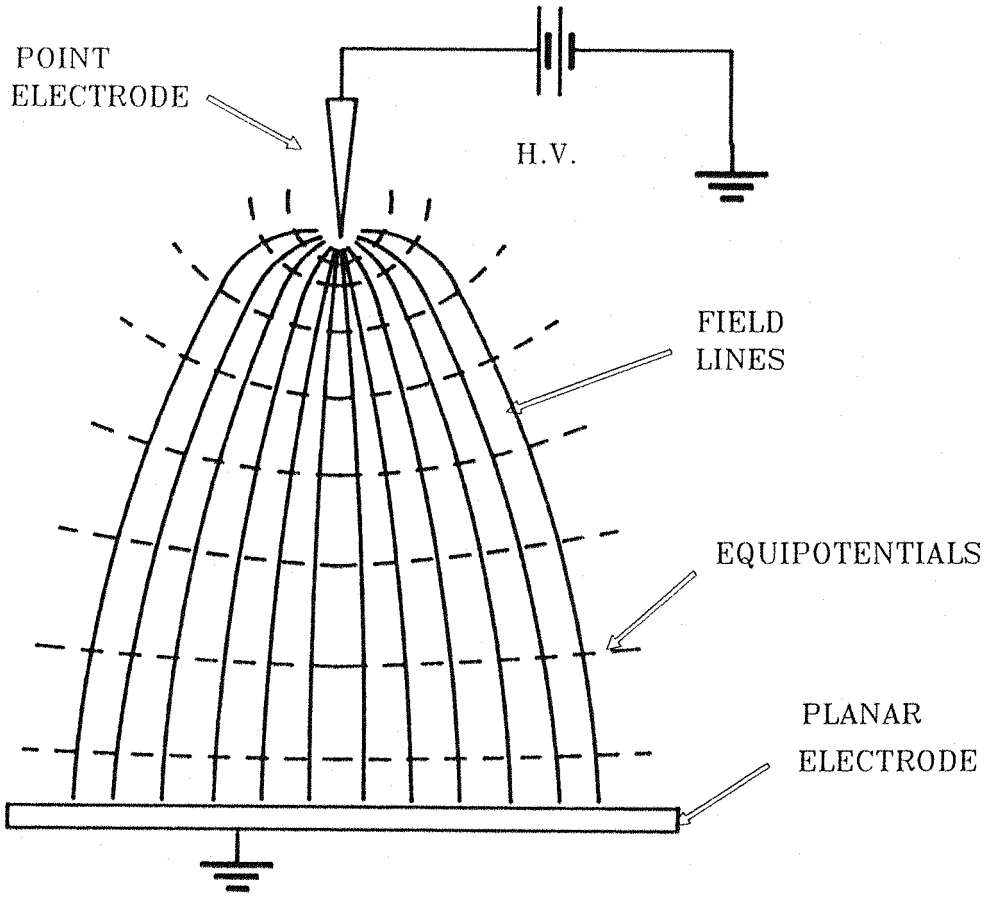

FIGURE 3.1.1 TYPICAL CORONA ELECTRODE SYSTEM

In air, the corona discharge can both be seen and heard. The corona will hiss or spit and emit a blue to red glow. The noise and the colour of the light emitted will be dependent on such factors as the polarity of the pointed electrode, the corona current and the molecules available within the gas for ionization. The term 'corona' comes from this luminous glow which is often seen manifesting itself in the shape of a crown.

Initiation of the corona discharge requires the availability of free electrons within the gas at the field intensification region, surrounding the pointed discharge electrode. Such free electrons are produced by the random ionization of gas molecules into a positive ion and an electron. This ionization will only occur when the molecule is excited by some form of radiation. This is usually in the form of cosmic rays or photo ionization by ultra violet light along with other naturally occurring radio activity. The free positive ion and electron are now acted upon by the electric field and migrate towards the negative and positive electrodes respectively. Any electrons that are within the high field region of the corona discharge electrode will be accelerated to high velocities, due to their high electrical mobility. Should these electrons then collide with a neutral gas molecule, one of several reactions may occur.

The first is that neither the electron nor the gas molecule is affected by the collision. In which case the collision is considered to be 'elastic' and all the kinetic energy is conserved. This reaction can be represented by the expression:

$$A + e^- \rightarrow A + e^-$$ **Equation (3.1.1)**

Where: A = The gas molecule.
e^- = The electron.

Secondly, if the kinetic energy of the electron is great enough some of that energy will be absorbed by the gas molecule during the collision. The gas molecule will thus be excited to a higher energy state. While the electron is then free to continue its journey under the influence of the electric field at a reduced speed, the gas molecule will recover its stable energy state by radiating a quantum of light. This reaction can be represented by the expression below:

$$A + e^- + kE \rightarrow A^* + e^- \rightarrow A + e^- + hv$$ **Equation (3.1.2)**

Where: A = The gas molecule.
e^- = The electron.
kE = kinetic energy.
A^* = The excited gas molecule.
hv = A quantum of light.

The wavelength and hence the colour of the quantum of light radiated will be dependent on the electron energy band structure of the gas molecule energised in the collision. Exciting the gas molecule moves one or more of the outer electrons from a less energetic band to a more energetic band. The energy gap between these two bands is constant. When the atom within the gas molecule relaxes to its original energy state the electrons return to their original band releasing this step of energy in the form of a quantum of light. The electron energy band structure is a property of the atoms within the gas molecule itself.

The third possibility of this collision is the formation of a positive ion and the liberation of a further electron. The two electrons then accelerate away, under the influence of the electric field, towards the positive electrode, while the positive ion moves away in the opposite direction, towards the negative electrode. This ionization of the gas molecule to produce a second electron is the avalanche effect which is characteristic of the corona discharge. This ionization process is represented by the expression:

$$A + e^- \rightarrow A^+ + 2e^-$$ **Equation (3.1.3)**

Where: A = The gas molecule.
e^- = The electron.
A^+ = The ionized gas molecule (positively charged).

The final possible outcome of the collision is the formation of a single negative ion:

$$A + e^- \rightarrow A^- + h\nu \qquad \textbf{Equation (3.1.4)}$$

Where: A = The gas molecule.
e^- = The electron.
A^- = The ionized gas molecule (negatively charged).
hv = A quantum of light.

Again any excess energy from this reaction may cause a quantum of light to be radiated from the gas molecule.

These reactions are repeated many thousands of times each second within the corona region and are self sustaining, i.e. no further external energization is required to continue the ionization process. So, a large number of charged ions and electrons are generated which then move off under the influence of the electric field.

If the sharp discharge electrode were positive with respect to the planar electrode then the discharge is called a positive corona. Conversely, if the point were at a negative potential with respect to the plate then we have a negative corona.

In a positive corona the electrons are accelerated towards the positive point, where the field strength is becoming greater and greater. These electrons thus become very energetic and frequently cause further ionizations of the gas molecules with which they collide. All these electrons rush towards the positive point causing the corona avalanche to develop. Meanwhile the positive ions with their lower mobility drift towards the negative plate. This moving positive space charge tends to reduce the field strength around the positive point electrode as a part of the electric field will be dropped between the positive ions and the grounded plate, thus producing a negative feedback effect, stabilizing the avalanche discharge.

In the case of the negative corona, the electron avalanche again develops within the high field region around the corona point but this time the electrons move away from the point source, where the field strength is reducing. Thus any collisions that occur in this region tend to have less kinetic energy and a greater tendency to form negative ions which then migrate outward towards the positive plate. This negative cloud of ions will then stabilize the corona discharge by reducing the field around the negative point electrode, in much the same way as the positive ions reduce the positive corona.

In both the positive and negative corona, the active ionization only exists in close proximity to the discharge point, while most of the space between the two electrodes constitutes the 'drift' region, in which only one polarity of ions exist. It is these ions which then serve to charge the dust particles.

The mechanism of the corona avalanche is schematically illustrated in Figure (3.1.2).

3.1.1.1 CORONA AVALANCHE SUMMARY

-Each collision between an electron and a neutral gas molecule is seen to produce another electron and a positive ion.

-In a positive corona the electrons move towards the positive point becoming more and more energetic as their velocity increases. While the positive ions formed in the collisions drift out of the high field region towards the negative plate to form the positive ion flux.

-In a negative corona the electrons move out away from the point electrode, where their collisions become less energetic and are more likely to form negative ions. These negative ions then migrate out of the high field region towards the positive plate to form the negative ion flux.

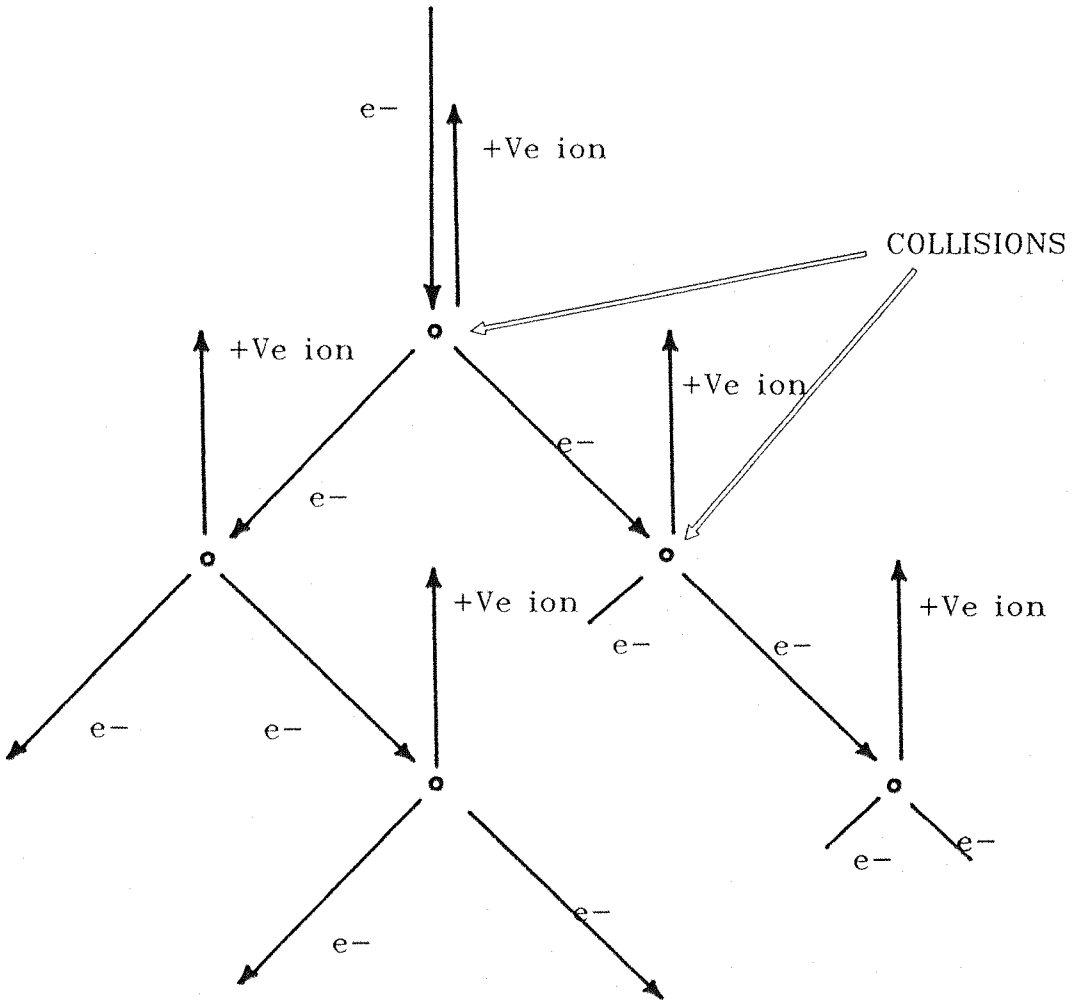

FIGURE 3.1.2 CORONA AVALANCHE

3.1.2 PARTICLE CHARGING

We have now seen how both the negative and the positive gas ions are produced by a corona discharge. We must now consider the mechanism by which these ions become attached to the dust particles in order to impart a charge upon them. This charging of the dust particles is considered to take place within the region between the corona glow and the plate electrode, i.e. in the 'drift' region where ions of only one polarity exist.

There are two mechanisms by which these gas ions may become attached

to the dust particle. These mechanisms are generally refereed to as ion bombardment or 'field charging', and ion diffusion or 'thermal charging'. Both of these mechanisms play a part in the charging of particles, although each is more significant for a particular particle size range. Basically a particle with a radius greater than 0.5μm will be predominantly charged by the ion bombardment process, while for a particle sub 0.2μm ion diffusion charging is more dominant.

3.1.2.1 ION BOMBARDMENT CHARGING

The mechanism of ion bombardment or field charging is the attachment of charged gas ions to the dust particle, moving under the influence of the electric field. The amount of charged ions arriving at the particle is thus dependent on the field strength at the particle surface.

Let us first consider a conducting spherical particle placed in a uniform electric field. The field will become distorted as the dielectric constants of the solid particle and the air are different. This distortion can be understood by remembering that the surface of the sphere must be an equipotential. So the field lines must distort in order to remain perpendicular to the equipotentials, as shown in Figure (3.1.3).

The arrow-heads on the field lines point from the positive to the negative electrode. If the field strength is great enough to cause one of these electrodes to go into corona, then the ions formed will travel along the field lines away from the corona and towards the un-charged particle. For a positive corona, positive ions will flow in the direction of the arrows and conversely for a negative corona, negative ions will move in the direction going against the arrows.

As an ion approaches an uncharged particle, the particle will undergo a redistribution of its charge so that the opposite charge to that of the ion will appear on the particle surface nearest to the ion. Thus an attractive force is set up between the ion and its image charge on the polarized particle. This redistribution of the charge is illustrated in Figure (3.1.4).

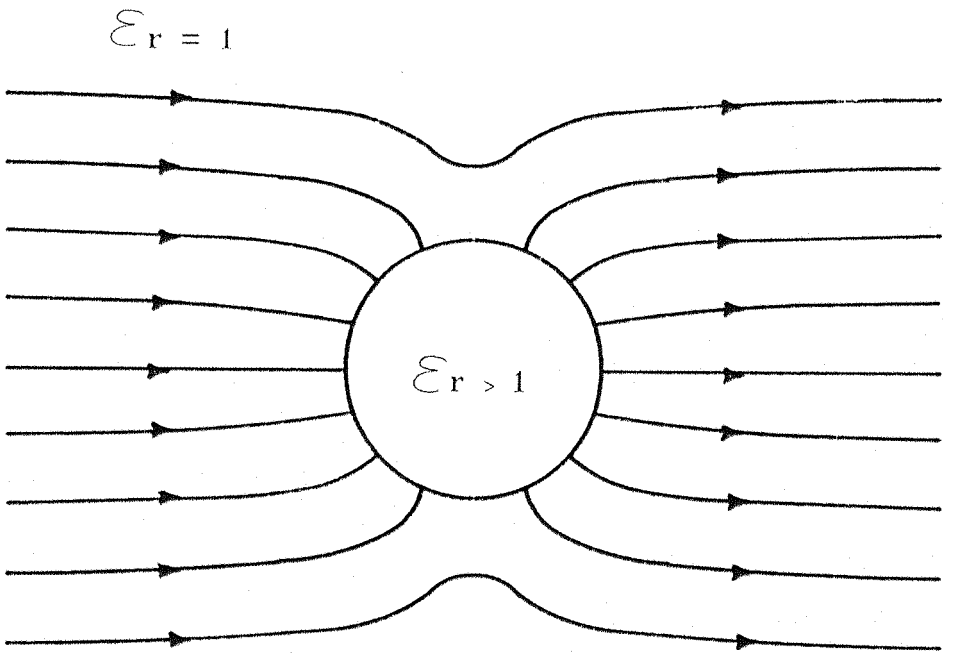

FIGURE 3.1.3 **FIELD DISTORTION DUE TO AN UNCHARGED CONDUCTING SPHERE IN A UNIFORM FIELD**

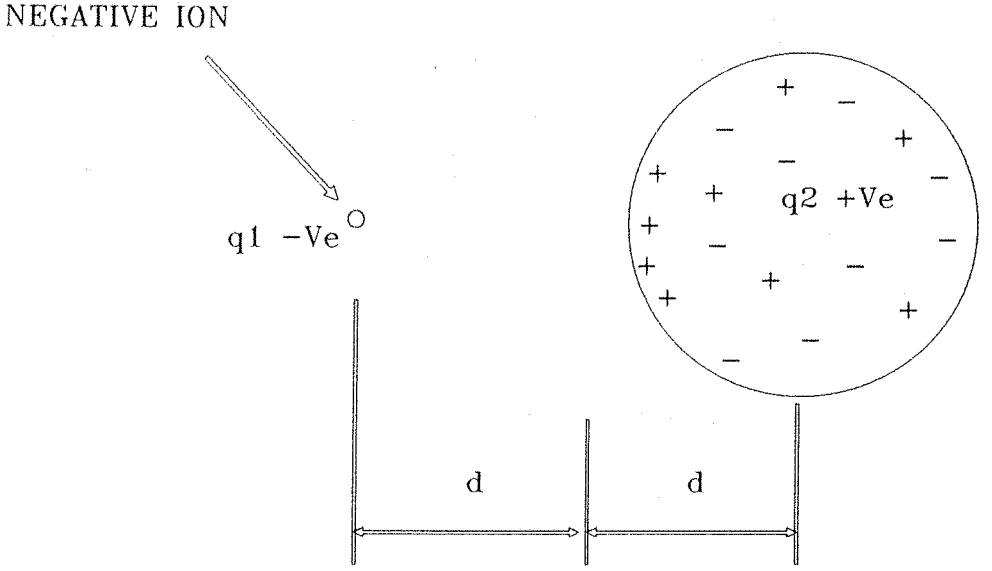

FIGURE 3.1.4 **NEGATIVE ION IN CLOSE PROXIMITY TO AN UNCHARGED PARTICLE**

The induced charge on the surface of the particle can be considered to be an image charge 'q_2' which is equal and opposite to the ion charge 'q_1'. The position of this image charge is also considered to be at a distance, behind the surface of the dust particle, equal to that of the distance between the particle surface and the ion. Hence, the force (F) of attraction between the two can be calculated, using Coulomb's law[ref 2.6]:

$$F = \frac{q_1 q_2}{4\pi \varepsilon_o \varepsilon_r d^2} \qquad \textbf{Equation (3.1.5)}$$

Where:
- F = The Force of attraction.
- q_1 = The charge on the ion.
- q_2 = The induced charge on the particle.
- ε_o = The permittivity of free space.
- ε_r = The relative permittivity.
- d = The distance between the charge q_1 and the image charge q_2.

However, it must be remembered that 'q_2' does not really exist but is only a representation of the charge distribution around the particle surface.

The illustration in Figure (3.1.4) shows the induced positive charge on the surface of the particle due to the approaching negative gas ion. However, it is important to remember that the net charge on the particle at this point remains unaltered.

As the ion becomes attached to the dust particle by the induced force of attraction between the two, they can be considered to be one particle with an increased net charge equal to the amount of charge carried by the ion. The ions from the corona will continue to impinge upon the surface of the particle until such a point that a sufficient electric field is established around the particle to repel any further inbound ions. The field in the vicinity of the particle can now be redrawn, as is shown in Figure (3.1.5).

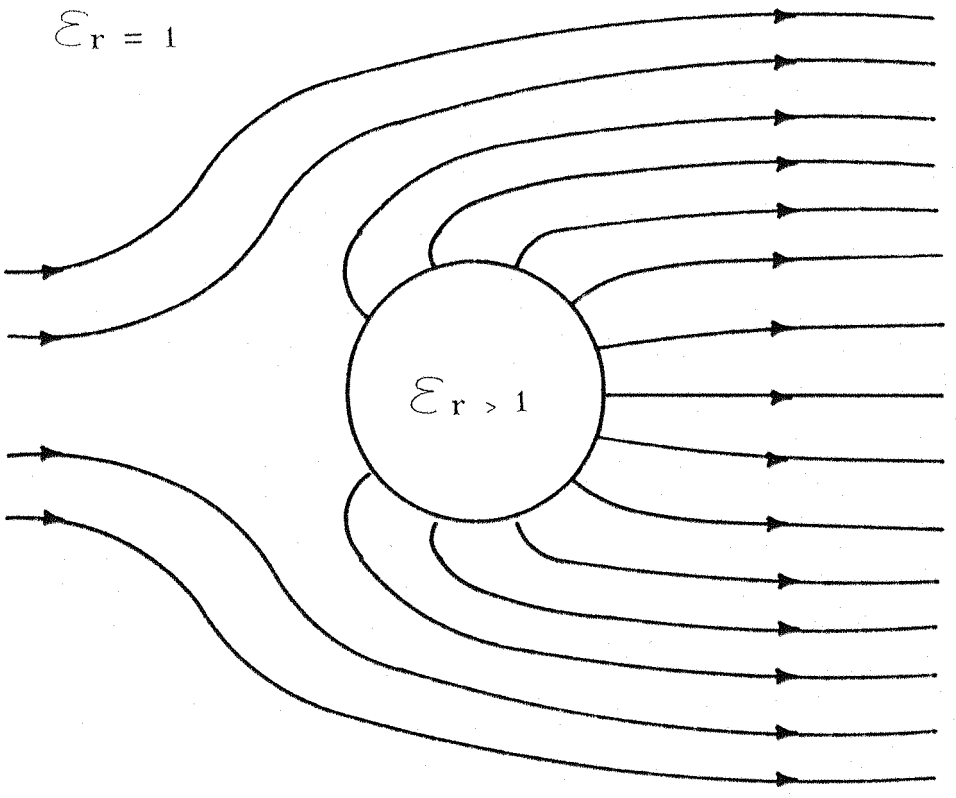

FIGURE 3.1.5 FIELD DISTORTION DUE TO A SPHERE CHARGED TO SATURATION

3.1.2.2 DERIVATION OF THE ION BOMBARDMENT EQUATION

The derivation of this equation is made simple by first making three assumptions.

1/ The particles to be charged are spherical.
2/ The electric field within the charging region is constant.
3/ The field from one particle does not modify the field of another.

The charge on the particle can now be calculated by equating the force due to the distorted field around the particle, to the force of repulsion due to the charge on the particle. This is found by solving Laplace's equation:

$$\nabla^2 V = 0 \qquad \textbf{Equation (3.1.6)}$$

or in cartesian coordinates:

$$\frac{\partial^2 V}{\partial x^2} + \frac{\partial^2 V}{\partial y^2} + \frac{\partial^2 V}{\partial z^2} = 0 \qquad \textbf{Equation (3.1.7)}$$

Solving this equation will require the use of high speed computation and a great deal of time for any fixed geometry. So any solutions are usually made through approximations[ref 3.5].

This calculation was reported by Pauthenier and Moreau-Hanot[ref 3.6] in 1932. They derived an expression for the charge at any instantaneous time, along with an expression for the saturation charge. This saturation charge is commonly known as the Pauthenier limit, and is given by the equation:

$$q_{pa} = 4\pi \varepsilon_o a^2 p E \qquad \textbf{Equation (3.1.8)}$$

$$also\ p = \frac{3 \varepsilon_r}{(\varepsilon_r + 2)} \qquad \textbf{Equation (3.1.9)}$$

'p' will vary between one and three. Three for a conductor ($\varepsilon_r \rightarrow$ inf) and one for an insulating particle ($\varepsilon_r = 1$).

Where:
- q_{pa} = The Pauthenier limit charge for the particle.
- E = The applied field strength.
- a = The particle radius.
- ε_o = The permittivity of free space.
- ε_r = The relative permittivity.

So the charge on a particle is dependent on the field strength, the square of the particle radius, and to a lesser extent, the relative permittivity of the particle. The charge carrier concentration, i.e. the number of ions available for the charging process, does not have an effect on the maximum charge, only the

time taken to reach this charge.

The charge on the particle at any given time can be found by multiplying equation (3.1.8) by:

$$\frac{t}{(t + \tau)} \qquad \textbf{Equation (3.1.10)}$$

Where: t = The time of the charging process.
τ = The time constant for the charging process.

The charging time constant 'τ' is the time taken for a particle to reach 50% of its maximum charge given by Pauthenier, and can be expressed in terms of the ion density and ion mobility within the charging region as:

$$\tau = \frac{4\ \varepsilon_o}{N_o\ e\ b} \qquad \textbf{Equation (3.1.11)}$$

Where: N_0 = The ion density.
e = The charge on an electron.
b = The ion mobility.

Equation (3.1.11) can also be written in terms of the current density and the electric field strength:

As:

$$J = N_o\ e\ u \qquad \textbf{Equation (3.1.12)}$$

and:

$$u = E\ b \qquad \textbf{Equation (3.1.13)}$$

Where: J = The current density.
u = The velocity of the ions in a field E.

So the time constant 'τ' can now be written as:

$$\tau = \frac{4\ \varepsilon_o\ E}{J} \qquad \textbf{Equation (3.1.14)}$$

This charging system time constant 'τ' can now be calculated, assuming typical electrostatic precipitator conditions:

Assume: $E = 5\times10^{5}\ Vm^{-1}$
$J = 3\times10^{-4}\ Am^{-2}$

So solving equation (3.1.14) gives:

$$\tau = \textbf{0.059 Seconds}$$

Hence a particle within the charging field will reach 50% of its Pauthenier limit charge in 0.059 seconds.

Also at any time 't' it will achieve a proportion of its Pauthenier limit charge given by equation (3.1.15):

$$q_{pa} = 4\pi\ \varepsilon_o\ a^2\ p\ E\ \frac{t}{t+\tau} \qquad \textbf{Equation (3.1.15)}$$

The Pauthenier equation can be solved as a function of particle size to give the maximum charge possible by the ion bombardment charging process, i.e. where the solution of equation (3.1.10) tends to 1.

A set of solutions has been worked out for a range of particle sizes, assuming typical precipitator charging conditions for both insulating and conducting particles. The results of these calculations are shown in Table (3.1.1) and are plotted in Figure (3.1.6).

3.1.2.3 GAUSSIAN LIMIT CHARGE

There is also a maximum charge limit that the particles can achieve. After which point the field around the particle will exceed the breakdown field strength of the air and the particle will discharge. This charge limit is called the Gaussian limit, and is defined as:

$$q_{ga} = 4\pi\ \varepsilon_o\ a^2\ E_b \qquad \textbf{Equation (3.1.16)}$$

Where:
- q_{ga} = The Gaussian limit charge.
- ε_o = The permittivity of free space.
- a = The particle radius.
- E_b = The Breakdown field strength of air.

A solution to the Gaussian limit charge for the range of particle sizes is also given in Table (3.1.1), and the result included in the graph in Figure (3.1.6) to allow comparison to the Pauthenier charge limits.

The graph has been plotted on a log/log scale and shows a straight line relationship for both the Gaussian limit charge and the Pauthenier limit charge.

CHARGING FIELD STRENGTHS
Charging Field Strength $E = 5\times10^5\ Vm^{-1}$ (for the Pauthenier solutions)
Breakdown Field For Air $E = 3\times10^6\ Vm^{-1}$ (for the Gaussian solutions)

FIELD STRENGTH ASSUMPTIONS FOR CALCULATIONS OF CHARGING LIMITS

PARTICLE RADIUS	PAUTHENIER LIMIT CHARGE		GAUSSIAN LIMIT CHARGE
	FOR AN INSULATOR $\varepsilon_r \to 1$ so $p \to 1$	FOR A CONDUCTOR $\varepsilon_r \to \infty$ so $p \to 3$	
(μm)	(Coulombs)		(Coulombs)
0.1	5.56×10^{-19}	1.67×10^{-18}	3.34×10^{-18}
0.3	5.01×10^{-18}	1.50×10^{-17}	3.00×10^{-17}
1	5.56×10^{-17}	1.67×10^{-16}	3.34×10^{-16}
3	5.01×10^{-16}	1.50×10^{-15}	3.00×10^{-15}
10	5.56×10^{-15}	1.67×10^{-14}	3.34×10^{-14}
30	5.01×10^{-14}	1.50×10^{-13}	3.00×10^{-13}
100	5.56×10^{-13}	1.67×10^{-12}	3.34×10^{-12}

TABLE 3.1.1 CALCULATED CHARGE LIMITS AS A FUNCTION OF PARTICLE SIZE

The Pauthenier limit charge for a conductor is seen to be about half an order of magnitude greater than that for an insulator. In reality this difference will be even less, as the calculations were made for a perfect insulator ($\varepsilon_r = 1$) and a perfect conductor ($\varepsilon_r = \infty$). Also this difference of half an order of magnitude compares to the two orders of magnitude increase in charge for each order of magnitude increase in radius. So the size of a particle being charged within a corona is more significant to the level of charge achieved than is the particle conductivity.

The Gaussian limit charge is seen to be a straight line, about half an order of magnitude greater than the Pauthenier limit charge for a conductor and running parallel to it. This is as expected, as both of the charge limits are proportional to the square of the particle radius. In fact the Pauthenier limit

equation, for an insulator, reduces to the Gaussian limit equation with only the value used for the field being different.

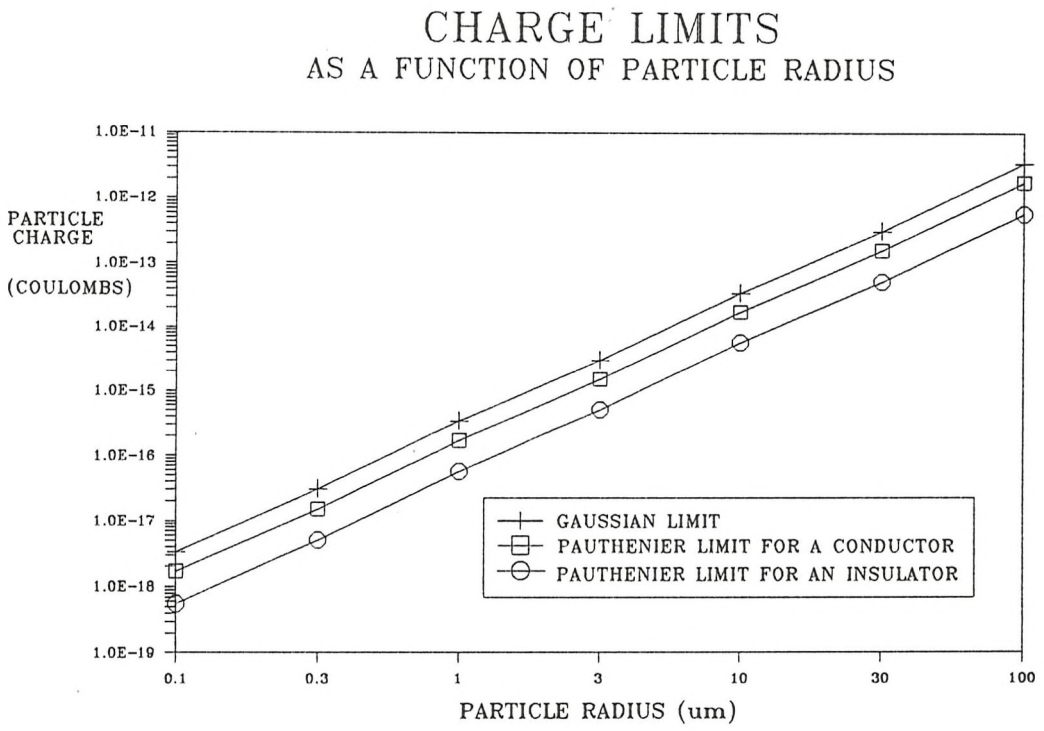

FIGURE 3.1.6 CALCULATED CHARGE LIMITS AS A FUNCTION OF PARTICLE SIZE

Although Pauthenier and Moreau-Hanot worked on spherical particles, other researchers have since shown that particle shape is of little importance[ref 3.7]. So the first assumption made regarding the shape of the particle can be ignored and the Pauthenier limit equation may be used for all particles.

3.1.2.4 ION DIFFUSION CHARGING

Ion diffusion or thermal charging is the process by which the particles become charged due to their random collisions with the charged gas ions and is thus independent of the electric field.

For an ion to impinge upon the surface of a dust particle the energy of its momentum towards the particle must exceed the energy of the repulsive force

from the particle. This Brownian type motion has been studied quantitatively by White[ref 3.8] in 1963 to give an expression for the charge on a particle due to ion diffusion charging. So using the standard kinetic theory of gasses the number of ions with sufficient energy to exceed the electrostatic force of repulsion from the particle and become attached to the particle can be calculated as:

$$N = No \exp(W/kT) \qquad \textbf{Equation (3.1.17)}$$

Where:
- W = The repulsive energy between the ion and the particle.
- N = The number of ions with an energy greater than W.
- No = The number of ions per unit volume.
- k = Boltzman's constant (1.38×10^{-23})
- T = The absolute temperature.

The force W can be found using the expression:

$$W = \frac{q\,e}{4\pi\,\varepsilon_o\,d} \qquad \textbf{Equation (3.1.18)}$$

Where:
- q = The charge on the particle.
- e = The charge on the ion.
- ε_o = The permittivity of free space.
- d = The distance between the ion and the particle.

The rate at which these collisions occur gives the rate of charge accumulation. This is dependent on three factors:

1/ The number density of sufficiently energetic ions.
2/ Their velocities.
3/ The cross sectional area of the particle (πa^2)

So:

$$\frac{dq}{dt} = \pi a^2 N ui = \pi a^2 e ui N_o \exp\left(\frac{q e}{4\pi \varepsilon_o d kT}\right) \qquad \textbf{Equation (3.1.19)}$$

Where: ui = The ion velocity.

This gives the instantaneous charge 'q' at any time 't' as:

$$q = \frac{(4\pi \varepsilon_o a d kT)}{e} \ln \frac{(a N_o q^2 ui t)}{(4 \varepsilon_o d kT)} + 1 \qquad \textbf{Equation (3.1.20)}$$

There is no theoretical maximum charge that can be achieved by diffusion charging as there is always a probability that there will be an ion with sufficient energy to overcome the opposing field of the charged dust particle. Hence the charge is only limited by the particle discharging itself when it reaches the Gaussian limit, given in equation (3.1.16).

3.1.2.5. BOMBARDMENT Vs DIFFUSION CHARGING

We have seen that bombardment charging is dependent on the size of the particle and the field strength, while diffusion charging is less dependent on the particle size but is dependent on the ion concentration and charging time. So it would appear that the larger particles are charged mainly through bombardment charging, while the smaller particles are charged by ion diffusion. This can be best shown by calculating the charge 'q' using equations (3.1.15) and (3.1.20) for a range of different particle sizes and substituting typical electrostatic precipitator values for all the other variables. Typical values are shown in Table (3.1.2) and the calculated results shown in Table (3.1.3). The result of these calculations, for a 10 second charging period, are also plotted in Figure (3.1.7).

TYPICAL PRECIPITATION ASSUMPTIONS	
E	5×10^{5} Vm^{-1}
J	3×10^{-4} Am^{-2}
ui	483.5 ms^{-1}
N_o	$4.7\times10^{+13}$
T	300 K
ε_r	1 (i.e. an insulator)
ε_o	8.854×10^{-12}

TABLE 3.1.2 TYPICAL PRECIPITATOR VALUES USED FOR CALCULATING THE CHARGE LIMITS BY PARTICLE RADIUS

So for this example the charging system time constant 'τ' can be calculated from equation (3.1.14) as:

$$\tau = \frac{4\ \varepsilon_o\ E}{J} \qquad \textbf{Equation (3.1.14)}$$

$$\tau = 0.059 \text{ Seconds}$$

If the graph produced were to be extrapolated back for particles even finer than the 0.1 μm particle considered, then the level of charge achievable by the two charging mechanisms will become even more significant, with the amount of charge from diffusion charging being far greater than that from the ion bombardment charging process. However, for particles much below 0.1 μm the level of charge reached by the process of ion diffusion will become limited by the Gaussian charge limit. Also the levels of charge being considered for particles of this order of magnitude is rapidly approaching the smallest unit of

electric charge, the charge on a single electron (1.6×10^{-19}C), the level of which has also been included on the graph in Figure (3.1.7). So the actual levels of charge that an individual particle can attain will in fact be a multiple of this minimum electric charge.

RADIUS	CHARGE TIME	ION BOMBARDMENT CHARGE LEVEL	ION DIFFUSION CHARGE LEVEL	GAUSSIAN CHARGE LIMIT
(μm)	(Seconds)	(Coulombs)	(Coulombs)	(Coulombs)
0.1	0.1	3.50×10^{-19}	8.00×10^{-19}	3.34×10^{-18}
0.1	1	5.25×10^{-19}	1.44×10^{-18}	3.34×10^{-18}
0.1	10	5.52×10^{-19}	2.08×10^{-18}	3.34×10^{-18}
1	0.1	3.50×10^{-17}	1.39×10^{-17}	3.34×10^{-16}
1	1	5.25×10^{-17}	2.05×10^{-17}	3.34×10^{-16}
1	10	5.52×10^{-17}	2.70×10^{-17}	3.34×10^{-16}
10	0.1	3.50×10^{-15}	2.05×10^{-16}	3.34×10^{-14}
10	1	5.25×10^{-15}	2.71×10^{-16}	3.34×10^{-14}
10	10	5.52×10^{-15}	3.37×10^{-16}	3.34×10^{-14}
100	0.1	3.50×10^{-13}	2.59×10^{-15}	3.34×10^{-12}
100	1	5.25×10^{-13}	3.58×10^{-15}	3.34×10^{-12}
100	10	5.52×10^{-13}	4.31×10^{-15}	3.34×10^{-12}

TABLE 3.1.3 CALCULATED CHARGE LIMITS DUE TO ION BOMBARDMENT AND ION DIFFUSION CHARGING

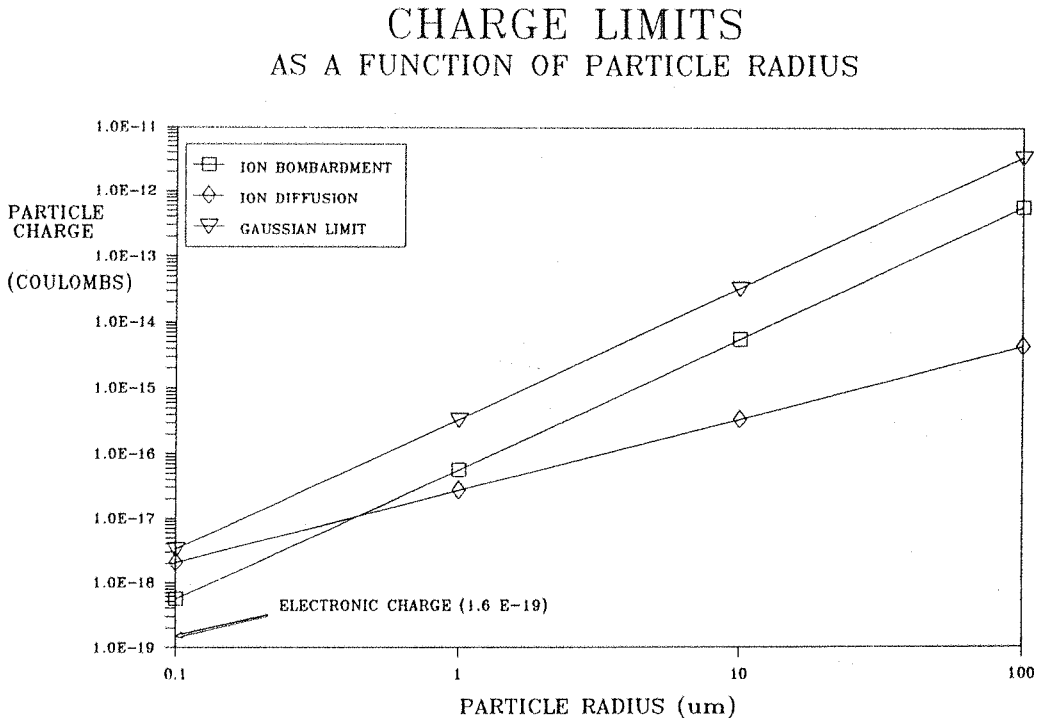

FIGURE 3.1.7 CONTRIBUTIONS TO PARTICLE CHARGE FROM ION BOMBARDMENT AND ION DIFFUSION CHARGING

The ion diffusion process takes considerable time and White[ref 3.8] suggests that, for precipitator charging times, diffusion charging becomes insignificant for all but the very smallest of particles. For this reason the graph in Figure (3.1.7) was plotted for a charging period of ten seconds, to exaggerate the contribution from the diffusion charging process. However, in reality no practical electrostatic precipitator or charging system will have charging periods of this order of magnitude.

3.2 DISCHARGING OF THE PARTICLES

So far in this chapter we have examined the mechanisms by which particles can become charged. We must now consider the mechanisms through which they can lose their charge.

3.2.1 CONDUCTION

The charge on a particle can be lost through the process of ohmic conduction when the particle comes into contact with another object.

3.2.1.1 SINGLE PARTICLE

When a charged particle comes into contact with a grounded object, the charge on the particle will be lost through conduction away to ground. The rate of this charge decay is given by the time constant 'τ' which is a constant of the material of the particle. This time constant is dependent on the permittivity and the resistivity of the particle. This time constant is given by the equation:

$$\tau = \varepsilon_o \, \varepsilon_r \, \rho \qquad \textbf{Equation (3.2.1)}$$

Where:
- τ = The charging/discharging time constant.
- ε_o = The permittivity of free space.
- ε_r = The relative permittivity.
- ρ = The resistivity of the particle.

This process of charge loss can be modeled electrically. The charge can be considered to be held on a capacitor, which then discharges to ground through a resistor. This equivalent circuit is shown in Figure (3.2.1).

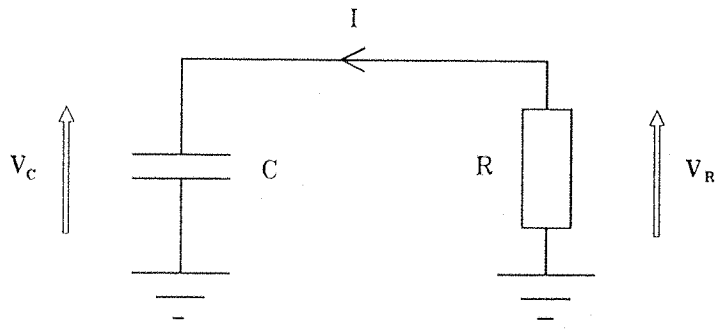

FIGURE 3.2.1 EQUIVALENT CIRCUIT FOR A SINGLE PARTICLE DISCHARGE

The electrical parameters of this simple circuit can de defined by equations (3.2.2) to (3.2.4).

$$V_C = V_R \qquad \textbf{Equation (3.2.2)}$$

$$V_C = \frac{q}{C} \qquad \textbf{Equation (3.2.3)}$$

$$I = \frac{V_R}{R} \qquad \textbf{Equation (3.2.4)}$$

Where:
- V_C = The voltage across the capacitor.
- V_R = The voltage across the resistor.
- q = The charge on the capacitor.
- C = The value of capacitance.
- I = The current flowing to ground.
- R = The value of resistance.

The rate at which the charge flows through the resistor to ground is

proportional to the voltage across the resistor by equation (3.2.4). This voltage is equal to the voltage across the capacitor by equation (3.2.2) and equation (3.2.3) shows that this voltage is proportional to the charge remaining on the capacitor.

So as the charge is lost the voltage across the resistor is reduced and hence the current flowing through it is also reduced. So the rate of charge loss from the capacitor will be reduced. Hence the time constant can be written in terms of the capacitance on which the charge is stored, and the resistance through which it flows as:

$$\tau = R\ C \qquad \textbf{Equation (3.2.5)}$$

Where: τ = The time constant.
R = The value of resistance.
C = The value of capacitance.

Thus the charge is seen to decay exponentially, and the charge loss can be written as an exponent:

$$q = q_o \exp(-t/\tau) \qquad \textbf{Equation (3.2.6)}$$

or

$$q = q_o\ e^{-t/\tau} \qquad \textbf{Equation (3.2.7)}$$

Where: q = The charge after time 't'.
q_o = The charge before time 't'.
τ = The time constant.
t = The time taken for charge to decay from q_o to q.

This equation can also be written in logarithmic form as:

$$\ln q = \ln q_o\ -t/\tau \qquad \textbf{Equation (3.2.8)}$$

or

$$2.3 \log q = 2.3 \log q_o - t/\tau \qquad \textbf{Equation (3.2.9)}$$

3.2.1.2 TWO OPPOSITELY CHARGED PARTICLES

Let us now consider the more complex case of two oppositely charged particles colliding and then discharging to one another. Let us assume that the particles to be considered are the same except that the charge on one of the particles is equal and opposite to the charge on the other. In this case the equivalent circuit can be drawn as shown in Figure (3.2.2).

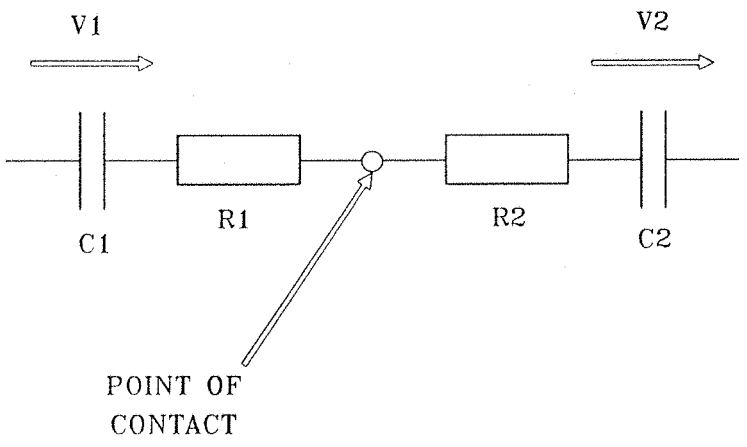

FIGURE 3.2.2 EQUIVALENT CIRCUIT OF TWO OPPOSITELY CHARGED PARTICLES DISCHARGING TO ONE ANOTHER.

Since we are considering the two particles to be identical but oppositely charged, this system can be simplified to the same equivalent circuit as was derived for the single particle discharging to ground, as was shown in Figure (3.2.1) by combining the resistances and capacitances:

$$R_{TOTAL} = R_1 + R_2 = 2R \qquad \textbf{Equation (3.2.10)}$$

$$C_{TOTAL} = \frac{1}{\frac{1}{C_1} + \frac{1}{C_2}} = \frac{C}{2} \qquad \textbf{Equation (3.2.11)}$$

So we have twice as much charge stored on half the capacitance discharging through twice the resistance. So the time constant 'τ' can now be written as:

$$\tau = 2R + \frac{C}{2} \qquad \textbf{Equation (3.2.12)}$$

Since we have twice the charge on half the capacitance, from equation (3.2.3) we can see we have four times the voltage across the capacitor.

As we have four times the voltage across the capacitor, we also have four times the voltage across the resistance, by equation (3.2.2).

So with four times the voltage across twice the resistance, by equation (3.2.4) we have twice the current.

So the rate of the charge decay will be twice that of the single particle discharging to an earthed body. However, we must also remember that we have twice the charge in the case of two particles discharging to one another. So the time taken to decay to a fixed percentage of the total charge will be the same in both cases.

3.2.2 IONIZATION

We have seen earlier in this chapter how particles are charged through the impingement of ions within an electric field. This process can also work the

other way around to discharge the particles.

There are three mechanisms by which the particles can become discharged through the ionization process; exceeding the Gaussian limit charge, random ionization and back ionization.

3.2.2.1 DISCHARGE FROM THE GAUSSIAN LIMIT

In the previous section of this chapter it was shown that there is a defined maximum charge that can be held by a particle, the Gaussian limit. This is the limit of charge on the particle where the field strength at the surface of the particle is equal to the breakdown field of the gas in which the particle is suspended. This charge level is found as:

$$q_{ga} = 4\pi\ \varepsilon_o\ a^2\ E_b \qquad \textbf{Equation (3.2.13)}$$

Where:
- q_{ga} = The Gaussian limit charge.
- ε_o = The permittivity of free space.
- a = The particle radius.
- E_b = The Breakdown field strength of the gas.

The breakdown field strength 'E_b' is the maximum field strength possible at the particle surface for the particle to not discharge. If the particle now moves towards an earthed object or an object with an opposite charge, the field around the particle will distort as the particle becomes polarized. This will result in an intensification of the field in the direction of the opposing object. This locally intensified field will now be above the breakdown field strength of the gas. This will cause the particle to emit ions until the intensified field at the particle surface is less than or equal to the breakdown field strength 'E_b'.

3.2.2.2 RANDOM IONIZATION

A particle can lose charge through the process of random ionization. This ionization will only occur when the particle has been excited by some form of external stimulation or radiation. This could be in the form of cosmic rays or through photo ionization by U.V. light as well as by other naturally occurring radioactivity.

3.2.2.3 BACK IONIZATION

The charge on the dust cloud can be significantly reduced by the mechanism of back ionization. The phenomenon of back ionization is an electrical breakdown in a collected dust layer. This breakdown is caused by the field between the charged layer of ash and the earthed surface on which it has collected, exceeding the breakdown field strength of the layer. At which point a spark will occur. This discharge ejects the dust particles from the local area along with ions of the opposite polarity to those of the corona. These ions will then act to reduce the charge on any particles in the vicinity.

This phenomenon should however be of little significance in the agglomeration process, as it is not intend for the charged ash particles to collect on any of the surfaces of the agglomerater.

3.3 PARTICLE MOVEMENT

The motion of the solid ash particles is dependent on the combination of the forces acting upon them. These forces can be gravitational, electrical or due to the exchange of momentum from collisions with other ash particles or gas molecules. The motion of the ash particles will also be dependent on the gas flow mode and their own momentum, i.e. how well they are entrained within the gas flow.

3.3.1 GAS FLOW MODE

The gas flow within the duct will basically follow one of two flow patterns, laminar or turbulent. The actual mode of flow the gas will take will depend on the gas velocity, the duct size and the physical properties of the gas[ref 3.9]. The mode of flow can however be determined from the Reynolds number, a dimensionless constant expressed by the equation:

$$R_e = \rho \frac{uD}{\eta} \qquad \textbf{Equation (3.3.1)}$$

Where:
- R_e = The Reynolds number.
- ρ = The gas density.
- u = The gas velocity.
- η = The gas viscosity.
- D = The equivalent duct diameter.

The equivalent duct diameter is defined as:

$$D = 4 \frac{\textit{The area of the duct}}{\textit{The perimeter of the duct}} \qquad \textbf{Equation (3.3.2)}$$

If the Reynolds number is less than a critical value, (about 2000), then the flow will be laminar and the velocity profile across the duct will be parabolic. In a laminar flow, the maximum velocity is at the centre of the duct and will be twice the average velocity of the net gas flow. The laminar flow velocity profile is illustrated in Figure (3.3.1).

However, if the Reynolds number is greater than the critical value, then any small disturbance in the gas flow will grow until the flow becomes fully turbulent. In this case the flow profile will have a boundary layer with increasing velocity from zero at the duct wall increasing rapidly up to a mean velocity within the core of the flow. The core velocity will be fairly constant across the width of the duct, with a range of about + or - 10% of the mean velocity. In the case of turbulent flow, the velocity profile will be almost parabolic in the

boundary layer, and nearly flat but fluctuating in the core. The velocity profile of a turbulent flow can be seen in Figure (3.3.2).

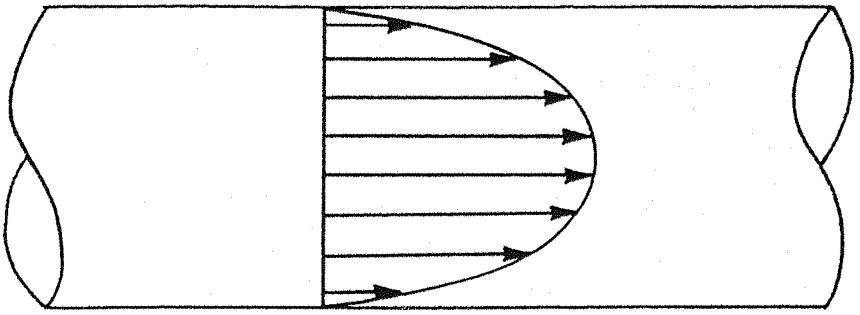

FIGURE 3.3.1 VELOCITY PROFILE OF A LAMINAR FLOW

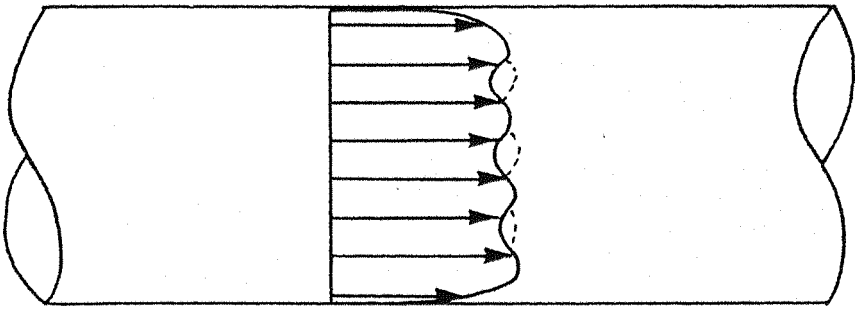

FIGURE 3.3.2 VELOCITY PROFILE OF A TURBULENT FLOW

3.3.2 GRAVITATIONAL FORCE

All of the particles within the gas flow will be influenced by the gravitational force acting upon them. This force will cause the particles to fall towards the base of the test rig and potentially out of the gas flow. The gravitational force acting upon a particle is dependent on the mass of the particle and is defined as:

$$F_g = m\ g \qquad \textbf{Equation (3.3.3)}$$

Where: F_g = The gravitational force on the particle.
m = The mass of the particle.
g = The gravitational pull, (≈ 9.81 N/m).

The particles will accelerate under the influence of the gravitational force until they reach their terminal settling velocity. This velocity is limited by the opposing viscous drag force exserted by the gas, defined by Stokes's law as:

$$F_d = 6\pi\ \eta\ a\ u \qquad \textbf{Equation (3.3.4)}$$

Where: F_d = The drag force acting on the particle.
η = The viscosity of the gas.
a = The radius of the particle.
u = The velocity of the particle.

The terminal velocity of a particle falling through the gas under the influence of gravity can be found when the viscous drag force 'F_d' is equal to the gravitational force on the particle 'F_g'. This is found by equating Stokes's equation (3.3.4) to the gravitational force equation (3.3.3) as:

If:

$$F_d = F_g \qquad \textbf{Equation (3.3.5)}$$

Then:

$$m\ g = 6\pi\ \eta\ a\ u \qquad \textbf{Equation (3.3.6)}$$

So:

$$u_{TERMINAL} = \frac{m\ g}{6\ \pi\ \eta\ a} \qquad \textbf{Equation (3.3.7)}$$

Since the mass of a particle is given by its density multiplied by its volume:

$$m = \rho \frac{4}{3} \pi a^3 \qquad \textbf{Equation (3.3.8)}$$

Where: ρ = The density of the particle.

Then:

$$u_{TERMINAL} = \frac{\rho \frac{4}{3} \pi a^3 g}{6 \pi \eta a} \qquad \textbf{Equation (3.3.9)}$$

Hence, $u_{TERMINAL}$ is proportional to a^2.

So the velocity of a particle falling under the influence of gravity is proportional to the square of the particle diameter, hence the larger particles will fall faster than the finer particles.

3.3.3 ELECTROSTATIC FORCE

If the particles have an electrostatic charge, then there will be a force of attraction or repulsion between the particles, depending on the polarity of their charges. Like charged particles repelling one another and oppositely charged particles attracting one another. There will also be a force of attraction between a charged particle and its image charge on the surface of any un-charged body.

Considering the force of attraction between two oppositely charged particles. This force of attraction is defined by Coulomb's law as:

$$F_c = \frac{q_1 q_2}{4\pi \varepsilon_o \varepsilon_r d^2}$$ **Equation (3.3.10)**

Where: F_c = The force of attraction between the two particles.
q_1 = The charge on one of the particles.
q_2 = The charge on the other particle.
ε_o = The permittivity of free space.
ε_r = The relative permittivity.
d = The distance between the two particles.

Again the velocity of the migration of the particles through the gas is limited by the viscous drag force as defined in equation (3.3.4). So the terminal velocity can be found when the viscous drag force 'F_d' is equal to the force of attraction between the two particles 'F_c'. This is shown by equating Stokes's equation (3.3.4), to Coulomb's equation (3.3.10), as:

If:

$$F_d = F_c$$ **Equation (3.3.11)**

Then:

$$\frac{q_1 q_2}{4\pi \varepsilon_o \varepsilon_r d^2} = 6 \pi \eta a u$$ **Equation (3.3.12)**

So:

$$u_{TERMINAL} = \frac{q_1 q_2}{24\pi^2 \varepsilon_o \varepsilon_r d^2 \eta a}$$ **Equation (3.3.13)**

Hence, $u_{TERMINAL}$ is proportional to 1/a.

So the velocity of the migration is inversely proportional to the particle radius. This implies that the smaller particles will travel faster than the larger particles. However, it must be remembered that the charge on the particle is

proportional to the square of its radius, as was seen earlier in this chapter. So assuming that all the particles were charged to the same proportion of their charge limit, then the terminal velocity of the electrostatic migration of the particles will be proportional to the radius of the particle.

So, $u_{TERMINAL}$ is now proportional to a.

3.3.4 PARTICLE ACCELERATION

We have seen that a particle under the influence of a force will move at a velocity limited by the viscous drag force. However, the particle will in fact accelerate up to its terminal velocity over a finite period of time, assuming that the force acting upon it remains constant.

The rate of acceleration will depend on the particle mobility, which is defined in terms of the force acting upon the particle and its terminal velocity as:

$$\beta = \frac{u}{F} \qquad \textbf{EQUATION (3.3.14)}$$

Where: β = The mobility of the particle.
u = The terminal velocity of the particle.
F = The force acting on the particle.

The product of the mass 'm' of the particle and its mobility 'β' is known as the relaxation time 'τ'. This constant has units of time and represents the time required for a particle to accelerate. The relaxation time depends only on the mass of the particle and the mobility of the particle and is not affected by the nature or magnitude of the external forces acting upon the particle. This relaxation time can be defined in terms of the particle diameter, the density of the particle and the viscosity of the gas, as:

$$\tau = m\beta = \rho \frac{\pi}{6} d^3 \frac{Cc}{3 \pi \eta d} = \frac{\rho d^2 Cc}{18 \eta} \quad \textbf{EQUATION (3.3.15)}$$

Where:
- τ = The relaxation time.
- m = The mass of the particle.
- β = The mobility of the particle.
- ρ = The density of the particle.
- d = The diameter of the particle.
- Cc = The slip correction factor.
- η = The viscosity of the gas.

The time taken for a particle to reach its terminal velocity is defined as three times the relaxation time, as it will be approaching 100% of this velocity. This can be seen in the graph in Figure (3.3.3) taken from W.Hinds[ref 3.10].

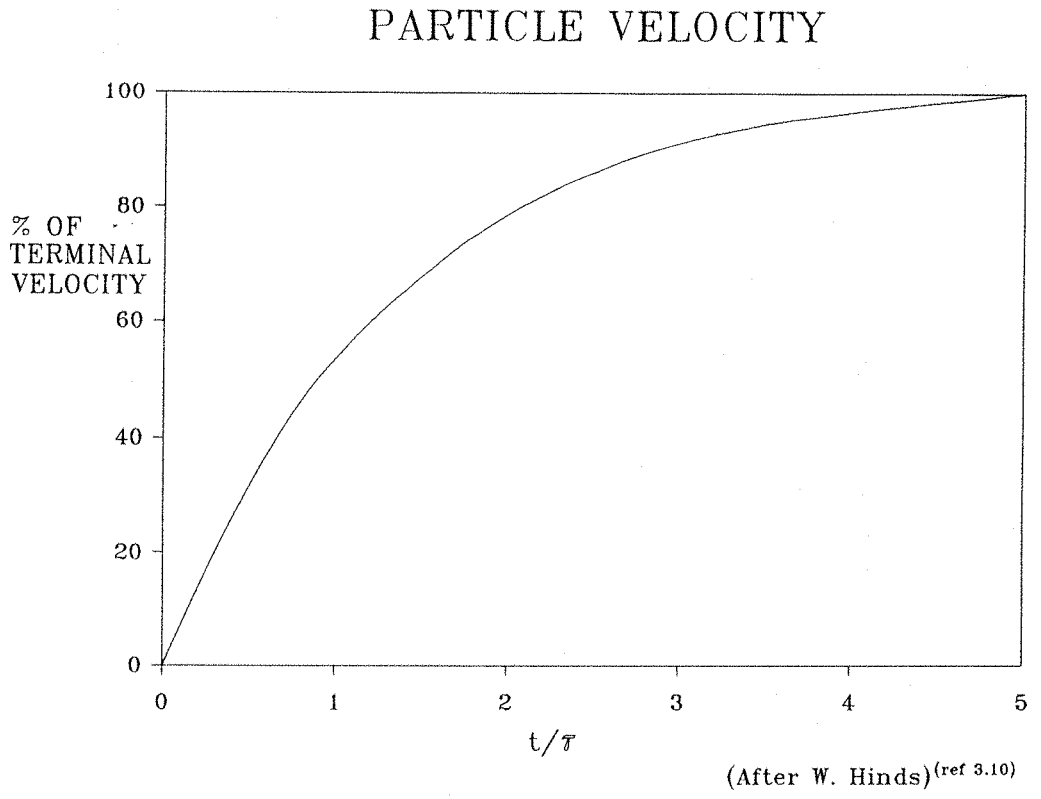

FIGURE 3.3.3 PARTICLE ACCELERATION

The relaxation time and the time taken to reach the terminal velocity '3τ' can be calculated from equation (3.3.15), assuming standard conditions for a particle of unit density in air. These results are shown for various particle diameters in Table (3.3.1).

PARTICLE DIAMETER (μm)	RELAXATION TIME (s)	TIME TO REACH TERMINAL VELOCITY ($3\times\tau$) (s)
0.01	6.8×10^{-9}	2.1×10^{-8}
0.1	8.8×10^{-8}	2.6×10^{-7}
1.0	3.6×10^{-6}	1.1×10^{-5}
10.0	3.1×10^{-4}	9.3×10^{-4}
100	3.1×10^{-2}	9.3×10^{-2}

TABLE 3.3.1 RELAXATION TIMES AS A FUNCTION OF PARTICLE SIZE

The relaxation time and hence the time taken for a particle to reach its terminal velocity are seen to increase rapidly with particle size, as the time constant is proportional to the square of the particle diameter.

In the case of two particles migrating towards one another under their mutual electrostatic force of attraction, the force is not constant but inversely proportional to the square of the distance between the particles, as can be seen in equation (3.3.10). So in this case the rate of acceleration will increase as the particles approach one another.

3.4 PARTICLE BONDING

The forces that act to bond particles together can be broken down into three main groups;

-Electrostatic forces:
-Van der Waals forces (dispersion forces):
-Chemical forces:

3.4.1 ELECTROSTATIC FORCES

The force bonding two particles together can range from light contact adhesion, to forces comparable to the forces of cohesion within solid materials. All of these forces of adhesion and cohesion can in fact be considered to be electrostatic as they all result from the interaction of charges on either a macroscopic or atomic level. However, the term electrostatic adhesion usually refers to the macroscopic effects of charge distributed about the surfaces of particles.

These adhesive forces can be further divided into three main groups;

1/ The mutual force of attraction between two oppositely charged particles.

2/ The force due to a charge exchange at the interface between two particles.

3/ The force of attraction due to an external electric field.

3.4.1.1 ATTRACTION BETWEEN OPPOSITELY CHARGED PARTICLES

Considering the mutual electrostatic force of attraction between two oppositely charged particles, given by Coulomb's law:

$$F = \frac{q_1 q_2}{4\pi \varepsilon_o \varepsilon_r d^2}$$ **Equation (3.4.1)**

Where: F = The force of attraction between the two particles.
q_1 = The charge on one of the particles.
q_2 = The charge on the other particle.
ε_o = The permittivity of free space.
ε_r = The relative permittivity.
d = The distance between the two particles.

If the two charges are of the same polarity, then the force will be one of repulsion and conversely if the two charges are of different polarities then the force will be a force of attraction.

Let us assume that the charge, that is in fact distributed about the surface of the particle, is located at a point in the centre of the particle. In which case the force of attraction is calculated between these two points.

If we also consider the two particles to be in contact with one another but without loosing any charge through the processes of conduction mentioned earlier in this chapter. Then if the two particles are of the same size, the distance between the two assumed point charges at the centre of each particle is twice the radius of the particle. Hence Coulomb's law of attraction can now be re-written as:

$$F = \frac{q_1 q_2}{4\pi \varepsilon_o \varepsilon_r 4a^2}$$ **Equation (3.4.2)**

Where: a = The radius of the particles.

Now let us consider the two particles separated by a short distance 's', now the force of attraction can be rewritten as:

$$F = \frac{q_1 \, q_2}{16\pi \, \varepsilon_o \, \varepsilon_r \, (a + s/2)^2} \qquad \textbf{Equation (3.4.3)}$$

Where: s = The distance between the two particles.

In practice the two charged particles will become polarized by the force of attraction between the opposite charges. So the effective distance between the point charges becomes less than (2a + s) and equation (3.4.3) will underestimate the force of attraction between the two particles.

The equipotentials for two point charges separated by a distance 's' are not spheres, but are distorted as shown in Figure (3.4.1). The field lines are perpendicular to these equipotentials, so there will be an intensification of the field between the two point charges as the field becomes more polarised. This will then produce a greater force of attraction between the two point charges.

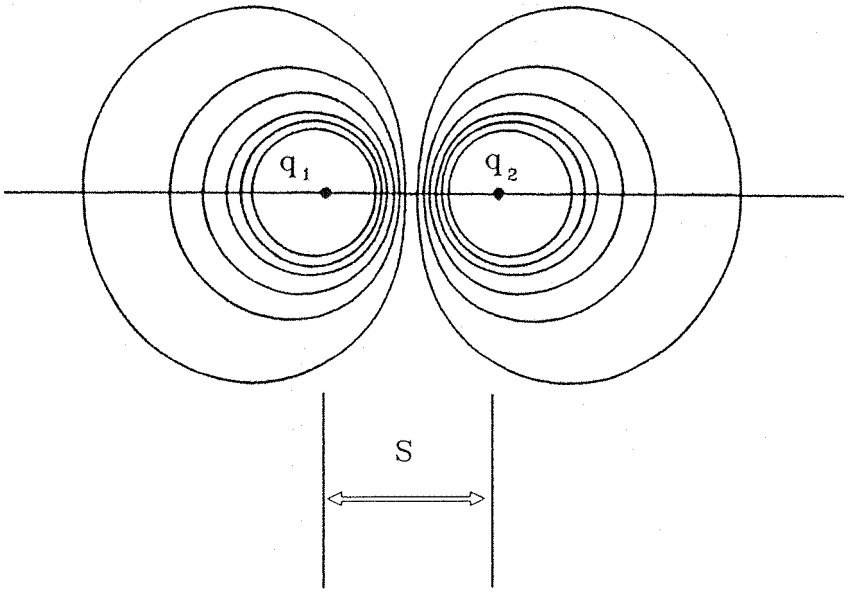

FIGURE 3.4.1 THE DISTORTED EQUIPOTENTIALS FOR TWO EQUAL AND OPPOSITE POINT CHARGES IN CLOSE PROXIMITY TO ONE ANOTHER

If the distance of separation between the two particles is small in comparison to the particle radius, then the charge distribution around the sphere can no longer be considered to be equivalent to a single point charge in the centre of the particle. However, an approximation can be made to the actual location of the equivalent point charge for the polarised particle to be at point 'P', where 'P' is defined such that:

$$b\ (d-b) = a \qquad \textbf{Equation (3.4.4)}$$

Where:
- a = The radius of the particle.
- b = The distance between the point 'P' and the centre of the particle.
- d = The distance between the centres of the two particles.

This calculation can be better understood by referring to Figure (3.4.2), which illustrates the polarization between two oppositely charged spherical particles.

The solution given to the location of point 'P', in equation (3.4.4), is an exact solution for a charged cylinder in front of a grounded plate and is thus only an approximation for the distortion of a charged sphere.

We can now rewrite equation (3.4.3), for the equivalent point charges at point 'P':

$$F = \frac{q_1\, q_2}{16\pi\ \varepsilon_o\ \varepsilon_r\ x^2} \qquad \textbf{Equation (3.4.5)}$$

Where:

$$x = \frac{1}{2}\, d - b \qquad \textbf{Equation (3.4.6)}$$

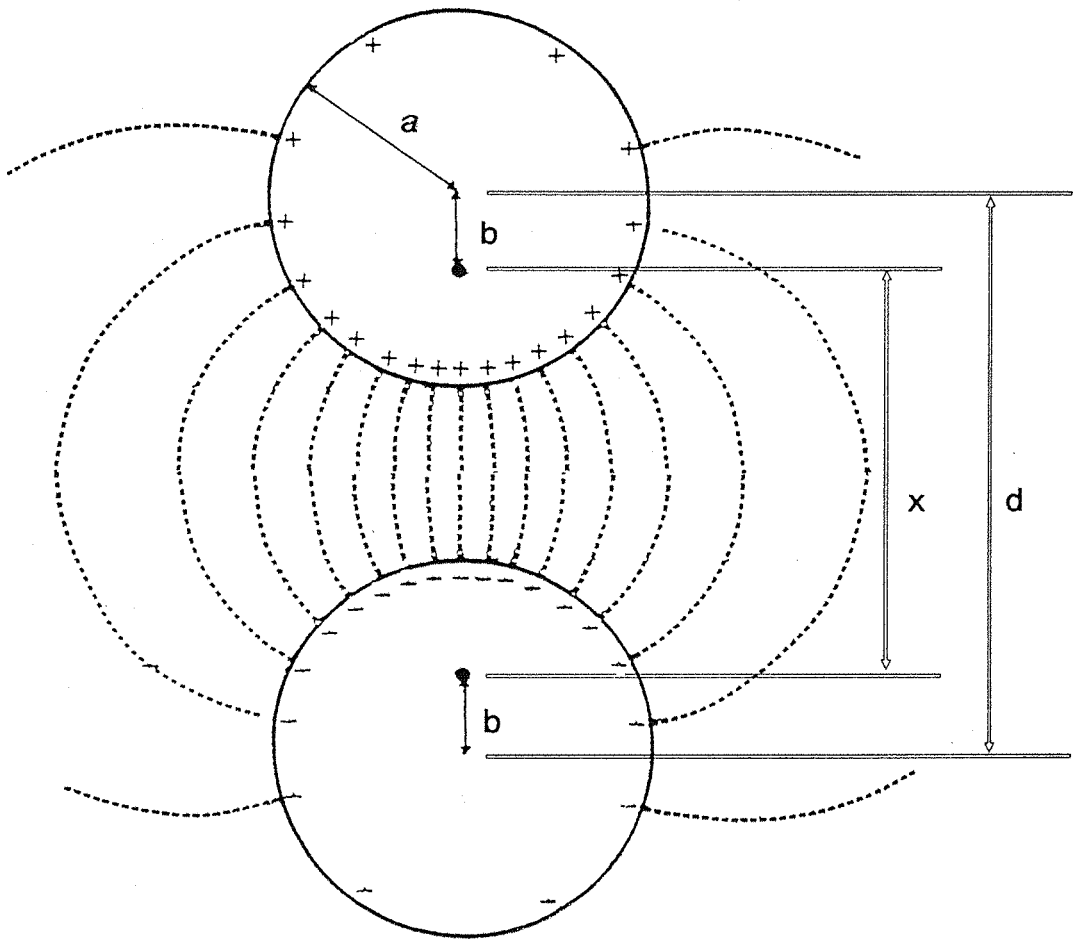

FIGURE 3.4.2 POLARIZATION OF TWO OPPOSITELY CHARGED PARTICLES IN CLOSE PROXIMITY

Equation (3.4.5) can be re-written with the separation between the point charge 'P' expressed in terms of the particle radius 'a' and the separation 's'.

$$x^2 = \frac{1}{4} d^2 - a^2 \qquad \textbf{Equation (3.4.7)}$$

as:

$$\frac{d}{2} = a + \frac{s}{2} \qquad \textbf{Equation (3.4.8)}$$

So:

$$x^2 = \frac{s}{2}\left(\frac{s}{2} + 2a\right) \qquad \textbf{Equation (3.4.9)}$$

$$F = \frac{q_1\, q_2}{16\pi\ \varepsilon_o\ \varepsilon_r \frac{s}{2}\left(\frac{s}{2} + 2a\right)} \qquad \textbf{Equation (3.4.10)}$$

If we assume the distance of the particle separation to be far less than the particle radius, then equation (3.4.10) will simplify to:

$$F = \frac{q_1\, q_2}{8\pi\ \varepsilon_o\ \varepsilon_r\ a\ \frac{s}{2}} \qquad \textbf{Equation (3.4.11)}$$

As the calculation of the equivalent point charge , for the polarized particle, was in fact only exact for a cylinder in front of an earthed plane, then equation (3.4.11) will produce an exact force of attraction per unit length between two cylinders but only an approximation of the force between two particles.

A more precise calculation of this force of attraction between two oppositely charged particles has been made by Russel[ref 3.11]. He considered the force between the two spheres in terms of the rate of change of stored energy as the two separate, as:

$$F = \frac{dU}{ds} \qquad \textbf{Equation (3.4.12)}$$

Where: F = The force of attraction between the particles.
dU = The change in the energy.
ds = The change in the separation of the two particles.

The energy 'U' between the two spheres is given by:-

$$U = \frac{1}{2} C V^2 \qquad \textbf{Equation (3.4.13)}$$

Where: C = The capacitance between the two particles.
V = The potential difference between the two particles.

The capacitance between the two particles can be written as:

$$C = 4\pi \varepsilon_o \varepsilon_r a \left(\psi + \frac{1}{2} \ln 2a/\frac{s}{2}\right) \qquad \textbf{Equation (3.4.14)}$$

Where: ψ = Euler's constant = 0.577

So:

$$F = \frac{d}{ds}\left(\frac{1}{2} C V^2\right) = \pi \varepsilon_o \varepsilon_r a V^2 / \frac{s}{2} \qquad \textbf{Equation (3.4.15)}$$

As:

$$C = q V \qquad \textbf{Equation (3.4.16)}$$

The force of attraction can now be written as:

$$F = \frac{q_1 q_2}{16\pi \varepsilon_o \varepsilon_r a \frac{s}{2} \left(\psi + \frac{1}{2} \ln 2a / \frac{s}{2}\right)^2} \qquad \textbf{Equation (3.4.17)}$$

Equations (3.4.3), (3.4.10) and (3.4.17) all give accurate solutions to the force of attraction between two particles, if the distance between the particles is great in comparison to their radius, as the particles will effectively be un-polarised. However, as the distance of separation becomes small in comparison to the particle radius then the particles will become polarised as the charge redistributes around the particle surface. In this case the solutions to the

different equations will begin to disagree. Equation (3.4.3), which assumes no polarization of the particles and the equivalent point charges due to the charge distribution to lie at the centre of the particles will give an underestimation to the force of attraction. While equation (3.4.10), which is the two dimensional approximation with the location of the equivalent point charge calculated assuming the spheres to be cylinders, will give an overestimation to the value of the force of attraction. Whereas, the force of attraction using equation (3.4.17) will give the exact solution.

This can best be seen by calculating this force using each of the equations for a known particle size and charge at set distances of separation.

Let us assume that the force of attraction is between two oppositely charged insulating particles with a radius of 10 μm charged to the Pauthenier limit:

$$q_{pa} = 4\pi\ \varepsilon_o\ (\frac{3\varepsilon_r}{\varepsilon_r+2})\ a^2\ E \qquad \textbf{Equation (3.4.18)}$$

Where:
- q_{pa} = The Pauthenier limit charge for the particle.
- E = The applied field strength.
- a = The particle radius.
- ε_o = The permittivity of free space.
- ε_r = The relative permittivity.

Assuming that:
- a = 10×10^{-6} m
- ε_r = 1
- E = $5\times10^{+5}$ Vm^{-1}

So:
- q = 5.56×10^{-15} Coulombs.

The results of these calculations are given in Table (3.4.1).

(All solutions are in Newtons)	SEPARATION OF THE PARTICLES		
	l = 4a	l = a/50	l = a/500
NO POLARIZATION EQUATION (3.4.3)	7.72×10^{-11}	6.67×10^{-10}	6.67×10^{-10}
CYLINDRICAL EQUATION (3.4.10)	8.68×10^{-11}	3.47×10^{-8}	3.47×10^{-7}
BY RUSSEL EQUATION (3.4.17)	8.68×10^{-11}	6.67×10^{-9}	3.62×10^{-8}

TABLE 3.4.1 COMPARISON OF THE ELECTROSTATIC ADHESIVE FORCES, BETWEEN TWO OPPOSITELY CHARGED INSULATING PARTICLES

3.4.1.2 THE FORCE OF ATTRACTION BETWEEN TWO PARTICLES IN AN APPLIED ELECTRIC FIELD

When two particles come into contact in an applied electric field, charge will flow from one to the other. This current is restricted to the narrow contact area between the two particles and thus there will be a considerable intensification of the field around this contact area. This field intensification acts to increase the force of attraction between the two particles.

This bonding force is an important consideration in the design of electrostatic precipitators, as the particle migration occurs under the influence of a strong electric field. However, in the case of agglomeration as a pre-precipitation enhancement stage this contact force of adhesion can be ignored as the migration and bonding of the particles to one another is to occur in a low field region.

3.4.1.3 THE FORCE OF ATTRACTION BETWEEN TWO PARTICLES DUE TO CHARGE EXCHANGE

When two particles come together in a collision, charge will flow from one to the other through the process of conduction. If both of the particles were conductors the charge will flow until such a point that the potential difference between the two particles is equal to the difference in the work functions of the materials. This voltage is constant and typically less than 0.5V, it may be substituted for 'V' in equation (3.4.15). So the force of attraction due to the charge transfer process for two 10 μm particles with a 0.5V potential difference can be calculated as:

$$F = 1.7\times10^{-7} \text{ Newtons}$$

3.4.1.4 DIPOLE FORCES

Another form of electrostatic attraction is the force of attraction between polar molecules. However, the force of adhesion due to the dipole force is very small indeed, less than 1×10^{-10} Newtons, unless the molecules within the particle are strongly polar.

3.4.2 VAN DER WAALS FORCES

Van der Waals force of attraction occurs between two atoms, and is due to the random fluctuations of electron density, within the atom. At any instant an atom will have a net dipole moment, which will induce a distortion in the charge of a neighbouring atom, so there will be a mutual force of attraction.

3.4.2.1 HARD PARTICLES

Bradley[ref 3.12] derived the following equations for the force 'F' and the energy 'U' between two smooth hard particles as:

$$U = \frac{-Aa}{12\ z_o}$$ **Equation (3.4.19)**

$$F = \frac{Aa}{12z_o^2}$$ **Equation (3.4.20)**

Where: U = The energy of the interaction.
F = The force of attraction.
a = The radius of the particle.
A = The Hamaker constant.
z_o = The bond separation.

In order to evaluate these equations, the Hamaker constant 'A' and the bond separation 'z_o' must be determined. This has been done by many workers including Lifshitz[ref 3.13], Krupp[ref 3.14] and Zimon et al[ref 3.15], giving a solution to equation (3.4.20) in the range of:

10^{-5} to 10^{-6} Newtons

3.4.2.2 ELASTIC PARTICLES

Equations (3.4.19) and (3.4.20) were defined for the adhesion between two solid particles assuming no deformation of the surfaces at the point of contact. However, if the particles were able to deform plastically or elastically, then the area of the molecular contact between the two particles will be increased, leading to an increased force of adhesion. Although the elastic stress of the deformation will oppose the bonding force between the two particles.

Hertz defined an expression for the radius 'r' of the contact area between the two particles with radius a_1 and a_2, under a pressure 'P', this is defined as:

$$r^3 = \frac{3}{4}\ \pi(k_1 + k_2)\ aP$$ **Equation (3.4.21)**

Where:

$$a = \frac{a_1 \times a_2}{a_1 + a_2} \qquad \textbf{Equation (3.4.22)}$$

also:

$$k = \frac{(1-\nu^2)}{\pi Y} \qquad \textbf{Equation (3.4.23)}$$

Where: P = The compression load acting on the particles.
a_1 = The radius of the first particle.
a_2 = The radius of the second particle.
r = The radius of the contact area.
υ = Poisson's ratio.
Y = Young's modulus.

These equations can be solved, and the force of attraction found to be of the order of:

10^{-4} to 10^{-6} Newtons

-An order of magnitude greater than was found for the hard particles.

3.4.3 CHEMICAL FORCES

All materials are covered in surface impurities and oxides. So there are no available chemical bonding points as they have all been satisfied. However, at high temperatures the surface impurities may be displaced or removed, leaving open ended links allowing two particles to form a chemical bond between their surface atoms. This process, known as sintering, will start to occur at only 50% of the melting temperature of the material and will produce a bond of comparable strength to the forces of cohesion within the material.

3.4.4 SUMMARY OF BONDING FORCES

A summary of all of the bonding forces is given in Table (3.4.2), along with the order of magnitude of the bond strength between two 10 μm particles for each mechanism.

FORCE	EQUATION	MAGNITUDE (Newtons) a = 10 μm
GRAVITY		10^{-10}
VAN DER WAALS FORCE	Bradley theory (smooth hard particles)	10^{-5} to 10^{-6}
	Derjaguin theory and JKR theory (elastic particles)	10^{-4} to 10^{-6}
ELECTROSTATIC FORCES	Mutual attraction between two particles, charged to the Pauthenier limit	10^{-8}
	Charge exchange	10^{-7}
	Surface tension	10^{-6}

TABLE 3.4.2 SUMMARY OF THE BONDING FORCES BETWEEN TWO 10 μm PARTICLES

CHAPTER FOUR

MEASUREMENT SYSTEMS

This chapter describes the various techniques utilised in the measurement and analysis of all the physical parameters involved in this study.

4.1 RESISTIVITY

It has been shown in the previous chapter that the maximum charge that can be deposited upon a particle is dependent on many factors, including its resistivity (from the Pauthenier equation).

The rate at which particles can gain or lose charge is indicated by the time constant 'τ', which is a constant for the material, as was shown in the previous chapter. This time constant was also shown to be dependent on the resistivity of the material, and is given by the equation:

$$\tau = \varepsilon_o \, \varepsilon_r \, \rho \qquad \textbf{Equation (4.1.1)}$$

Where:
- τ = The time constant of the material.
- ε_o = The permittivity of free space.
- ε_r = The relative permittivity.
- ρ = The resistivity of the material.

The time constant can also be written in terms of the size of the capacitance on which the charge is stored and the resistance through which it flows:

$$\tau = R\ C \qquad \textbf{Equation (4.1.2)}$$

Where: R = The resistance of the sample.
C = The capacitance of the sample.

Hence the time required for a particle to gain or lose its charge will be dependent on the resistance of the particle. The higher its resistivity the longer it will take to charge or discharge. So optimally a particle of very low resistivity is required within the charging region of the test rig in order to produce rapid and efficient charging. Whereas a high resistivity is required after the charging stage, so as to ensure that the particle does not become discharged through collisions with any uncharged bodies or by going into corona itself. Also to aid the agglomeration process, the resistivity should be as high as possible so that the oppositely charged particles do not discharge to one another on contact thus reducing their force of attraction for one another.

4.1.1 DEFINITION

When a potential difference is placed across a body, a charge will flow from one electrode to the other. This moving charge is an electric current, the rate of charge movement is the value of current. The ratio between the voltage across the body and the rate of charge flow is called the resistance and is defined by Ohms law (for an Ohmic material) as:

$$V = I\ R \qquad \textbf{Equation (4.1.3)}$$

Where: R = The resistance of the body.
V = The applied potential difference.
I = The current flowing through the body.

R has units of OHMS (Ω)

The resistance of a body is a property of that particular body only.

However, the resistivity is a property of the material of the body. The relationship between the resistance and the resistivity are the physical dimensions of the body. The greater the cross sectional area of the object the higher the current will be for the same applied voltage. A greater distance between the electrodes will require the charge carriers to move through more material and will thus produce a lower current for the same applied potential.

If we consider a sample of unit length and unit cross sectional area then the resistance measured will be a property of the material of the sample. Hence, the relationship between the resistance and the resistivity is a function of its size and is given by the equation:

$$\rho = R\frac{A}{l} \qquad \textbf{Equation (4.1.4)}$$

Where: ρ = The resistivity of the sample.
R = The measured resistance.
A = The cross sectional area of the sample.
l = The length of the sample between the electrodes.

ρ has units of OHM METRES (Ω.m).

The reciprocal of the resistance is the conductance, which has units of siemens ($\mho$) or (S). The reciprocal of the resistivity is the conductivity and is measured in siemens per metre (S/m).

4.1.2 BULK RESISTANCE Vs SURFACE RESISTANCE

When applying a potential across a sample it is particularly important to be aware that the current being measured is the current due to the charge carriers following the desired path. The current will either flow around the surface of the particle or through the body of the particle. These are called the bulk and surface currents.

4.1.2.1 BULK CURRENT

The bulk current is the current that flows through the body of the sample under test when the potential is applied across it, as illustrated by the diagram in Figure (4.1.1). In this case the path of least resistance is the shortest path, straight through the body of the particles.

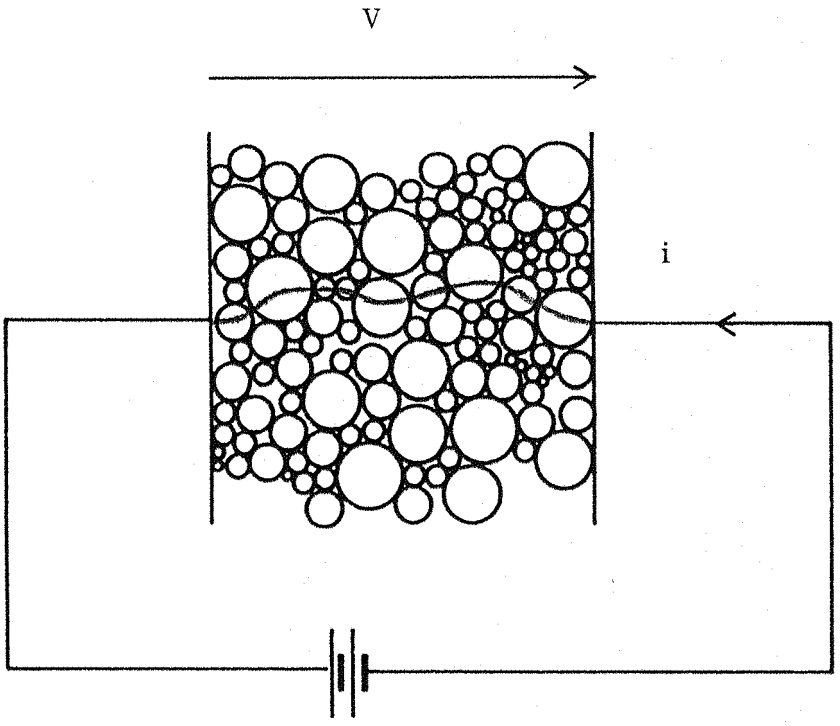

FIGURE 4.1.1 BULK CURRENT CONDUCTION PATH

4.1.2.2 SURFACE CURRENT

This is the current that will flow over the surface of the body under test. This will occur if the surface resistance of the body is less than the bulk resistance. This may be due to surface impurities or a surface wetness. Hence currents will be recorded that do not reflect the resistivity of the sample but the condition of the particles surfaces. This current path is shown in Figure (4.1.2).

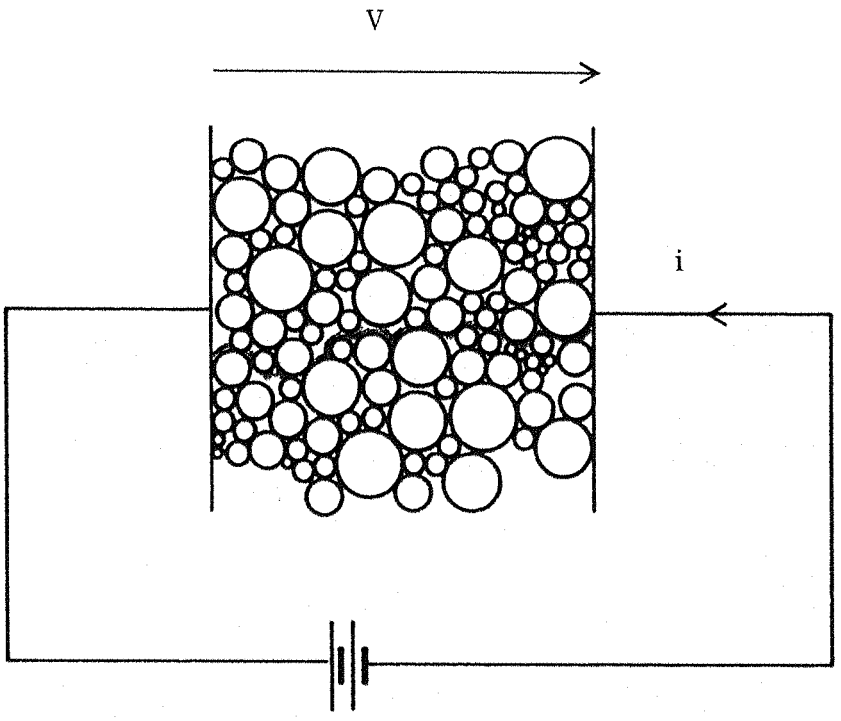

FIGURE 4.1.2 SURFACE CURRENT CONDUCTION PATH

4.1.3 RESISTIVITY MEASUREMENT

Measuring the resistivity of a powdered sample by placing a potential across it will give the resistivity of the path of least resistance. At lower temperatures this is the surface conduction path, as impurities such as water can easily become adsorbed onto the surface of the particle. Fortunately the parameter we are interested in measuring is the surface resistance, as it is the surface of a particle to which the charge carriers become attached. The measurements were made by using a specially designed resistance cell as shown in Figure (4.1.3).

The cell in the diagram consists of a teflon chamber with two electrodes, one at either end. The top electrode is constructed from a large piece of brass, to provide a compression mass, with a bolt on the top for the electrical connection. This electrode is connected to the E.H.T. end of a high voltage power supply while the low voltage end of the supply is connected to ground, to complete the electrical circuit. A high voltage power supply is used as the values

of resistance measured were very high, therefore requiring a very large potential in order to be able to measure the current flow. The top electrode also has a small groove cut along its length so as to allow the air to escape from the cell as the electrode is lowered into place. The bottom electrode consists of a conducting disk surrounded by a conducting ring which is separated by a teflon insulator. The disk forms the second electrode of the circuit, while the ring acts as a guard electrode. The disk is connected to ground via an ammeter, completing the measuring circuit. The guard ring is connected directly to the ground, hence any current reaching this electrode is not measured and plays no part in the calculation of resistivity. The purpose of this guard ring is to eliminate any current that is conducted along the surface of the test cell which would be independent of the sample under test.

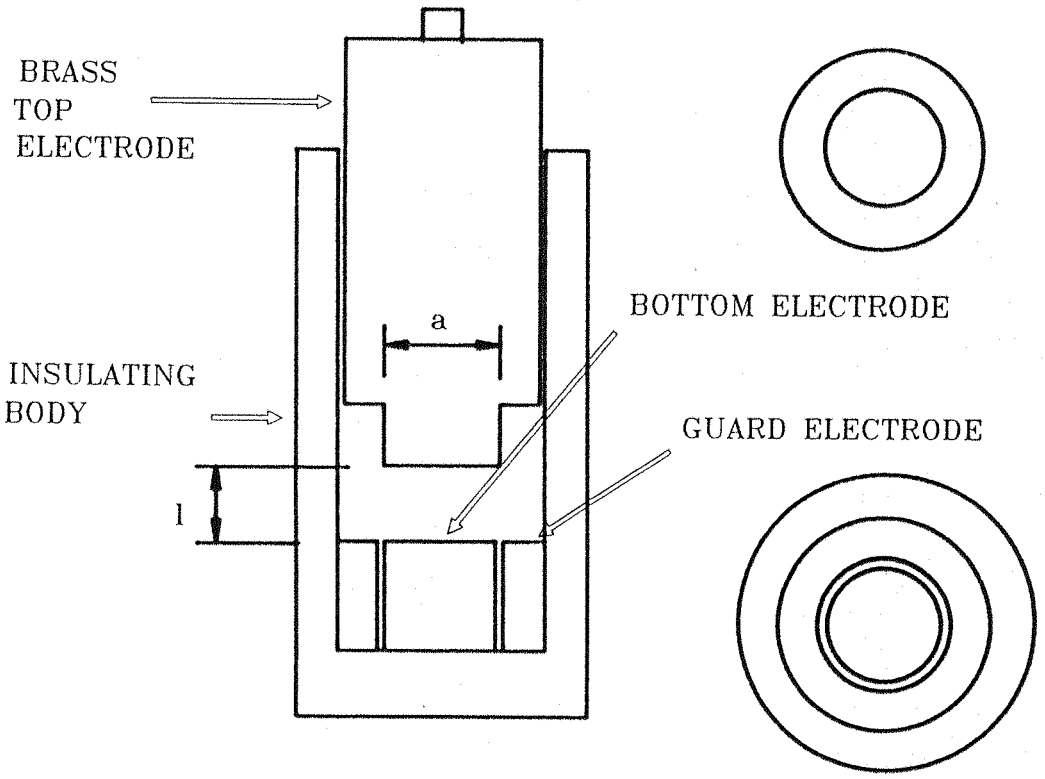

FIGURE 4.1.3 RESISTIVITY CELL

4.1.4 EXPERIMENTAL PROCEDURE

1/ A sample of the ash to be measured was placed in the resistance cell.

2/ The top electrode was then placed over the sample and tapped down lightly so as to eliminate as much trapped air as possible but without placing the sample under pressure which may affect the value of resistance recorded.

3/ The height of the sample was then recorded.

4/ The electrical connections were made and the cell placed in a grounded steel cage in order to eliminate the effect of any stray electric fields.

5/ The temperature and humidity of the ambient conditions were recorded and noted. (Both of these will have an effect on the results obtained, as detailed later in this chapter.)

6/ The power supply was then turned on and the current recorded as a function of time. (The current will slowly fall to a minimum, as all the molecules within the sample polarise and align with the electric field between the two electrodes).

7/ The resistance of the sample can then be calculated from the voltage and the minimum current. The resistivity of the material can then be calculated from the physical dimensions of the test sample and its resistance.

4.1.4 RESISTIVITY CALCULATION

The value of the resistivity can be found by substituting equation (4.1.3) into equation (4.1.4) and then solving for the values obtained in the experiment:

$$\rho = \frac{V A}{I l} \qquad \textbf{Equation (4.1.5)}$$

Where: ρ = The resistivity of the material.
V = The applied voltage.
A = The cross sectional area of the sample.
I = The recorded current.
l = The sample height.

The time constant 'τ' can also be calculated from these results by measuring the rate of decay of the current through the sample. The time constant is the time taken for the current to reach 37% of its initial value. This can be found by solving equation (4.1.6).

$$\ln i = \ln i_o \frac{-t}{\tau} \qquad \textbf{Equation (4.1.6)}$$

Where: i = The value of the current after time 't'.
i_o = The initial value of the current.
t = The time taken for the current to decay from i_o to i.
τ = The time constant for the material.

4.2 ELECTRIC CHARGE

In order to asses the performance of the charging system, and to ensure that a bi-polarly charged ash cloud was generated with a net charge of zero and with equal proportions of the ash charged equally and oppositely, it was necessary to measure the magnitude and polarity of the charge on the particles. Rather than trying to collect and analyze individual particles a sample of the ash was taken and its charge compared to its mass, so as to give the 'Charge To Mass Ratio'.

4.2.1 THE FARADAY CUP

Charge is usually measured using a Faraday Cup, as shown in Figure (4.2.1).

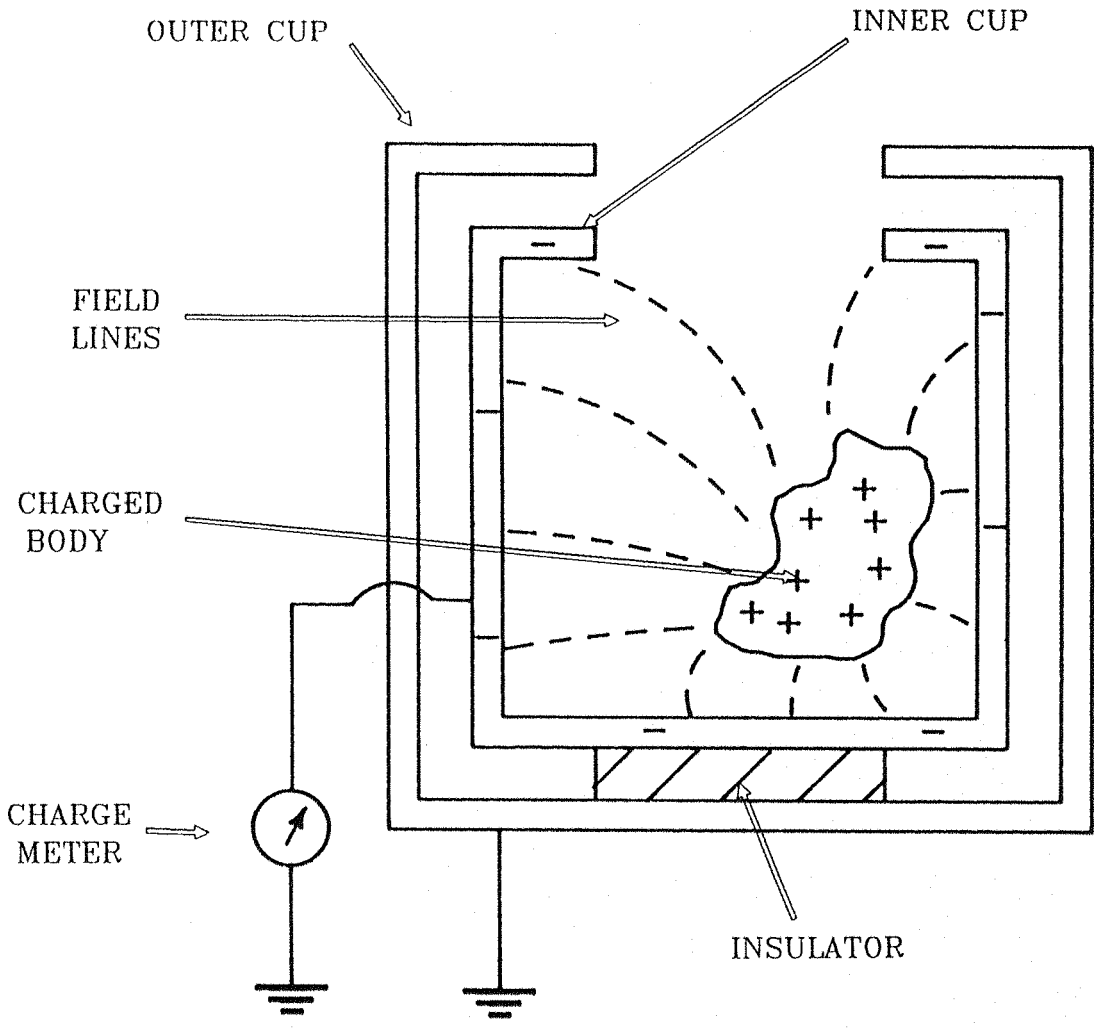

FIGURE 4.2.1 FARADAY CUP

Here the cup is shown to consist of two concentric conducting cans, one inside the other. The outer can is connected to ground, which then forms an electrical screen to shield the inner can from any stray electric fields. The inner can is electrically isolated from the outer and is connected to an electrometer. This meter will allow the charge from the Faraday cup to flow into a known capacitance and then display the voltage developed across the capacitor. The value of the capacitor in the meter is large in comparison with the capacitance of the Faraday cup, so as to ensure a maximum charge transfer from the cup to the instrument. This is best seen by considering the equivalent circuit of this system as shown in Figure (4.2.2).

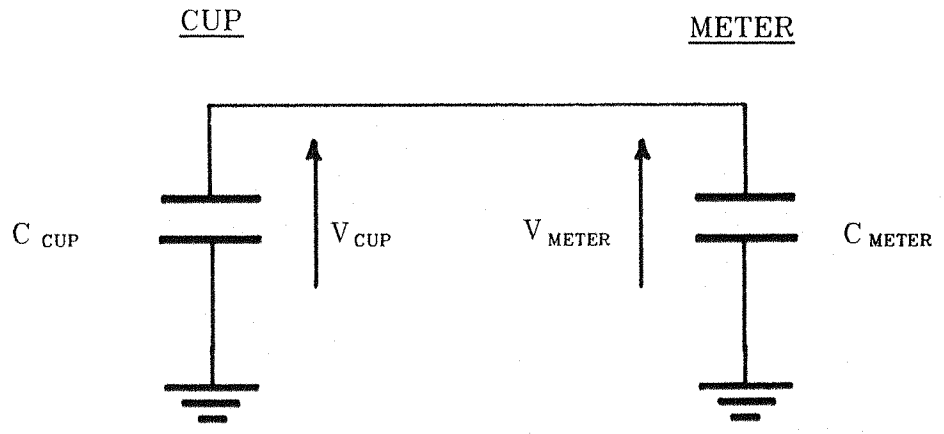

FIGURE 4.2.2 CHARGE TRANSFER EQUIVALENT CIRCUIT

The amount of charge transfer from the cup to the meter can be calculated if the capacitance of each is known. A typical example is shown below.

Assume that:

1/ A charge of 1×10^{-6} Coulombs is deposited within the cup.

2/ $C_{meter} = 10{,}000\ C_{cup}$

As:

$$Q = C\ V \qquad \textbf{Equation (4.2.1)}$$

Where: Q = The charge held in the system.
C = The capacitance of the system.
V = The voltage across the system.

So from equation (4.2.1), we can write:

$$V_{meter} = \frac{Q_{meter}}{C_{meter}} \quad and \quad V_{cup} = \frac{Q_{cup}}{C_{cup}} \qquad \textbf{Equation (4.2.2)}$$

And since:

$$V_{meter} = V_{cup} \qquad \textbf{Equation (4.2.3)}$$

We can substitute equation (4.2.2) into equation (4.2.3) giving:

$$\frac{Q_{meter}}{C_{meter}} = \frac{Q_{cup}}{C_{cup}} \qquad \textbf{Equation (4.2.4)}$$

Since: $C_{meter} = 10{,}000\ C_{cup}$

And as the charge deposited in the cup is shared so:

$$Q_{meter} = 10{,}000\ Q_{cup}$$

And:

$$Q_{cup} = 9.9990\times10^{-11}$$
$$Q_{meter} = 0.9999\times10^{-6}$$

Hence almost all of the charge is transferred from the cup to the meter, in fact 99.99% is transferred.

For this charge transfer to occur it is not however necessary for the charge on the body within the cup to transfer to the cup, or even for the charged body to come into contact with the cup. This can be seen by referring back to Figure (4.2.1), where such a case is shown. An equal and opposite charge to that on the particle is induced onto the walls of the cup. This re-location of charge is balanced by a current that is equivalent and equal to the current that would have flowed to the meter had the body discharged to the cup.

However, a conventional Faraday cup, as previously described can not be

used within the agglomerator test rig, primarily as only a proportion of the ash would be deposited within the cup (as both the aerodynamic and electrostatic forces favour an external deposition). Secondly, The finer particles of the distribution will not be deposited within the Faraday cup, as they will simply follow the gas streamlines into the cup and then follow them back out again. Finally, as the Charge to Mass ratio is required and not just the charge, this type of cup would be far too heavy to allow accurate readings to be taken of the very small quantities of ash that would be collected. Thus a continuous flow light weight cup was developed to overcome these problems.

4.2.2 CONTINUOUS FLOW FARADAY CUP

This cup is essentially the same as the conventional Faraday cup described earlier. However, it is far lighter, has an opening at both ends and is filled with wire wool in order to retain the particles that enter the cup. This design of cup is illustrated in Figure (4.2.3).

This cup consists of a thin aluminum tin containing wire wool and fitted with light weight plastic connectors at either end. The tin is also screened from free ions and external fields by surrounding it with a grounded aluminum mesh which forms the outer cup. This mesh is located and electrically isolated from the tin by the plastic connectors at either end of the tin. This mesh also extends over the inlet aperture of the cell, so as to divert and collect any stray ions, thus preventing them from entering the tin. When weighing the cell, it is not however necessary to measure the mesh as it can easily be removed therefore disallowing for any errors incurred through weighing the ash deposited on the mesh which has not contributed to the charge recorded for the sample.

The ash is drawn into the cup by applying a suction to the down stream end of the cup. The ash particles are then captured by the wire wool filter. The suction was generated by using a venturi connected to a high pressure air line and the flow rate calibrated so that the flow at the input connecter of the cup was equal to the flow rate within the test rig, thus ensuring that the sampling is isokinetic with the test duct. This flow was measured using a hand held anemometer and regulated by controlling the air pressure to the venturi.

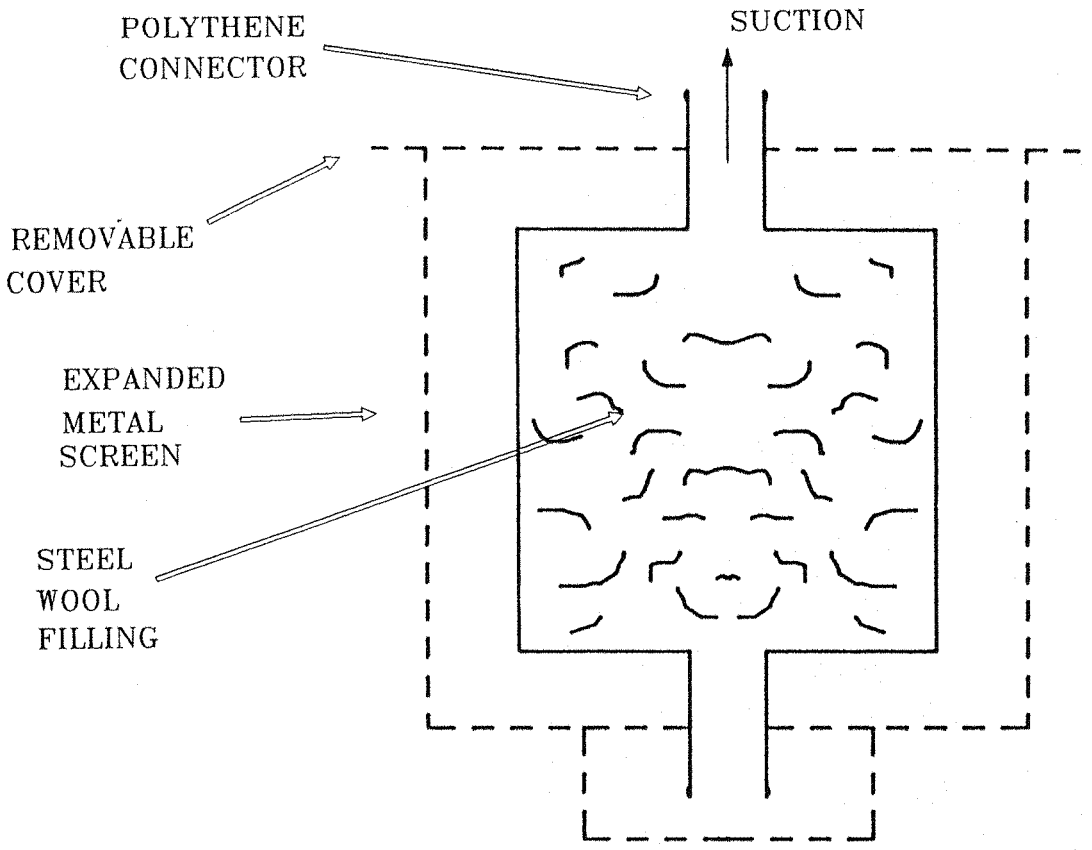

FIGURE 4.2.3 CONTINUOUS FLOW FARADAY CUP

The continuous flow Faraday cup could either be placed inside the rig, feeding directly from the ash cloud, or alternatively could be positioned outside the rig with a flexible tube leading from the sample site to the input of the cup. The second arrangement would help to alleviate the problems associated with the free ions generated by the corona discharge used to charge the ash. However, it was decided to place the cup within the rig. This position was chosen so as to avoid any undesirable effects the feed tube leading to the cup may have on the sample. These include the loss of the ash sample within the tube and the possibility of the tribo-electrification of the ash particles by collisions with the tube walls.

Plate (4.2.1) shows the continuous flow Faraday cup in position within the

rig. The electrical connections to the tin can be seen, the earth connection to the mesh being of particular importance as any charge on the mesh will register on the electrometer if it is not grounded. The air extraction tube is also shown leading away from the back of the cup. The extraction tube was shrouded with a grounded copper pipe, which also provided physical support for the cup, so no clamp stand which may have disrupted the air flow, was required within the rig. The front mesh has been removed from the cup in the photo, as it was found that there was no problem with free ions reaching the Faraday cup when it was so far back in the rig.

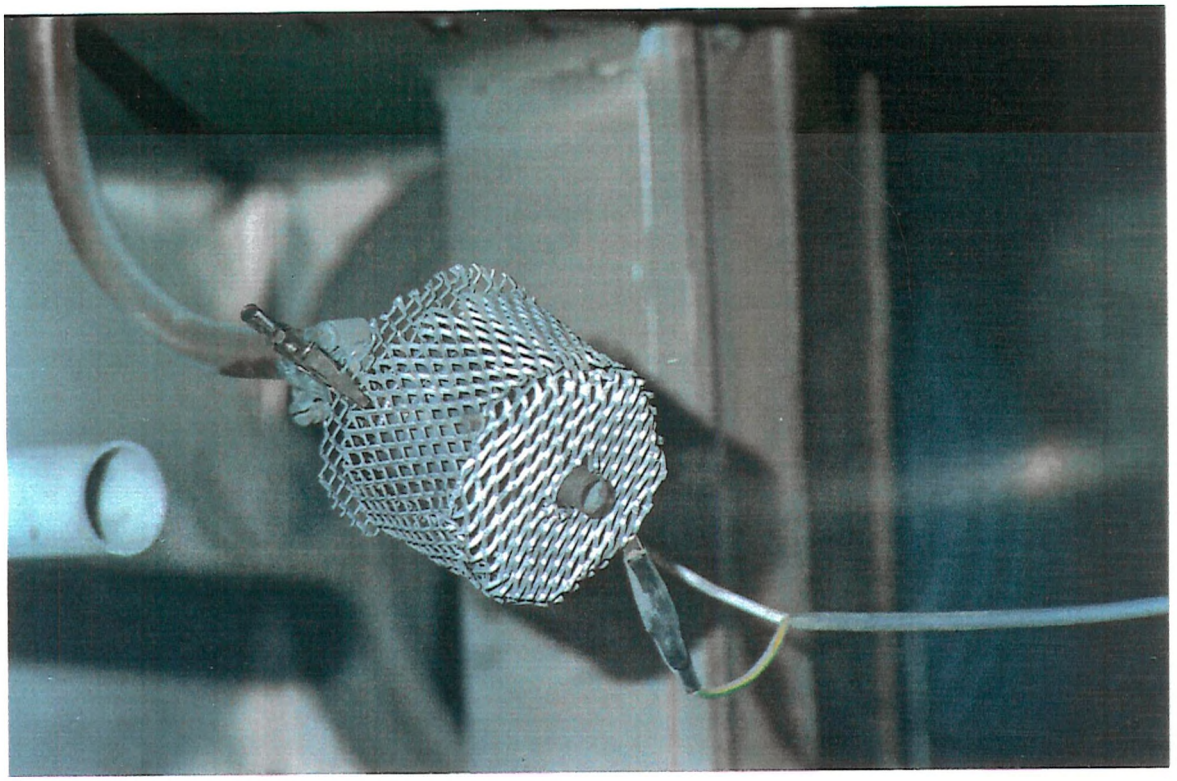

PLATE 4.2.1 CONTINUOUS FLOW FARADAY CUP

4.2.3 EXPERIMENTAL PROCEDURE

Measurements of the Charge to Mass ratio were made by using the following procedure:

1/ First a tare weight was determined for the tin with the outer mesh

removed.

2/ The outer mesh was then replaced and the cup located in the required position within the test rig.

3/ The suction tube leading to the venturi was connected to the back of the cup and the electrical connections made, the inner tin was connected to the electrometer and the outer mesh connected to ground.

4/ To take a sample the venturi air supply was turned on for the required time and the charge deposited within the cup noted from the electrometer.

5/ The cup was then taken from the rig, the outer mesh removed and any ash deposited on the plastic connecters removed, as this ash would have made no contribution to the charge recorded by the electrometer.

6/ The tin, now containing the ash sample, was reweighed.

7/ The ash sample was then removed from the tin by blasting air under high pressure alternately into one end of the tin and then the other.

8/ The tin was again weighed so as to obtain the new tare weight.

The continuous flow Faraday cup requires no calibration of its ability to register a charge on the sample. However, should a sample of ash come into contact with the wire wool, deposit its charge, and then fly out of the cup, the charge to mass ratio would be artificially high as the escaped particles would only contribute to the measured charge but not the mass. For this reason the cup was calibrated for its loss of mass over a fixed sample period.

4.2.4 MASS LOSS CALIBRATION PROCEDURE

1/ The test rig was run with its normal ash load.

2/ The venturi for the Faraday cup was opened and a normal charge to mass sample was taken for a period of 60 seconds.

3/ The mass of the cup and the trapped ash was then measured.

4/ The ash supply was turned off and the rig run with only the air stream flowing.

5/ The Faraday cup was then replaced within the rig and the venturi opened for a further 60 seconds.

6/ The cup was then reweighed and the percentage of ash lost calculated.

This process of replacing the cup and running with no ash was repeated ten times and the graph was plotted of the percentage of the ash retained after each 60 second interval. The entire test was then repeated twice more. The table of results and graph of the ash retained is shown in Tables (4.2.1) and Figure (4.2.4) respectively.

The ash contained in the tin after the first 60 seconds of the test period was assumed to be 100% of the sample for the purpose of the calculations, even though it is the percentage of the ash that is lost in these first 60 seconds that we require.

In order to determine the mass of ash lost in the first 60 seconds the graph plot can be extrapolated back to the t=0 point. This is shown in Figure (4.2.4) as a dotted line, which intersects the t=0 line at approximately 102%. So only 2% of the mass of the ash is lost in a 60 second sample time. This volume of ash lost from the cup during the sample period is insignificant and can be ignored.

4.3 TEMPERATURE AND HUMIDITY

Both the temperature and the humidity within the laboratory were constantly monitored for the entirety of the experimental period. Both of these will effect the charging and discharging mechanisms of the ash.

If the humidity is high the dew point is approached and the amount of

water vapour in the air condensing onto the surfaces is increased. The effect of this on an ash sample is to increase the amount of water adsorbed onto the surface of the particle and hence increase its conductivity.

The increased conductivity of the particles will then affect the charging process, the maximum charge level and the time required for the charging process to occur.

Total Test Period	**Recorded Ash Mass**			**Average Mass**	**Percentage of Ash Remaining**
(minutes)	**($Kg \times 10^{-5}$)**			**($Kg \times 10^{-5}$)**	**(%)**
1	4.87	6.23	5.16	5.42	100
2	4.79	6.14	5.06	5.33	98.34
3	4.71	6.03	4.97	5.24	96.68
4	4.65	5.97	4.93	5.18	95.57
5	4.64	5.94	4.89	5.16	95.20
6	4.59	5.91	4.86	5.12	94.46
7	4.60	5.89	4.84	5.11	94.28
8	4.57	5.87	4.82	5.09	93.91
9	4.56	5.84	4.81	5.07	93.54
10	4.55	5.84	4.80	5.06	93.36

TABLE 4.2.1 CONTINUOUS FLOW FARADAY CUP CALIBRATION RESULTS

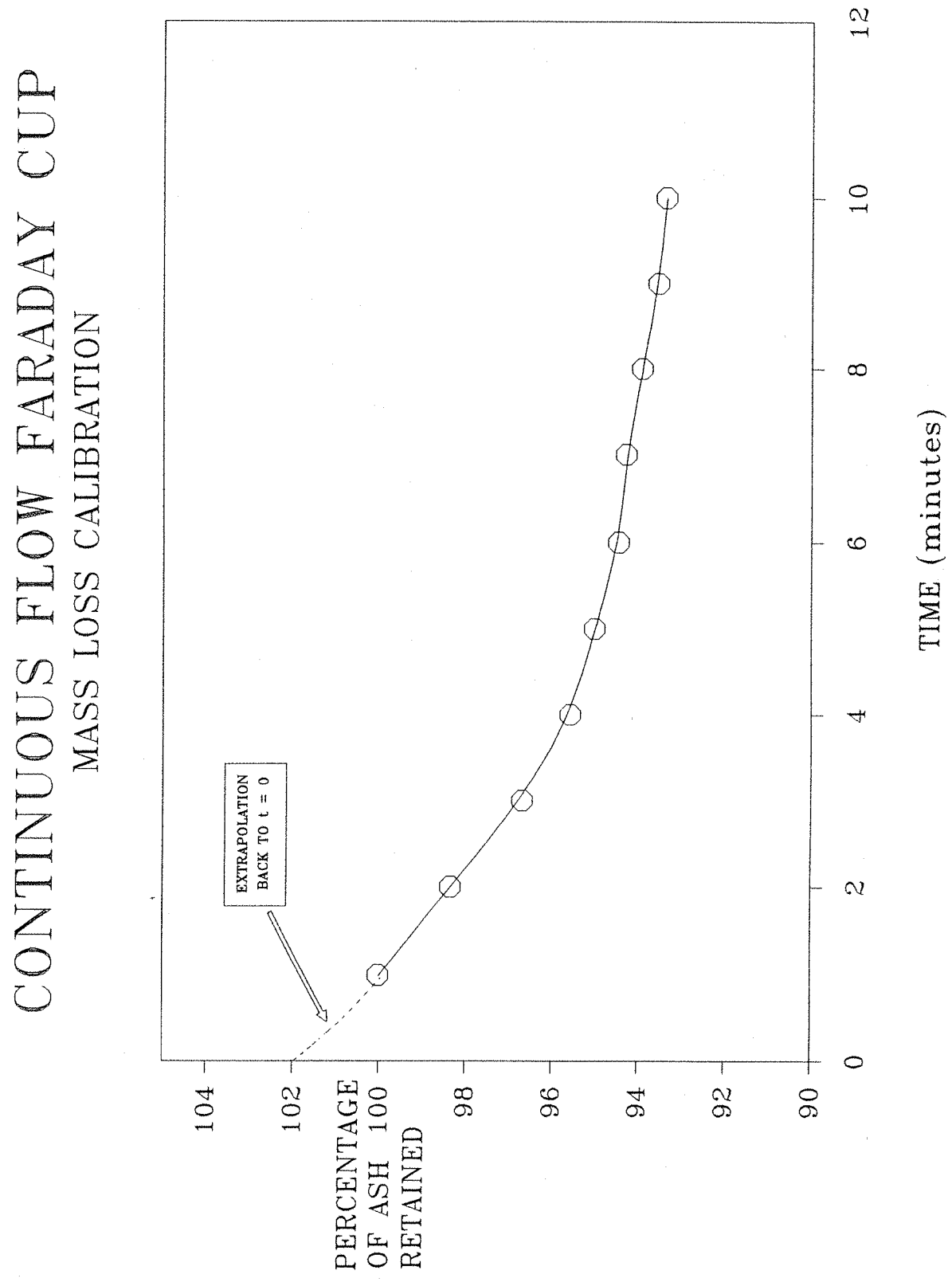

FIGURE 4.2.4 LOSS OF MASS FROM THE CONTINUOUS FLOW FARADAY CUP

4.4 ELECTRIC FIELD SIMULATION

In order to optimise the bi-polar charging system it was necessary to evaluate the field distribution within the charger. This can be found by solving Poisson's equation:

$$\nabla^2 V = \frac{Q_v}{\varepsilon_o \varepsilon_r} \qquad \textbf{Equation (4.4.1)}$$

Where: Q_v = The volume charge density.
ε_o = The permittivity of free space.
ε_r = The relative permittivity.

However, if the volume charge density is reduced to zero, Poisson's equation will reduce to Laplace's equation:

$$\nabla^2 V = 0 \qquad \textbf{Equation (4.4.2)}$$

For our system of high voltage electrodes, where the Gaussian limit is exceeded for the radius of curvature of the discharge electrodes, and hence they will be in corona, there will be a net flow of charge and hence the volume charge density will not be zero and Laplace's equation should not be used. However, in practice it is difficult to solve Poisson's equation analytically and even Laplace's equation can only be solved for fixed geometries where the physical position and the shape of the boundaries of the problem can be defined.

A solution to Laplace's equation can be modeled on a computer, by transforming the equation into cartesian coordinates:

$$\frac{\partial^2 V}{\partial x^2} + \frac{\partial^2 V}{\partial y^2} + \frac{\partial^2 V}{\partial z^2} = 0 \qquad \textbf{Equation (4.4.3)}$$

A two dimensional solution of this equation within the defined boundaries can be made using a finite element analysis and a tubes and slices computer program was used to do this[ref 4.1].

4.5 PARTICLE SIZE

Accurate measurement of particle size is of the utmost importance in this study, as it is a shift in the size distribution of the solid particles within the dust cloud that is desired. Also, knowing the size distribution of the fly-ash entering the system is imperative if the charging stages are to be optimised. This is because both the charging mechanism and the maximum charge achievable on the individual particles will be dependent on the particle size of the particles, as described in the previous chapter.

The particle sizing techniques used in this study can be divided into two broad groups; invasive and dynamic.

4.5.1 INVASIVE SIZE MEASUREMENTS

Particles can be extracted from any point within the test rig and analyzed for their size distribution. This process of extraction may however affect the results obtained, especially if weakly formed agglomerates are subjected to excessive aerodynamic stress. Also ensuring that the sample extracted is uniform to the parent sample may present difficulties especially when considering the range of particle sizes that require capture. Another problem with invasive measurement of agglomerate size is the inability to distinguish between an agglomerate and two particles that are captured on the same location.

The invasive measurement systems used were;

1/ Optical Microscopy of captured particles.
2/ Scanning Electron Microscopy of captured particles.
3/ Laser Diffraction Analysis of an ash sample.

4.5.2 DYNAMIC SIZE MEASUREMENTS

In order to overcome the problems associated with the extraction of a sample from the rig in order to measure its particle size distribution a non-invasive method of particle sizing was required. The method that could satisfy these requirements was Fraunhofer diffraction of a laser beam by the particles within the ash cloud.

4.5.3 OPTICAL MICROSCOPY

The ash samples were examined under the optical microscope by first dispersing a sample on to a microscope slide that had previously been coated with petroleum jelly. Two methods of dispersion onto the slides were used. One, by simply sprinkling the ash on the slide from above and allowing it to settle under gravity and secondly by placing the jelly coated slides vertically within the ash laden gas stream.

4.5.4 SCANNING ELECTRON MICROSCOPE

A small sample of the ash was examined under the scanning electron microscope so as to determine the general physical appearance of the finer particles, that could not be resolved under the optical microscope.

This sample was prepared by first placing a sample of the ash onto a piece of paper and then tipping it off. The remaining grey patch on the paper thus consists of only the finest ash particles and in a very low concentration. An electron microscope stub that had previously been coated with a conductive carbon 'dag' was then pressed lightly onto the piece of paper holding the ash particles. Once the dag had dried, a fine layer of gold was evaporated onto the surface of the ash particles, in order to increase their surface conductivity. This

stub was then examined at various magnifications under the scanning electron microscope and micrographs were taken of the images produced.

4.5.5 LASER DIFFRACTION PARTICLE SIZE ANALYSIS

The measurements of particle size were made using a Malvern Laser Particle Size Analyzer. This instrument is based on a technique developed by Swithenbank et al[ref 4.2], using the Fraunhoffer diffraction patterns formed by the scattering of laser light by the particles being measured. The basic laser system arrangement of the Malvern system is shown diagrammatically in Figure (4.5.1).

4.5.5.1 PARTICLE SIZE ANALYZER OPERATING PRINCIPLES

A 2 mW HeNe laser is used to produce a monochromatic beam of light, known as the analyzer beam. This beam is then collimated and expanded up to a diameter of 9 mm, which will then be scattered by any particles that may pass through it. The lower resolution size limit of the instrument is limited by the wave length of the laser radiation (633 nm), giving a lower resolution limit of 2 λ (approximately 1.2 μm). The upper size limit of resolution is however only limited by the minimum angle of scatter that can be detected. For the Malvern instrument used, this limit was about 1000 μm.

The scattered light and the un-scattered remainder then pass into the detector unit, through the receiver lens. This lens acts as a fast Fourier Transform lens, forming a far field diffraction pattern of the scattered light at its focal plane. Located at the focal plane is a detector in the form of 31 concentric photo diode rings and one central photo diode. The central detector measures the amount of un-scattered light from which the obscuration of the laser beam can be measured and the particle concentration calculated. The concentric ring detectors measure the scattered light over a range of solid angles, from which the particle size distribution of the measured sample can be calculated. The detector is detailed in Figure (4.5.2).

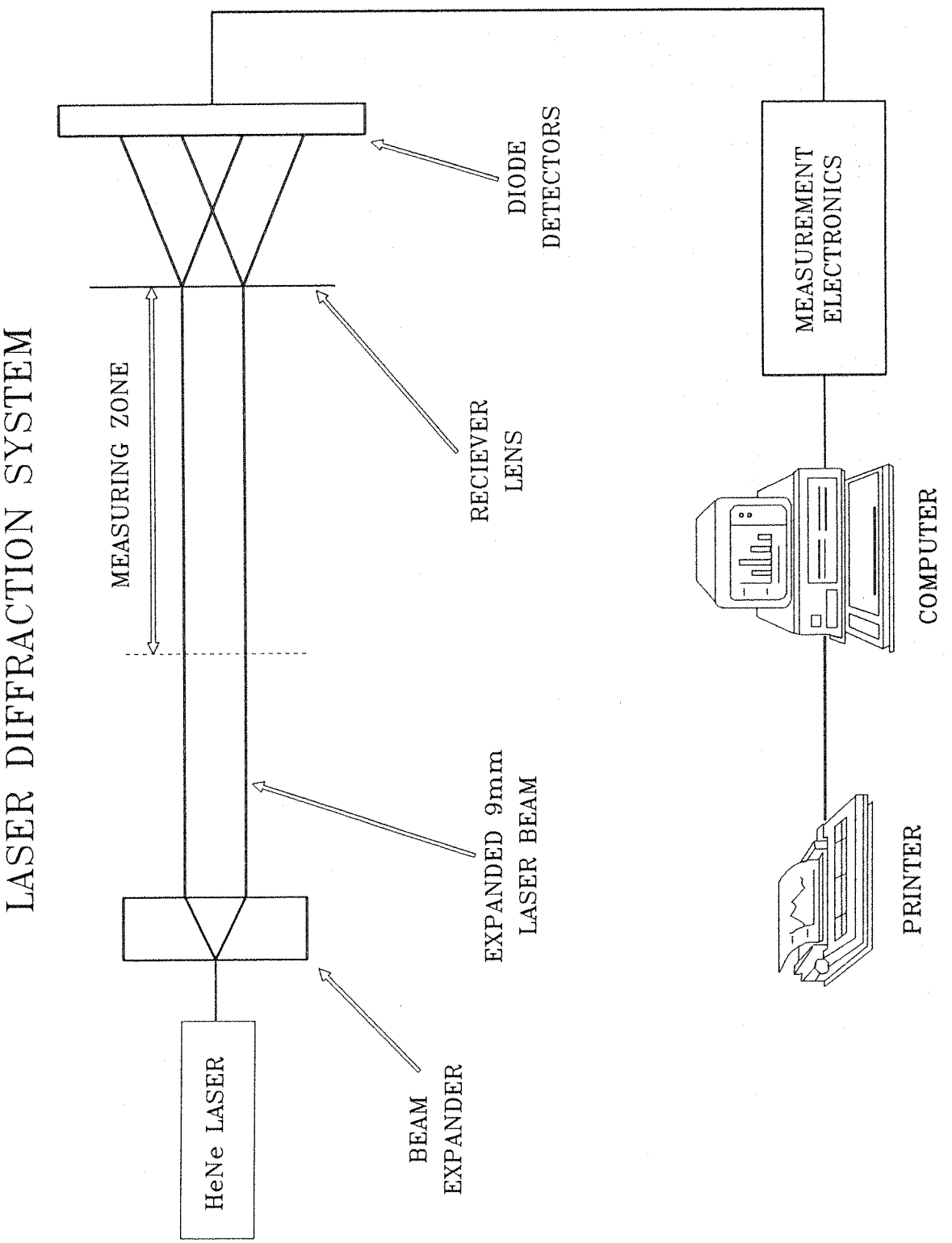

FIGURE 4.5.1 LASER DIFFRACTION PARTICLE SIZE MEASUREMENT SYSTEM

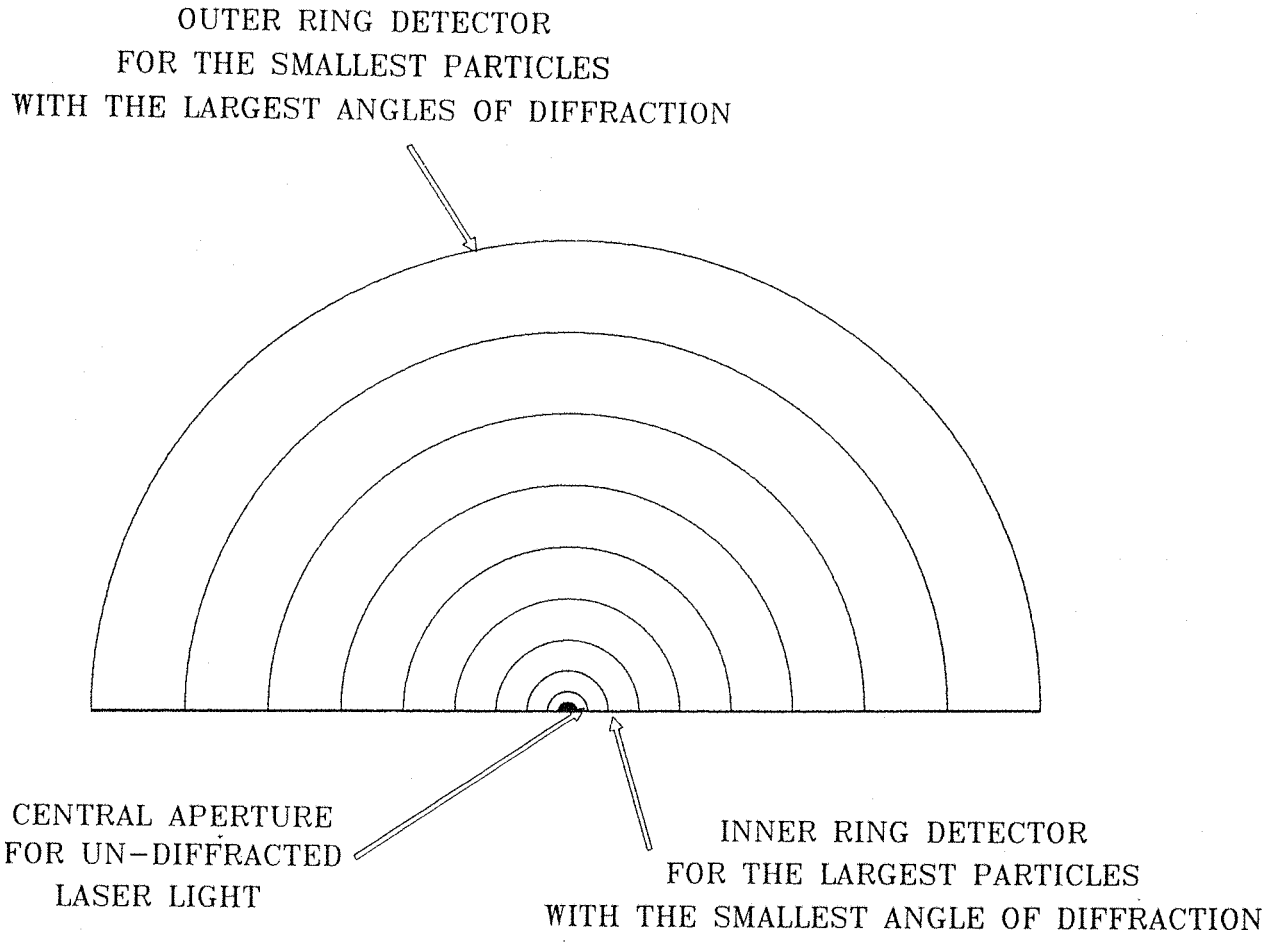

FIGURE 4.5.2 DETECTOR DIODE GEOMETRY

The Fourier transform receiver lens configuration has the interesting and useful property that wherever a particle is within the laser beam, its diffraction pattern is stationary and centred on the optical axis of the receiver lens. This is shown diagrammatically in Figure (4.5.3).

From Figure (4.5.3) it is shown that it does not matter if a particle is moving through the analyzer beam, Its diffraction pattern will always remain incident on the same set of detector rings. Also it does not matter where in the analyzer beam the particle passes. The lens transformation is optical and is therefore instant, so no practically encountered sample velocities are high enough to cause significant errors in this transformation. However, the reading of the diodes is not continuous but is sampled at a fixed rate.

In practice many particles are simultaneously present within the analyzer beam and the scattered light measured on the detector is the sum of the patterns from all the individual particles. Thus the system inherently measures the integral scattering from all particles present within the beam.

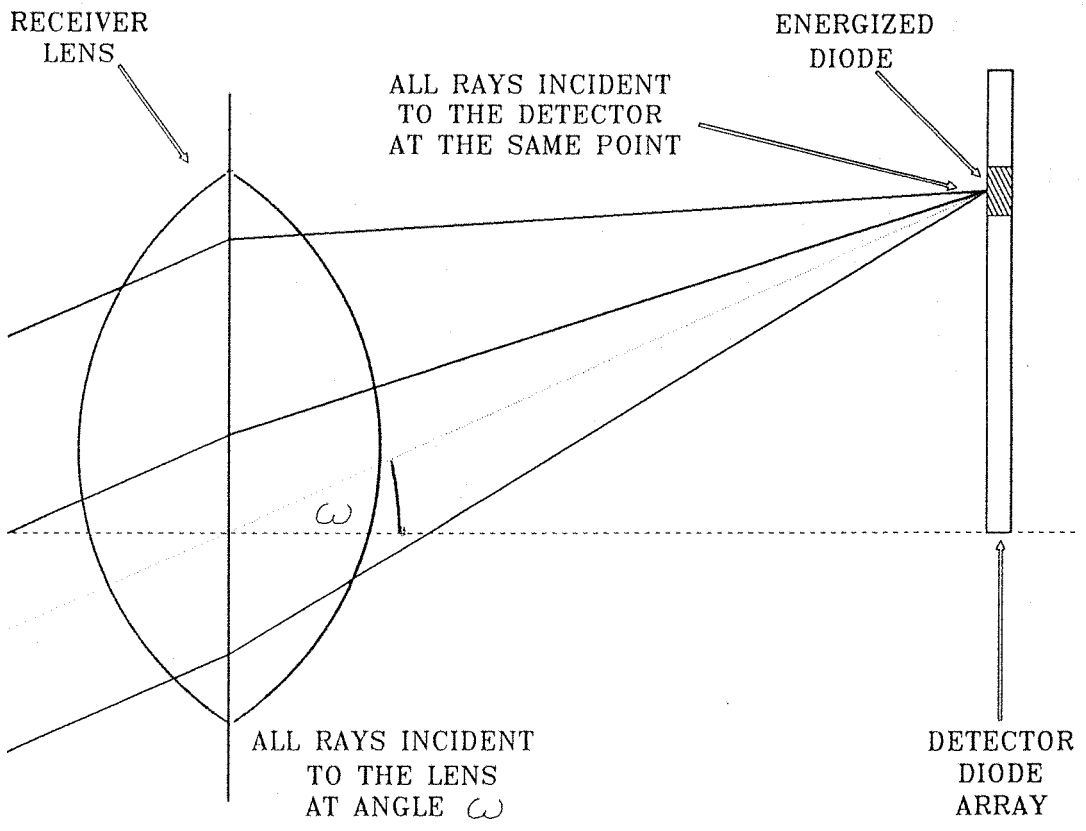

FIGURE 4.5.3 FOURIER TRANSFORM RECEIVER LENS

One instantaneous measurement of the scattered light would give a size distribution based on only the cross section of the sample within the beam at that instant, which may not be uniform to the parent sample. This would produce two problems; inadequate statistical significance and unrepresentative sampling. This can be avoided by time average observation, i.e. by running the test for longer. Typically the number of particles needed in the beam simultaneously to obtain an adequate measurement of the scattering would be 100 - 10,000.

When a particle scatters the light it produces a unique light intensity

characteristic with angles of minimum and maximum light intensities. These angles are dependent on the particle size, as represented in Figure (4.5.4). To simplify this explanation let us consider that a particle only scatters light at one angle, which is dependent on its size. Basically large particles scatter light into smaller angles than small particles, as is illustrated in Figure (4.5.5).

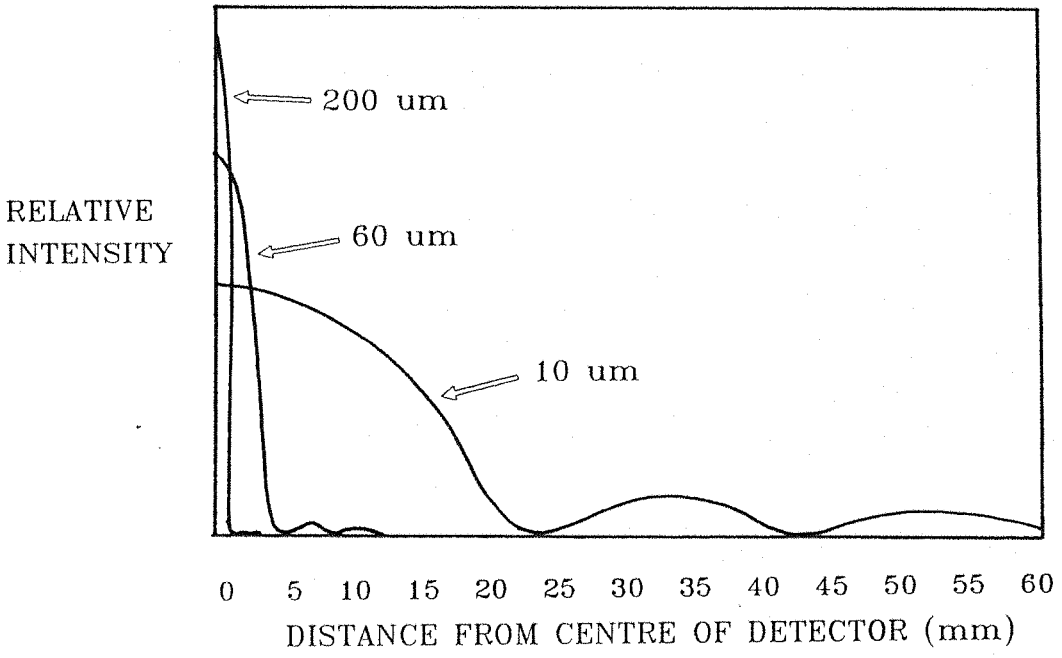

FIGURE 4.5.4 LIGHT INTENSITY DISTRIBUTION OF SCATTERED LIGHT

Over the size range of interest, typically 1.2 um and upwards, the scattering angle is independent of the optical properties of the material or the medium of suspension.

4.5.5.2 RESULT ANALYSIS

The computer deduces the Volume Size Distribution that gives rise to the observed scattering characteristics. It achieves this by a process of constrained least squares fitting of theoretical scattering characteristics to the observed data. The data can be analyzed as a best fit to a number of statistical models, these

being Normal, Log Normal and Rossin-Ramler. However, it is usual to allow the best fit result to be obtained with no assumed form of size distribution, in which case the system is set to model independent.

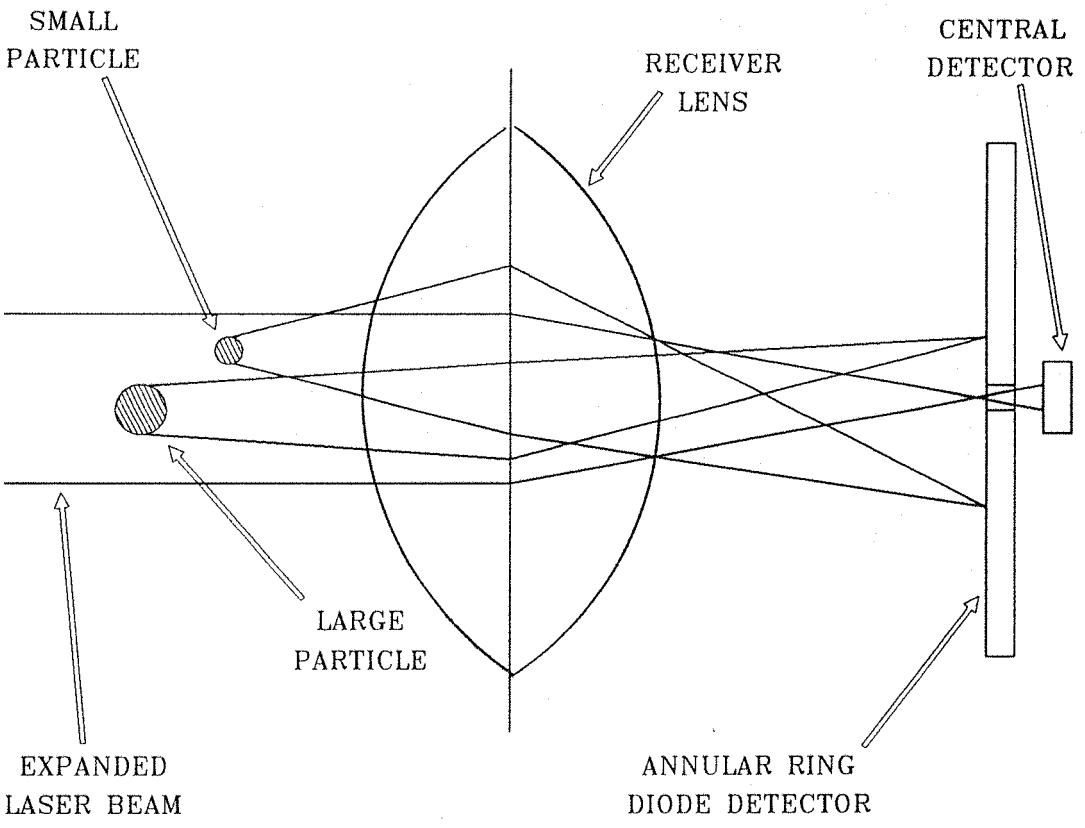

FIGURE 4.5.5 ANGLE OF LIGHT SCATTERING FOR DIFFERENT PARTICLE SIZES

4.5.5.3 PARTICLE SIZE OUTPUT

The output from the system is in the form of a particle size histogram, on a logarithmic scale of particle size. This histogram can be a number, size or volume distribution. The computer also gives various parameters of the distribution, these are given in Table (4.5.1).

The computer also gives a parameter which indicates the adequacy of the fit of the measured sample to the theoretical scatter pattern. This is the log difference of the error in the least squares fit. Its value can be used as a guide-

line to the validity of the measured results. As shown in Table (4.5.2).

It is important to remember that the sample being measured may in fact not fit to an expected model, in which case a perfect measurement of the sample may produce a large log difference. This is especially true if the sample being measured is a blend of more than one powder.

OUTPUT	DESCRIPTION
The Mass Median Diameter	The particle diameter above and below which 50% of the mass of the sample lies.
(D 90%)	The particle diameter above which 10% of the mass of the sample lies.
(D 10%)	The particle diameter below which 10% of the mass of the sample lies.
SPAN = $\frac{(D\ 90\%) - (D\ 10\%)}{(D\ 50\%)}$	A dimensionless number representing the range of particle sizes in the distribution.

TABLE 4.5.1 SIZE PARAMETERS

4.5.5.4 LASER DIFFRACTION MEASUREMENTS

The Malvern particle size analyzer was used for both invasive and dynamic measurements of the ash particle size distributions.

4.5.5.4.1 DRY POWDER FEED (INVASIVE)

The invasive measurements were made by collecting samples of the ash and then blowing them through the laser beam. A dry powder feeder, also produced by the Malvern company, was used for this purpose.

The dry powder feeder uses a vibrating hopper to feed the powder sample into an orifice. The sample is then pounded by steel balls as it passes through a sieve. From there a high velocity air stream is used to drive the sample across the laser beam. This process of dispersing the sample was particularly successful at smashing any clumps of particles into single particles. As such, it was no use in the analysis of samples captured from the test rig, as it would destroy any agglomerates that had been formed through the electrostatic processes. However, this technique was ideal for analyzing the original samples of the ash, or any samples removed from the surfaces of the test rig. Between 10 and 20 grams of the ash was required for each dry powder feed test. So quite large volumes of the ash had to be deposited onto and then collected from any surface before the dry powder feed system could be used.

LOG DIFFERENCE VALUE	SIGNIFICANCE
Greater than 6.0	Poor results presentation.
5.5 to 6.0	Poor fit of results to expected model, the results obtained are good for comparative purposes only.
5.0 to 5.5	Reasonable fit to expected model.
4.0 to 5.0	Good fit of the data to the expected model.
Less than 4.0	An unlikely result from measured data.

TABLE 4.5.2 ERROR VALUES

4.5.5.4.2 ASH CLOUD MEASUREMENTS (DYNAMIC)

In order to make dynamic measurements of the particle size distributions of the ash within the test duct it would be necessary to shine the laser beam through the duct. However, the laser measurement system requires that the sample to be analyzed passes through only the measuring zone of the laser beam

and no other part of the beam. The measuring zone is shown in Figure (4.5.1). The measuring zone extends out from the receiver lens to a distance determined by the focal length of the lens. As it was required to measure particles as small as 1.2 μm the 63 mm receiver lens had to be used, which has a measuring zone extending out to only 55 mm. Particles passing through the laser beam outside the measuring zone are measured incorrectly and a faulty result obtained.

It was not possible to shine the beam through the test duct, as the width of the duct is considerably greater than the maximum 55 mm measuring zone. A system to extract a sample of the ash from the rig had to be developed.

This extraction system consisted of a 30 mm diameter plastic tube, that could be inserted into the test duct from the down stream end up to any distance. The sample was then drawn along the tube by an 'air mover', a device that induces a gas flow along a tube by forcing compressed air through a venturi in line with the required flow. The air mover was located downstream of the measuring point, as it was expected that large shear stresses would be induced into the sampled gas from the introduction of the high pressure air.

The rate of the gas flow within the sample tube could be set by adjusting the compressed air pressure to the air mover. The velocity of the extracted gas was controlled so as to produce isokinetic sampling of the gas within the rig. The hot wire anemometer described later in this chapter was used at the orifice of the extraction tube to ensure that the two flow rates were equal.

The extraction tube passed through the Malvern instrument and a hole was cut in both sides of the tube to allow the laser beam to pass through the ash sample. The hole for the input of the laser beam had to be a minimum of 9 mm, to allow the full expanded laser beam to enter the measuring zone. However, the hole through which the laser beam must exit had to be cut large enough for the scattered light to pass through un-attenuated. These holes had to be sealed with glass windows to stop air from outside of the rig being drawn into the sampling system. These windows were supported on a tube glued to the sample tube. The glass was held in place with large spring clips and 'O' rings were used to make an air tight seal. This arrangement allowed the glass to be removed and cleaned after each measurement, as a small amount of the ash was found to deposit onto the glass surfaces. Care was required to ensure that the test zone in the

extraction tube was located within the measuring zone of the receiver lens and that neither the expanded input laser beam nor the diffracted output beam were obstructed by the sample system. The entire arrangement of the Malvern laser transmitter and receiver, along with the ash extraction system can be seen in Plate (4.5.1) and is illustrated in Figure (4.5.6).

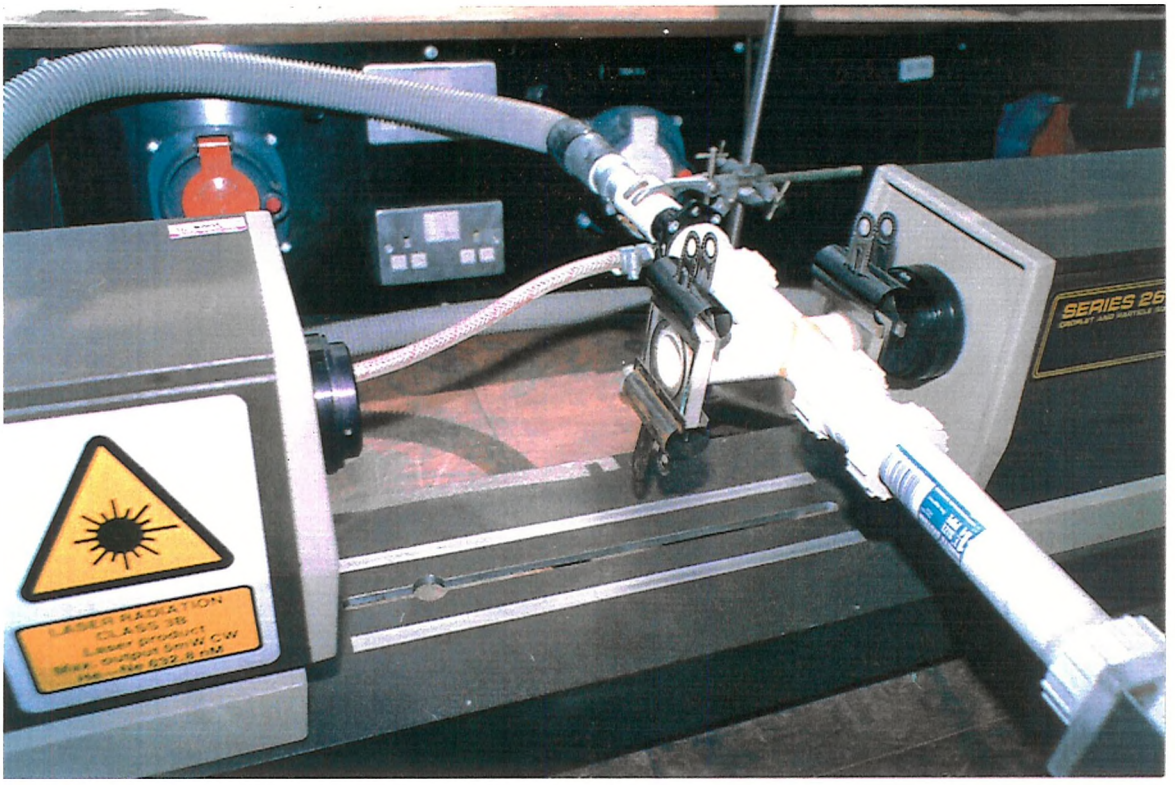

PLATE 4.5.1 MALVERN LASER PARTICLE SIZE ANALYZER DETAILING THE OPTICAL ASH SAMPLING SYSTEM

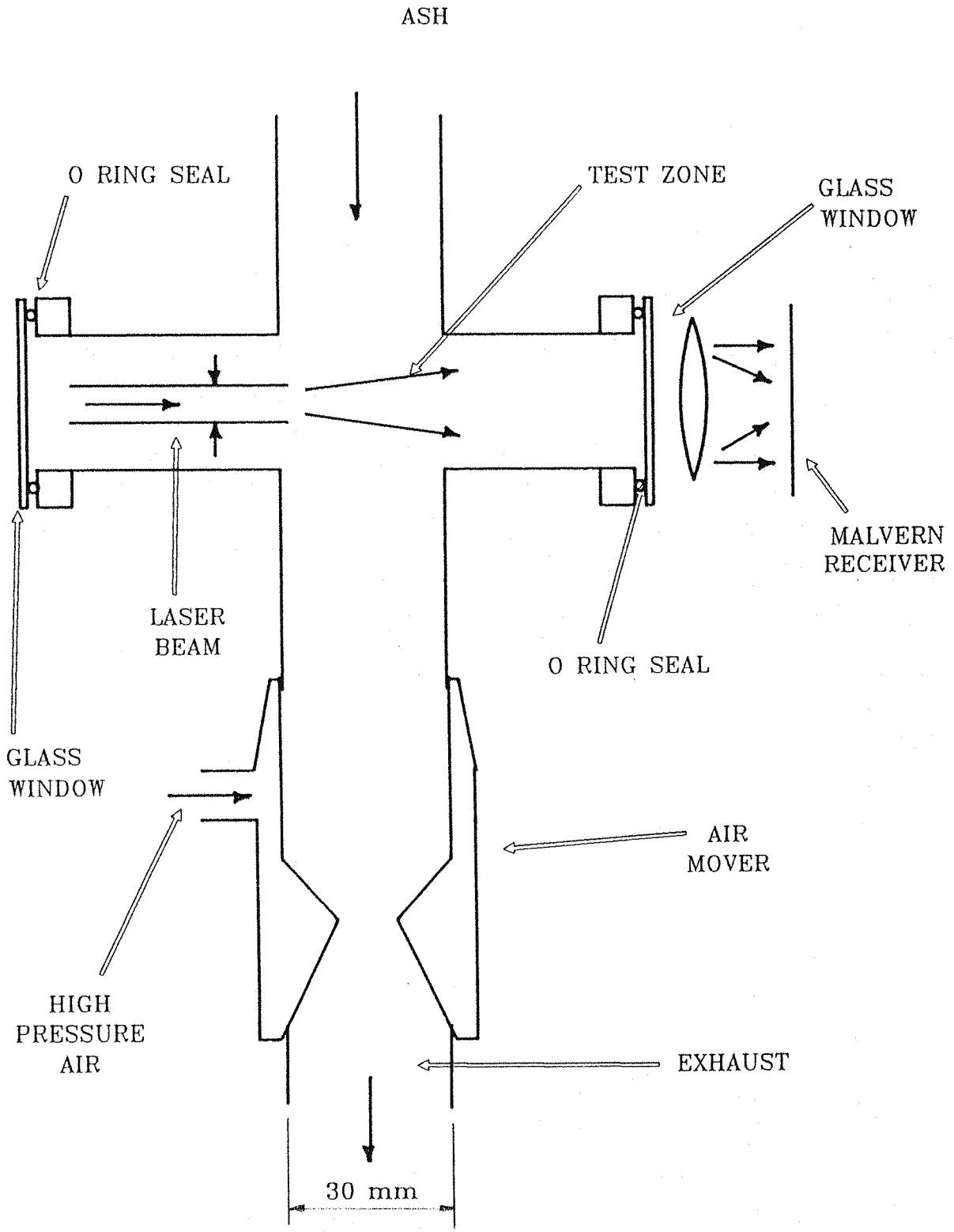

FIGURE 4.5.6 **OPTICAL ASH SAMPLING SYSTEM**

4.6 GAS FLOW

The measurements of the air flow patterns within the test duct were of particular importance. If the bi-polarly charged ash cloud is to be mixed in the test duct in such a way as to promote agglomeration, then the mode of the flow must be carefully controlled and monitored. A highly turbulent region is required immediately after the charging stage, where the two oppositely charged gas streams are to be mixed together. This should be followed by a region of fairly low turbulence where the particles are allowed to migrate towards one another under their mutual electrostatic force of attraction and form agglomerates. This 'drift' region must have minimal aerodynamic shear stresses, as these will break any agglomerates that have formed.

4.6.1 GAS FLOW INSTRUMENTATION

A hot wire anemometer was used to measure the direction and the rate of the gas flow at various points throughout the test rig. The velocity was determined by slowly rotating the anemometer head through a few degrees and recording the maximum velocity registered on the metre. The mean direction of the gas flow at that point was also found by noting the angle to which the head of the anemometer had been rotated. This was done by attaching a protractor to the shaft of the anemometer and a stationary pointer to the lab clamp which held the anemometer. This measurement system is illustrated if Figure (4.6.1).

It must be remembered that the gas flow vector measured in a turbulent flow will be the time average of more than one gas flow vector. So the resultant vector, with an angle (gas flow direction) close to the net gas flow direction, and a small amplitude (gas flow velocity) may in fact be the resultant of two or more vectors with large amplitudes and greatly opposing direction. Such a case is illustrated in Figure (4.6.2), where a small resultant vector is produced from the sum of two large vectors.

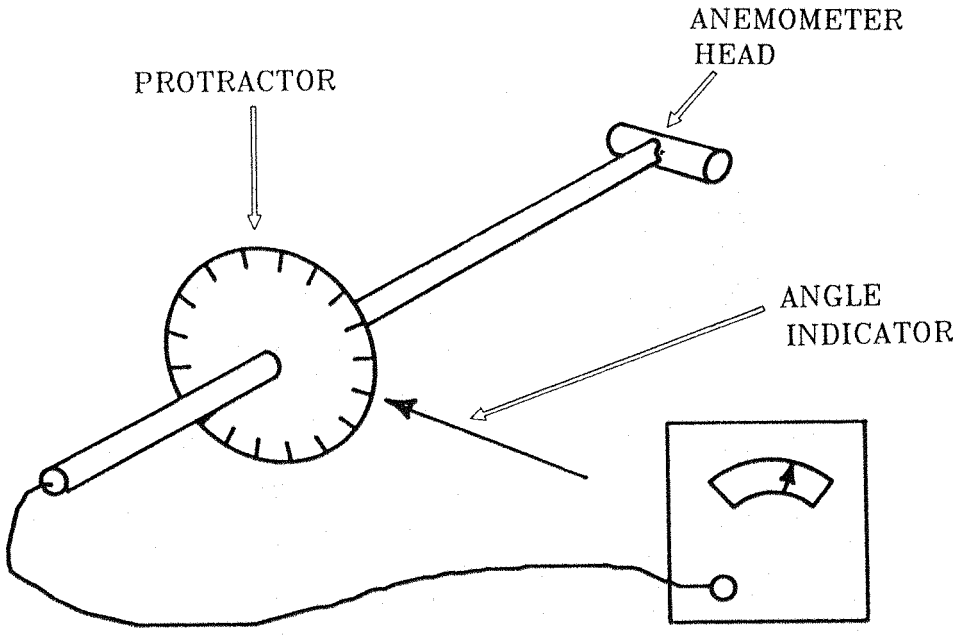

FIGURE 4.6.1 GAS FLOW RATE MEASUREMENT APPARATUS

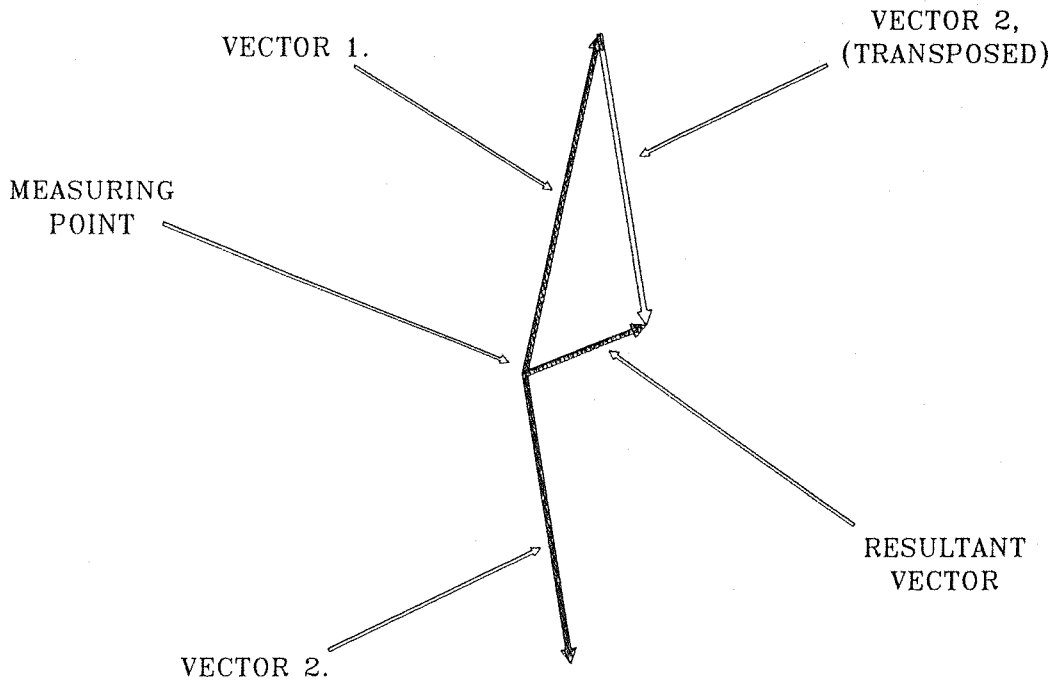

FIGURE 4.6.2 VECTOR ADDITION OF GAS FLOW

4.7 PARALLEL PLATES

A continuous flow Faraday cup has been described earlier in this chapter, this cup could be used to extract samples of the ash from the test duct and measurements of the net charge to mass ratio of the sample made. However, this cup cannot differentiate between particles with different charge levels or different polarities. In order to make measurements on only one polarity of charged particles or particles with specific charge levels a simple electrostatic precipitator was fabricated. As no additional charge is required on the ash particles, only a deposition field, this precipitator can consist of a pair of parallel plates.

4.7.1 PHYSICAL DESCRIPTION

A pair of parallel plates were fabricated from aluminium sheet. These measured 200 mm by 200 mm with a variable spacing between the plates of 10 mm to 80 mm. Both plates were connected to high tension cables, and all the sharp protrusions, corners and edges were smoothed in order to stop any corona discharge from the plates.

The plates could be placed in either a horizontal or a vertical orientation. If placed horizontally, the electrostatic forces will be acting in parallel to the gravitational force. However, if the plates were to be placed vertically, the electrostatic and gravitational forces will be acting perpendicularly to one another and the effect of the gravitational force on the captured particles can be ignored. The parallel plate arrangement is illustrated in Figure (4.7.1), where the location of the ash particle size sample tube, leading to the Malvern instrument, is also shown.

4.7.2 PLATE CONFIGURATION

The plates could be connected to either a high voltage power supply, through the high tension cable or to an electrometer, allowing the charge of any

particles that alight onto the surface of the plate to be measured.

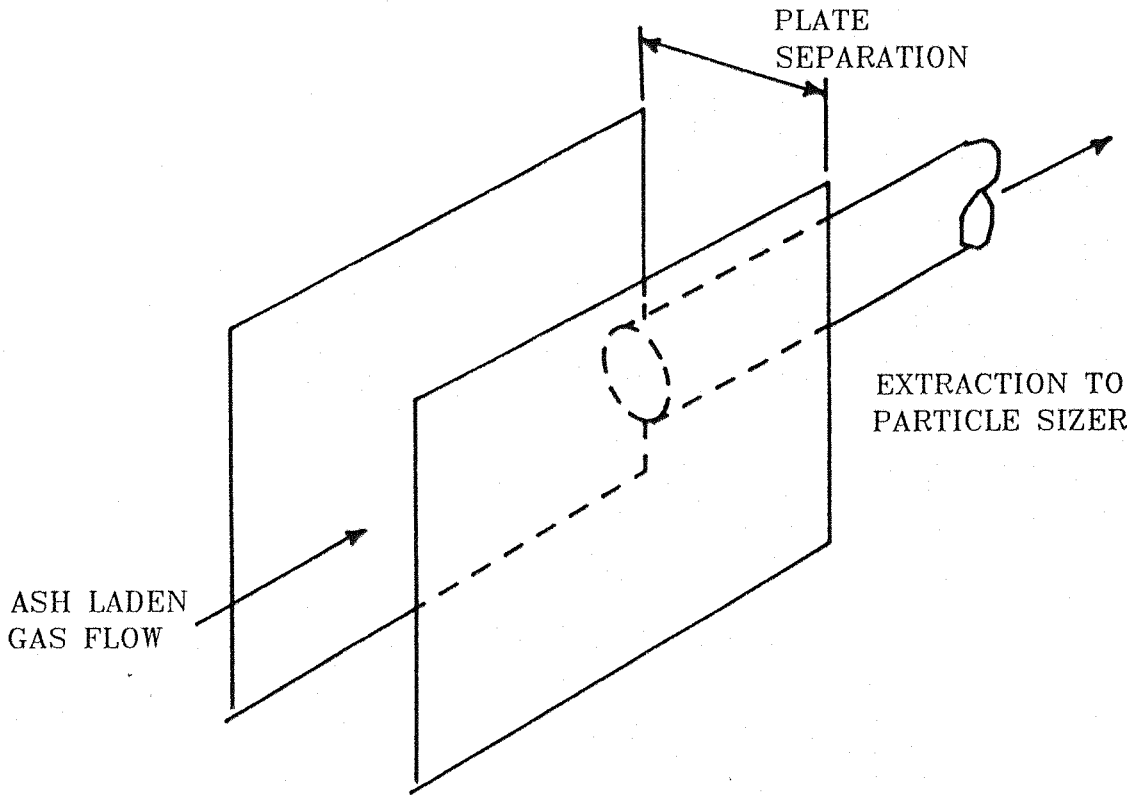

FIGURE 4.7.1 PARALLEL PLATE ARRANGEMENT

4.7.2.1 BOTH PLATES ENERGIZED

If both plates are connected to high voltage power supplies of opposite polarity, a strong electric field will be set up between the two plates. As the bi-polarly charged ash cloud passes between the energised plates the positively charged particles will deposit onto the negative plate and conversely the negatively charged particles will deposit onto the positive plate. So only uncharged and agglomerated particles with a net charge of zero will pass straight past the plates. The Malvern particle size system can then be used to measure the size of the particles which were not captured by the plates. Comparisons can then be made to ash size distributions found when either the plates or the charging system were not energised. For these tests the current to the plates would have to be carefully monitored, as neither plate should be allowed to go

into corona, as ions will be formed within the intensified electric field which will act to charge or discharge the ash as it passes through the system.

4.7.2.2 ONE PLATES ENERGIZED

If one plate is grounded through an electrometer and the other energised with a high voltage, then the particles of the same polarity as the energized plate will be deposited onto the plate that is connected to the electrometer. The charge to mass ratio of the collected ash can be calculated by recording the charge on the plate and weighing the plate before and after the test. Again care is required to ensure that the energised plate does not go into corona, as the gas ions produced will be attracted to the opposite plate and will be registered by the electrometer as a charge, hence giving a higher charge to mass ratio than should be recorded for the ash alone.

CHAPTER FIVE

ASH CHARACTERISTICS

Eight different samples of ash were used throughout the experimental period of this study. All were supplied by C.E.R.L., although in some cases the exact origin of the sample was unclear. These eight samples were labelled as follows:

NAME	SOURCE	
OLD ASH	Laboratory sample	- Source unknown -
NEW ASH	Supplied by C.E.R.L.	- Source unknown -
S1	Supplied by C.E.R.L.	- Source unknown -
S2	Supplied by C.E.R.L.	- Source unknown -
S3	Supplied by C.E.R.L.	- Source unknown -
S4	Supplied by C.E.R.L.	- Source unknown -
SD1	Supplied by C.E.R.L.	- From Didcot -
SD2	Supplied by C.E.R.L.	- From Didcot -

Samples SD1 and SD2 were labelled as coming from Didcot, a fluidized bed pulverised coal burning power station. Although samples S1 through to S4 were unlabelled, it can be assumed that they were also from Didcot as they were packaged in the same way and arrived in the same delivery.

5.1 ASH COLLECTION

All of these ash samples were collected from the hoppers of the electrostatic precipitator at the power station. For this reason it was reasonable to assume that the samples were not exactly uniform with that of the original ash discharged from the power station furnaces. This is due to the deficiencies in the collecting efficiencies of the precipitators, which are unable to capture the finest particles of the distribution. Hence it is probable that these finest particles of fly-ash were absent from the received samples.

The ash samples were delivered in paper sacks and were of an unspecified age. Freshly generated ash is very hygroscopic and will quickly adsorb water vapour from the atmosphere. Also hot newly formed ash has an acidic outer coating which is lost to the atmosphere in a very short period of time. Hence the exact physical condition of the ash delivered was unclear. However to avoid any further degradation of the samples, they were all decanted into air tight plastic containers on arrival at the laboratory.

5.2 PHYSICAL CHARACTERISTICS

5.2.1 EXAMINATION BY EYE

All of the samples were first inspected by eye, in order to obtain an overall impression of their physical make-up and consistency. With the exception of the 'OLD ASH' sample, all the ash samples were of a darker than expected grey colour. The dark colour possibly indicating a higher than normal carbon content. The sample that was found in the laboratory 'OLD ASH', which had been left over from the previous work on electrostatic precipitation, was of the expected light grey colour. If the darker grey colour detected in the other seven samples was due to a high carbon content, then this carbon would be unburnt fuel. Hence the dark colour is a good indication of the efficiency of the coal burners at the power station.

When the ash was poured from the paper sacks into the air tight

containers, a plume of the finest particles was seen to rise into the air. These particles seemed to 'hang' in the air for quite some time and not to immediately fall under the influence of gravity, indicating that these clouds were consistent of very fine particles (possibly even less than 1 μm in diameter).

It was expected that the ash would be fairly free flowing but in fact all the samples seemed clumpy and would not pour easily. This sticky property of the bulk powder was probably an indication of the surface condition of the individual particles, giving an indication of the amount of humidity that had been adsorbed by the ash from the atmosphere.

5.2.2 EXAMINATION UNDER THE OPTICAL MICROSCOPE

All eight of the ash samples supplied were examined under the optical microscope. This test was to verify the types and shape of the particles that were present within the sample, as well as to give an overall picture of the particle size range present within the ash.

5.2.2.1 OPTICAL SLIDE PREPARATION

The samples to be viewed under the microscope were produced by first coating a microscope slide in petroleum jelly. The ash was then distributed onto the surface of the slide by gently blowing the sample over the sticky surface. Care was taken to disperse only a small amount of the ash onto the slide as an excessive number of particles would have made differentiating the single particles from the clumped particles difficult. Once coated the slide was turned on its side and gently tapped, to remove any particles that were not stuck to the jelly. The preparation of the slide in this manner had probably not produced a good representation of the original sample. As the finer particles within the air blown stream would preferentially follow the air and not fall under the influence of gravity. Also the sample produced is very small and can therefore not be considered uniform to the original sample. Two photographs of the slide produced from the sample 'S3' are shown in Plates (5.2.1) and (5.2.2), along with a photograph of the graticule so as to allow approximations to be made of the particle sizes. In both cases the smallest division of the graticule is 25μm.

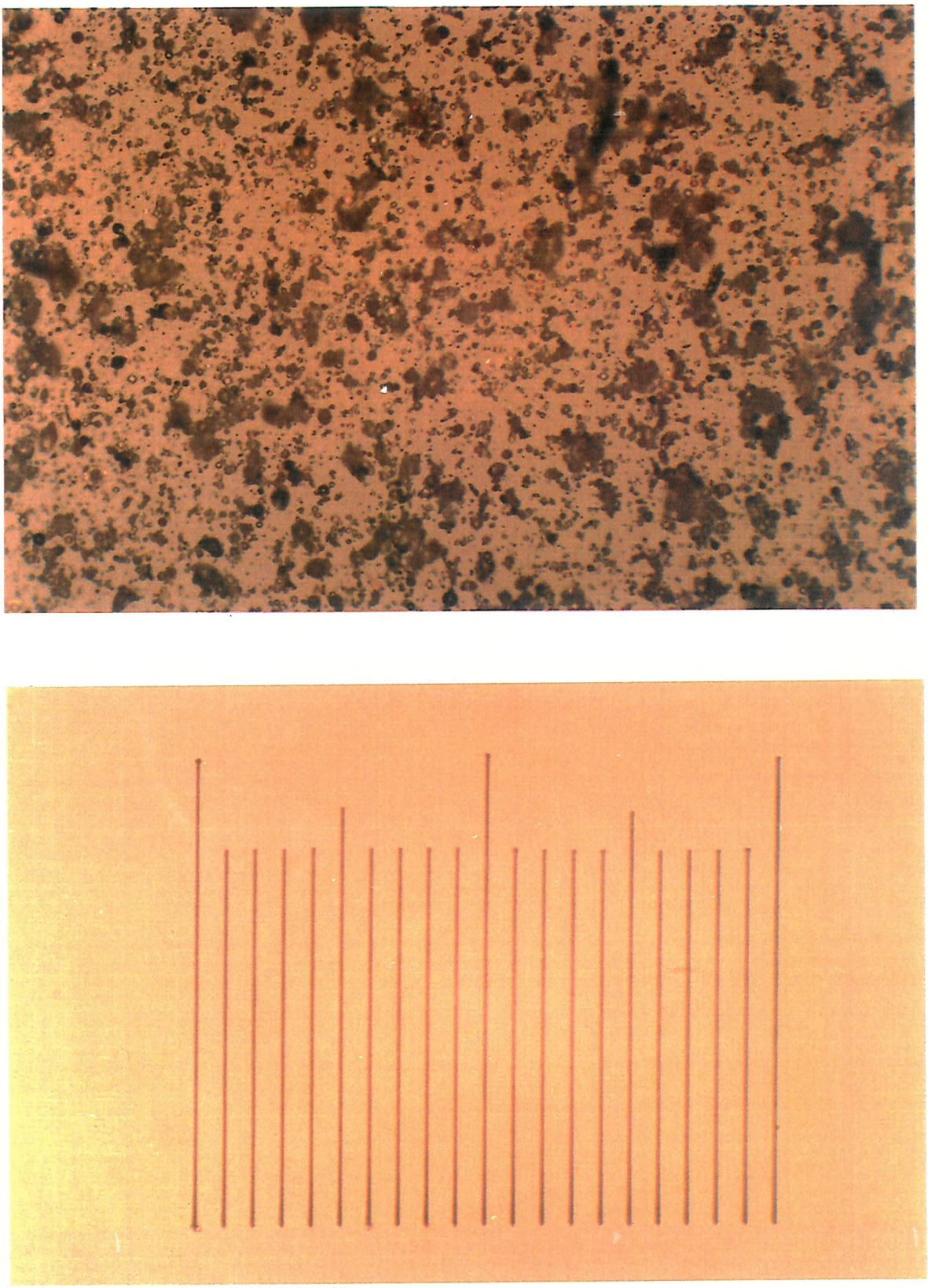

PLATE 5.2.1 ASH SAMPLE S3 VIEWED UNDER AN OPTICAL MICROSCOPE

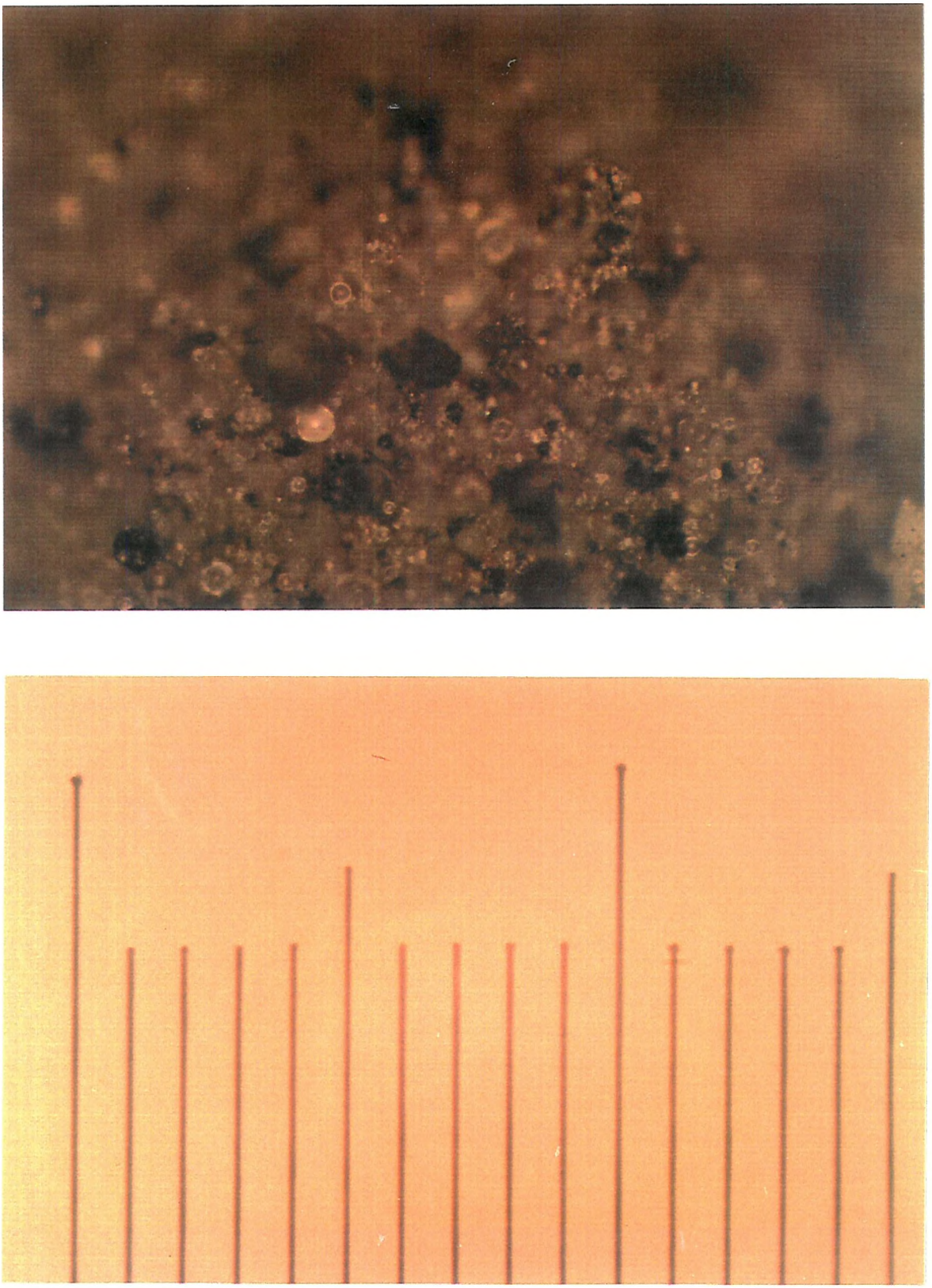

PLATE 5.2.2 ASH SAMPLE S3 VIEWED UNDER AN OPTICAL MICROSCOPE

5.2.2.2 OBSERVATIONS

All eight of the samples were of a very similar composition, consisting of a majority of very small grey/white spherical particles, thought to be the ash. Also a smaller number of large black particles seen on all the slides except that produced from the sample 'OLD ASH'. These larger particles were irregular in shape and thought to be the unburnt fuel.

The fact that all the ash particles seen were spherical in shape is of particular importance, as the theoretical equations derived in the third chapter of this report, to calculate the charge levels on the particles and the particle size assume spherical geometry.

Although by far the majority of the ash particles seen under the microscope were smaller than 10 μm in diameter, a number of particles were seen in all the samples with diameters up to 100 μm. However, it is unclear by looking at the slide whether the particles that have clumped together are agglomerates or simply the result of more than one particle landing on the same spot.

The large black un-burnt fuel particles seem to be of a far larger size distribution than that of the genuine ash particles. While none of the black irregularly shaped particles were seen with a diameter less than 10 μm several were found with diameters up to 500 μm.

However, it is important to remember that while trying to assess the make up of the ash samples under the optical microscope, the fact that the human eye is biased towards the largest particles, giving them un-due significance in the estimated size distribution. Also the eye will be drawn to the particles that are not consistent with the overall distribution, by the simple fact that they are different. Hence un-due significance may be placed to the effect of these particles on the estimated particle size distribution of the ash sample. It is also important to remember that when counting the number of particles seen that there is a cube relationship between particle diameter and number, as detailed in the earlier section on particle size measurement. This cube relationship will bias the eye to the greater number of fine particles, which hold less volume of the sample.

5.2.3 SCANNING ELECTRON MICROSCOPE

In order to gain a clearer picture of the ash particles and verify the existence of the finest particles of the distribution, a sample of ash was taken from the 'NEW ASH' sample and examined using the scanning electron microscope.

5.2.3.1 SAMPLE PREPARATION

A very small sample of 'NEW ASH' was poured onto a piece of paper and then gently poured off. This process left only a very light residue of grey particles on the paper. This residue would thus only consist of the finest particles of the original sample. An electron microscope stub, which had previously been coated in a conducting carbon dag, was then pressed onto the ash residue remaining on the paper. This action transferred a very thin layer of the ash onto the stub. This technique was used so as to prevent any of the larger particles of the original sample becoming part of the measured sample. Also the particle concentration on the stub had to be kept sufficiently low, so as not to produce a conductivity problem once the sample is examined.

A very fine layer of gold was then evaporated onto the surface of the stub, to increase the surface conductivity of the sample. This was necessary as a low conductivity of the ash would cause the sample to warm as the electron current passed through it, this would cause the image produced to blur.

The ash was then viewed under several magnifications and two photographs were taken. The first photograph '001' was taken on a scale of 7.5 μm/cm and the second '002' on a scale of 1.5 μm/cm. Both of these photographs can be seen in Plate (5.2.3).

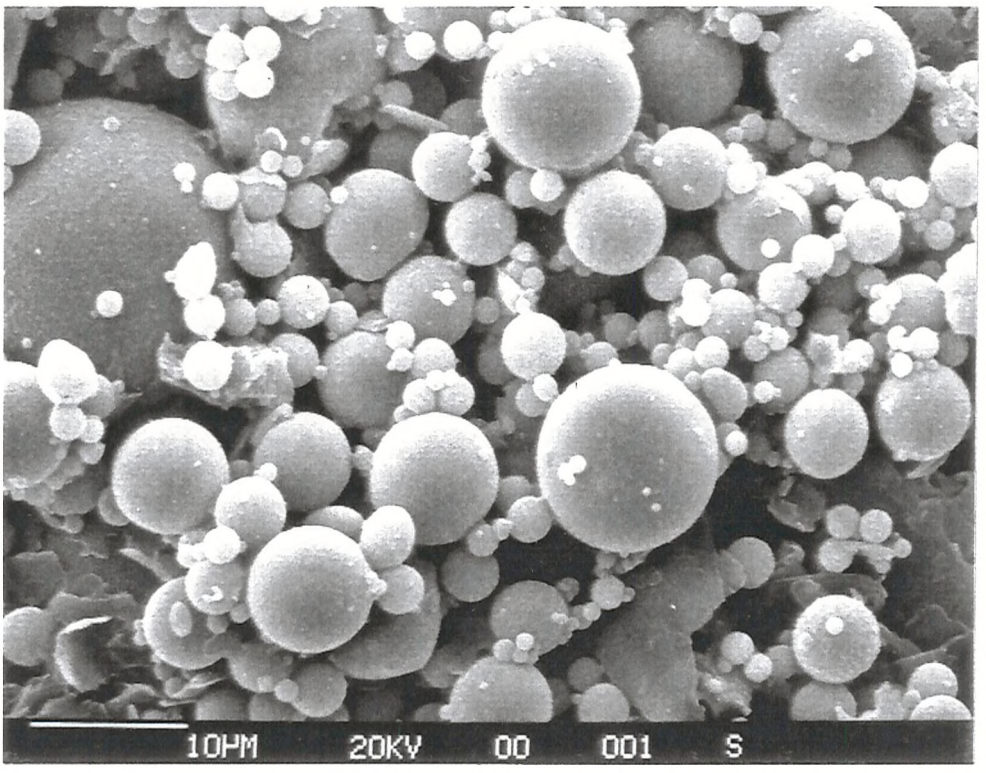

PRINT 001 at 7.5 μm/cm

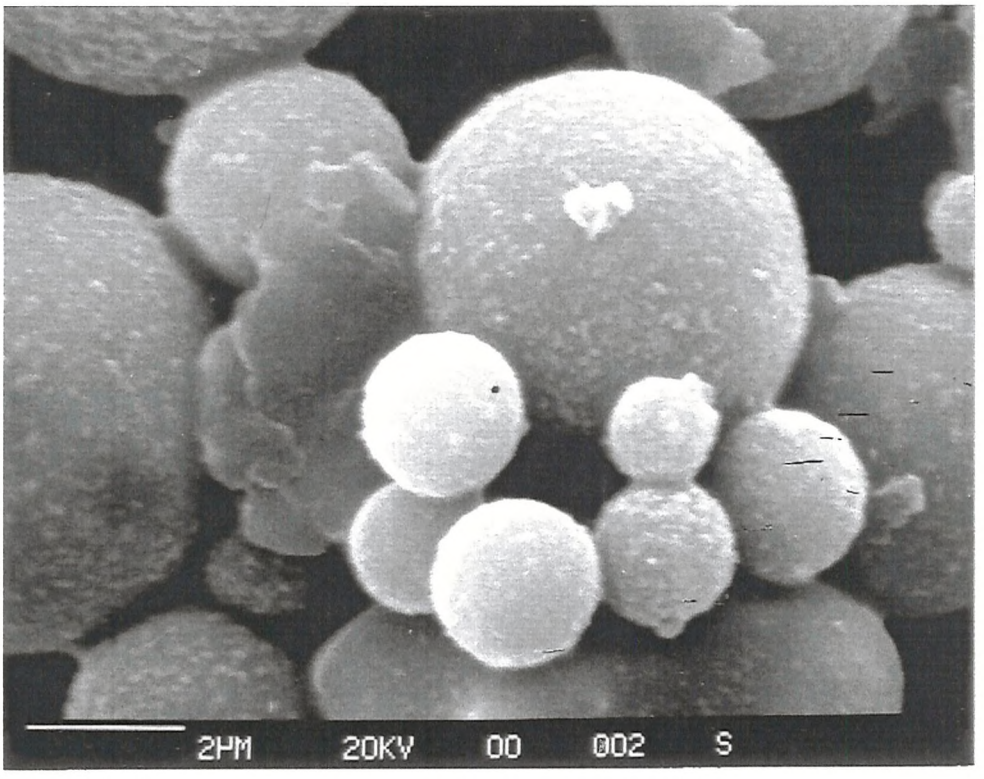

PRINT 002 at 1.5 μm/cm

PLATE 5.2.3 FLY-ASH VIEWED BY A SCANNING ELECTRON MICROSCOPE

5.2.3.2 OBSERVATIONS

Ash particles were seen throughout a wide range of sizes, from the smallest particles, with a diameter of only 500 nm up to the largest with a 40 μm diameter. However, there were no particles to be seen larger than 40 μm even though they had been seen in the previous work using the optical microscope. This deficiency of the larger particles was due to the sample preparation technique as described earlier and not their genuine absence from the original 'New Ash' sample. All of the particles seen in the photographs were spherical in shape, which again confirms the assumptions made in the theoretical calculations and also allows us to use the light diffraction sizing techniques, previously described, without including any correction for particle shape.

Flaky particles can also be seen in both photographs, these are especially apparent in photograph '002'. However, these flakes were probably not part of the ash sample and are simply part of the dag used to stick the ash to the stub.

Print '002' seems to show some form of bonding between some of the particles. However care should be taken in assessing these bonds as they may only be due to the sample preparation techniques used in the preparation of the stub.

5.3 LASER DIFFRACTION PARTICLE SIZING

5.3.1 DRY POWDER FEED

In order to determine the particle size distributions of the ash samples, all eight of the samples were analyzed using the Malvern particle size analyzer, as described in chapter four of this report. The Malvern system was used with the dry powder feeder and its 63 mm focal length lens. This gave a measuring range from 1.2 μm to 118 μm. Initially tests were also performed with the 300 mm lens, which gave a wider measuring range of 5.8 μm up to 564 μm. However, the top end of this range (above 100 μm) did not hold much information whereas a great deal of information on the finer particles was obscured by only

measuring down to 5.8 μm.

All of these measurements were repeated three times, to ensure the statistical accuracy of the particle size distributions obtained and the histograms were plotted of the output. A summary of the results obtained for all eight of the samples is given in Table (5.3.1) and the histograms of the particle size distributions can be seen in Figures (5.3.1) through to (5.3.8).

SAMPLE NAME	MASS MEDIAN DIAMETER	90% POINT	10% POINT	SPAN	LOG DIFFERENCE
	(μm)	(μm)	(μm)	---	----
OLD ASH	7.9	19.5	3.7	2.0	----
NEW ASH	17.9	76.0	3.5	4.0	1.29
S1	16.2	70.0	3.6	4.1	1.63
S2	18.5	72.8	3.8	3.7	1.55
S3	17.9	70.6	3.9	3.7	2.25
S4	21.1	76.7	3.4	3.4	2.44
SD1	17.1	70.5	3.7	3.9	1.18
SD2	18.9	73.2	3.8	3.7	2.34

TABLE 5.3.1 PARTICLE SIZE DISTRIBUTIONS
DRY POWDER FEED RESULTS SUMMARY

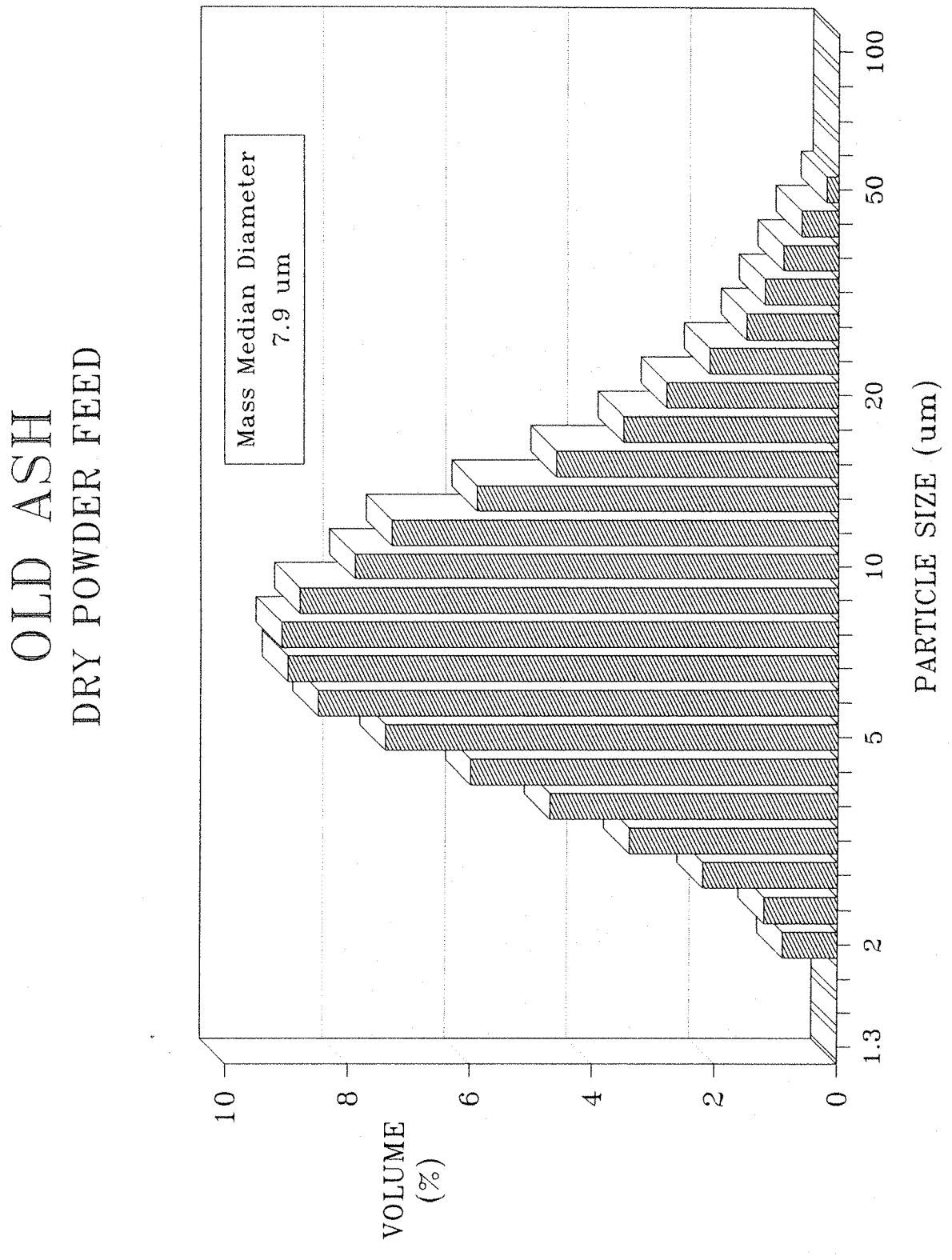

FIGURE 5.3.1 **SAMPLE: OLD ASH**

63mm DRY POWDER FEED

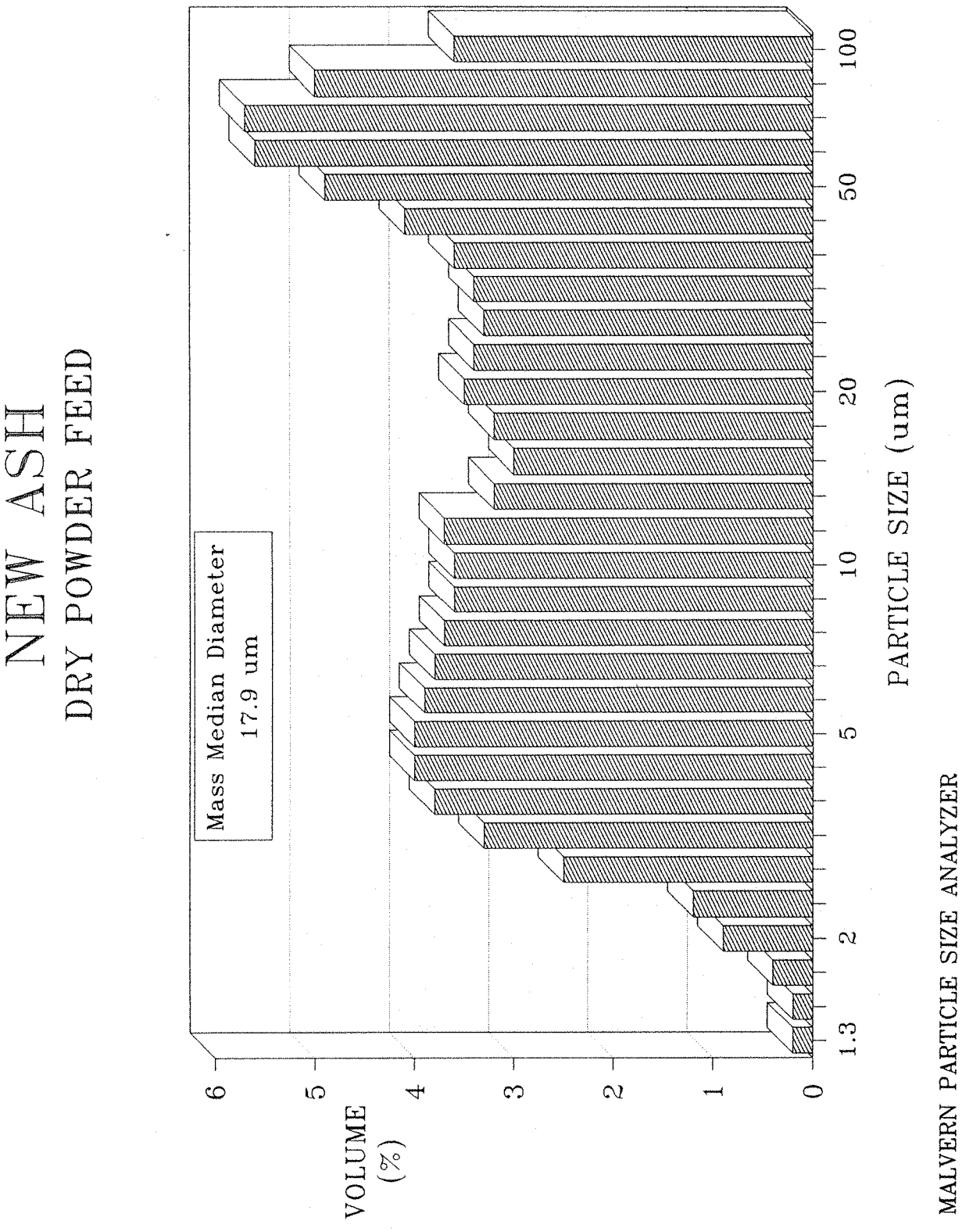

FIGURE 5.3.2 **SAMPLE: NEW ASH**
63mm DRY POWDER FEED

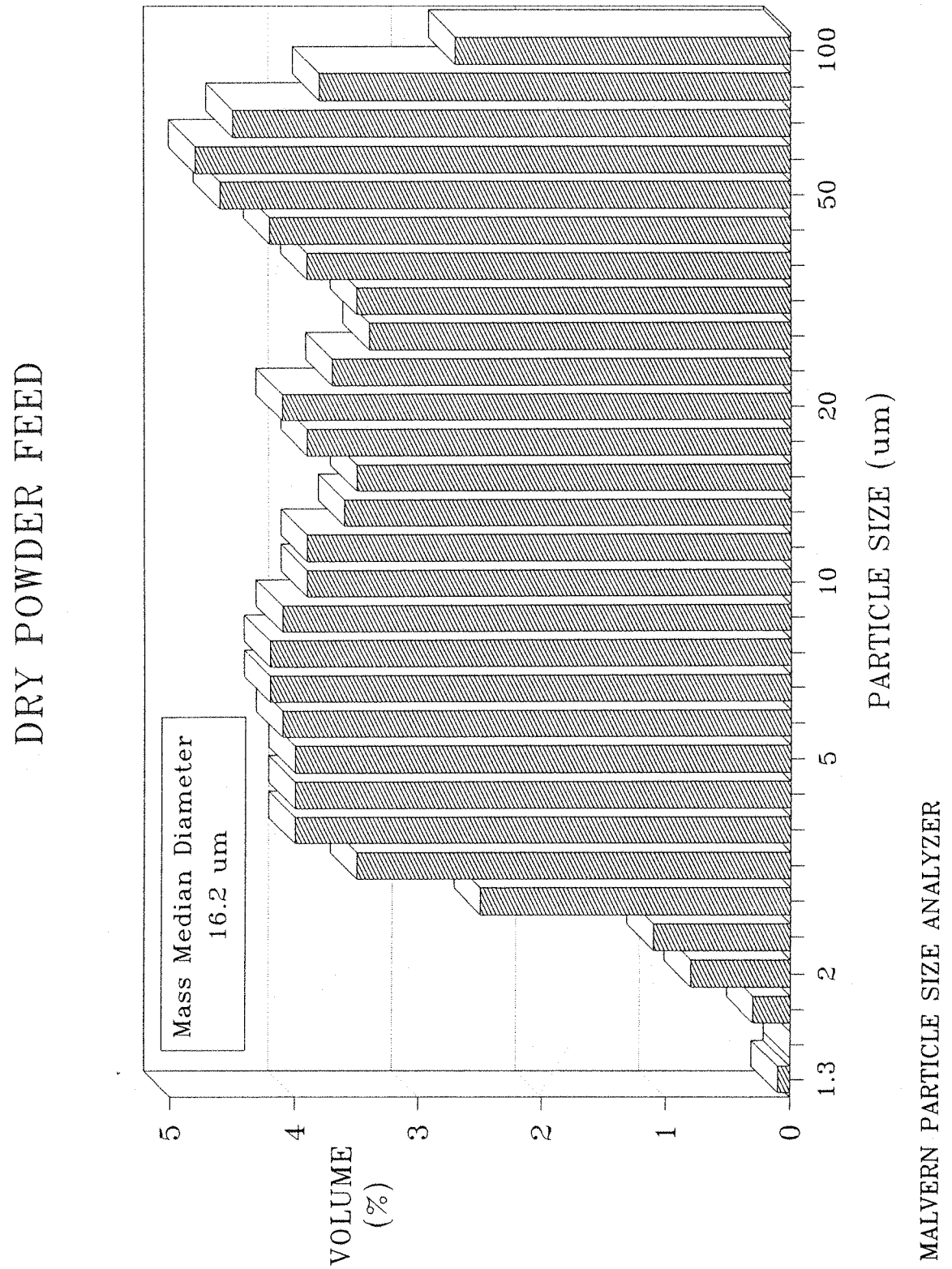

FIGURE 5.3.3 **SAMPLE: S1**

63mm DRY POWDER FEED

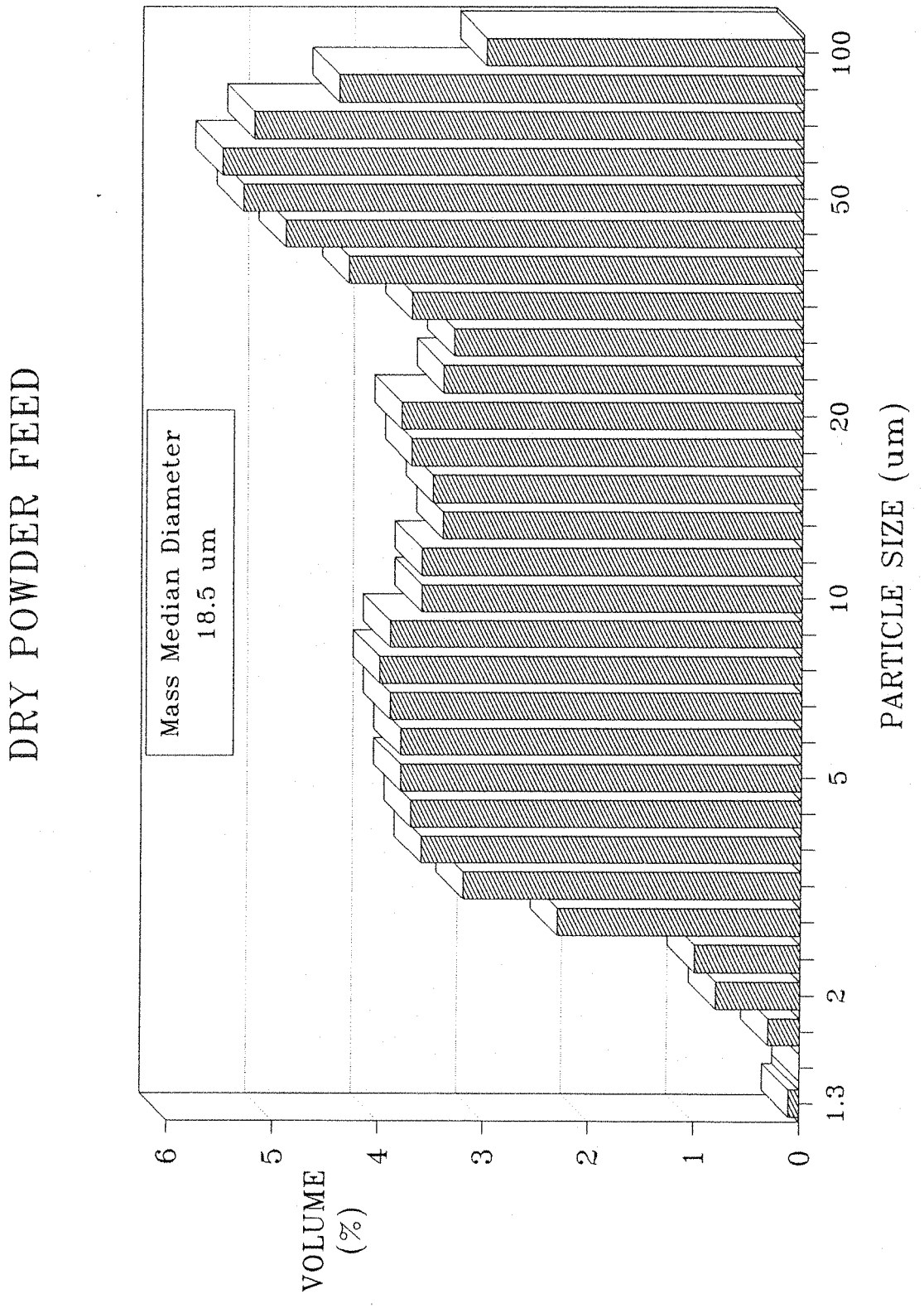

FIGURE 5.3.4 **SAMPLE: S2**

63mm DRY POWDER FEED

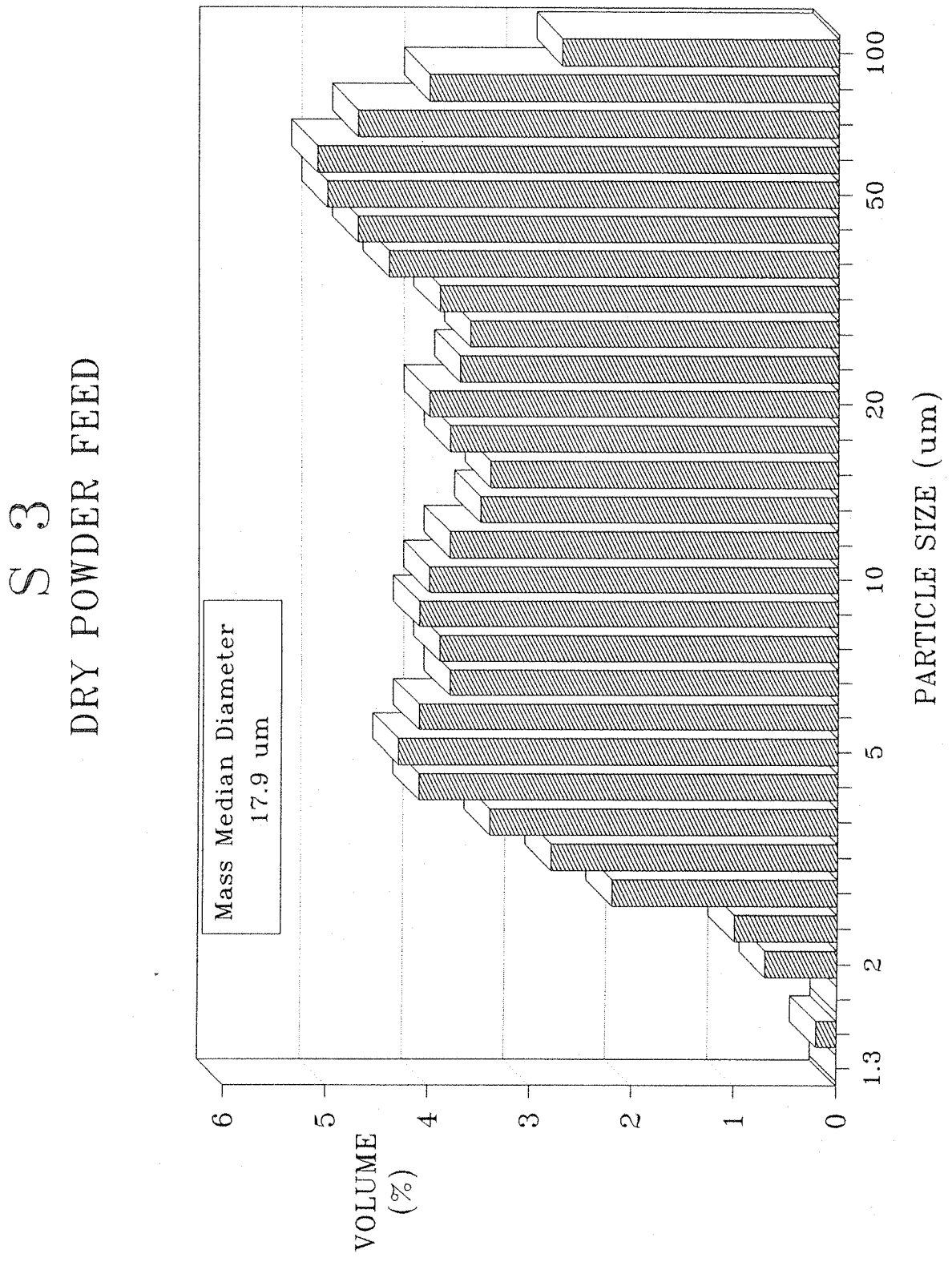

FIGURE 5.3.5 **SAMPLE: S3**

63mm DRY POWDER FEED

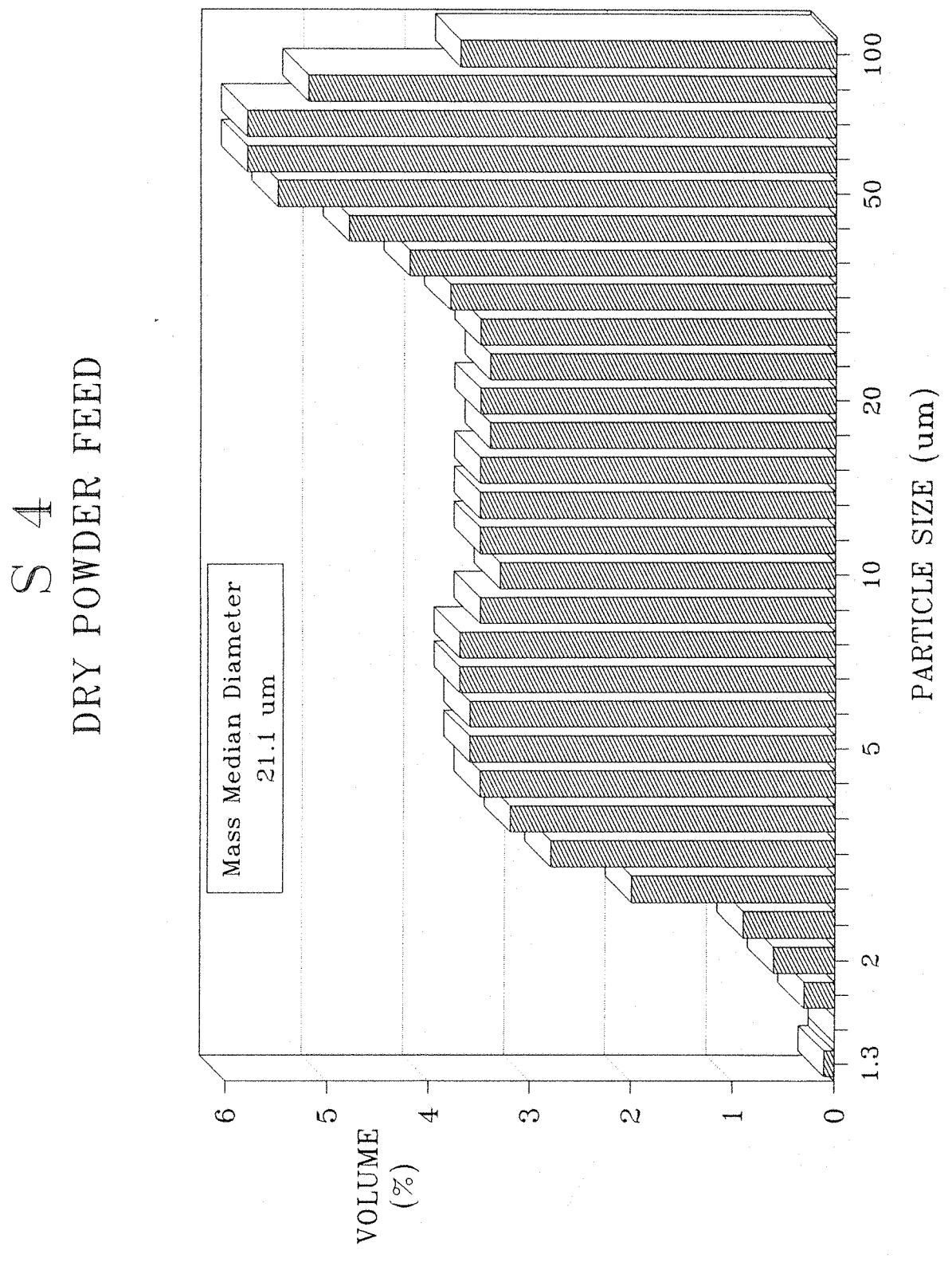

FIGURE 5.3.6 **SAMPLE: S4**

63mm DRY POWDER FEED

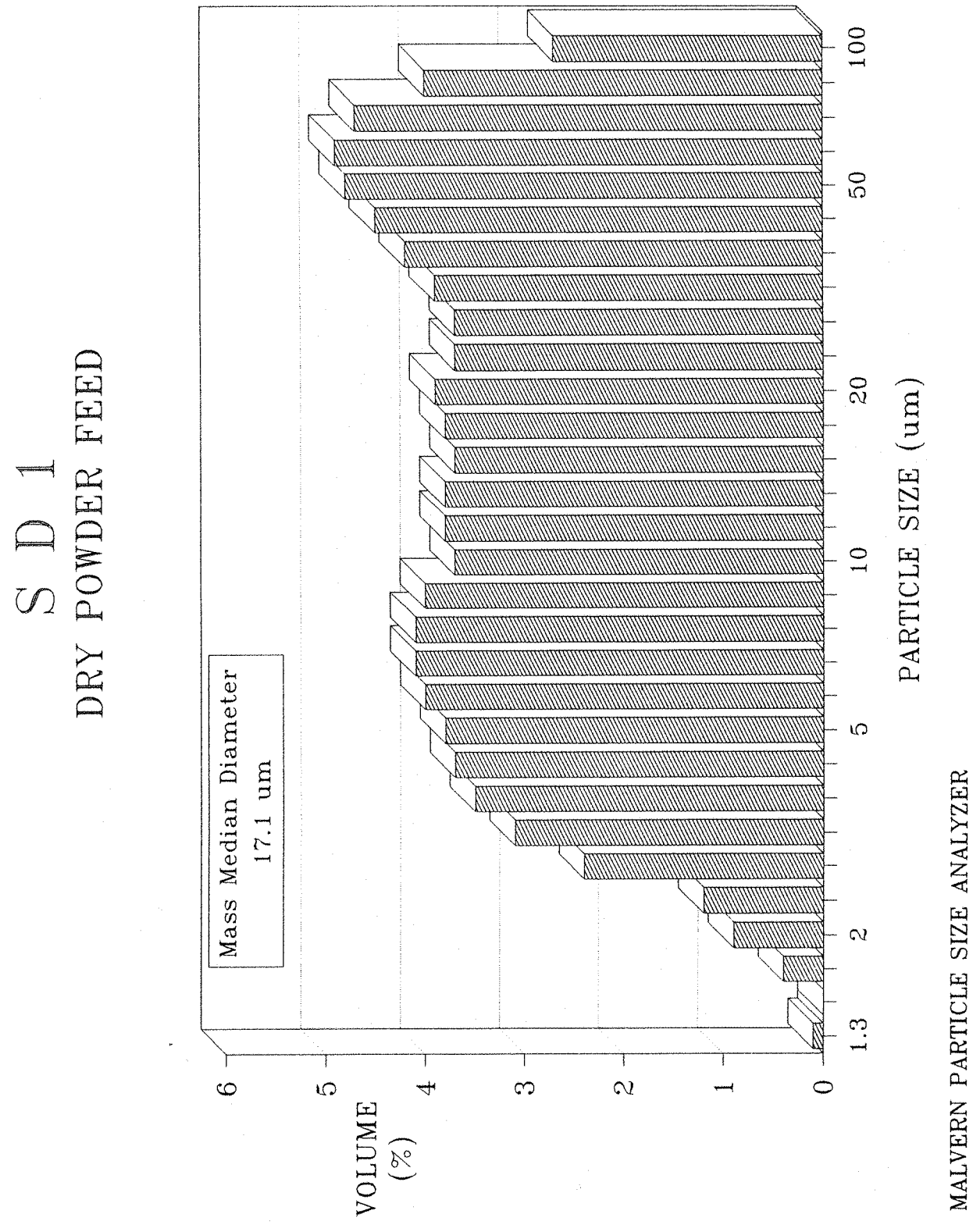

FIGURE 5.3.7 **SAMPLE: SD1**

63mm DRY POWDER FEED

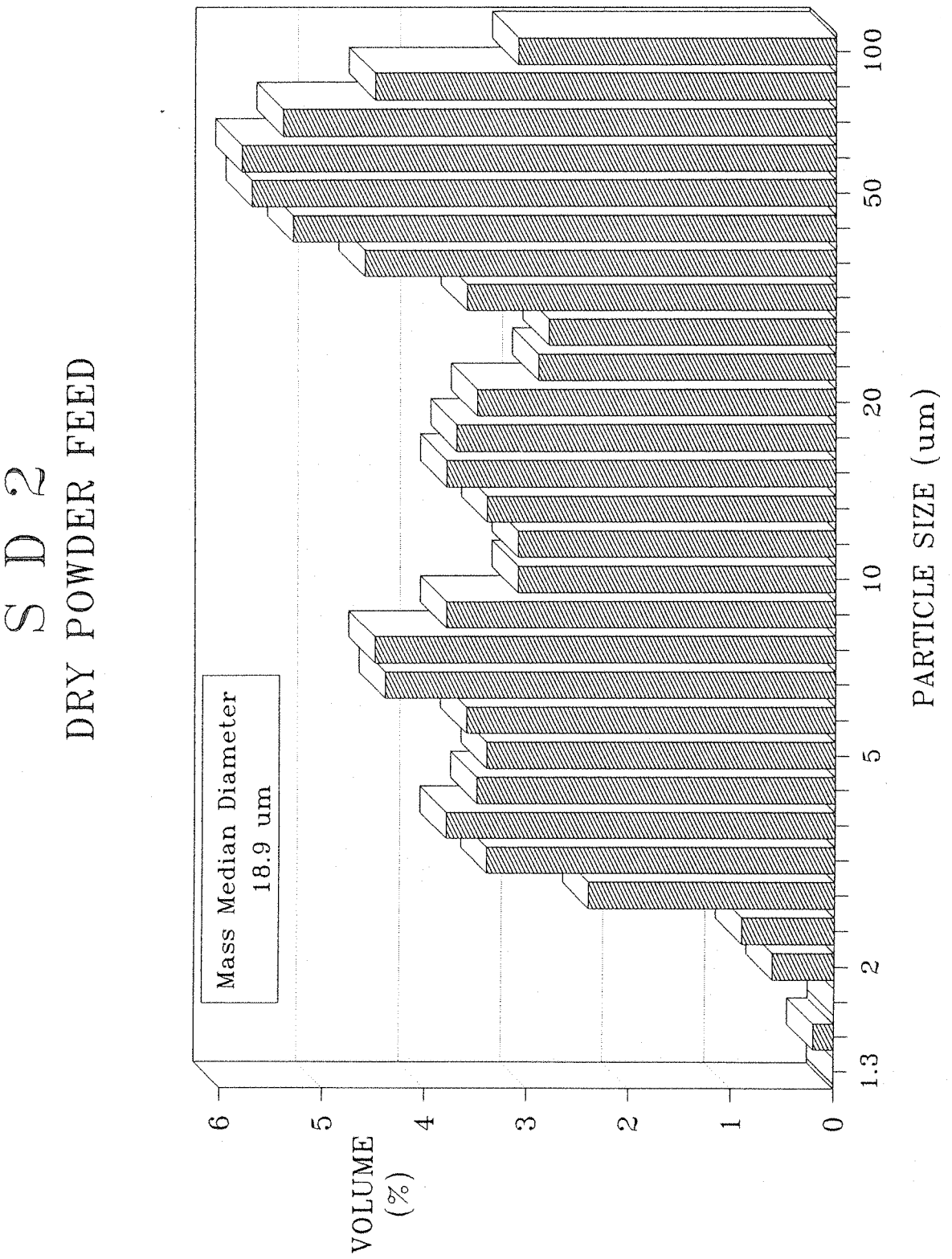

FIGURE 5.3.8 **SAMPLE: SD2**

63mm DRY POWDER FEED

5.3.2 OBSERVATIONS

By simply looking at the histograms of the particle size distributions produced it is immediately apparent that seven of the histograms show essentially the same particle size distribution, while one the plot from the 'OLD ASH' is totally different.

Considering first the histogram of the distribution from the 'OLD ASH' sample. This histogram is drawn on a log axis of particle size and can be seen to be symmetrical about its peak. Thus indicating that the result produced is a good approximation to a log normal distribution. From the table of data results we see that the sample has a mass median diameter of 7.9 μm, with 80% of the volume of the sample consisting of particles with a diameter greater than 3.7 μm and less than 19.5 μm, This gives a span of 2.0. This particle size distribution is representative of the expected distribution of a fly-ash, although slightly deficient of the finest particles. However, the absence of these finer particles from the distribution may not be a result of their absence from the original sample but may be due to an insufficient amount of agitation from the dry powder feeder. Hence resulting in some of the particles remaining stuck to one another. This is quite probable as the original sample was found in the laboratory and is of an unknown age. So it may have in fact adsorbed a large amount of water vapour from the atmosphere causing the particles to stick together.

The remaining seven plots, showing the size distributions produced from the newer samples, were all very similar to one another. Although, they had very little similarity to the histogram produced from the 'OLD ASH' sample.

Considering first the similarities between the seven particle size distributions. We see from the data table that all the parameters for these samples produce almost equal results. In fact the average mass median diameter is 18.2 μm with a standard deviation of 1.43, indicating that it is safe to assume that all of the samples came from the same 'parent population'. For these samples 80% of the volume of the sample is consistent of particles with diameters within the range of 3.8 μm to 72.8 μm, giving an average span value of 3.8. Hence these distributions are far broader than that of the 'OLD ASH' and also have a larger mass median diameter.

Now comparing the particle size distribution histogram of the 'OLD ASH' with the other seven histograms. It can be seen that the seven wider distributions seem to be representative of a bi-modal distribution with two distinct populations. The population consisting of the finer particles seems to have a median at about the 8 μm diameter point, while the population of larger particles has a median of about 70 μm. This assumption of the samples consisting of two distinct populations is supported by the observations made under the optical microscope and by eye, where two different types of particle were seen. As the finer particle median value is almost equal to the mass median diameter of the 'OLD ASH' sample, in which no irregular black particles were seen, it is safe to assume that this population of smaller sized particles is representative of the ash particles. In which case the larger median population can be considered to be representative of the large un-burnt fuel particles that were only seen in these seven samples.

It is however important to remember that the histograms plotted are representative of the particle volume distributions and not the number distributions; also that the histograms are drawn on a logarithmic size axis with logarithmical increasing sampling bands. Both of these attributes of the histograms will bias the plotted result towards the larger particles within the sample. These characteristics of the Malvern laser system were discussed in the chapter on the measurement systems.

5.4 FINE PARTICLES

All of the particle size distributions so far produced, whether from the 'OLD ASH' sample that had been left in the laboratory absorbing water vapour for a considerable length of time or from one of the newer samples containing the unburnt fuel, show a lower than expected volume of fine particles (sub 2 μm), than would usually be expected to be seen in a fly-ash. Even though a number of particles within this size range were seen to be present within the sample under the scanning electron microscope. However, as stated earlier in this chapter, the sample preparation techniques used for this examination would bias the results towards these finer particles. It was also unclear if these particles were free or stuck to the larger particles within the sample.

There are several reasons why these fine particles were not detected by the Malvern system. First, these very small particles may in fact not be present in the ash samples received from C.E.R.L. and the histograms generated therefore correct. Secondly, the fine particles may have been present but in some way had become attached to the larger particles and hence were not registered as individual particles by the Malvern instrument. The third possibility is that the particles were present within the original sample but in such low volumes that their contribution to the entire histogram becomes insignificant compared to the vast number of large particles which make up the majority of the volume of the sample. The resolution of the Malvern system will detect particles in an individual size range down to a concentration of 0.1% by volume. So if there were a predominance of very large particles the amount of light scattered by the finer particles would become almost insignificant compared to that scattered by the larger particles. The third supposition seems most probable as these very fine particles were seen to be present when the sample was examined under the scanning electron microscope.

5.4.1 ASH DRYING

A proportion of the 'OLD ASH' sample was taken and placed in an oven at 200 degrees centigrade for a period of two hours. This ash sample was then allowed to cool, prior to being analyzed with the Malvern particle size analyzer and dry powder feeder. It was hoped that this process would evaporate any adsorbed water from the sample and weaken any agglomerates that had formed within the original sample. So that the agglomerates would be broken up and dispersed as single particles by the dry powder feeder.

The size distribution results of this test are given in Table (5.4.1), along with the size distribution results from the untreated dry fed 'OLD ASH' sample. The histograms of both of these particle size distributions are plot in Figure (5.4.1).

SAMPLE TYPE	MASS MEDIAN DIAMETER	90% POINT	10% POINT	SPAN	LOG DIFFERENCE
	(μm)	(μm)	(μm)	---	----
ORIGINAL	7.9	19.5	3.7	2.0	----
DRIED	7.8	37.3	2.9	4.4	1.55

TABLE 5.4.1 OLD ASH PARTICLE SIZE RESULTS

5.4.1.1 OBSERVATIONS

The significant change in the data set shown in Table (5.4.1), is that the range of sizes seen for the dried sample were far greater than that seen for the original un-dried sample. In fact the dried sample has a span figure over twice that of the original sample. However, if we look at Figure (5.4.1), the histograms of the particle size distributions, we see that the actual range of sizes has remained un-altered, only the distribution of the particle sizes within that range has changed. The plot does however show an increase in the number of fine particles, in the dried sample, below about 3 μm, although no particles were seen below 2 μm as was true for the original sample. So drying the sample had released the fine particles from the agglomerates but very few fines exist within the ash sample below 2 μm.

The histograms also show a second peak of particles at about 40 μm in diameter. There are no reason why more particles should be present in this size range after drying the sample. It is possible that this peak is due to large agglomerates which had been baked so hard during the drying process that the dry powder feeder was unable to break them.

The reduction of the volume of particles in the mid size ranges of the dried sample was due simply to the increase in the number of particles at the extremities of the distribution.

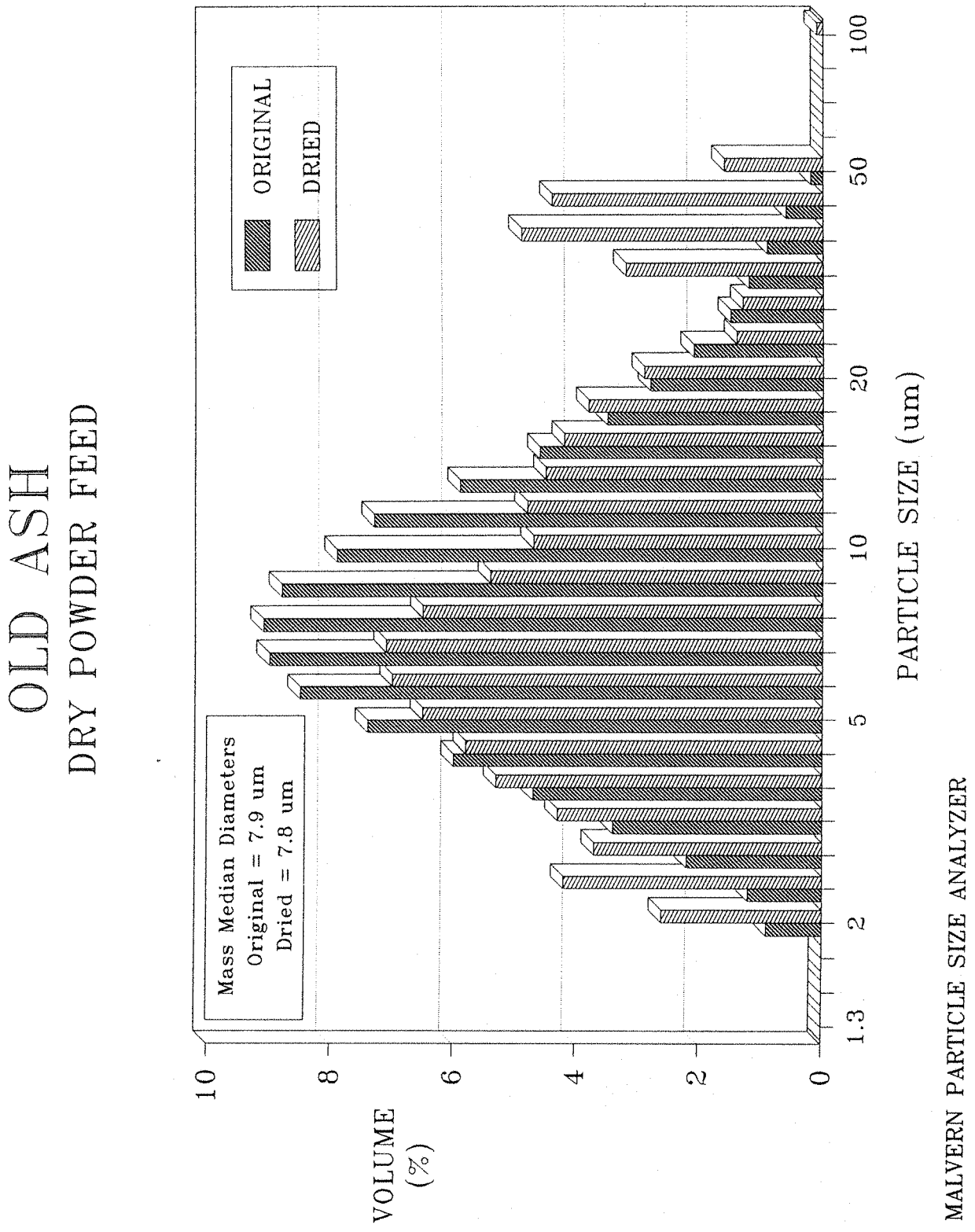

FIGURE 5.4.1 **SAMPLE: OLD ASH**
DRIED / UN-DRIED
63mm DRY POWDER FEEDER

5.4.2 ASH SUSPENSIONS

In order to determine whether these very fine particles were actually present in our newer ash samples, as individuals or even as weakly bonded agglomerates the following tests were carried out using ash sample number 'S2'.

5.4.2.1 SAMPLE PREPARATION

The ash was first dispersed in water so as to form a suspension. The size distribution of the ash sample held within the suspension could then easily be measured using the Malvern particle size analyzer. The ash particles have a density that is over twice that of the water in which they are suspended and will hence slowly separate out to the base of the test vessel. As the viscous drag on an individual particle will be dependent on its size, the largest particles will settle out of the measuring zone first. Leaving the particle size distribution remaining within the measuring zone becoming more and more biased towards the finer particles. This preferential loss of the larger particles can be seen by equating the force on a particle due to gravity to the opposing viscous drag force in order to determine the terminal velocity of the particle. George Stokes in 1846 defined the relationship for the viscous drag as:

$$F_d = 6\pi \eta a u \qquad \textbf{Equation (5.4.1)}$$

Where:
- F_d = The drag force acting on the particle.
- η = The viscosity of the medium through which the particle is passing.
- a = The radius of the particle.
- u = The velocity of the particle.

The gravitational force acting on the particle is defined as:

$$F_g = m\ g \qquad \textbf{Equation (5.4.2)}$$

Where: F_g = The gravitational force on the particle.
m = The mass of the particle.
g = The gravitational pull, (≈ 9.81 N/m).

So the terminal velocity of the particle is reached when these two forces become equal:

If:

$$F_d = F_g \qquad \textbf{Equation (5.4.3)}$$

Then:

$$m\ g = 6\pi\ \eta\ a\ u \qquad \textbf{Equation (5.4.4)}$$

So:

$$u_{TERMINAL} = \frac{m\ g}{6\pi\ \eta\ a} \qquad \textbf{Equation (5.4.5)}$$

Since the mass of a particle is given by its density multiplied by its volume:

$$m = \rho\ \frac{4}{3}\ \pi\ a^3 \qquad \textbf{Equation (5.4.6)}$$

Where: ρ = The density of the particle.

Then:

$$u_{TERMINAL} = \frac{\rho \frac{4}{3} \pi a^3 g}{6 \pi \eta a} \qquad \textbf{Equation (5.4.7)}$$

Hence, $u_{TERMINAL}$ is proportional to a^2.

So the velocity of a particle falling under the influence of gravity is proportional to the square of the particle diameter, hence the larger the particle the faster it will fall.

Two different methods of producing the suspension were tried each giving slightly different results. The first was to disperse the ash into the water using a magnetic stirrer and the second was to place the suspension in an ultra-sonic bath. The ultra-sonic bath was used in an attempt to further breakup any agglomerates that may be present within the sample that the simple stirring was not able to break.

The magnetic stirrer seemed to produce a uniform suspension of all the ash particles. While the ultra sound was not able to disperse the very large particles, which hence fell to the bottom of the mixing vessel. Once mixed the ash suspensions were placed in optically flat glass cells and in turn placed within the laser beam of the Malvern particle size analyzer. A series of size distributions were then recorded from both suspensions at different time intervals.

5.4.2.2 RESULTS

A summary of the recorded mass median diameters of the ash particles from both of the suspensions at the different time intervals is given in Table (5.4.2). These mass median diameters were then plotted as a function of time and the graph produced can be seen in Figure (5.4.2). The particle size distribution histograms for all the measurements are shown in Figure (5.4.3) for the magnetically stirred suspension and Figure (5.4.4) for the sonically agitated

suspension. The particle size distribution of the original sample, 'S2', measured using the dry powder feeder, along with the histogram of the 'OLD ASH' and the final plots from both suspensions are also shown in Figure (5.4.5).

SETTLEMENT TIME	MASS MEDIAN DIAMETER OF THE SUSPENSIONS	
	MAGNETICALLY STIRRED	SONICALLY STIRRED
(minutes)	(μm)	(μm)
0	14.8	12.5
1	11.4	----
2	9.8	8.6
3	9.2	---
4	---	6.3
5	8.6	---
10	7.8	4.2
30	7.0	3.7

TABLE 5.4.2 MASS MEDIAN DIAMETERS OF SUSPENDED ASH PARTICLES

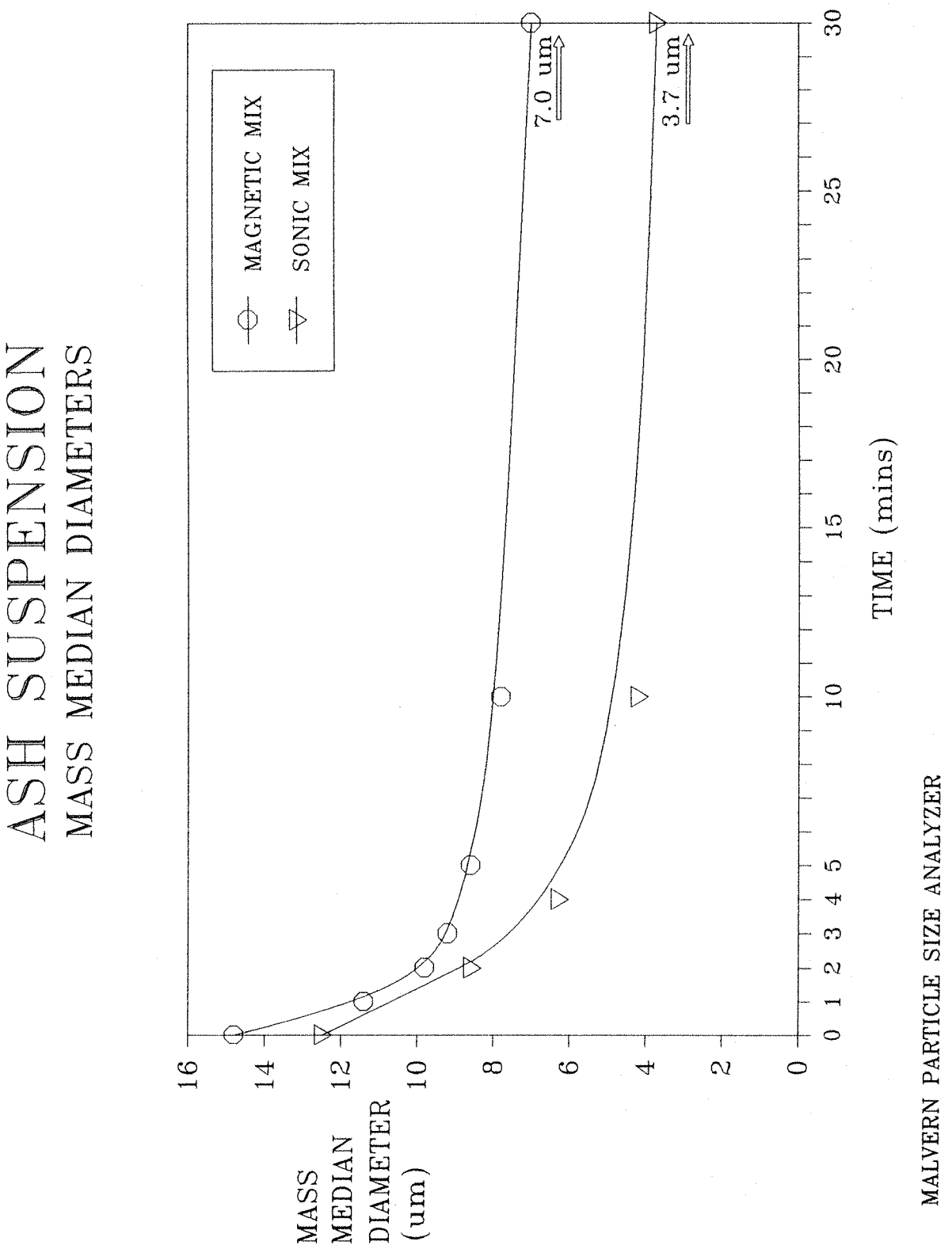

FIGURE 5.4.2 MASS MEDIAN DIAMETER OF SUSPENDED ASH PARTICLES AS A FUNCTION OF TIME

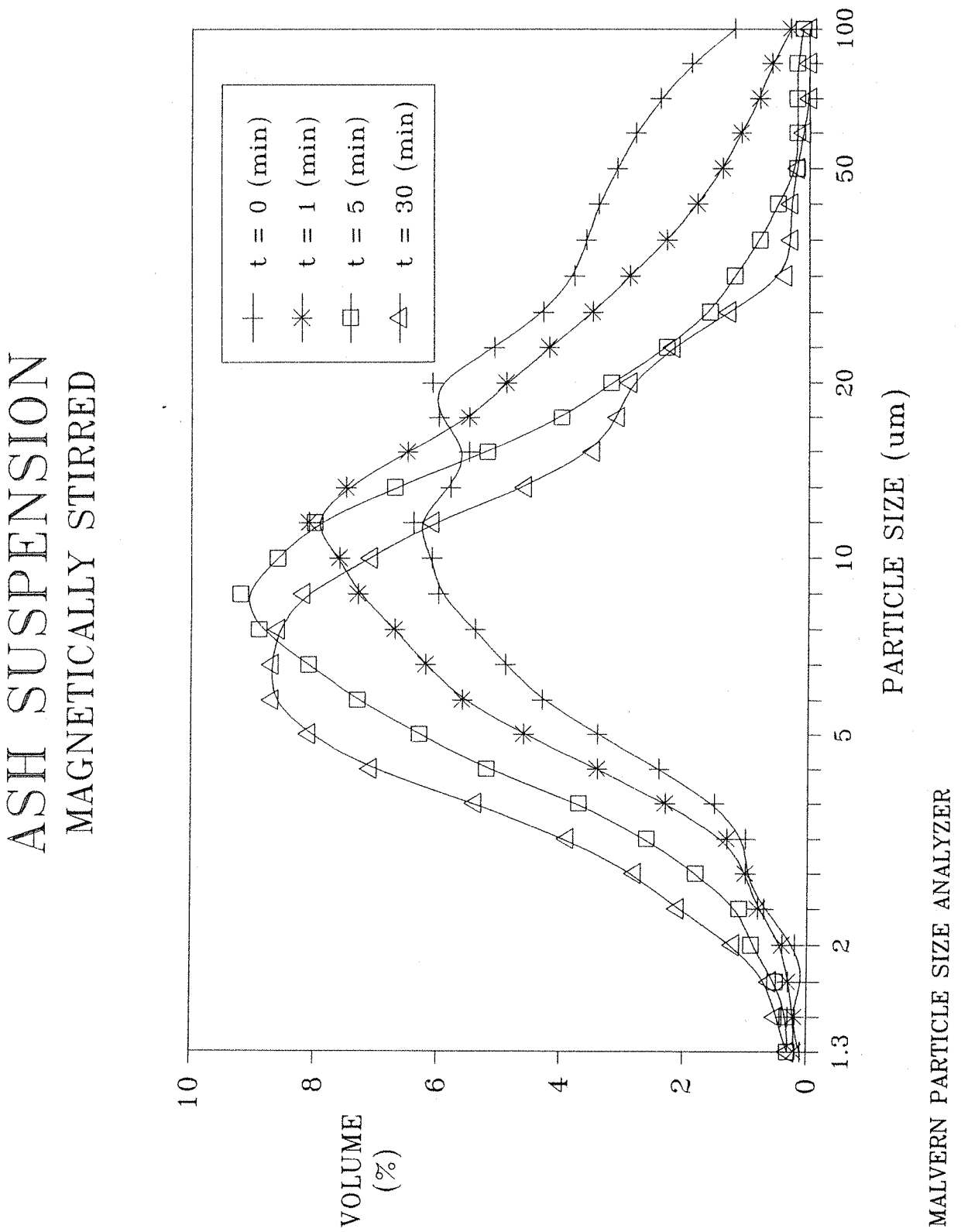

FIGURE 5.4.3 MAGNETICALLY STIRRED PARTICLE SIZE DISTRIBUTIONS

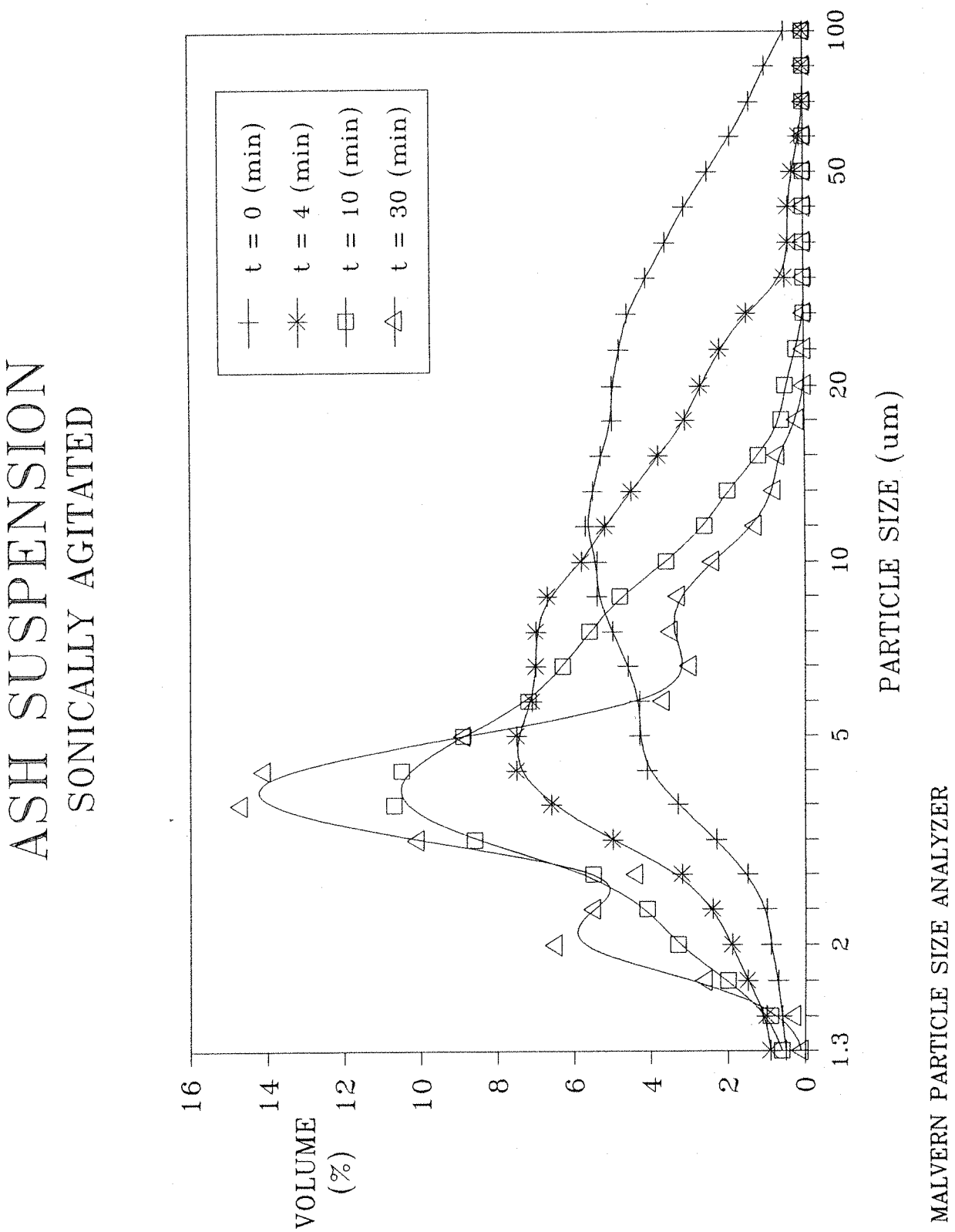

FIGURE 5.4.4 SONICALLY AGITATED PARTICLE SIZE DISTRIBUTIONS

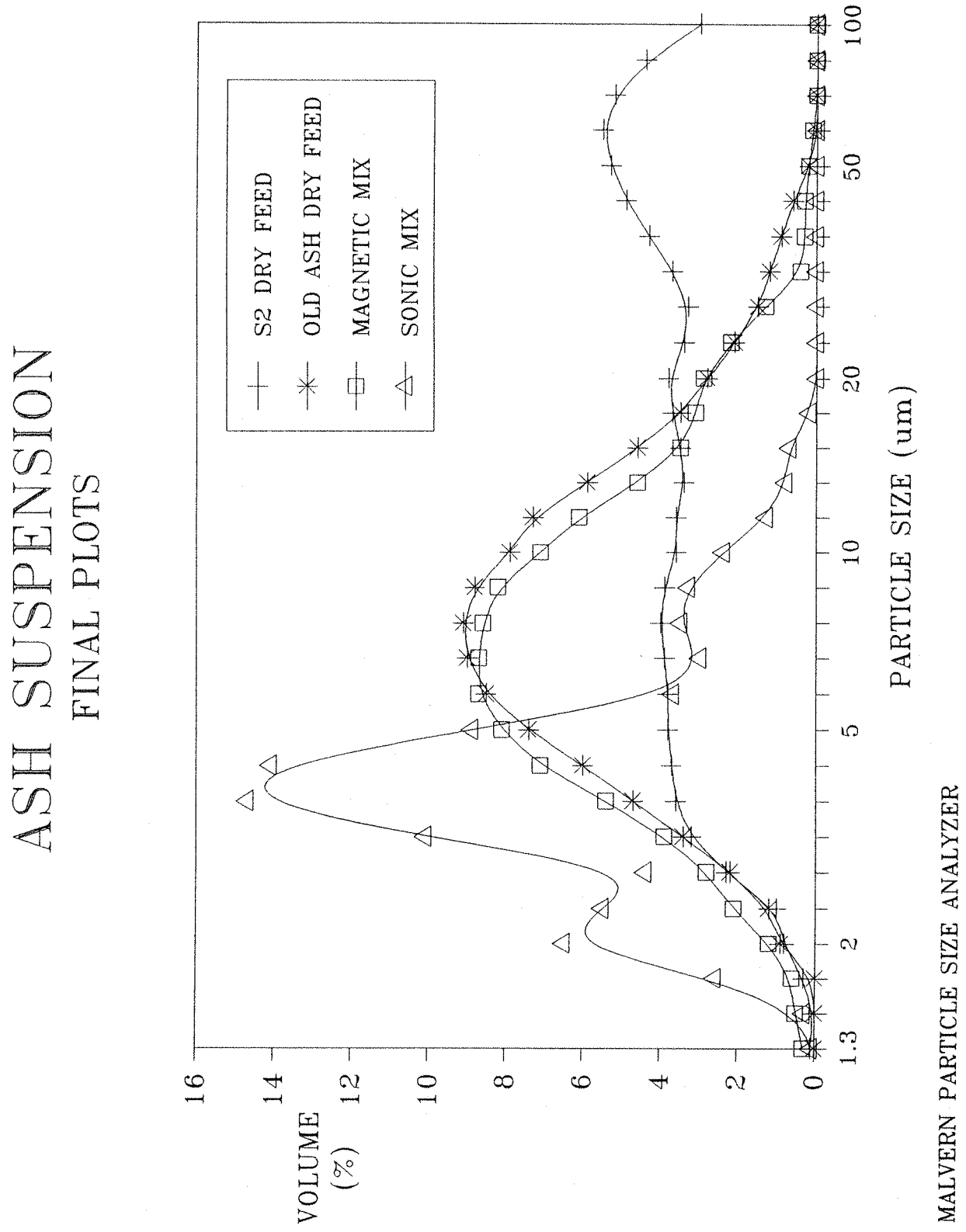

FIGURE 5.4.5 PARTICLE SIZE COMPARISONS

5.4.2.3 OBSERVATIONS

It can be seen from the histograms plotted in Figures (5.4.3) and (5.4.4) that the particle size distributions of both the magnetically mixed and sonically agitated suspensions shifts to the left, the smaller size ranges, with time. This shows that the larger particles are indeed being lost from the suspension as they fall under the influence of gravity, causing the contribution to the distribution from the finer particles to become more significant. However, in order to determine whether there were any fine particles within the suspended distributions that had not previously been seen using the dry powder feeder, it was necessary to compare the final histograms produced from each of the suspensions with the histogram of the original dry fed sample. This graph can be seen in Figure (5.4.5).

First by comparing the final plot from the magnetically mixed suspension to that of the dry fed sample, we see the loss of the largest of the particles but no significant change in the number of fine particles present within the sample. However, if the final plot of the sonically agitated suspension is compared with the original dry fed sample, then we see a very large increase in the number of very fine particles within the suspension but still very few particles can be seen below the 2 μm point.

As the suspension created using the ultra-sonic bath shows a greater number of fine particles than had previously been seen, it can be assumed that any agglomerated particles within the original sample were adequately broken up by this agitation. Since no extra particles were seen with a diameter less than about 1.5 μm it is also safe to assume that there were insignificant numbers of these particles within the original sample to be recorded by the Malvern instrument.

The two decay curves in Figure (5.4.2) show the reduction in the mass median diameters of the suspended ash samples, as the larger particles settle under the influence of gravity. The mass median diameter for the magnetically stirred distribution was seen to fall quite rapidly from an initial value greater than 15 μm. This starting value is close to the value obtained from the particle size distribution of the original dry fed sample, which produced a mass median diameter of 18.5 μm. The similarity in these values indicates that an acceptable

degree of dispersion of the ash was obtained by the magnetic stirrer. After a period of about ten minutes the value of the mass median diameter was seen to begin to settle to a fairly constant value of about 8 μm. This value is surprisingly close to the mass median diameter obtained from the 'OLD ASH' sample when dispersed through the dry powder feeder. The 'OLD ASH' sample was the only ash that was not found to contain any un-burnt fuel, it was found to have a mass median diameter of only 7.9 μm. So it appears that the particles that were preferentially lost from the magnetically stirred suspension were the un-burnt fuel particles, the remaining distribution being representative of the ash particles alone. Figure (5.4.5) of the final particle size distributions also includes the plot obtained from sample 'OLD ASH' using the dry powder feeder. By comparing this distribution to the final distribution taken from the magnetically stirred suspension it is apparent that the two samples were almost identical. This similarity confirms the hypothesis that the newer samples of ash contain both the ash particles, with a mass median diameter of about 8 μm and a large number of unburnt fuel particles with a much greater mass median diameter.

The reduction of the mass median diameter of the distribution from the sonically agitated suspension was not as fast as the change seen in the magnetically stirred suspension. However, the final value of the mass median diameter from the sonically agitated suspension was far lower than had previously been seen, at 3.5 μm. This very low value is an indication of the greater number of fine particles that were being liberated from agglomerates by the vibration of the ultra sonic bath.

The graphs drawn in Figure (5.4.4) show the change in the distribution of particle size for the sonically agitated suspension. It is interesting to note that the initial value for the mass median diameter of the suspension does not come close to the mass median diameter value obtained from the dry powder fed sample, even though the magnetically stirred sample did. This can be explained simply by the fact that the ultra sonic bath was not able to agitate the largest particles into a suspension and they had fallen to the base of the test vessel prior to starting the particle size measurements.

A comparison between the final distribution from the sonically agitated suspension and the distribution obtained from the dry fed sample 'S2' can also be made from the plots in Figure (5.4.5). At the larger particle size end of the

distribution we see the loss of the large particles from the suspension as expected. At the fine particle end of the scale the sonically agitated suspension is seen to produce far more fines than had previously been noted. However, there was no significant increase in the number of particles seen below 1.5 μm. So we can assume that these very fine particles were never present in the original sample to any significant level. As there they would have been measured in the distribution seen in the suspension from the ultra sonic bath, which has been shown to have the ability to break any agglomerates within the sample.

5.4.3 MAGNETIC PROPERTIES OF THE ASH

Whilst preparing samples for the previous tests, where a sample of ash was dispersed in water to form a suspension and then allowed to settle. It was noticed that if a magnetic stirrer was used in this process, that when the sample was poured from the mixing vessel a small proportion of the ash remained attached to the magnet. It was decided to further examine this magnetic property of the ash, so as to ascertain whether it would be of any use to us in the capture of agglomeration of the particles.

5.4.3.1 SEPARATION TEST

A suspension of the ash in water was again created but in this instance a non-magnetic stirrer was used so as not to lose any of the ash or to magnetise the sample in any way. This sample was then passed through a magnetic separator and the process recorded using a high magnification video camera. The design of the magnetic separator was as illustrated in Figure (5.4.6).

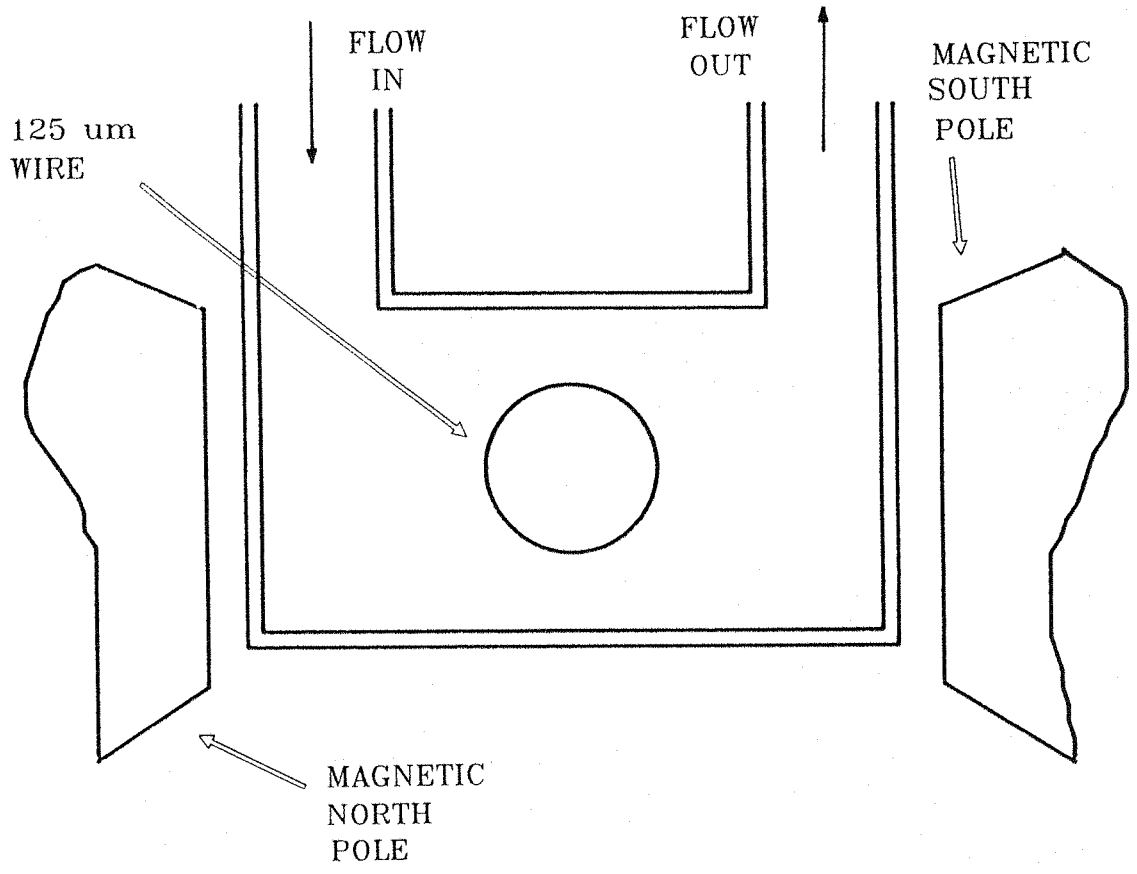

FIGURE 5.4.6 MAGNETIC SEPARATION TEST CELL

The magnetic separator consists of a small continuous flow cell, bisected by a 125 μm wire. This cell is placed within an intense magnetic flux. The ash suspension is then passed through the test cell where it comes into close proximity to the wire. The wire, when in the magnetic flux, divides itself into four quadrants. Two in line with the applied flux denoted with a '+' sign and two transverse to the magnetic flux, denoted with a '-' sign. When the solid particles of the suspension pass these wire quadrants they may or may not become attached depending on their magnetic properties. Non-magnetic material will pass straight through the test cell, while the magnetic material will become trapped on the wire. If the captured particles were para-magnetic, they will attach themselves to a '-' quadrant, while ferro-magnetics will attach to a '+' quadrant. The para-magnetic attachment is in a globular form while the ferro-magnetic is spiky, much like iron fillings on the pole of a magnet. Figure (5.4.7) shows the detail of the wire and its quadrants.

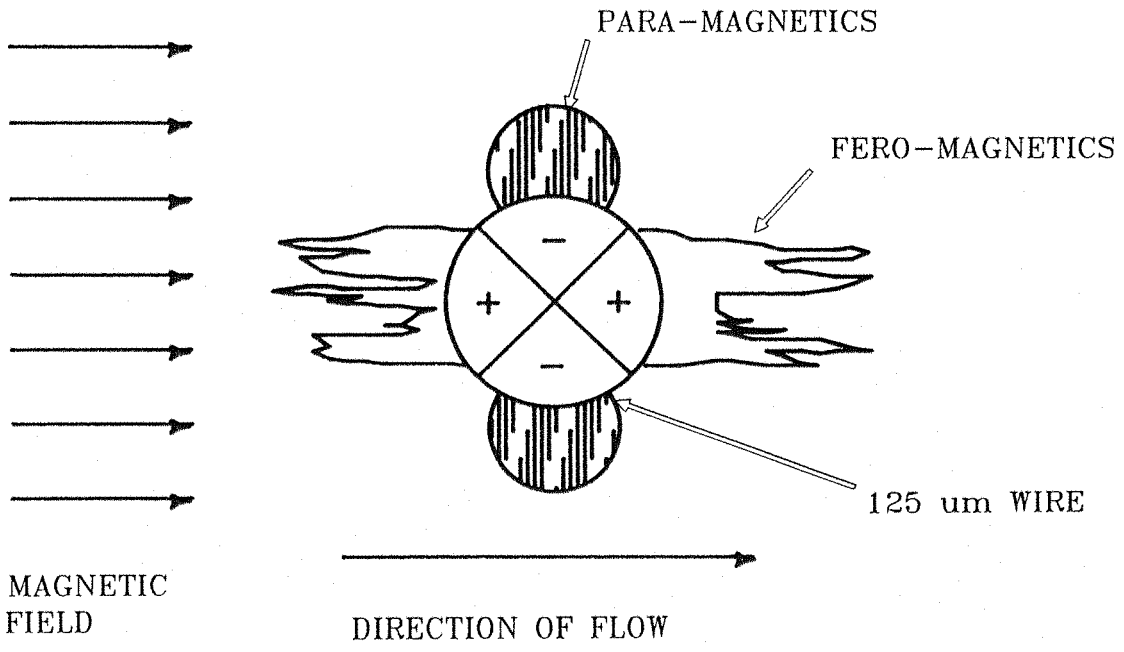

FIGURE 5.4.7 DETAIL OF MAGNETIC SEPARATION WIRE

5.4.3.2 MAGNETIC SEPARATION RESULTS

When the magnetic separation test was performed on the ash suspension, the amount of ferro-magnetic material was found to be very great. However, which of the particle types from the original sample were these ferro-magnetic particles and which were non-magnetic is still unclear, as is the actual volume of the sample that is magnetic. There was no significant amount of para-magnetic material seen in the sample.

5.4.3.3 MAGNETIC SEPARATION SYSTEM DEVELOPMENT

Should it seem necessary to analyses the magnetic and non-magnetic components of the ash, they can be separated quite easily and then analyzed in any way required. This separation can be achieved by using a separation devise as illustrated in Figure (5.4.8). This separator could work in either a wet or dry phase.

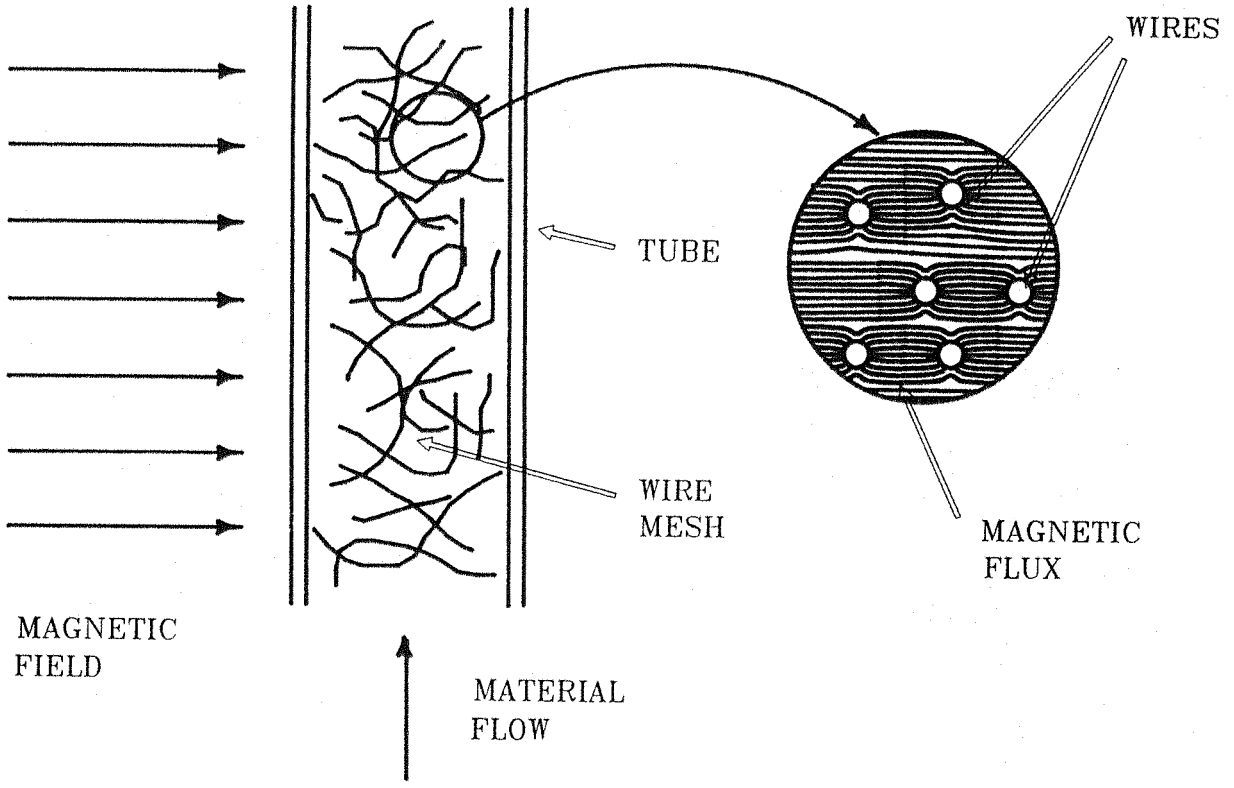

FIGURE 5.4.8 MAGNETIC PARTICLE FILTER

The wire mesh within the tube distorts the magnetic flux lines, the magnetic particles then follow these lines to the wire where they become attached. These particles will then remain on the wires until the flux is removed, allowing their extraction. The wires within the tube can be replaced with permanent magnets, thus releasing the requirement for an external flux. In this case the trapped magnetic material will then have to be removed with a strong purge of the dispersing substance (gas or liquid).

The results of such an analysis would be significant if it were found that the ferro-magnetic material were to consist of only the very fine particles, as this would facilitate their capture. Or, more likely, should it be found that these ferro-magnetic particles were the unburnt fuel particles. Again capture of these particles would be beneficial as this would increase the bulk resistivity of the original sample, increasing the chances of seeing agglomerates of the actual ash particles. Also, if a high proportion of un-burnt fuel is common-place within the power generation industry then such a system could be used to extract the un-burnt fuel from the flue gasses and feed it back into the furnace.

5.5 ASH PARTICLE RESISTIVITY

The electrical resistivity of the ash samples is an important consideration in the design of the agglomerater for two reasons. First, the rate of charge accumulation of the ash is proportional to its conductivity. In chapter three it was shown that particles with a higher resistivity will take longer to charge than particles with a lower resistivity and the higher resistivity particles will also not reach the same charge level. So in order to achieve a rapid and large level of charge on the particles it is important to have a fairly low resistivity ash. The second consideration is the bonding of the particles to one another in the formation of agglomerates. In this case a high resistivity ash is required, so that the particles do not rapidly discharge to one another hence reducing their force of attraction and hence bonding strength.

5.5.1 CONDUCTION PATH

In chapter four, on the measurement systems, two different conduction paths were discussed, bulk conduction and surface conduction.

The conduction mechanism for fly-ash is complex and very temperature dependent. At relatively high temperatures, above 250°C, the conduction is primarily governed by the ionic content of the ash particle and is through the volume of the particle. Whereas, at lower temperatures the path taken by the charge carriers is around the surface of the particles and hence the conductivity is dependent on the surface conditions of the particles[ref 5.1].

To understand the conduction paths of an ash particle, the resistance can be considered to be made of two temperature dependent resisters connected in parallel. One corresponding to the surface conduction path, whose value increases with temperature and the other corresponding to the volume conduction path, with a value falling with temperature. The relationship between the temperature and the conduction can be represented graphically and is summarised in Figure (5.5.1). The actual value of resistance measured would be the parallel combination of both conduction paths and is drawn as a dotted line

on the figure.

An industrial agglomerater will be working just down stream from the furnace of the power plant and would therefore be operating in flue gas temperatures in the excess of 200°C. So the resistivity of the ash particles will be towards the maximum of the range, at the peak of the composite curve in Figure (5.5.1). However, the laboratory system will be operating at room temperature. So the conduction path will be around the surface of the particles and the resistivity will be considerably lower than the industrial application.

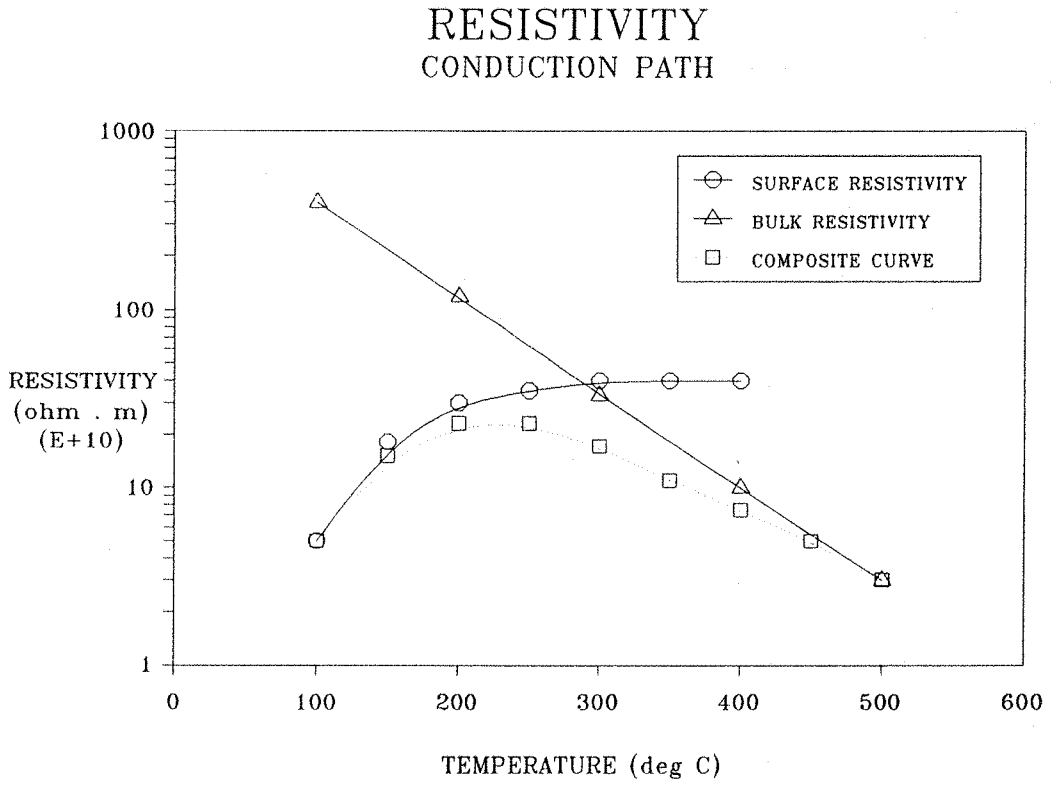

FIGURE 5.5.1 FLY-ASH RESISTIVITY

Showing the contributions from both the surface and the bulk conduction paths.

(After Bickelhaupt (1974)[ref 5.1])

The charge carriers in the surface conduction process tend to be the alkali metal ions that are present within the sample. So the value of resistance will be dependent on the concentration of these ions within the particle.

However, the ash particles are particularly hygroscopic and the surface resistivity is very dependent on the atmospheric conditions. The alkali metal ions on the surface of the particle will react with atmospheric water vapour through a process of ion exchange, forming metal hydroxides which will then further react with the water vapour to form mobile ions on the surface of the particles. These mobile ions are then free to move under the influence of an electric field and hence act as the charge carriers and produce a very low surface resistivity.

5.5.2 RESISTIVITY MEASUREMENT

The resistivity of all eight of the ash samples was measured using the method described in chapter four. The values of the resistivity were calculated for each sample using the sample geometry used in each case and a table of results drawn up in Table (5.5.1), this table also shows the system parameters and ambient conditions of the test. The current decay curves were also plotted for all the samples but were plotted on three separate axis. The first in Figure (5.5.2) is from sample 'OLD ASH' and sample 'NEW ASH', the second, in Figure (5.5.3) shows the current decay from samples S1 through to S4, while, Figure (5.5.4) shows the decay for samples SD1 and SD2.

TEST CONSTANTS
APPLIED POTENTIAL = 10 KV
TEST CELL AREA CROSS SECTIONAL AREA = 6.44×10^{-4} m^2

SAMPLE NAME	SAMPLE LENGTH	TEMPERATURE AND HUMIDITY		RESISTIVITY (FINAL VALUE)
	(m)	(°C)	(%RH)	(Ω.m)
OLD ASH	0.013	27.0	12.0	$61.9\times10^{+6}$
NEW ASH	0.016	28.0	33.2	$53.7\times10^{+6}$
S1	0.017	25.3	23.0	$31.6\times10^{+6}$
S2	0.016	27.1	16.6	$10.9\times10^{+6}$
S3	0.016	27.1	12.5	$7.9\times10^{+6}$
S4	0.013	26.9	19.0	$14.6\times10^{+6}$
SD1	0.0165	28.0	18.0	$7.0\times10^{+6}$
SD2	0.017	27.6	14.2	$21.1\times10^{+6}$

TABLE 5.5.1 ASH RESISTIVITY TABLE

5.5.3 OBSERVATIONS

If we first look at the current decay curves plotted for all the samples, we can see the characteristic fall in current to a steady state level. The steady level current represents the value of current that is flowing through the sample under test once all the polarization and other charging effects have ceased. From this value of current the resistivity of the ash sample can be calculated. Neither the initial nor the final values of current can be compared from one sample to another, as the length of the sample under test was not kept constant for all the ash samples.

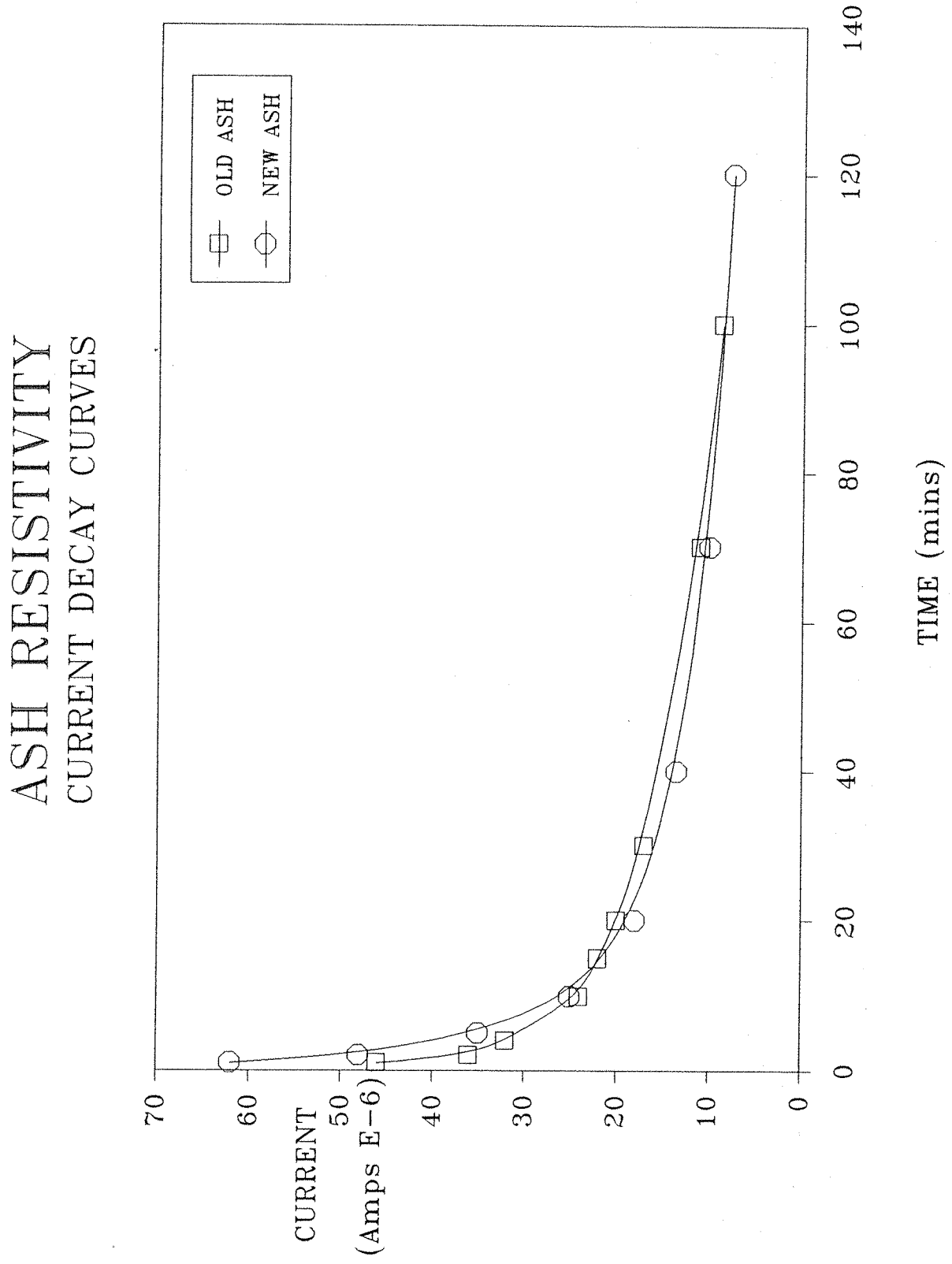

FIGURE 5.5.2 CURRENT DECAY CURVES FOR RESISTIVITY MEASUREMENTS OLD ASH and NEW ASH

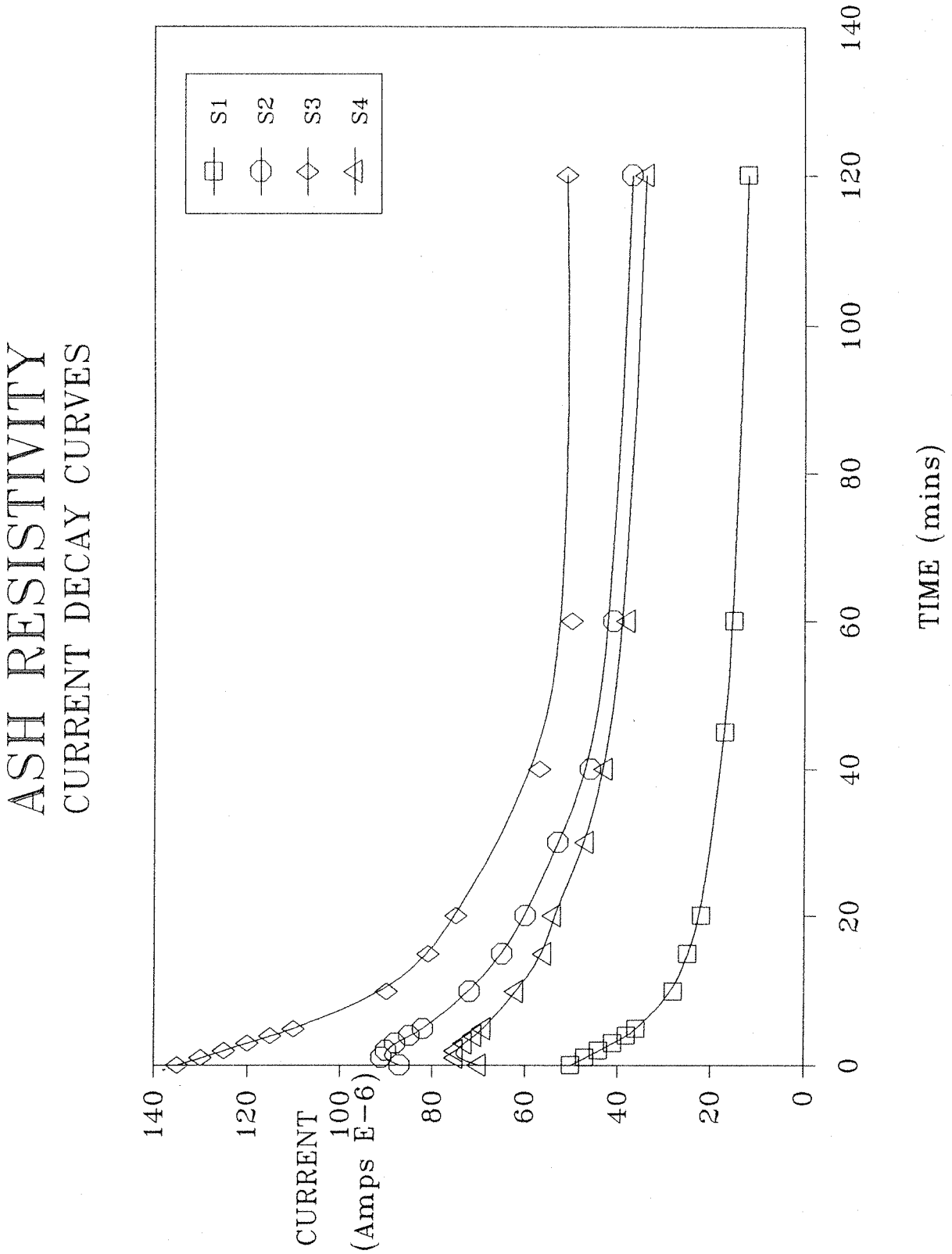

FIGURE 5.5.3 CURRENT DECAY CURVES FOR RESISTIVITY MEASUREMENTS S1, S2, S3, and S4

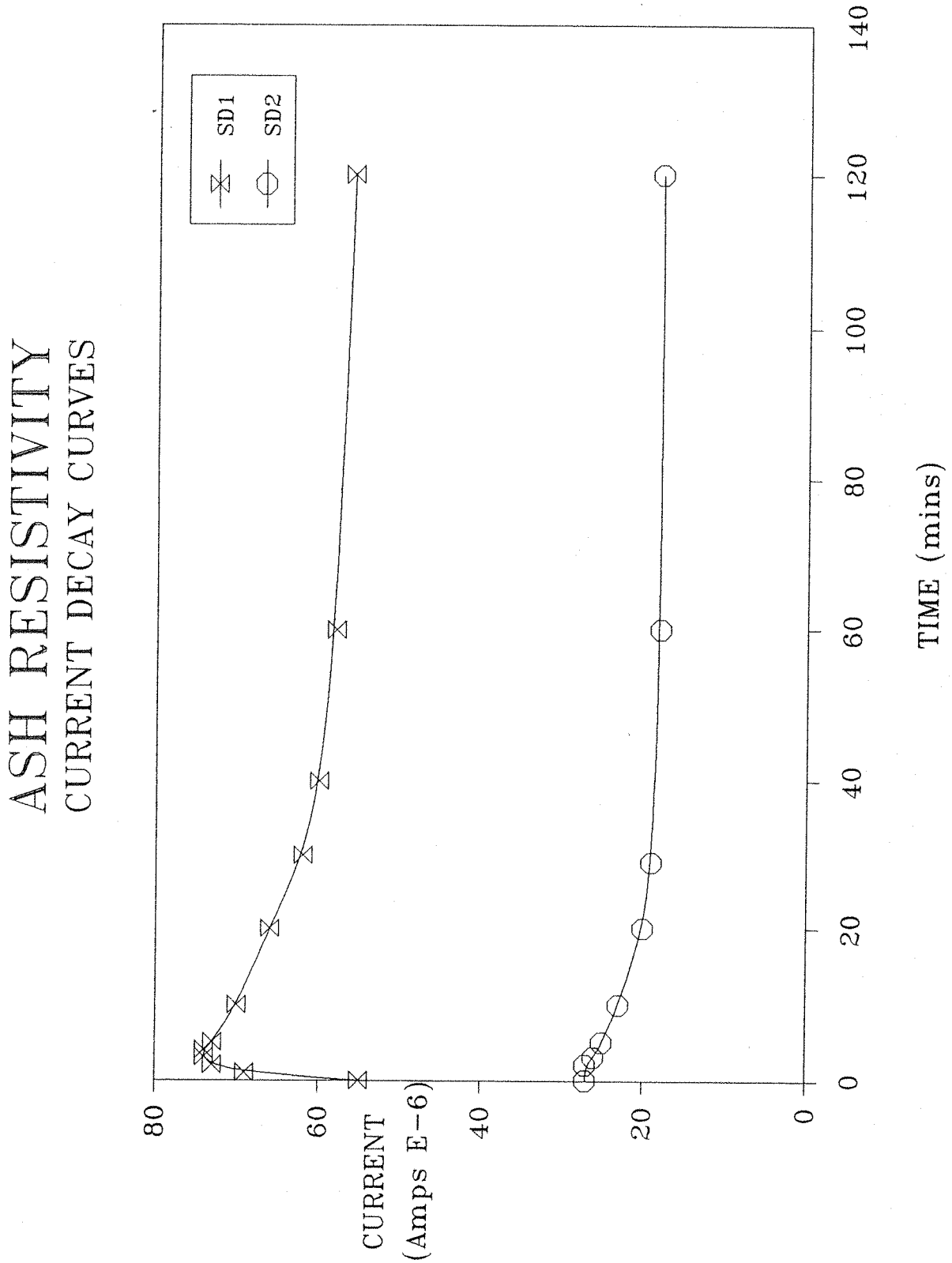

FIGURE 5.5.4 CURRENT DECAY CURVES FOR RESISTIVITY MEASUREMENTS SD1 and SD2

The initially high value of current followed by the decay down to the steady state value is due to the changing state of charge within the sample under test. The rate of the decay current can be expressed in terms of a time constant 'τ', which is a fixed parameter for the type of material under test. This time constant can be calculated from the data in several ways. First, the rate of the decay plot in the graph can be used and the following equation solved:

$$\ln i = \ln i_0 \ \frac{-t}{\tau} \qquad \textbf{Equation (5.5.1)}$$

Where: i = The value of the current after time t.
i_o = The initial value of current.
t = The time to decay from i_o to i.
τ = The time constant of the decay.

Solving this equation for sample S1, a typical example, gives a time constant of:

$\tau \approx$ 35 minutes.

However, if we write the equation for the time constant in terms of the dielectric constant of the ash ($\varepsilon_r = 3$ typically for ash) and its resistivity and then again solve the equation for ash sample S1, the result obtained is entirely different.

$$\tau = \varepsilon_r \ \varepsilon_o \ \rho \qquad \textbf{Equation (5.5.2)}$$

Where: τ = The time constant.
ε_o = The permittivity of free space.
ε_r = The relative permittivity.
ρ = The resistivity of the particle.

So: $\tau = 8.85\times10^{-12} \times 3 \times 31.6\times10^{+6}$

τ = 0.00084 Seconds

The vast difference between these two calculated values, from the same experiment, can be explained by considering what the time constants are showing in each case.

Using equation (5.5.1) we are calculating the time constant of the longest electrical reaction within the ash sample under test, whereas, equation (5.5.2) is calculating the time constant of known parameters, i.e. the charge decay rate through the sample itself. The difference occurs because these two time constants are not both of the same reaction. Equation (5.5.2) gives the time constant for the flow of charge through the sample, in this case around the surface of the ash particles. The very fast value indicated is a function of the very low resistivity measured. Equation (5.5.1) gives the time constant for the slowest electrical reaction of the system as it is this reaction that will limit the current decay rate recorded. This reaction is the polarization of the molecules within the volume of the ash particles. A high current flows at first, as the charge within the molecules is randomly arranged but as these charges begin to line up opposing the applied electric field, the current is reduced as the field from the polarised molecules opposes the applied field. Thus reducing the total field applied to the charge carriers within the sample hence reducing the current. This polarization and the opposing field from the polarized molecules is illustrated in Figure (5.5.5). So this larger time constant calculated from equation (5.5.1) is a property of the molecular structure of the ash particles and is not related to the surface conduction path.

The current decay curves of the ash samples tested, have been drawn on three separate axis, with the curves producing similar decay characteristics drawn together. The fastest decay was seen from samples 'OLD ASH' and 'NEW ASH', which were plotted in Figure (5.5.2). Although these two ash samples had previously been seen to have totally different particle size distributions and the 'OLD ASH' having none of the un-burnt fuel particles that were seen in the 'NEW ASH' sample, they produced very similar current decay characteristics. The next fastest decays were seen from ash samples S1 through to S4. These samples all had very similar physical appearances and size distributions and all exhibit similar current decay characteristics, these decay graphs were all plotted in Figure (5.5.3). The final figure in this series is Figure (5.5.4) showing the current decay of the samples SD1 and SD2. These two samples produced a much slower decay than any of the previous samples, even though they were of

a similar physical appearance to samples S1 to S4.

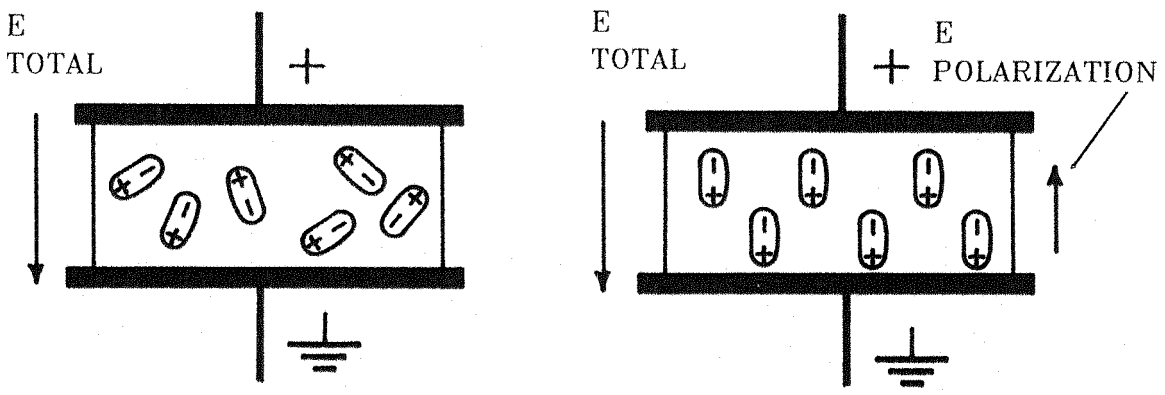

$E_{TOTAL} = E_{APPLIED}$

This illustration shows the moment that the field is applied to the sample, the molecules within the sample are still randomly aligned.

$E_{TOTAL} = E_{APPLIED} - E_{POLARIZATION}$

This illustration is some time later, polarization is complete and the electric field from the polarized molecules opposes the applied electric field

FIGURE 5.5.5 POLARIZATION EFFECT

Despite the differences seen in the rate of current decay for the different samples, they do all have a time constant 'τ' for the polarization of the same order of magnitude, ranging from 20 minutes to 50 minutes. Again it is important to remember that this is not the charge relaxation time but the polarization time constant and has no effect on the charging or discharging of the ash particles within the temperature range we are operating in.

The resistivity values calculated for all the ash samples were very similar. All being of the same order of magnitude. Even the 'OLD ASH' sample, that has previously been shown to have a different physical appearance from all the other samples, with no un-burnt fuel particles, produce a resistivity of the same order of magnitude.

However, the values obtained were considerably lower than would have been expected from a fly-ash. A resistance value five orders of magnitude higher would not have been un-expected.

It is known that the conduction path is over the surface of the particles under test. So it is reasonable to assume that the very low value of resistivity recorded was in some way due to an impurity on the surface of the particle. It was suggested earlier in this chapter that even very small amounts of water vapour can react with the alkali metals within the ash surface to produce free ions which will then act as the charge carriers. As the ash samples tested were not straight from the hot flue the amount of exposure to atmospheric water vapour and what effect that exposure has had on the samples was unknown. Also all of the ash samples under test, except the 'OLD ASH' sample, were seen to have a large number of un-burnt fuel particles mixed in with the ash particles. These un-burnt fuel particles could have been carbon based and hence provide a low resistance path for the charge carriers through the ash sample. To determine if the water content of the ash sample had played a part in the low resistivity values recorded it was decided to try to dry a sample prior to testing and see if the resistivity was altered.

5.5.4 DRIED ASH

A sample of the 'OLD ASH' (which was free of the un-burnt fuel particles) and a sample of the 'NEW ASH' were taken and placed in an oven at 200°C for a period of two hours. The ash samples were then allowed to cool in a dry atmosphere (Relative Humidity < 10%) until they reached ambient temperature. The resistivity test was then repeated for both samples. It was important for this test that the temperature of the ash had cooled to room temperature prior to testing, as the conduction path would alter if the temperature was higher. The results of these tests were tabulated along with the results of the un-dried samples and can be seen in Table (5.5.2). The current decay curves were also plotted and can be seen in Figure (5.5.6). However, it should be noted that the current for the 'OLD ASH DRY' has been drawn six orders of magnitude higher than it should be.

NAME	STATE	SAMPLE LENGTH	TEMPERATURE AND HUMIDITY		RESISTIVITY (FINAL VALUE)
		(m)	(°C)	(%RH)	(Ω.m)
OLD ASH	UN-DRIED	0.013	27.0	12.0	$61.9\times10^{+6}$
OLD ASH	DRIED	0.012	28.4	10.0	$77.8\times10^{+12}$
NEW ASH	UN-DRIED	0.016	28.0	33.2	$53.7\times10^{+6}$
NEW ASH	DRIED	0.016	28.2	10.0	$16.1\times10^{+7}$

TABLE 5.5.2 ASH RESISTIVITY WITH AND WITHOUT DRYING

5.5.4.1 OBSERVATIONS

By looking first at the current decay curves in Figure (5.5.6), we can see that drying the sample has had little effect, if any, on the rate of current decay. However, the curve for the old ash dry had been shifted up six orders of magnitude in order to be able to compare it to the other decay plots.

These resistivity values show two very significant results. First, drying the 'OLD ASH' sample, that was free of the un-burnt fuel, has had a very dramatic effect on the resistivity measured. In fact the value of resistivity for the dried sample was six orders of magnitude larger than for the un-dried sample. This result was also very close to the expected value for a fly-ash. This confirms that the original ash sample had absorbed an unacceptable amount of water vapour from the atmosphere. However, the same dramatic change in the measured resistivity was not seen by drying the 'NEW ASH' sample. The change in

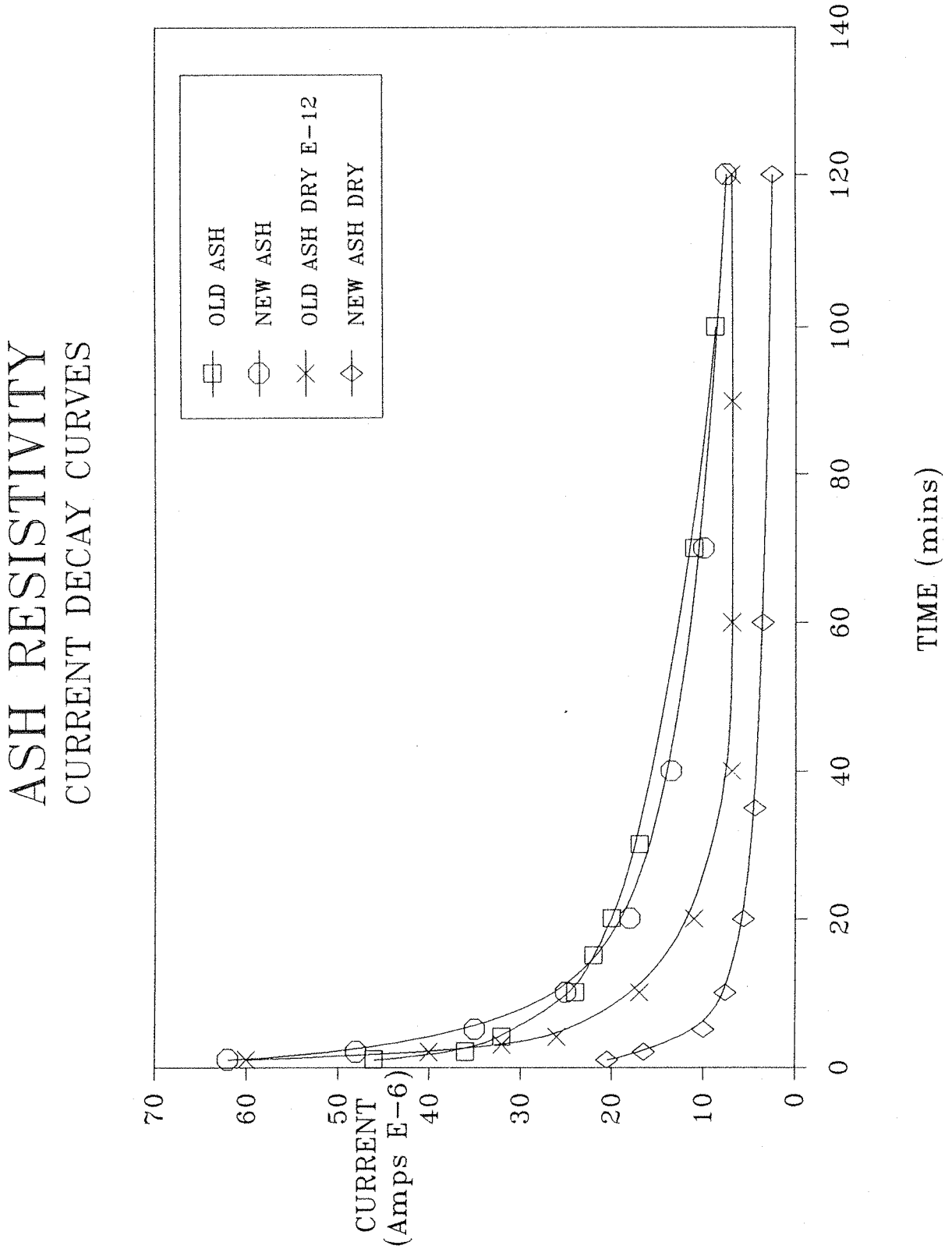

FIGURE 5.5.6 CURRENT DECAY CURVES WITH AND WITHOUT DRYING

resistivity value was only by one order of magnitude in this case. This would indicate that the low resistivity readings found for the newer samples of ash were caused by the presence of the un-burnt fuel providing a conduction path for the charge carriers. The water content of the ash may still play a part in the reduction of the resistivity value, it is not possible to isolate this effect from the presence of the un-burnt fuel.

Equation (5.5.2) can now be resolved using the resistivity value of the dried 'OLD ASH' sample, in order to find the time constant of the charge transfer process.

$$\tau = \varepsilon_o \varepsilon_r \rho \qquad \textbf{Equation (5.5.2)}$$

Where: τ = The time constant.
ε_o = The permittivity of free space.
ε_r = The relative permittivity.
ρ = The resistivity of the particle.

Assuming the relative permittivity 'ε_r' to be 3.

Then: $\tau = 8.85\times10^{-12} \times 3 \times 77.8\times10^{+12}$

τ = 34 minutes 26 seconds

This value for the time constant is much more acceptable for our agglomeration system than the value calculated from the un-dried ash. As the ash particles, once charged, will be able to retain their charge even after agglomeration. However the time constant for the charge transfer that can be calculated for the 'NEW ASH' sample is still unacceptably low for agglomeration (or precipitation). It must however be remembered that this Figure was calculated from the resistance value measured for the sample which has been shown to be artificially low due to the presence of the un-burnt fuel particles

within the sample. So the true value of the resistivity of the ash particles alone is still unknown. However, it can be considered that the resistivity of the ash particles from the newer samples if free from the un-burnt fuel particles would be similar to the value obtained for the dried 'OLD ASH' sample, as long as their physical conditions are maintained the same.

CHAPTER SIX

THE TEST RIG

The experimental rig used in this study was an adaption of a test rig which had previously been used by Dr.Paul Coventry[ref 6.1] for his studies, at the University of Southampton, into electrostatic precipitation.

6.1 PRECIPITATION RIG

This rig consisted of a one metre long vertical box section duct with a cross section measuring 300 mm by 500 mm. The 500 mm sides were constructed of thin aluminum sheet, which acted as the precipitation plates in the original model. While the 300 mm sides were made of clear acrylic sheeting, which allowed for the examination of the ash flow within the rig by eye or using optical instruments.

The air flow through the duct was maintained by using an induced draft fan driven by a d.c. motor. The flow velocity of the ash laden air stream could be varied up to a velocity of four meters per second. The fan had originally been connected to the top of the test duct by a length of flexible tubing.

The ash was fed into the bottom of the system through the use of a fluidized bed. This fluidized bed was connected to the test duct via a flow straightener which was used to promote laminar flow within the rig. This system is illustrated in Figure (6.1.1).

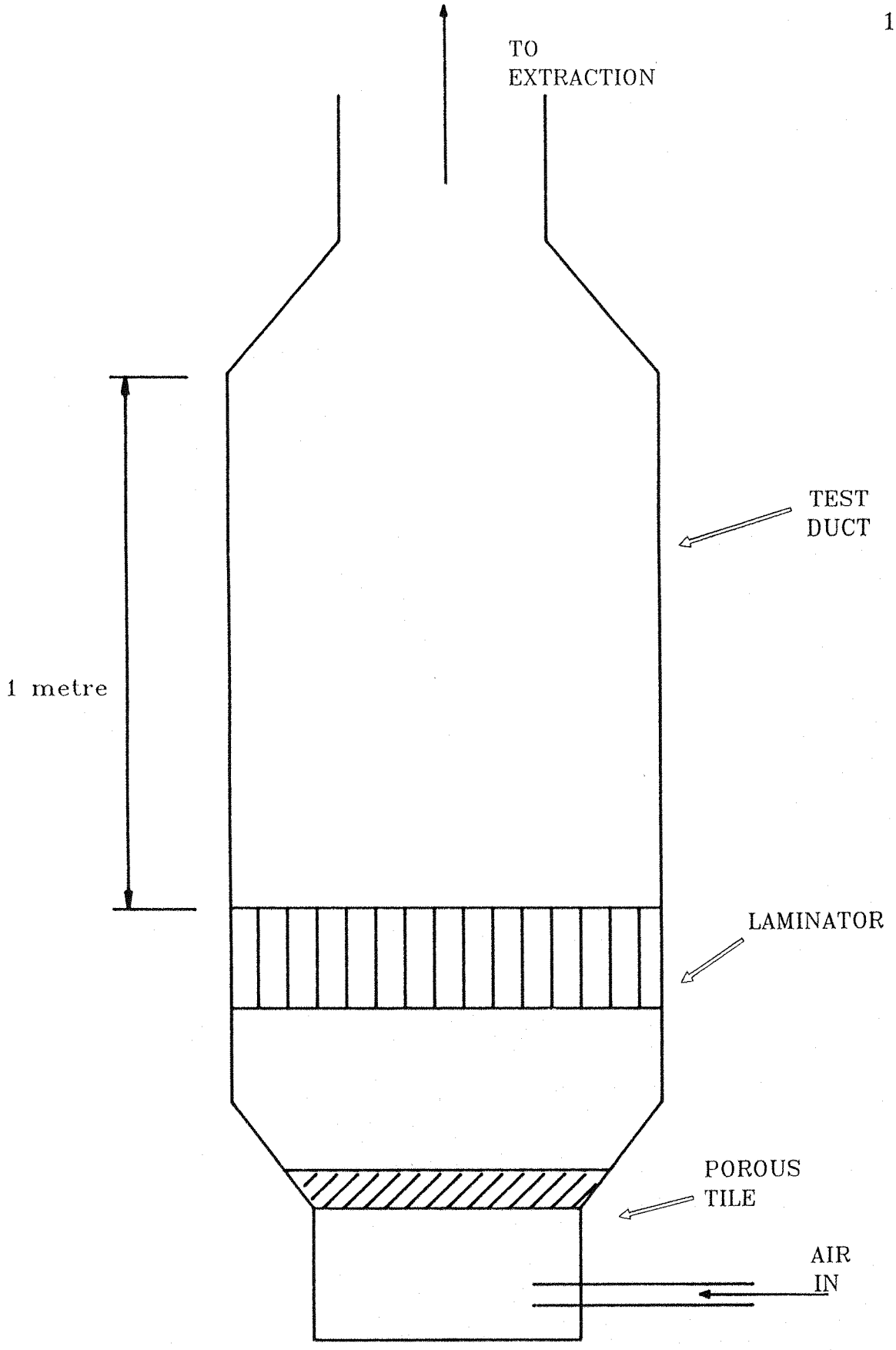

FIGURE 6.1.1 THE PAUL COVENTRY MODEL ELECTROSTATIC PRECIPITATOR

6.1.1 AGGLOMERATION RIG

The test duct, as inherited, would have a few drawbacks if it were to be used as an agglomerater.

Firstly as the duct stands vertically, there would be a tendency for the larger particles within the ash laden gas flow to sink under the influence of gravity, while the finer particles will be better entrained within the air stream. This preferential entrainment would also produce a changing size distribution profile of the ash within the rig, as there would be a build up of the larger particles which move much more slowly than the fines. As these larger particles are moving slower they will remain within the test region for longer, thus having a greater influence on the observed results than they otherwise would have.

Secondly, the ash feed system that had previously been used, the fluidized bed, was found to not adequately disperse the ash. There were several problems with this entrainment system. It was not easy to control the ash load within the air stream. Also, the ash within the fluidizer required constant manual agitation just to lift the ash from the porous tile. The size distribution profile of the dispersed ash was not constant over a period of time. It was found that the finest particles were initially dispersed, as they were easily entrained by the air coming through the fluidized bed. This then left the particle size distribution within the fluidizer becoming more and more consistent of only the larger particles, until it could be seen that the remaining ash consisted of only the very large particles. Finally, dispersing solid particles through the use of a fluidized bed does not generate a great deal of shear stress, so any agglomerates or clumped particles that may have existed within the original ash sample were not adequately broken.

To allow the use of this test duct as an agglomerater, the rig was taken and placed on its side so that it now ran horizontally. The top and bottom walls being the 500 mm conducting surfaces and the side walls being the 300 mm acrylic sheet. The extraction system consisting of fan and d.c. motor was left unaltered. However, at a later date the ducting used to connect the flexible tubing from the fan to the top of the test duct was replaced with a similar piece of ducting but with a right angle bend. This was to facilitate the extraction of ash samples directly from and in line with the test duct without subjecting any

agglomerates that may have formed to any undue stress prior to their testing.

The fluidized bed was removed from the rig and a new ash feed system developed.

6.2 ASH ENTRAINMENT SYSTEM

The design of the ash entrainment system had to exhibit the following five characteristics.

1/ The feed system was required to produce an evenly dispersed ash cloud, whose instantaneous particle size distribution was constant to that of the initial sample.

2/ The velocity of the ash laden air stream should be variable and controllable. (This requirement should be adequately regulated by the extraction fan motor control).

3/ The ash load within the air stream should also be variable and independent of the velocity of the air flow.

4/ The net charge on the ash as it enters the test duct would also have to be maintained at a zero level. Any residual charge on the cloud would affect the ability of the bi-polar charger to produce two equal and oppositely charged streams after the flow has been split.

5/ The ash laden air flow should be as straight and as even as possible prior to entering the test duct so that any turbulence added to assist in the agglomeration process can be controlled.

6.2.1 ELECTROSTATIC POWDER COATING GUN

These five requirements for the ash dispersion system were satisfied by employing the use of an electrostatic powder coating spray gun.

The gun used was a Volstatic unit. This unit allowed for accurate control of the ash feed and hence the ash load. The gun also uses a purge air to help feed the ash from the hopper to the gun nozzle and a final air blast at the nozzle, used for spray pattern shaping in paint spraying operations. These air supplies can for our purposes be turned up to full pressure so as to induce the maximum shear stresses on any clumped particles, in order to promote as near as possible single particles within the generated ash cloud.

6.2.2 ASH DISPERSION FROM THE GUN

The degree to which the powder feed gun was able to breakup clumped particles and disperse the ash was verified by setting the Malvern instrument up in a spray booth and blowing the ash generated by the gun through the laser beam. It was important for this test to ensure that no part of the ash from the gun passed through the laser beam outside the measuring zone, while at the same time ensuring that the sample recorded was uniform with that produced by the gun. This was done by using a system of baffles and guides. The test was repeated three times to ensure that the results obtained were consistent.

6.2.2.1 PARTICLE SIZE RESULTS

Ash sample 'NEW ASH' was used for these tests and the histogram of the particle size distribution produced plotted in Figure (6.2.1), along with the histogram produced from the 'NEW ASH' sample when measured using the dry powder feeder. The results of these two distributions are also summarized in Table (6.2.1).

DISPERSION METHOD	MASS MEDIAN DIAMETER	90% POINT	10% POINT	SPAN	LOG. DIFF.
	(μm)	(μm)	(μm)		
DRY POWDER FEEDER	17.9	76.0	3.5	4.0	1.29
VOLSTATIC GUN (Average of three) (results)	13.8	72.4	3.7	5.0	5.12

TABLE 6.2.1 VOLSTATIC GUN PARTICLE SIZE DISTRIBUTION

6.2.2.2 PARTICLE SIZE OBSERVATIONS

By looking first at the histograms in Figure (6.2.1) of the two particle size distributions, it can be seen that there is a good overall correlation between the two results produced. However, there seems to be a fraction less of the finer particles and also less of the very large particles within the distribution from the powder feed gun, with a corresponding increase in the percentage of particles seen in the mid size ranges.

The data in Table (6.2.1) allows for the direct comparison of various parameters of the measured particle size distributions. The first point to note is that the log difference value is significantly greater for the distribution generated through the gun than for the original sample from the dry powder feeder. This shows that the new distribution is no longer a good fit to a geometrical model. However, particles within certain size bands may not have passed through the laser beam as the baffle system used to avoid particles passing through the laser beam outside of the measuring zone may have biased certain sizes of the distribution. Although the mass median diameter value of the distribution measured using the gun to disperse the ash is 23% lower than that from the dry

powder feeder, the range of the distribution, from the 10% point to the 90% point was found to be very similar. The reduction in the measured mass median diameter is likely to be due to the small loss of very large particles, which hold a very large amount of the total mass of the sample and hence significantly shifting the measured mass median diameter. However, their apparent loss is of little significance, as they were probably just excluded from the laser beam in the measuring process as the Volstatic gun can neither break up these large particles nor preferentially disperse the finer particles. So in conclusion we can consider that the Volstatic gun was adequately dispersing the ash.

6.2.3 INPUT DUCT

The powder feed gun was originally designed to produce an evenly dispersed plume of particles spraying into a comparatively large area of still air. However, in the case of the agglomeration duct the area is relatively small and the air into which the ash is being sprayed is moving.

For these reasons a one metre long input duct was attached between the test duct and the powder gun. This duct allowed the ash to disperse evenly throughout the width of the duct prior to reaching the charging stage. As well as allowing time for all the different sized particles of ash to become fully entrained within the moving air stream.

An illustration of the ash entrainment system is shown in Figure (6.2.2), detailing the powder feed gun and the one metre long input duct.

6.2.4 AIR VELOCITY AND ASH LOAD

With the ash entrainment system now attached to the test duct via the metre long input duct, the air flow rates and ash load values were measured and calibrated.

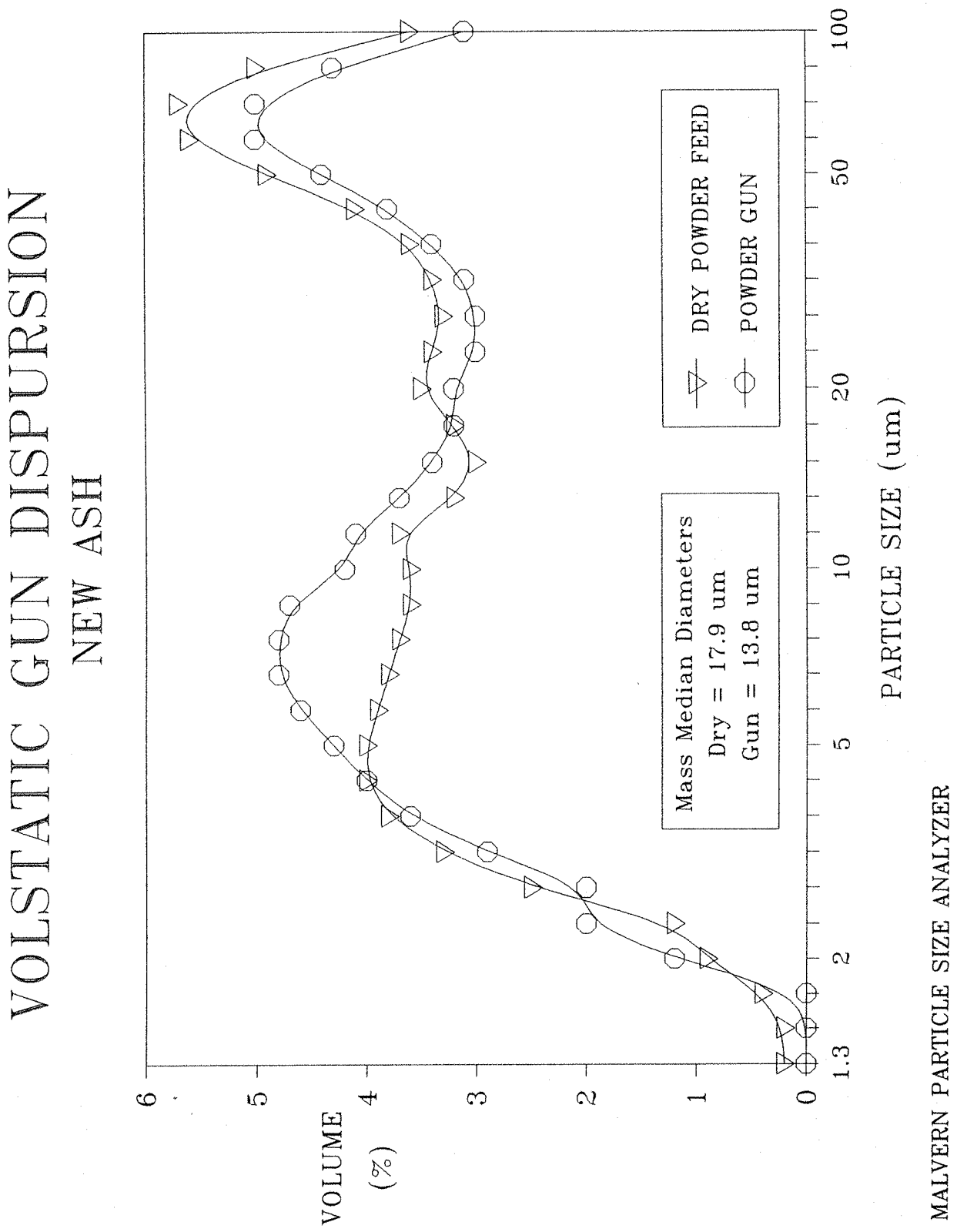

FIGURE 6.2.1 PARTICLE SIZE DISTRIBUTION
VOLSTATIC GUN COMPARED TO DRY POWDER FEEDER

The values of the load and flow rate for typical industrial precipitator units was sought from C.E.R.L., and are given below;

AIR VELOCITY	1.3 m s^{-1} up to 2.3 m s^{-1}
ASH LOAD	100 mg m^{-2} up to 20 g m^{-2}

These industrial rates were used as targets, to mimic the real conditions with our model as close as possible. However, it must be remembered that our test duct is only a fraction of the size of an industrial unit.

6.2.4.1 AIR VELOCITY

The air velocity within the agglomeration rig was measured with a hot wire anemometer using the experimental procedure described in Chapter four, although in this case the velocity was taken at only one point and in only one direction.

The detector of the anemometer was placed in the centre of the duct, at the far down stream end. Pointing directly downstream parallel to the net gas flow. This position was chosen as the fluctuations in the gas velocity within the rig were found to reduce with the distance along the rig. This turbulence within the gas flow has been further studied and is described later in this chapter. The values of the gas velocity were then recorded for various settings of the motor speed controller and the results given in Table (6.2.2). A graph of this data was also plotted, and can be seen in Figure (6.2.3).

6.2.4.1.1 AIR VELOCITY RESULTS

The air flow rates were measured with velocities up to 3 m/s with the extraction fan running at full speed. This range of velocities adequately covers the required range indicated by C.E.R.L. in section (6.2.4).

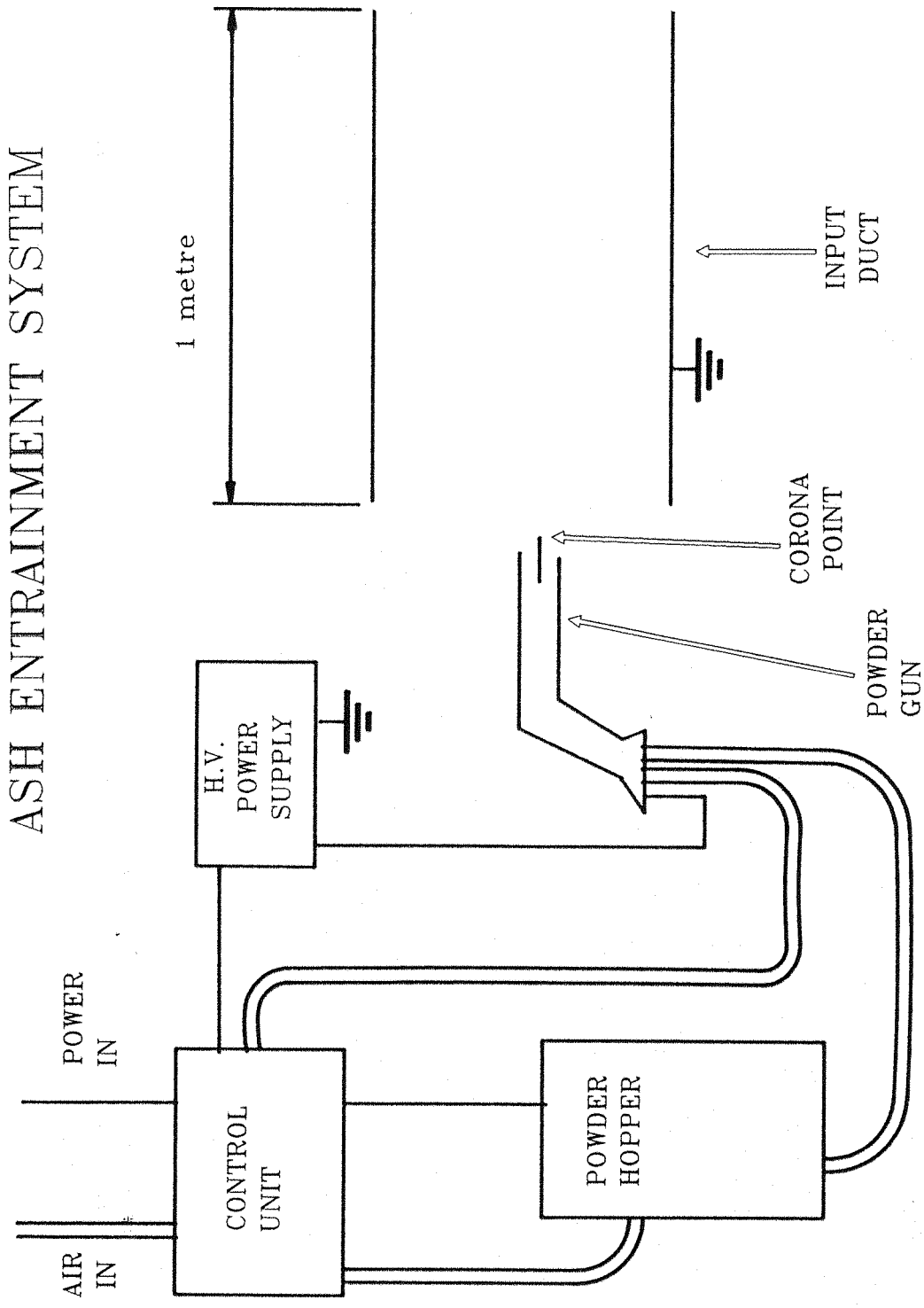

FIGURE 6.2.2 ASH ENTRAINMENT SYSTEM
DETAILING THE POWDER FEED GUN AND INPUT DUCT

It was decided to aim to run the rig at a gas velocity of 2.5 m/s, a setting of 160 on the motor controller. This velocity was chosen as it was not full power for the motor thus allowing for the possibility of more power to be provided should there be an increased pressure drop from the addition of the experimental apparatus within the rig.

MOTOR CONTROL POWER SETTING	AIR VELOCITY (m/s)
0	0.0
20	0.2
40	0.45
60	0.8
80	1.25
100	1.7
120	2.0
140	2.3
160	2.5
180	2.7
200	2.9
220	3.0
240	3.0
260	3.0

TABLE 6.2.2 AIR FLOW CALIBRATION RESULTS

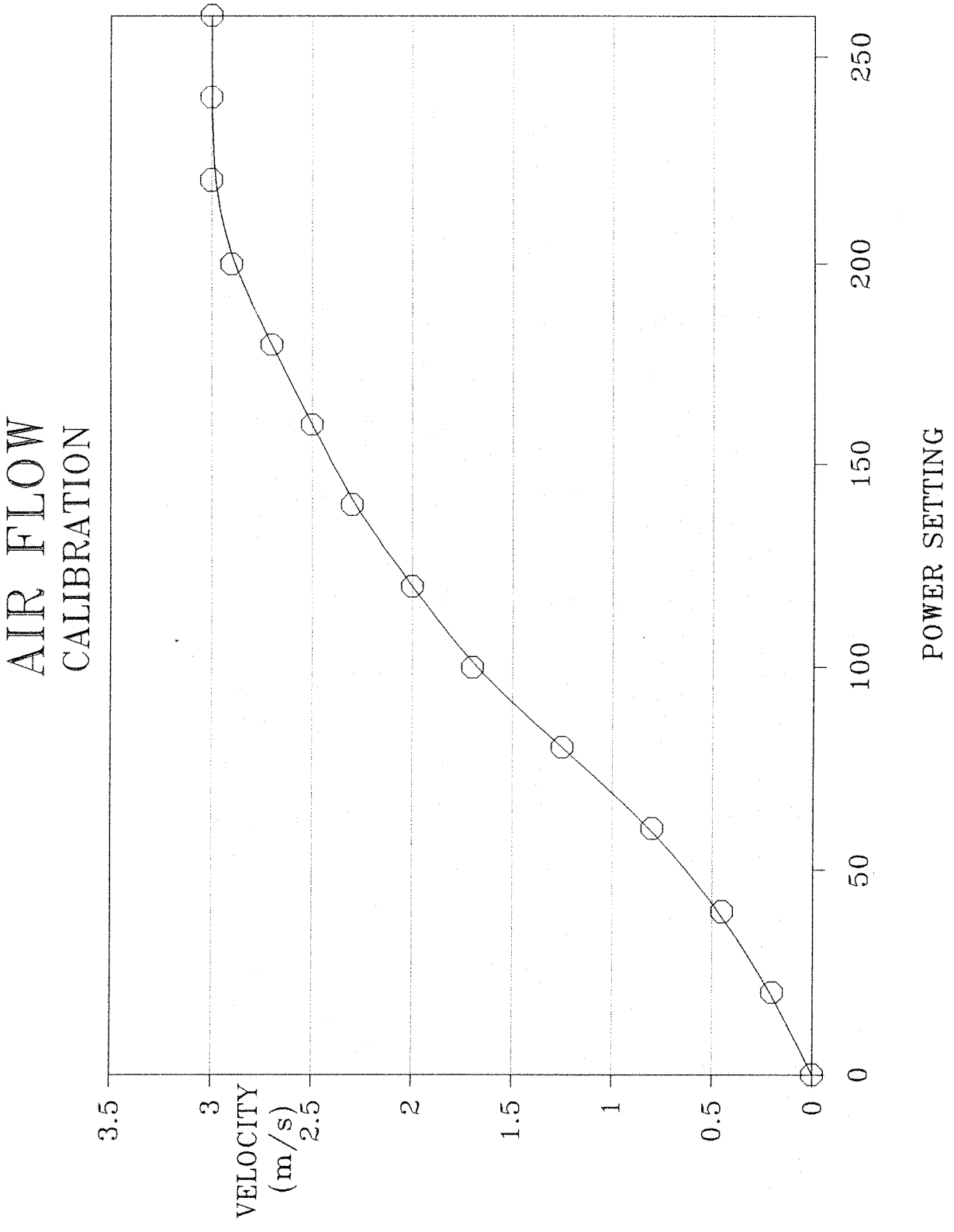

FIGURE 6.2.3 AIR FLOW RATE CALIBRATION

6.2.4.2 ASH LOAD

The ash load within the rig could be controlled by adjusting the powder feed rate through the Volstatic gun. This adjustment was made by varying the air pressure to the powder hopper. The ash load, as a function of the hopper pressure was measured by increasing the pressure from zero to 30 psi, the maximum achievable, in 5 psi steps. The mass of the ash lost from the hopper throughout a fifteen minute test period was measured for each step. The results of this calibration are shown in Table (6.2.3) and the calibration curve plotted in Figure (6.2.4).

FLOW RATE FOR ALL TESTS	2.5 ms^{-1}
SAMPLE TIME FOR ALL TESTS	15 minutes

AIR PRESSURE	**TOTAL MASS OF ASH USED**	**MASS OF ASH USED PER SECOND**	**ASH LOAD**
(psi)	**(Kg)**	**(g/s)**	**(g/m^3)**
0.0	0.00	0.00	0.00
5.0	0.00	0.00	0.00
10.0	0.12	0.13	0.35
15.0	0.50	0.56	1.49
20.0	0.86	0.96	2.56
25.0	1.18	1.13	3.49
30.0	1.34	1.49	3.97

TABLE 6.2.3. ASH LOAD CALIBRATION RESULTS

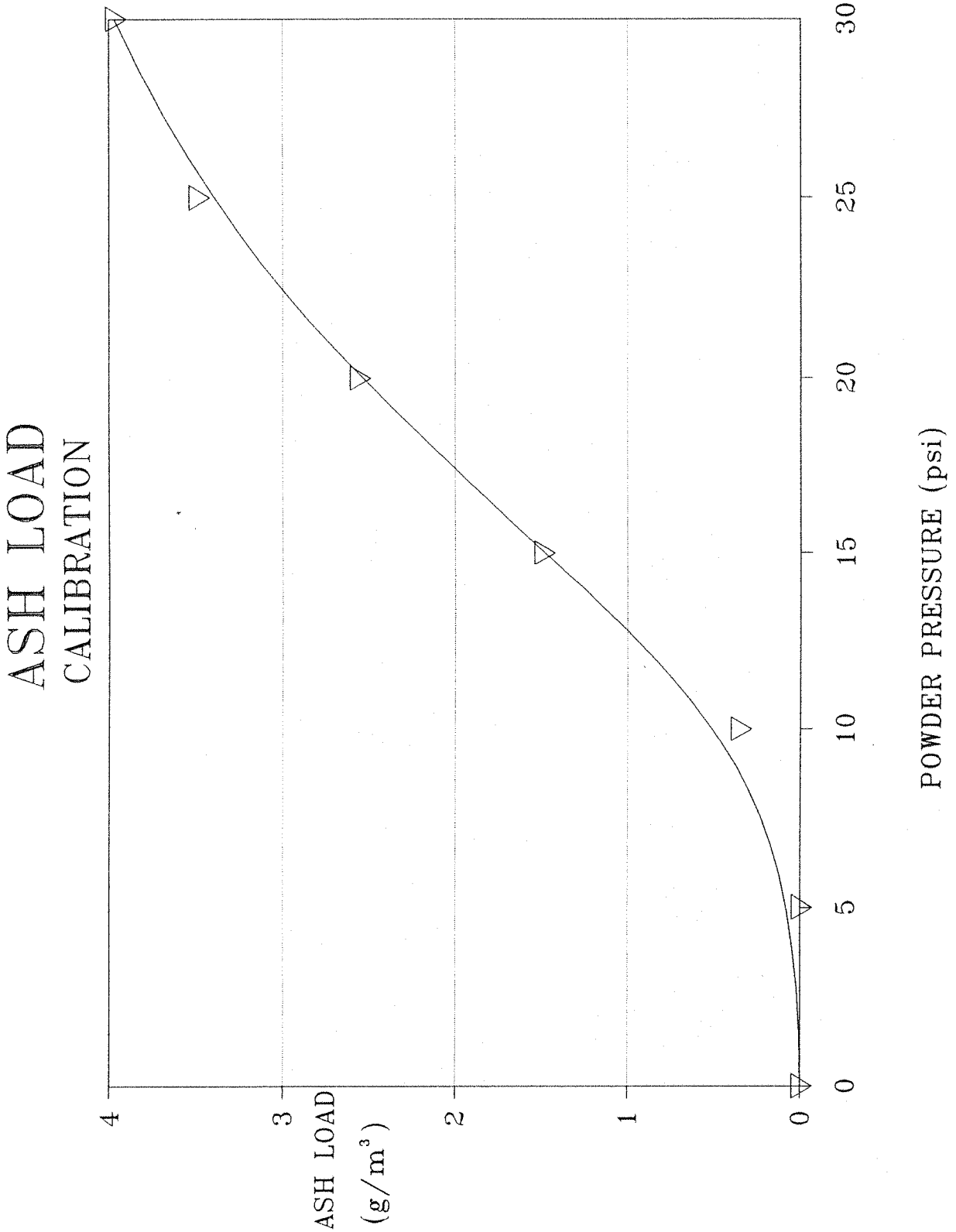

FIGURE 6.2.4 ASH LOAD CALIBRATION

6.2.4.2.1 ASH LOAD RESULTS

It was seen that the ash load could be increased up to a maximum value of about 4 g/m^3, with the powder feed gun running at full pressure. This value is only 25% of the maximum target load but is acceptable as it is well within the target range. It should be pointed out however that the ash load pressure was not easily controlled and in the mid pressure ranges tended to drift if left unattended.

6.2.4.3 ASH LOAD STABILITY

It had been noted during the running of the tests on the ash load that the output rate of the Volstatic gun seemed to be greater with the powder hopper nearly empty. In order to ensure that the ash load remained constant as a function of time, i.e. regardless of the volume of ash within the hopper, the air flow was set to a constant 2.5 m/s and the powder gun run at the full pressure of 30 psi. The mass of the hopper and ash was then noted every thirty minutes for a period of 3 hours. The results of these tests are given in Table (6.2.4) and the graph of this data plotted in Figure (6.2.5).

FLOW RATE	2.5 ms^{-1}

DURATION OF TEST	TOTAL MASS OF ASH USED	MASS OF ASH USED PER SECOND	ASH LOAD
(minutes)	(Kg)	(g/s)	(g/m^3)
30	2.56	1.42	3.79
60	2.63	1.46	3.89
90	2.87	1.59	4.24
120	2.73	1.52	4.04
150	3.09	1.72	4.59
180	2.69	1.49	3.97

TABLE 6.2.4 ASH LOAD STABILITY RESULTS

6.2.4.3.1 ASH LOAD STABILITY RESULTS

The ash load was found to remain fairly constant over the entire period of the test. The graph in Figure (6.2.5) was plotted as a trend and shows the load to slightly increase as the hopper empties. This increase in load is about 0.5 g/m^3 (12.5 %) for the three hour test period. This figure compares to a standard deviation in the recorded values of 0.26. So care was needed in performing any tests that required a constant ash load. This was done by maintaining as little change in the ash depth within the hopper as possible.

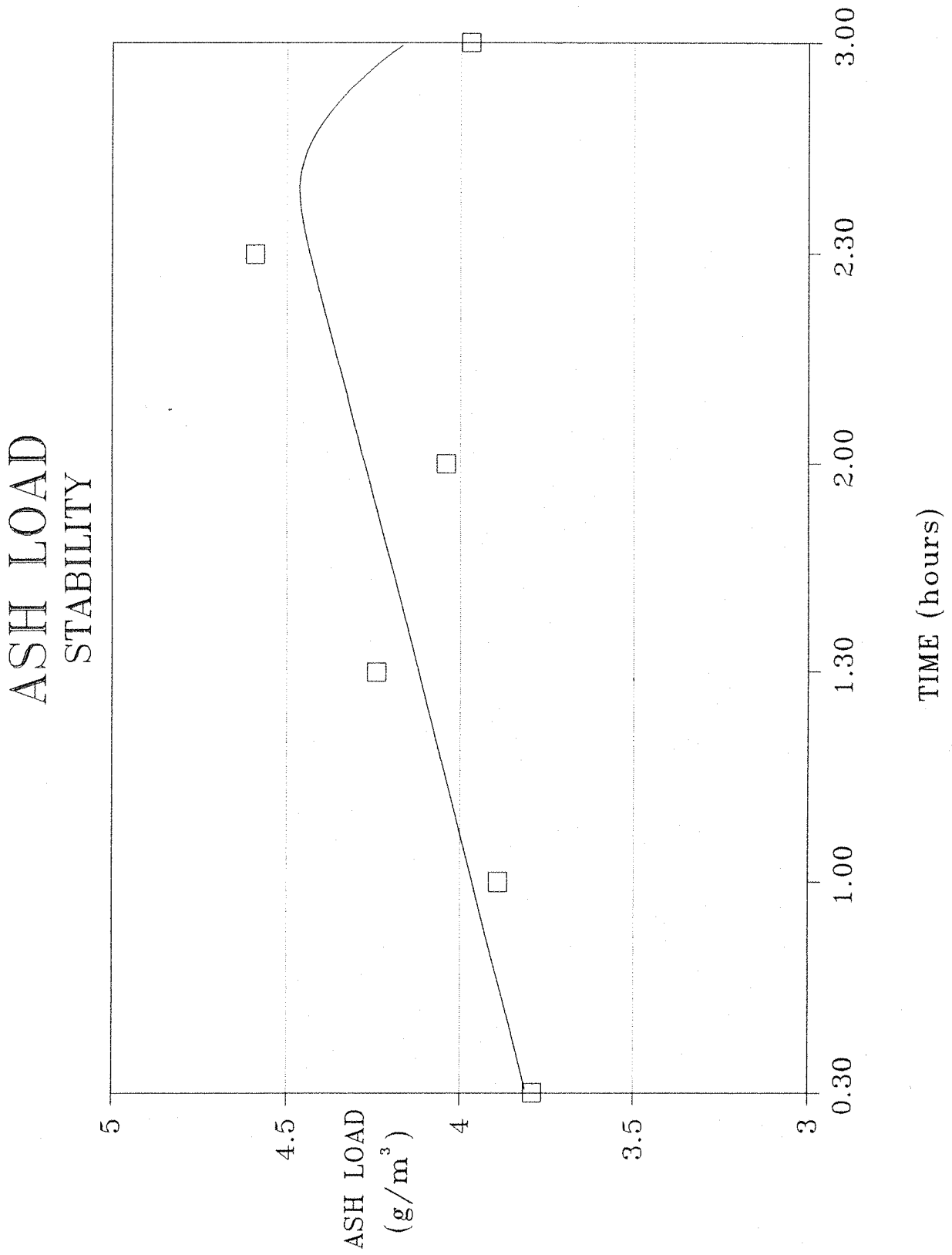

FIGURE 6.2.5 ASH LOAD STABILITY

6.2.5 FLOW STRAIGHTENER

It is also important that the ash laden gas stream on arriving at the test duct is not only as evenly dispersed as is possible, but the flow is as straight as possible.

For this reason a flow straightener was placed between the one metre long input duct and the test duct. This flow straightener was fabricated in the form of a box section honeycomb, with cells 30 mm tall, 30 mm wide and 100 mm long.

6.2.5.1 GAS FLOW MODE

In Chapter three it was shown how the mode of the gas flow can be determined from the Reynolds number, as:

$$R_e = \rho \frac{u D}{\eta} \qquad \textbf{Equation (6.2.1)}$$

Where:
- R_e = The Reynolds number.
- ρ = The gas density.
- u = The gas velocity.
- η = The gas viscosity.
- D = The equivalent duct diameter.

Where the equivalent duct diameter is defined as:

$$D = 4 \frac{\textit{the area of the duct}}{\textit{the perimeter of the duct}} \qquad \textbf{Equation (6.2.2)}$$

If $R_e \leq 2000$ then the flow will be Laminar.
If $R_e > 2000$ then the flow will be Turbulent.

Equation (6.2.1) can be solved for the dimensions of the test duct and the flow straightener in order to evaluate the mode of the gas flow within each.

First solving equation (6.2.2) to determine the equivalent duct diameter of each:

Test Duct:

$$D = 4\times \frac{(0.3 \times 0.5)}{(0.3 + 0.5 + 0.3 + 0.5)}$$

$$= \underline{0.375 \text{ m}}$$

Flow Straightener:

$$D = 4 \times \frac{(0.03 \times 0.03)}{(4 \times 0.03)}$$

$$= \underline{0.03 \text{ m}}$$

Equation (6.2.1) can now be solved for each, substituting in typical values for all the other variables:

Assuming: ρ = The gas density. = 1 Kg m^{-3}
u = The gas velocity. = 2.5 ms^{-1}
η = The gas viscosity. = 1.71×10^{-5} Ns m^{-2}

So:

$$R_{e\,DUCT} = 1 \times \frac{2.5 \times 0.375}{1.71\times10^{-5}}$$

$$= \underline{54825}$$

$$R_{e\ STRAIGHTNER} = 1 \times \frac{2.5 \times 0.03}{1.71 \times 10^{-5}}$$

$$= \underline{4386}$$

The gas flow within the duct has a Reynolds number about 30 times greater than the critical value, and hence will be turbulent. The flow through the straightener although an order of magnitude smaller in size than the duct will still have turbulent flow within it as its Reynolds number is about 2 times greater than critical. However, the main requirement of the straightener is not to generate a laminar flow within the agglomerater but to eliminate the large eddies that are generated in the input duct.

6.2.5.2 GAS FLOW MEASUREMENTS

It was important to know at this stage just how good the flow straightener was at stopping the large eddies. In order to asses the amount of turbulence that existed within the test duct the anemometer, as described in Chapter four, was placed at specific points along the test duct and the velocity and direction of the air flow measured. The test duct has two planes of symmetry along the direction of flow, so it was only necessary to make the measurements of air flow in one quarter of the duct in order to be able to asses the entire duct.

Measurements were taken at set height intervals along two planes, one along the centre of the duct and the other 5 cm from the edge. The test was repeated with and without the flow straightener and the results are drawn in Figures (6.2.6) to (6.2.9). The results are shown as a series of arrows, the base of the arrow being at the sample point, while the length of the arrow is proportional to the air velocity measured and the direction of the arrow indicates the direction of the air flow.

It is important to remember that a short arrow may be the result of rapidly changing direction of the air flow, with a small average in one direction. This is particularly prevalent in areas of high turbulence.

For these tests only the air supply and extraction system were turned on and not the ash feed, as the solid ash particles would block the anemometer.

6.2.5.3 GAS FLOW RESULTS

Figures (6.2.6) and (6.2.7) are the gas flow patterns without the flow straightener. At the up stream end of the test duct, large fluctuations in both the gas velocity and the direction of the flow were seen, this would indicate an area of great turbulence. Further down stream the vast changes in the gas flow direction diminish and the flow rate becomes more constant across the width of the duct. By looking at the velocity profile across the duct no real trend could be seen indicating that the flow was turbulent. The gas velocity measured near to the edges of the duct were not considerably lower than those in the centre of the flow, indicating that the boundary layer was very thin.

The next two figures, (6.2.8) and (6.2.9), are the flow patterns once the flow straightener had been installed into the rig. Immediately it is apparent that the area of great turbulence that had been seen in the previous measurements without the straightener had gone. Also the gas velocity profile is straight and of uniform velocity across the entire duct, indicating that the flow was still turbulent.

The measurements taken 200 mm into the duct were seen to approach the form of a laminar flow, with a very flat parabolic velocity profile. With a Reynolds number for the test duct 3000 times greater than the critical value required for laminar flow, this was an unlikely effect of the straightener and the gas flow would immediately return to being turbulent but without the large eddies that could be seen in the tests performed without the flow straightener.

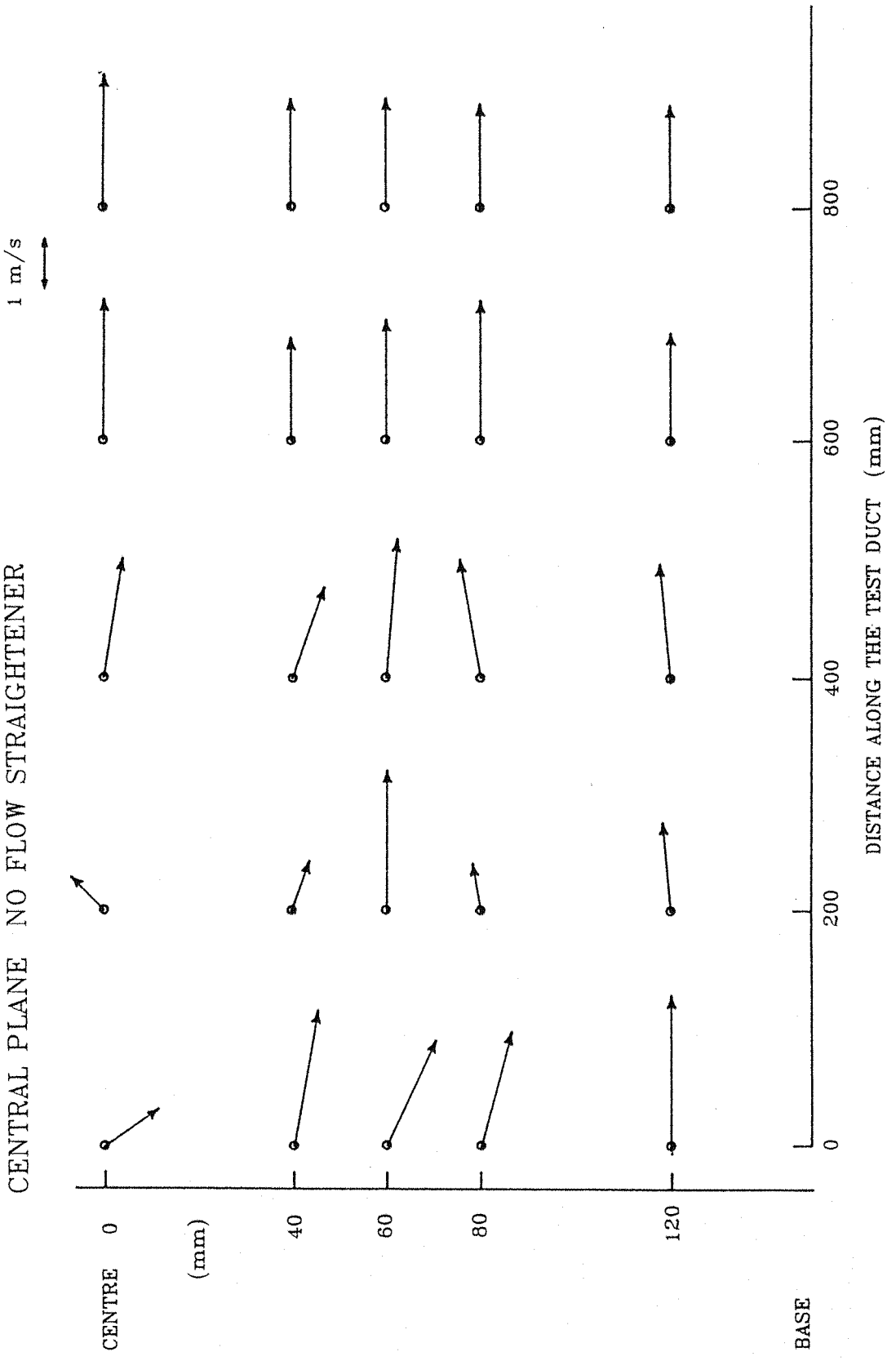

FIGURE 6.2.6 GAS FLOW AT THE CENTRE OF THE DUCT WITH NO STRAIGHTENER

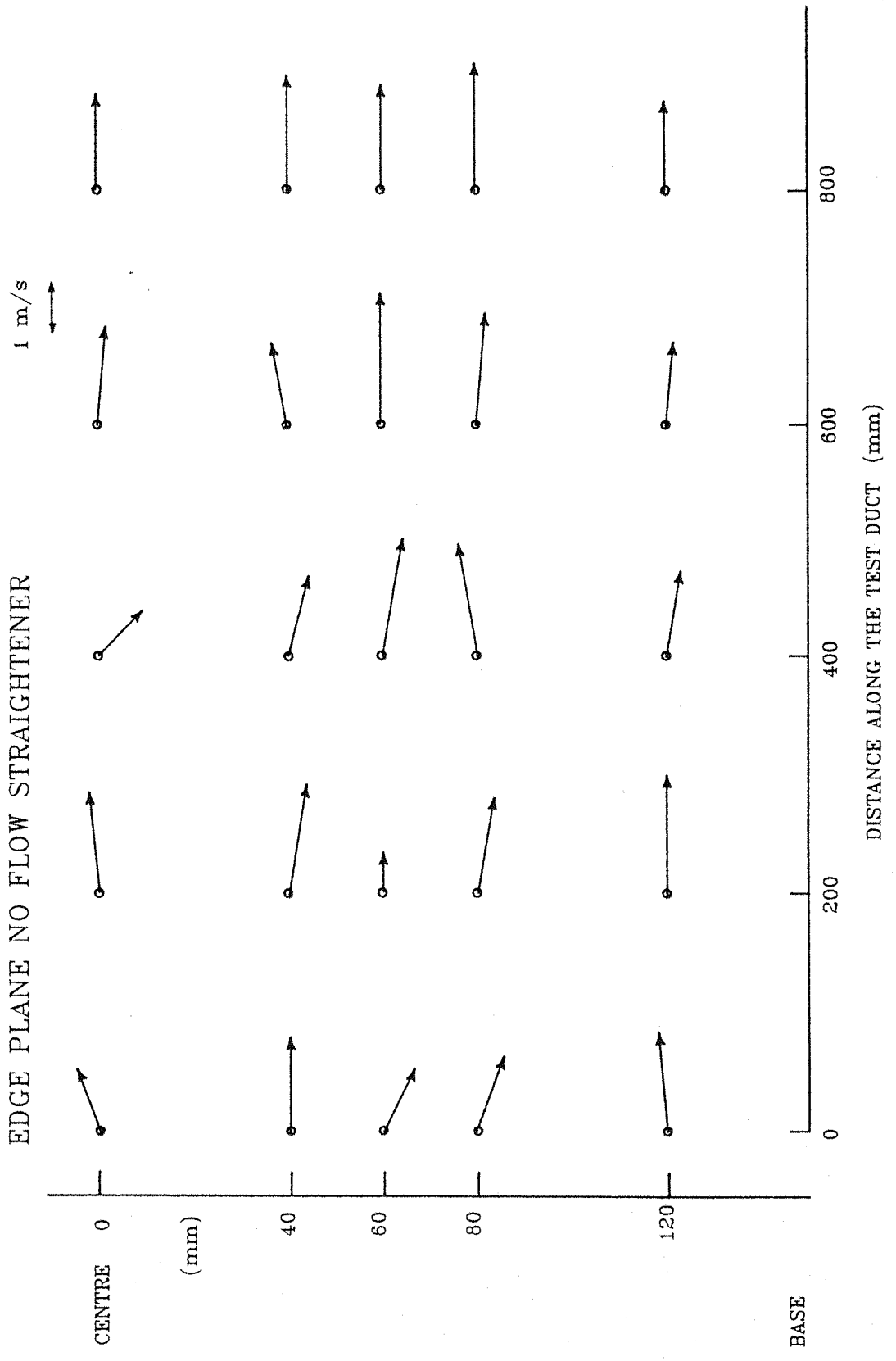

FIGURE 6.2.7 GAS FLOW AT THE EDGE OF THE DUCT WITH NO STRAIGHTENER

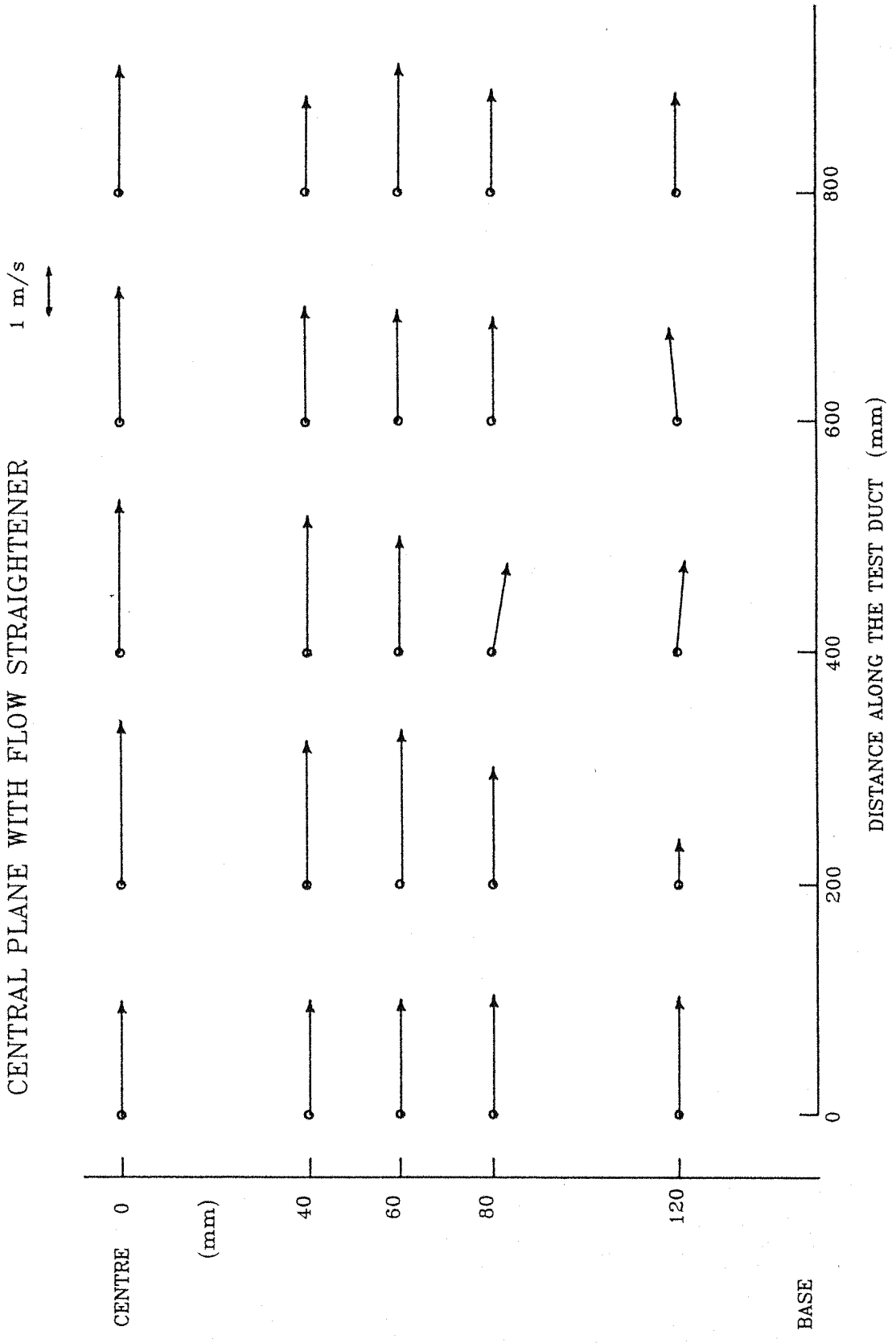

FIGURE 6.2.8 GAS FLOW AT THE CENTRE OF THE DUCT WITH FLOW STRAIGHTENER

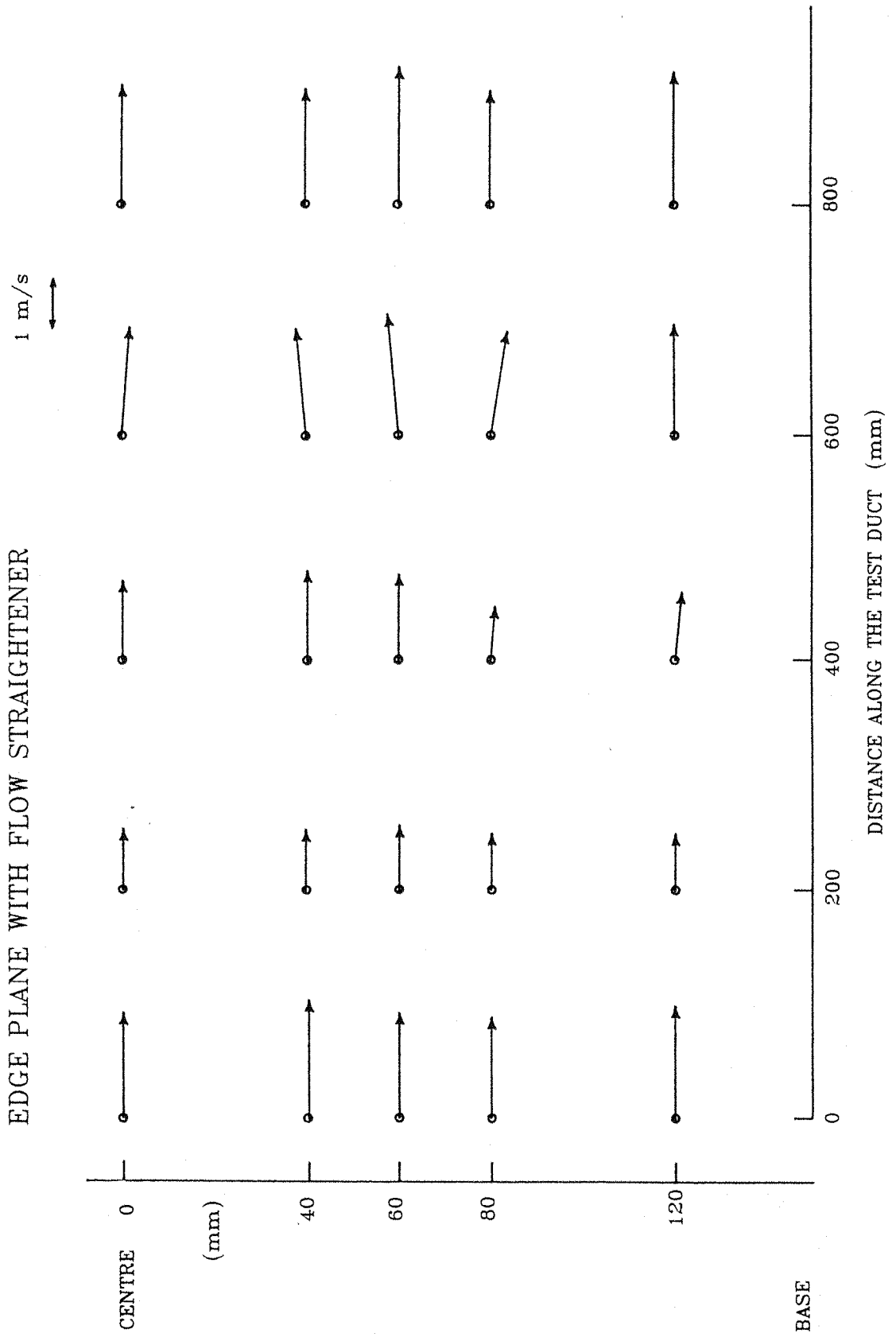

FIGURE 6.2.9 GAS FLOW AT THE EDGE OF THE DUCT WITH FLOW STRAIGHTENER

6.2.6 CHARGING CHARACTERISTICS OF THE FEED SYSTEM

The fourth point of the requirements for the ash feed system specified that the net charge on the ash cloud should be zero as it enters the test duct. In order to determine if this requirement had been satisfied, the charge to mass ratio of the ash was measured. This was done by placing the continuous flow Faraday cup about 200 mm down stream of the flow straightener. Various tests were then performed to asses the ability of the ash dispensing system to control the level of charge on the ash.

6.2.6.1 IONIC CURRENT

In order to determine whether any charge would be deposited in the continuous flow Faraday cup through the capture of gas ions generated from the corona point of the powder feed gun, three tests were performed. One with only the high voltage turned on, one with the high voltage and the air purge and the third with the air purge and the ash feed. The air velocity within the duct was set to 2.5 m/s and all three tests were run for 60 seconds. The results of these tests are given in Table (6.2.5).

POWDER FEED STATUS	SUPPLY CURRENT	ASH CHARGE	ASH MASS	CHARGE TO MASS RATIO
	(Amps)	(Coulombs)	(Kg)	(C/Kg)
H.T. only	0.1×10^{-3}	-0.48×10^{-8}	0.0	----
H.T. & AIR	0.1×10^{-3}	-0.58×10^{-8}	0.0	----
AIR & ASH	0.0	-6.70×10^{-8}	6.36×10^{-5}	-1.05×10^{-3}

TABLE 6.2.5 GAS ION EFFECT ON THE FARADAY CUP

6.2.6.1.1 IONIC CURRENT RESULTS

The ionic current reaching the Faraday cup in both the tests with the high voltage turned on and no ash flowing produced a current that was less than 10% of the current recorded, for the same period, when the ash was turned on. Also the percentage of free ions reaching the Faraday cup with the ash running will be less than when the ash feed is turned off, as a large proportion of the free ions will become attached to the ash particles through the normal corona charging processes. So the effect of the free gas ions reaching the continuous flow Faraday cup can be ignored.

6.2.6.2 CHARGE TO MASS RATIO

The charge to mass ratio that could be developed on the ash by the powder feed system was then measured. These measurements were made for a range of corona currents for both positive and negative coronas.

The charge to mass ratio with the corona point un-energized gave the tribo charge that would accumulate on the ash. This is the natural charge that deposits on the ash by friction during its transportation through the powder feed system.

The results of these teste are given Table (6.2.6) and the corona charging relationship plotted in Figure (6.2.10).

SUPPLY CURRENT	ASH CHARGE	ASH MASS	CHARGE TO MASS RATIO
(Amps)	(Coulombs)	(Kg)	(C/Kg)
-100×10^{-6}	---------	--------	---------
-90×10^{-6}	-17×10^{-8}	3.14×10^{-5}	-5.41×10^{-3}
-80×10^{-6}	-20×10^{-8}	4.30×10^{-5}	-4.65×10^{-3}
-70×10^{-6}	-16×10^{-8}	41.5×10^{-5}	-3.86×10^{-3}
-60×10^{-6}	-13×10^{-8}	3.82×10^{-5}	-3.40×10^{-3}
-50×10^{-6}	-10×10^{-8}	3.27×10^{-5}	-3.06×10^{-3}
-40×10^{-6}	-10×10^{-8}	3.55×10^{-5}	-2.82×10^{-3}
-30×10^{-6}	-9.7×10^{-8}	3.90×10^{-5}	-2.49×10^{-3}
-20×10^{-6}	-9.4×10^{-8}	4.24×10^{-5}	-2.22×10^{-3}
-10×10^{-6}	-10×10^{-8}	7.17×10^{-5}	-1.39×10^{-3}
0	-6.7×10^{-8}	6.36×10^{-5}	-1.05×10^{-3}
$+10\times10^{-6}$	-1.0×10^{-8}	3.74×10^{-5}	-0.27×10^{-3}
$+20\times10^{-6}$	-0.2×10^{-8}	4.17×10^{-5}	-0.05×10^{-3}
$+30\times10^{-6}$	$+1.8\times10^{-8}$	4.15×10^{-5}	$+0.43\times10^{-3}$
$+40\times10^{-6}$	$+2.6\times10^{-8}$	3.62×10^{-5}	$+0.72\times10^{-3}$
$+50\times10^{-6}$	$+4.9\times10^{-8}$	3.67×10^{-5}	$+1.34\times10^{-3}$
$+60\times10^{-6}$	$+9.0\times10^{-8}$	4.26×10^{-5}	$+2.11\times10^{-3}$
$+70\times10^{-6}$	$+11.0\times10^{-8}$	4.26×10^{-5}	$+2.58\times10^{-3}$
$+80\times10^{-6}$	$+9.4\times10^{-8}$	3.41×10^{-5}	$+2.76\times10^{-3}$
$+90\times10^{-6}$	$+16.0\times10^{-8}$	4.62×10^{-5}	$+3.46\times10^{-3}$
$+100\times10^{-6}$	$+15.0\times10^{-8}$	3.81×10^{-5}	$+3.98\times10^{-3}$

TABLE 6.2.6 CHARGE TO MASS RATIO RESULTS

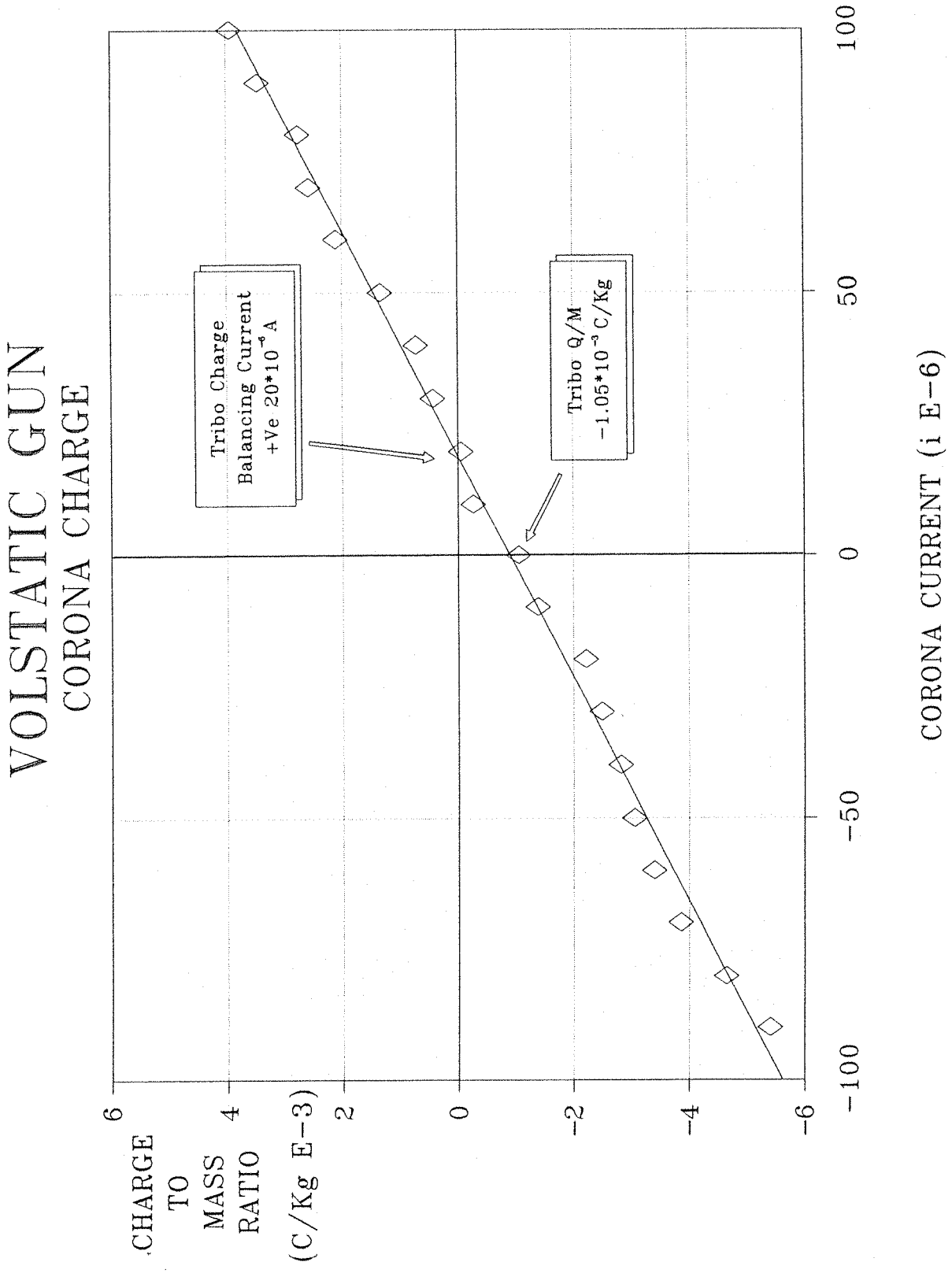

FIGURE 6.2.10 CHARGE TO MASS RATIO PRODUCED BY THE POWDER FEED SYSTEM

6.2.6.2.1 CHARGE TO MASS RATIO RESULTS

The relationship between the measured charge to mass ratio of the ash and the corona current is seen to be linear throughout the entire range of charging currents. There are two points on the graph which hold great significance, these are the points where the plotted line crosses the axis. First, the intersection of the charge to mass ratio axis where the corona current is zero gives the tribo charge level for the charge to mass ratio of the ash dispersed from the gun. Secondly, the intersect of the corona current axis where the charge to mass ratio equals zero gives the level of corona current required to cancel the tribo charge. These values were:

The Tribo Charge to Mass Ratio:

$$\underline{-1\times10^{-3}\ C/Kg}$$

The Corona Current required to zero the charge:

$$\underline{+20\times10^{-6}\ A}$$

To ensure that the ash laden air stream has a net charge of zero as it enters the test duct, the corona point of the powder feed gun should be energized to a positive potential, with the current set to $+20\times10^{-6}$ A.

6.2.7 ASH LOST FROM AIR STREAM

After the previous tests to measure the ash loads and the charging characteristics of the gun it was noticed that a considerable proportion of the ash had fallen out of the gas stream and was seen to accumulate on the base of the test duct.

It is known that the finer particles are better entrained in the gas stream than the larger. This can be seen by assuming that the air stream is neither accelerating nor decelerating and hence all the particles are entrained within the flow and all have a velocity relative to the gas flow of zero. So there are only

two velocity vectors to be considered in evaluating the motion of the particles within the rig. The first is simply their forward velocity, which is constant and equal to the velocity of the air stream. The second vector is their downward motion under the influence of gravity. It can be seen by equating the gravitational pull force to the viscous drag force (Stokes's law), that the larger particles will have a greater downward force acting upon them and will reach a greater downward velocity.

Stokes's law defines the viscous drag on a particle as:

$$F_d = 6\pi \eta a u \qquad \textbf{Equation (6.2.3)}$$

Where:

F_d = The drag force acting on the particle.
η = The viscosity of the medium through which the particle is passing.
a = The radius of the particle.
u = The velocity of the particle.

The gravitational force acting on the particle is defined as:

$$F_g = m g \qquad \textbf{Equation (6.2.4)}$$

Where:

F_g = The gravitational force on the particle.
m = The mass of the particle.
g = The gravitational pull, (≈ 9.81 N/m).

So the terminal velocity of the particle is reached when these two forces become equal:

If:

$$F_d = F_g \qquad \textbf{Equation (6.2.5)}$$

Then:

$$m\ g = 6\pi\ \eta\ a\ u \qquad \textbf{Equation (6.2.6)}$$

So:

$$u_{TERMINAL} = \frac{m\ g}{6\pi\ \eta\ a} \qquad \textbf{Equation (6.2.7)}$$

Since the mass of a particle is given by its density multiplied by its volume:

$$m = \rho\ \frac{4}{3}\ \pi\ a^3 \qquad \textbf{Equation (6.2.8)}$$

Where: ρ = The density of the particle.

Then:

$$u_{TERMINAL} = \frac{\rho\ \frac{4}{3}\ \pi\ a^3\ g}{6\ \pi\ \eta\ a} \qquad \textbf{Equation (6.2.9)}$$

Hence, $u_{TERMINAL}$ is proportional to a^2.

So the velocity of a particles falling under the influence of gravity is proportional to the square of the particle diameter, hence the larger the particle the faster it will fall.

For particles with a diameter greater than about 20 μm, 99% of its terminal velocity is reached within a few hundredths of a seconds.

6.2.7.1 DROP OUT ASH PARTICLE SIZE MEASUREMENT

A sample of the ash from the base of the rig was collected and fed through the dry powder feeder and a particle size distribution measurement made with the Malvern laser particle size analyzer. The histogram produced from this measurement along with the original dry fed sample of the 'New Ash' is shown in Figure (6.2.11).

It can be seen immediately from the shape of the histogram of the 'Drop out' sample that it was almost entirely made up of the larger particles, with the peak of the distribution coinciding with the peak due to the unburnt fuel in the original sample.

The fact that the largest of the particles have been lost from the air stream is not a great problem, as these large particles are predominantly the unburnt fuel and will play no part in the agglomeration process.

However, when measuring particle size distributions of the entrained ash from the down stream end of the test duct the loss of these large particles should be taken into account as the distribution will have been shifted towards the finer particles. Maybe even disguising a shift of the particle size distribution towards the larger particle sizes, an indication of successful agglomeration.

6.2.8 TOTAL ENTRAINMENT SYSTEM

The photograph in Plate (6.2.1) shows the entire ash feed system. The powder gun can be seen in the foreground, attached by three supports to the input duct. The flow straightener can also be seen at the far end of the input duct and the large unit standing on the floor is the powder feed hopper.

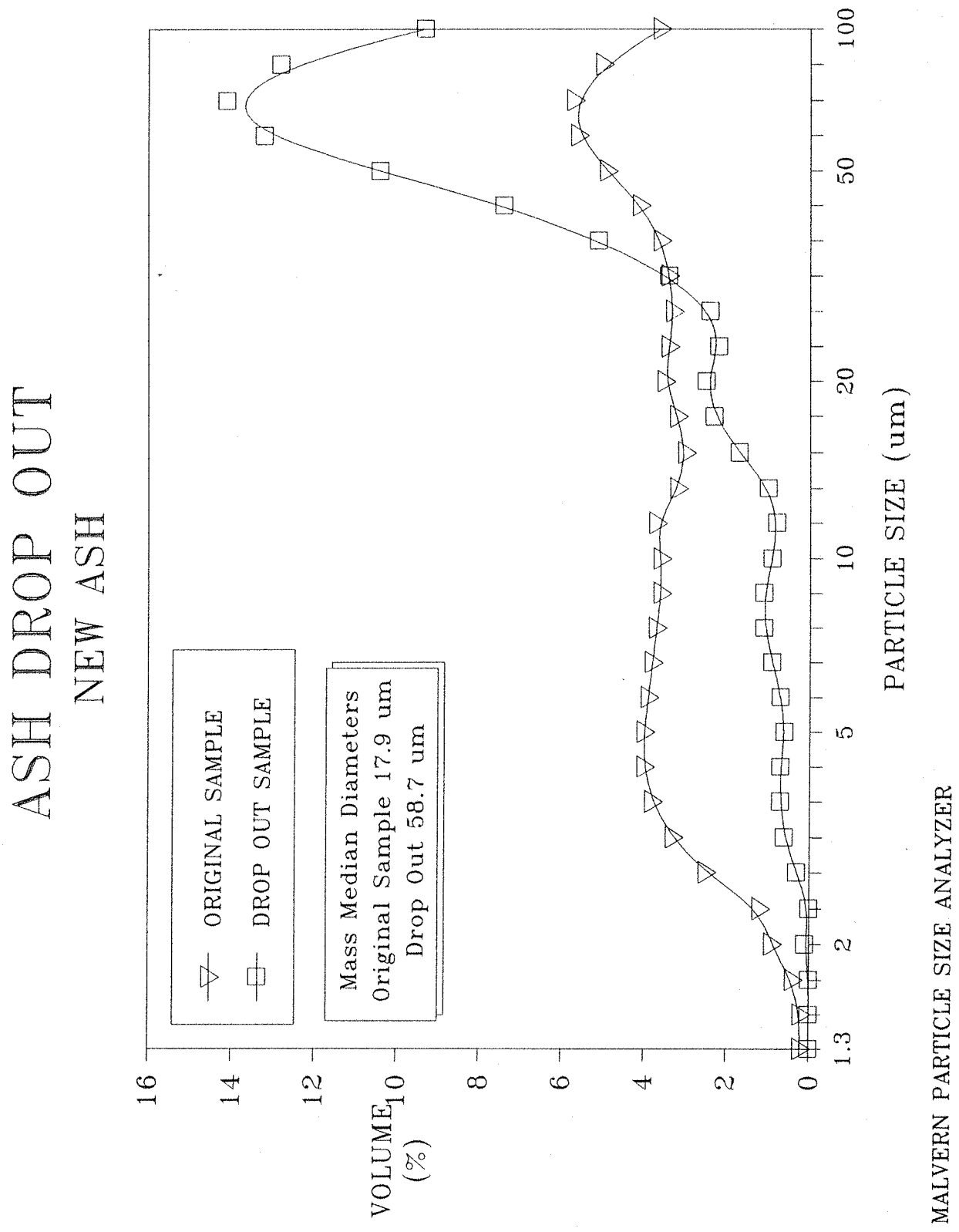

FIGURE 6.2.11 PARTICLE SIZE DISTRIBUTION OF THE ASH FOUND ON THE BASE OF THE TEST RIG

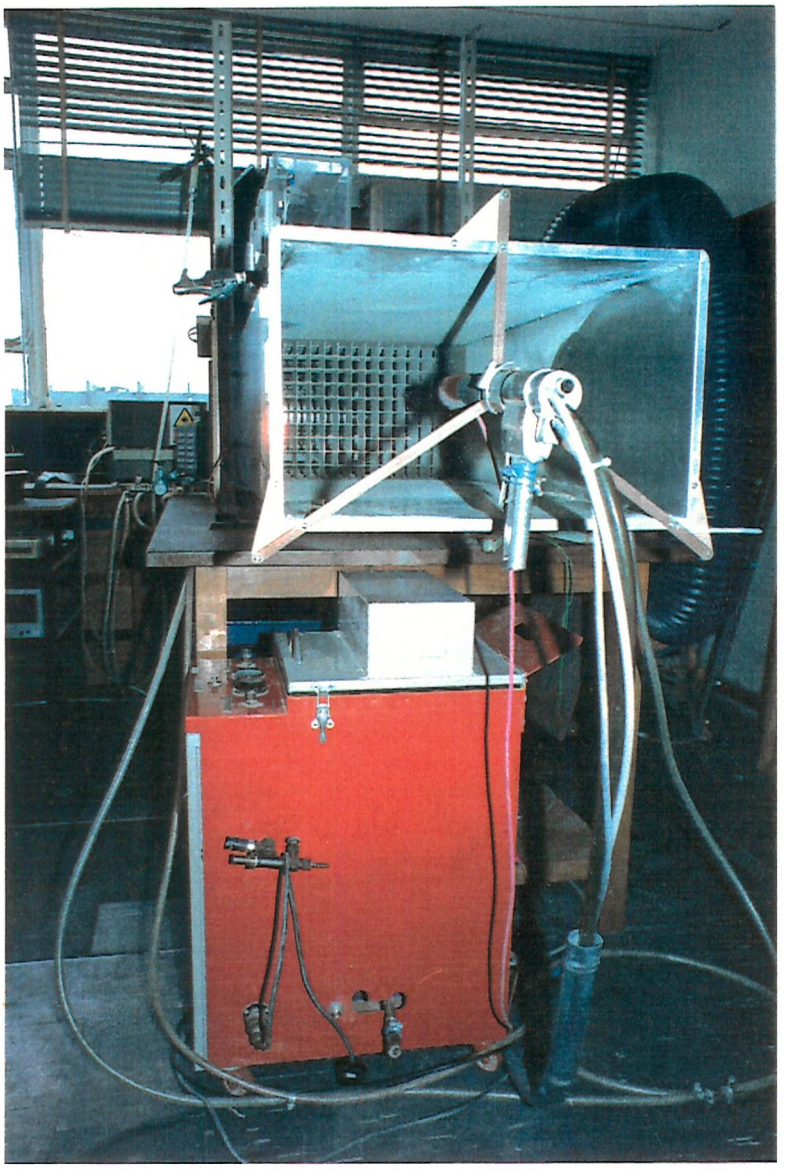

PLATE 6.2.1 ASH ENTRAINMENT SYSTEM

6.3 THE AGGLOMERATION RIG

The agglomeration test rig consisting of the adapted model electrostatic precipitator along with the modified ash feed system and flow straightener was now complete and ready for the charging, agglomeration and measuring systems to be added.

The different sections of the test rig can be seen in the illustration in Figure (6.3.1) and the entire system along with the instrumentation and power supplies used for the experimentation can be seen in Plate (6.3.1).

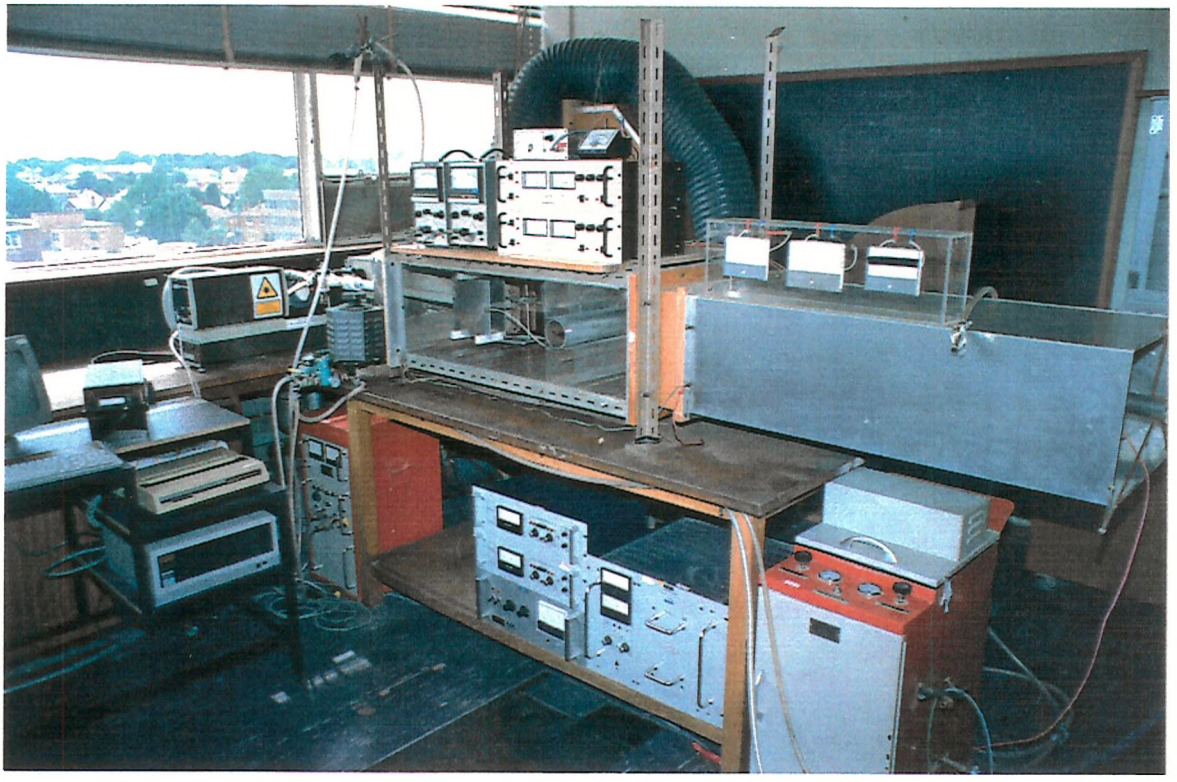

PLATE 6.3.1 AGGLOMERATION RIG

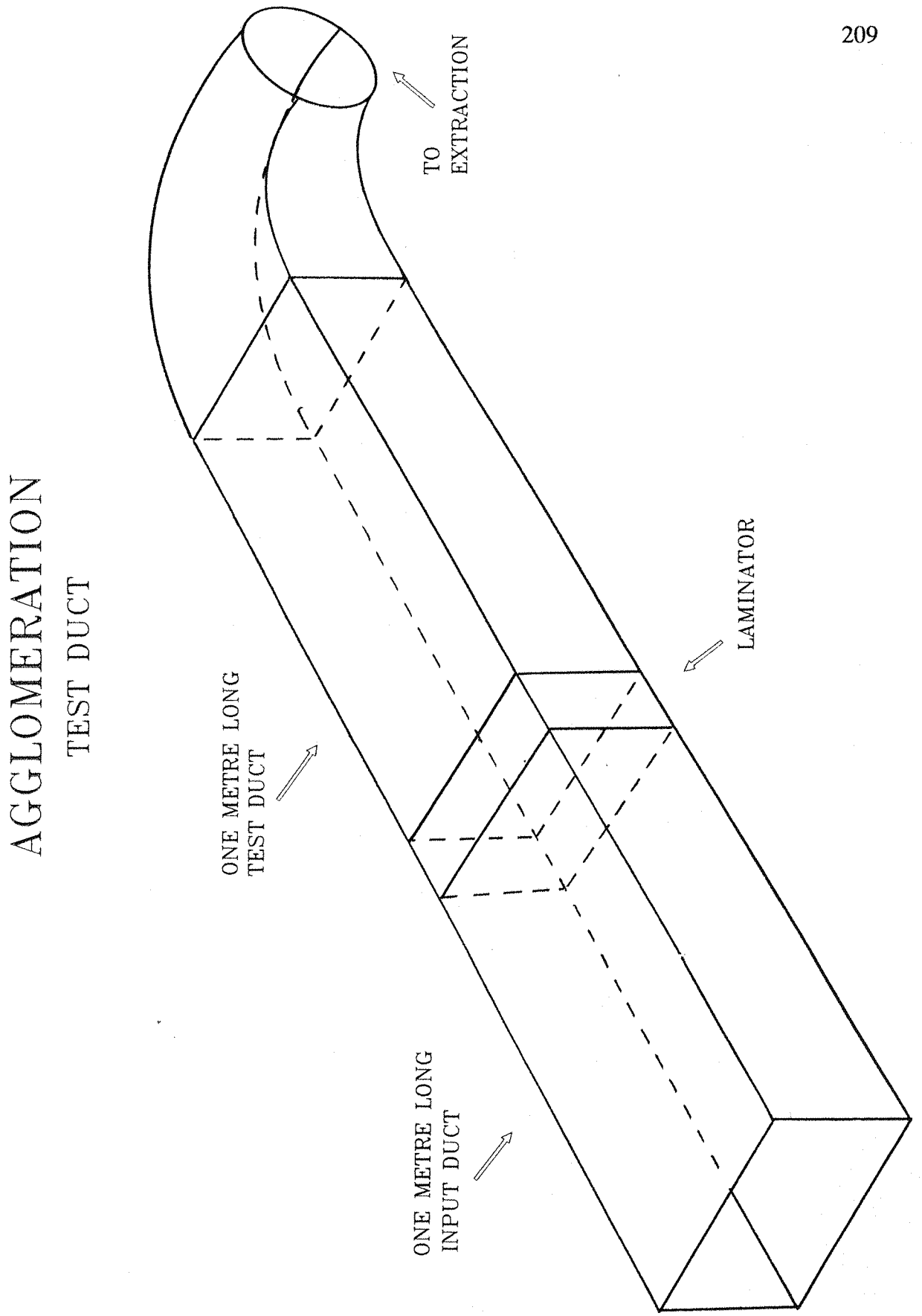

FIGURE 6.3.1 ILLUSTRATION OF THE AGGLOMERATION RIG SHOWING MAIN SECTIONS

CHAPTER SEVEN

BI-POLAR CHARGER

7.1 CHARGING SYSTEM REQUIREMENTS

The ash laden air stream from the powder feed system enters the test duct through the flow straightener. This stream now requires splitting into two separate streams, charging in opposite polarities and then recombining in such a way as to promote the formation of the agglomerates.

Several charging systems were designed to perform these tasks although only one of these proved effective and was further developed.

7.2 BI-POLAR CHARGER PHYSICAL DESCRIPTION

The bi-polar charger consisted of two double edged saw toothed electrodes measuring 500 mm long with 38 corona points along each side. Each of these electrodes were surrounded by a metallic box section mesh measuring 500 mm long by 100 mm wide and 100 mm tall. The mesh, constructed from wire with a spacing of 5 mm, was grounded so as to act as the intensifying electrode for the corona discharge. The spacing of 5 mm was chosen so as to allow the charged ash particles to pass through the mesh but to capture the free gas ions which have a higher electrical mobility than the ash particles, as they are so much smaller.

The two charging units were separated by a large central cylinder measuring 500 mm long and 100 mm in diameter. This cylinder not only functioned as a flow splitter in dividing the gas flow but was also designed to induce as much turbulence downstream of the chargers as possible, to promote

the turbulent mixing of the two gas streams.

This bi-polar charger is illustrated in Figure (7.2.1) and is also shown in Plate (7.2.1), which shows the charging unit in location within the test duct, just down stream of the box section flow straightener.

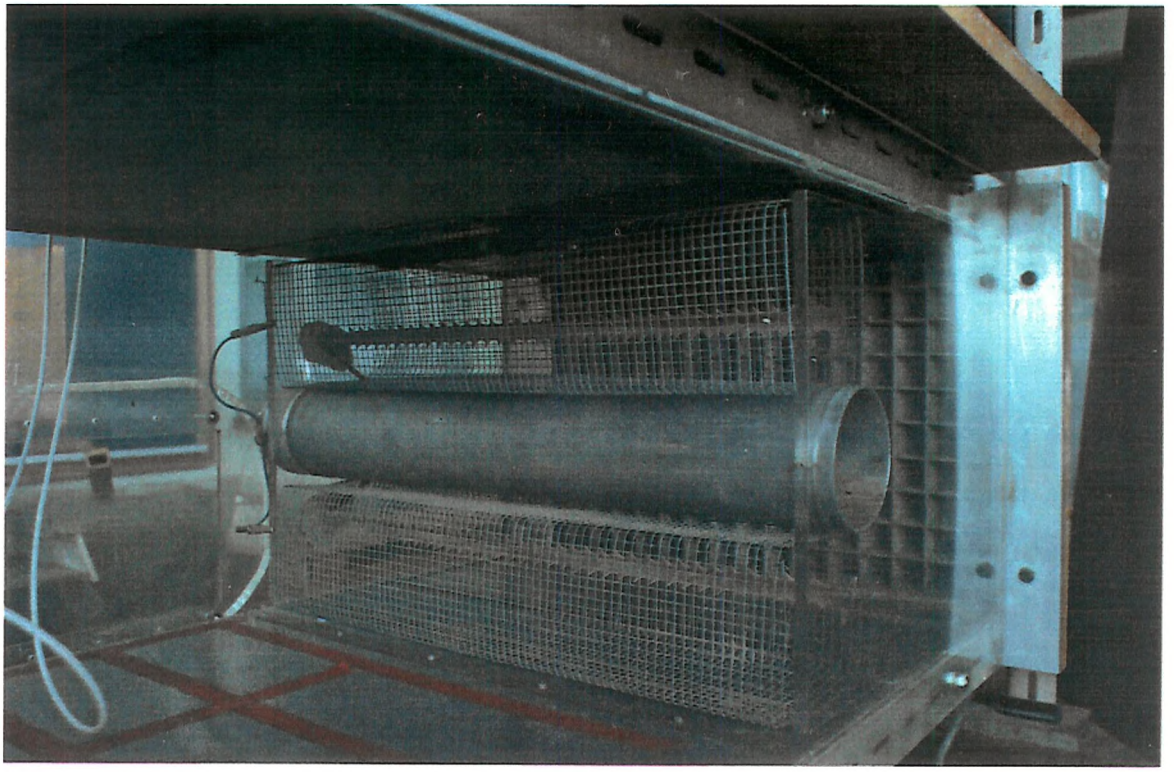

PLATE 7.2.1 BI-POLAR CHARGER

The illustration in Figure (7.2.1) shows a cross sectional view of the bi-polar charger, with the discharge electrodes drawn as a 'V' shape. The electrodes were in fact bent along their central axis in order to optimise the flux within the charging region. The exact design of the electrode system and the angle of the bend was determined through the use of a field simulation computer package. The photograph in Plate (7.2.1) also shows the angled discharge electrodes.

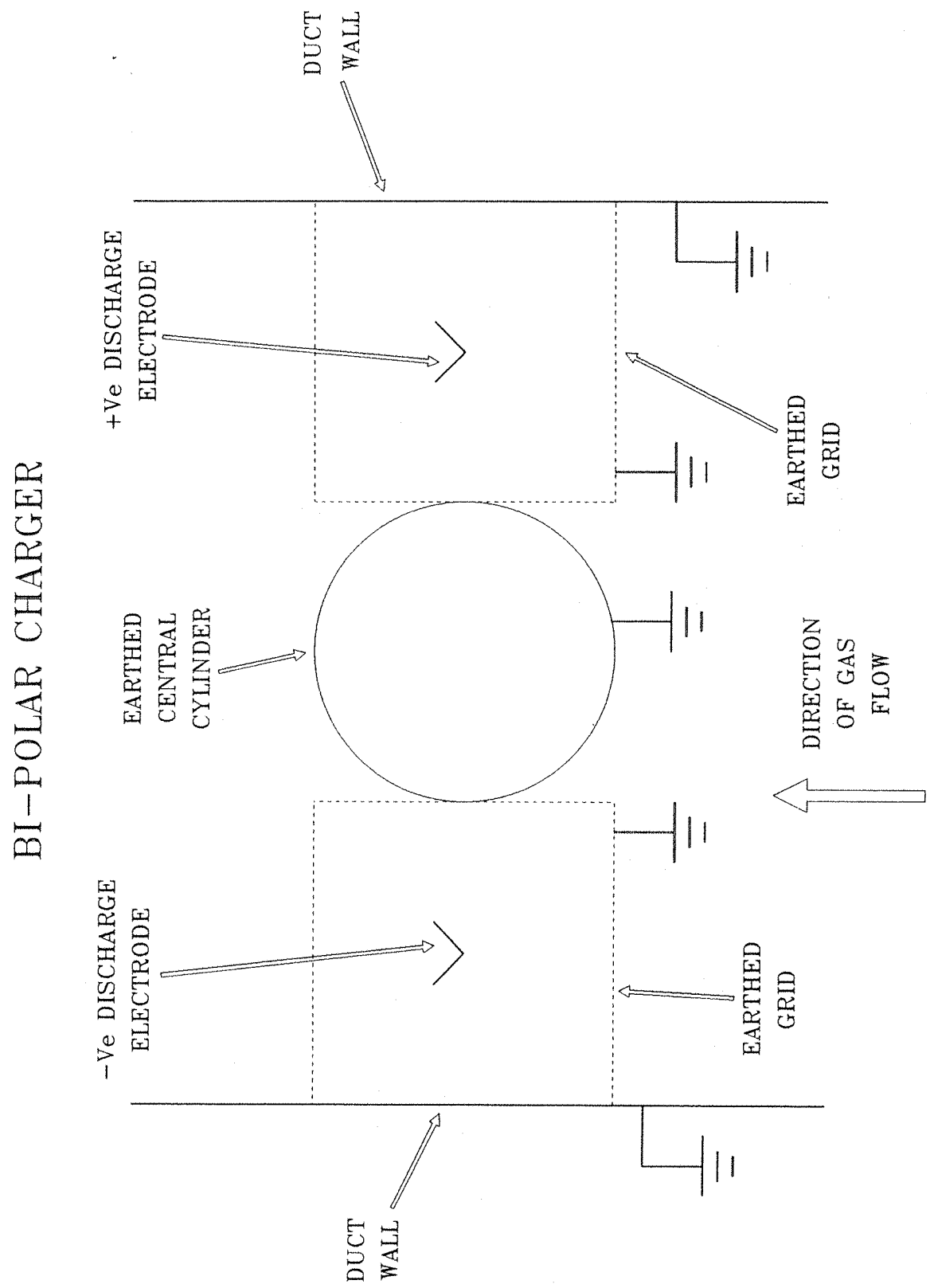

FIGURE 7.2.1 BI-POLAR CHARGER
DETAILING ANGULAR DISCHARGE ELECTRODES

7.3 TUBES AND SLICES

In order to optimise the charging system a two dimensional field calculating package was used to determine the form of the electric field within the individual charging units[ref 7.1]. This system, as described in Chapter four, generates a solution to Laplace's equation in two dimensions for any fixed geometry.

The field plots produced are for the electrodes just prior to going into corona, as the space charge due to the ions generated by the corona discharge could not be included in the computer model. However, if we consider the ion generation process, as discussed in Chapter three, to occur at the corona points, then as the gas ions generated follow the field lines from the points to the grid we can determine if there is a section of the charging unit through which the ash particles can pass without passing through the ion flux.

In all the plots produced from the computer system, the black lines represent the field lines and the grey lines represent the lines of equipotential.

7.3.1 FIELD INTENSIFICATION

The first two geometries considered on the computer system were two cross sectional views of one of the 'saw tooth' discharge electrodes. The first shown in Figure (7.3.1), is of a 50 mm section of the electrode. In the computer simulation the electrode's curved corona points have been drawn as triangular points. This was due to the limit of the number of points that were available to define the electrode surface within the package. The second geometry to be considered is the same as the first but this time the scale is such that the detail of only one corona point of the electrode is defined, this plot is shown in Figure (7.3.2).

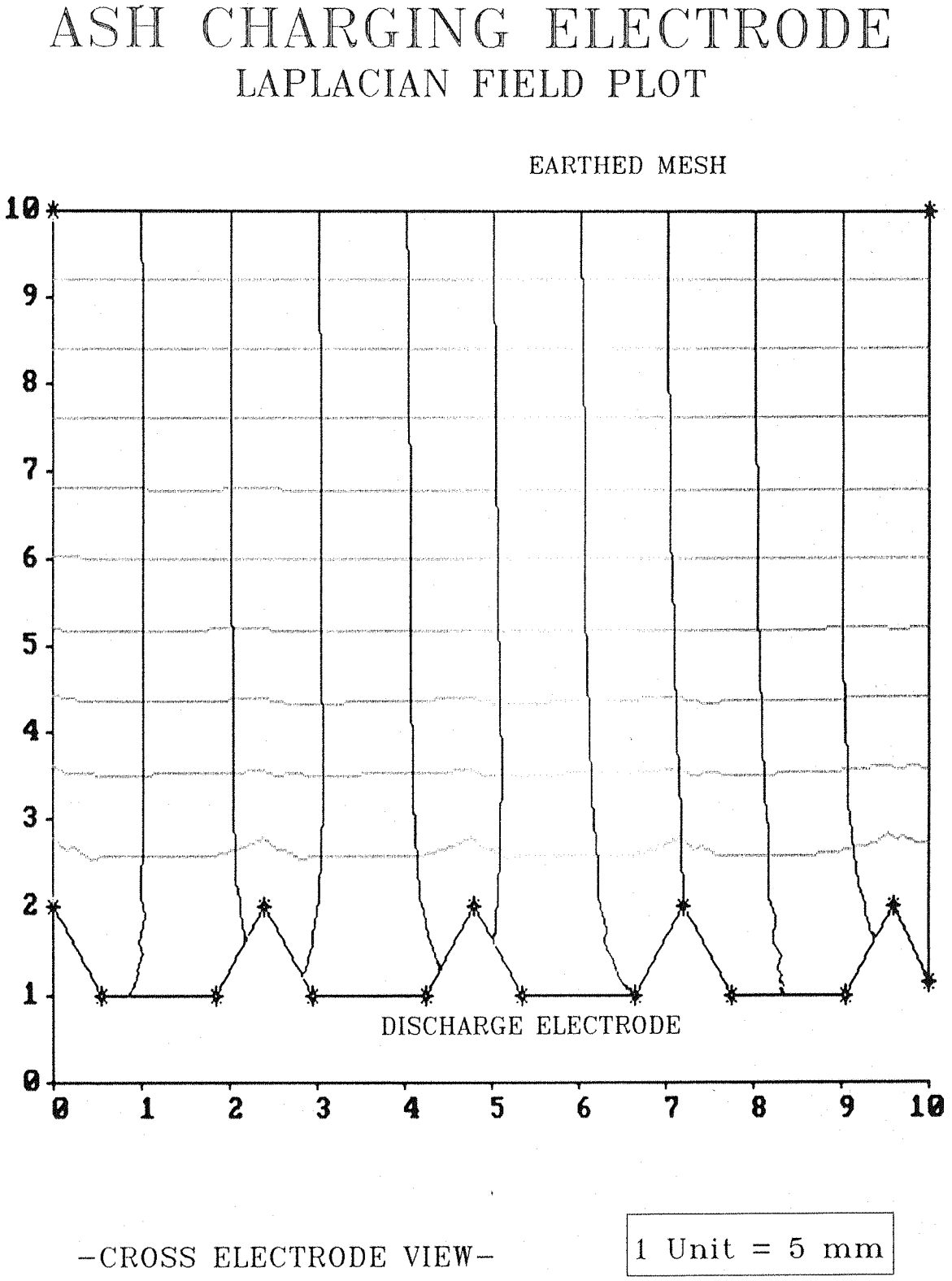

FIGURE 7.3.1 TAS FIELD ANALYSIS PLOT OF A 50 mm SECTION OF THE 'SAW TOOTH' DISCHARGE ELECTRODE.

ASH CHARGING ELECTRODE
LAPLACIAN FIELD PLOT

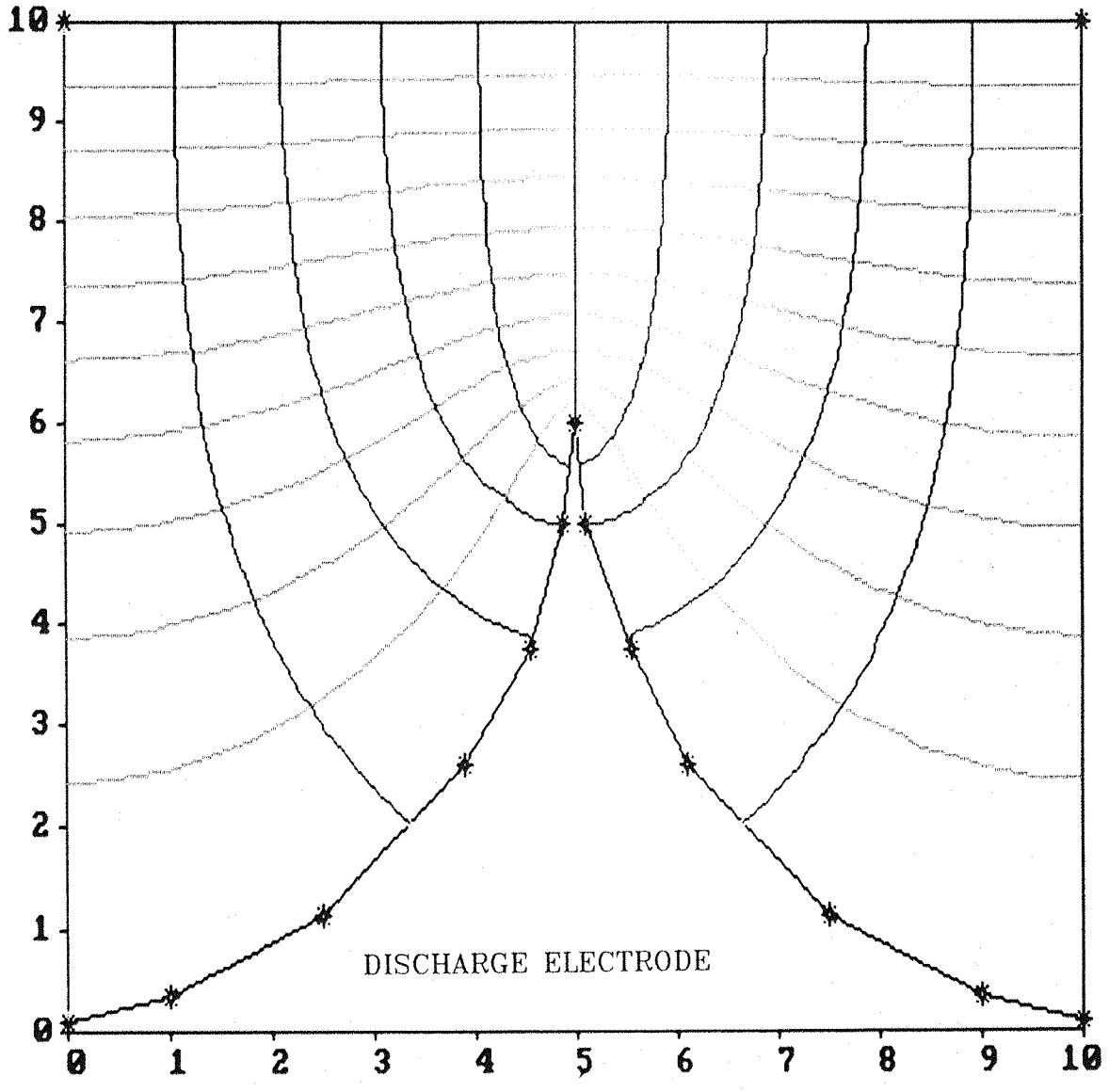

-DETAIL OF THE FIELD DISTRIBUTION-
-AT THE CORONA POINT-

1 Unit = 1 mm

FIGURE 7.3.2 TAS FIELD ANALYSIS PLOT OF A SINGLE 'SAW TOOTH' DISCHARGE POINT.

7.3.2 FIELD INTENSIFICATION RESULTS

The first plot, Figure (7.3.1), of the 50 mm section of the 'saw tooth' discharge electrode, also shows the grid which acts as the opposite electrode for the corona. The field line and equipotential line distribution is very much as would be expected, showing that in this plane the field is fairly uniform across the entire width of the electrode. However, the cross section of the field across the electrode would produce the characteristic corona inducing field intensification, seen in Chapter Two.

The second plot, Figure (7.3.2), detailing the field intensification around a single corona point of the 'saw tooth' electrode, shows the area of greatest intensification to be at the very tip of the point. It is at this point of maximum field intensification that the corona discharge will occur.

7.3.3 CHARGE OPTIMIZATION

In order to optimise the charge on the ash it would be best if all the ash passed through the region of greatest flux. i.e. the region through which the gas ions pass as they move away from the corona point and towards the grounded mesh electrode. Hence the discharge electrodes must be designed such that all the ash passes through this region. However, should the 'ion wind' produced by the corona oppose the gas flow, then as an ash particle enters this region of opposing flow its forward velocity will be greatly reduced. Depending on the momentum of the particle, (i.e. its size), it may be stopped by this wind or even have its direction of flow reversed. This has been found to result in the precipitation of the finest of the ash particles onto the upstream end of the earthed mesh surrounding the discharge electrode. This deposition is undesirable as the layer of insulating particles may go into back ionization under the influence of the incoming gas ions and greatly reduce the charging efficiency of the charging unit. Also a reduction of the number of finer particles from the ash laden gas stream will impair the ability of the monitoring systems to detect the reduction of these fine particles through the agglomeration process.

In order to determine the optimum angle to which the discharge electrodes should be bent, five simulations were carried out at different angles

and orientations of the discharge electrode. The generated Laplacian field plots are illustrated in Figures (7.3.3) to (7.3.7).

7.3.4 ELECTRODE ANGLE OPTIMIZATION

The first Laplacian field plot of this series, shown in Figure (7.3.3), was produced with the discharge electrode drawn straight and aligned parallel to the gas flow. In this case the gas ions generated at the down stream corona points of the discharge electrode will migrate in the same direction as the gas flow, from the corona point towards the mesh electrode. From the plot produced it can be seen that the field lines from the point to the mesh, which the gas ions follow, do not cover the entire 100 mm width of the charging unit. So it would be possible for the ash particles to pass either side of the high flux region and enter the test duct without being sufficiently charged. The up stream corona points of the discharge electrode will produce an ion wind opposing the ash laden gas flow, unless these tips are capped with an insulator to stop them going into corona. This ion wind will oppose the flow of the incoming ash particles and slow them sufficiently for the finest of the particles to deposit on the grounded mesh. These deposited layers of ash may result in the associated charge reducing back ionization.

The second plot, Figure (7.3.4), was also drawn with the discharge electrode straight, although in this case it has been drawn perpendicular to the gas flow. All the ash within the gas flow will have to pass through the high flux regions at either end of the corona discharge electrode hence no ash can escape becoming charged. However, both ends of the discharge electrode will produce an ion wind that is perpendicular to the gas flow and towards the up stream end of the electrode the ion wind will again cause the precipitation of the finer ash particles. So this arrangement, although ideal for charging the entire ash sample will suffer from back ionization from the deposited fine particles.

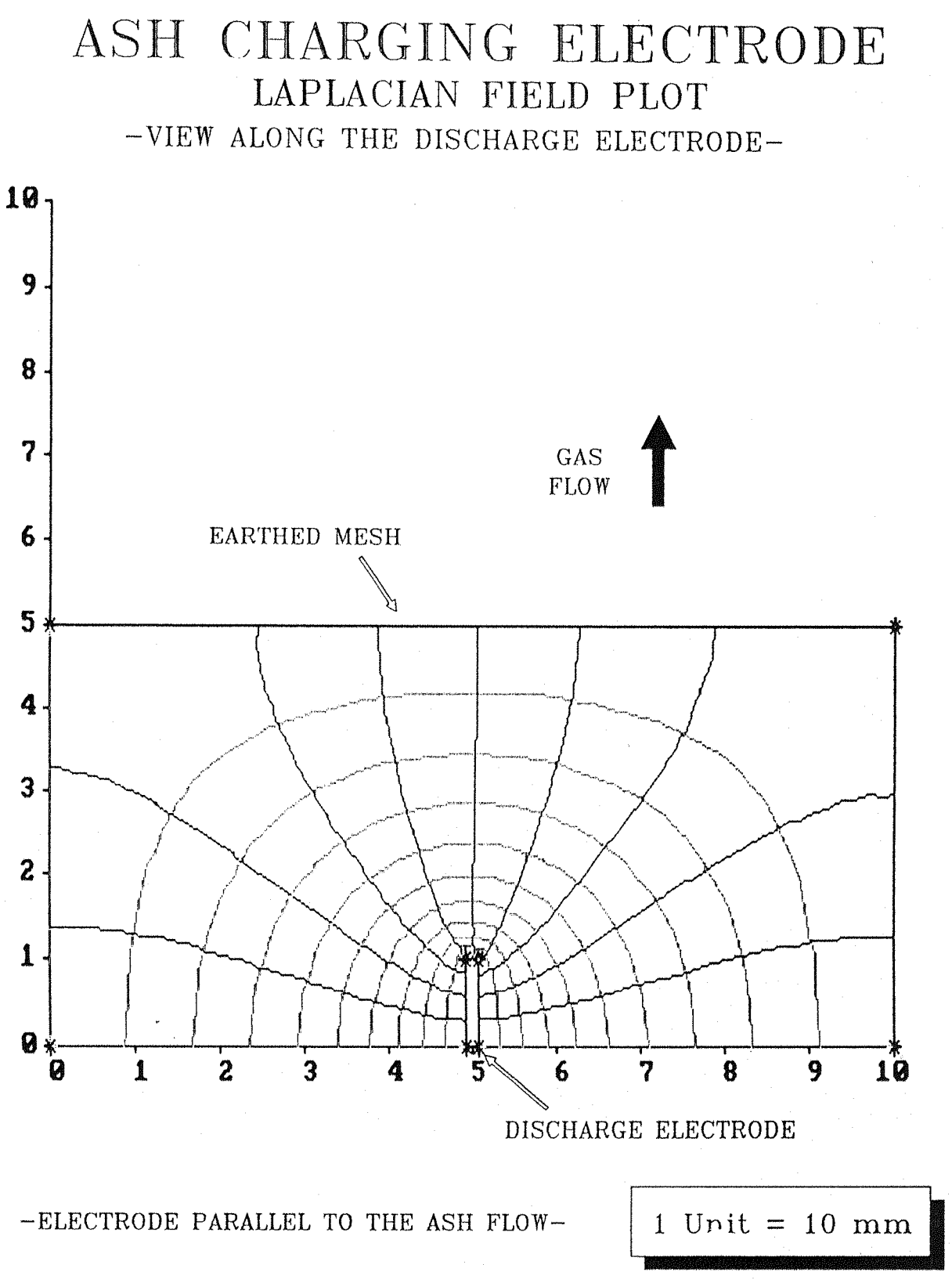

FIGURE 7.3.3 TAS FIELD ANALYSIS PLOT SHOWING THE DISCHARGE ELECTRODE STRAIGHT AND PARALLEL TO THE GAS FLOW

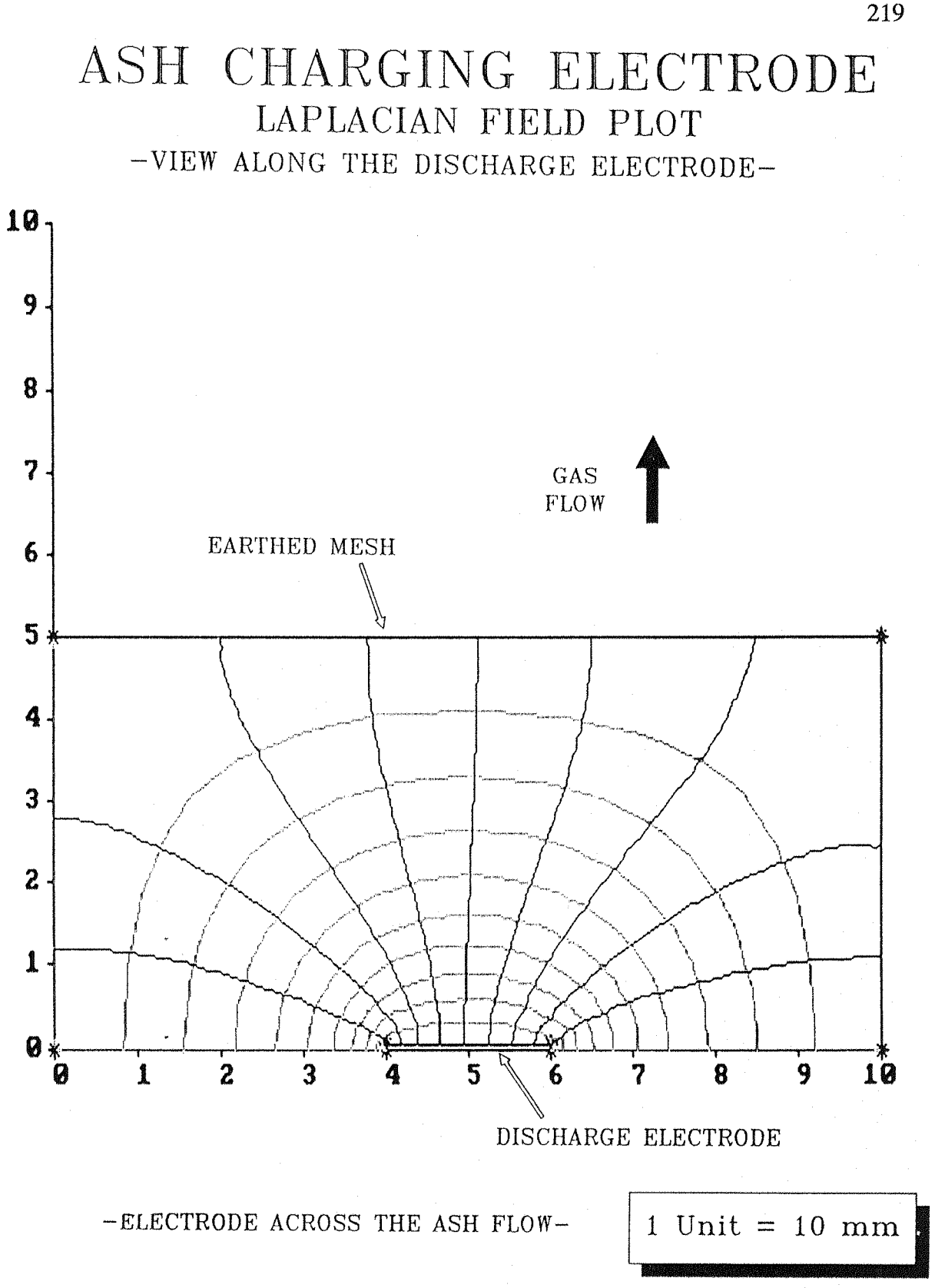

FIGURE 7.3.4 TAS FIELD ANALYSIS PLOT SHOWING THE DISCHARGE ELECTRODE STRAIGHT AND PERPENDICULAR TO THE GAS FLOW

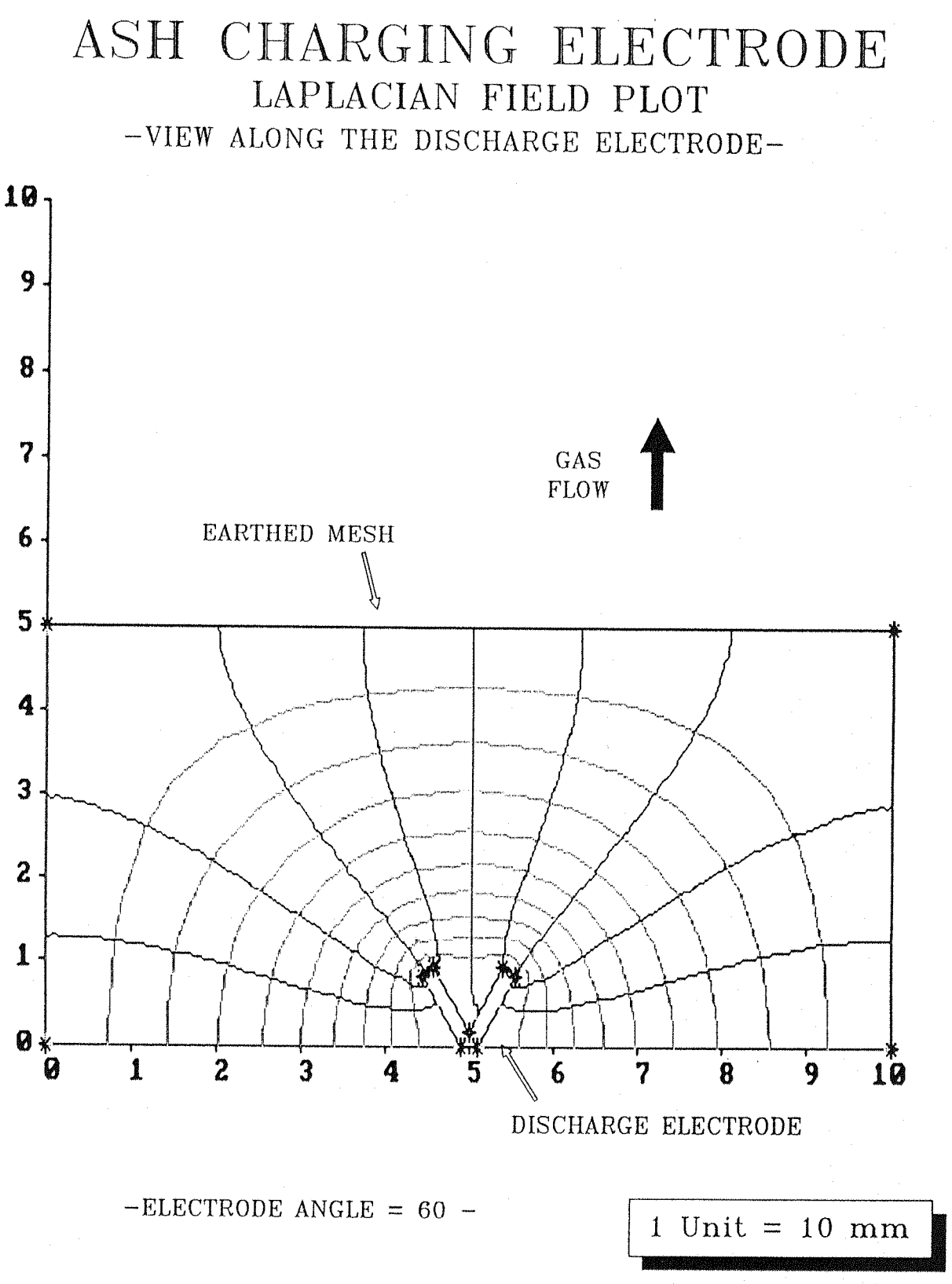

FIGURE 7.3.5 **TAS FIELD ANALYSIS PLOT SHOWING THE DISCHARGE ELECTRODE BENT TO AN ANGLE OF 60°**

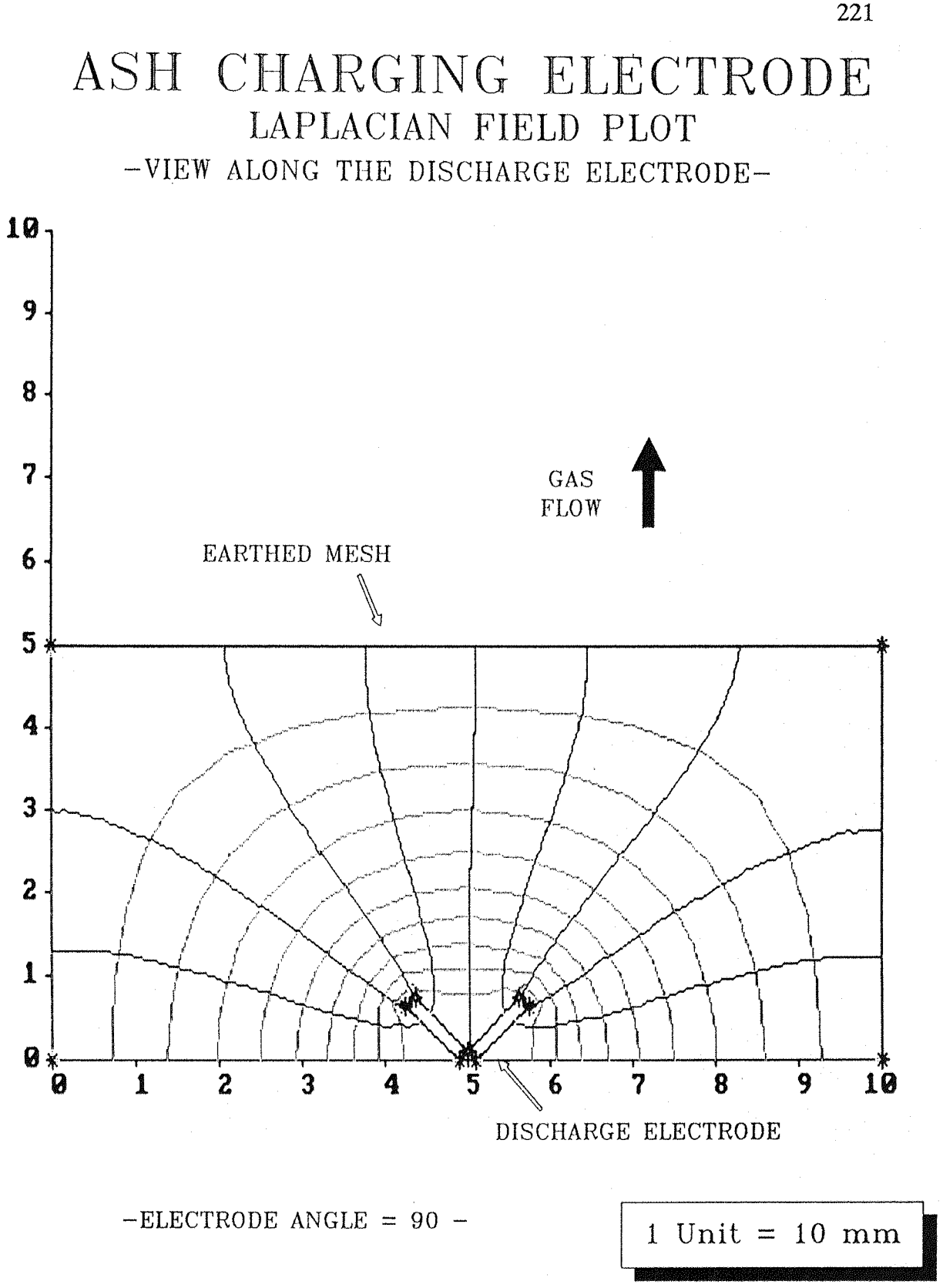

FIGURE 7.3.6 **TAS FIELD ANALYSIS PLOT SHOWING THE DISCHARGE ELECTRODE BENT TO AN ANGLE OF 90°**

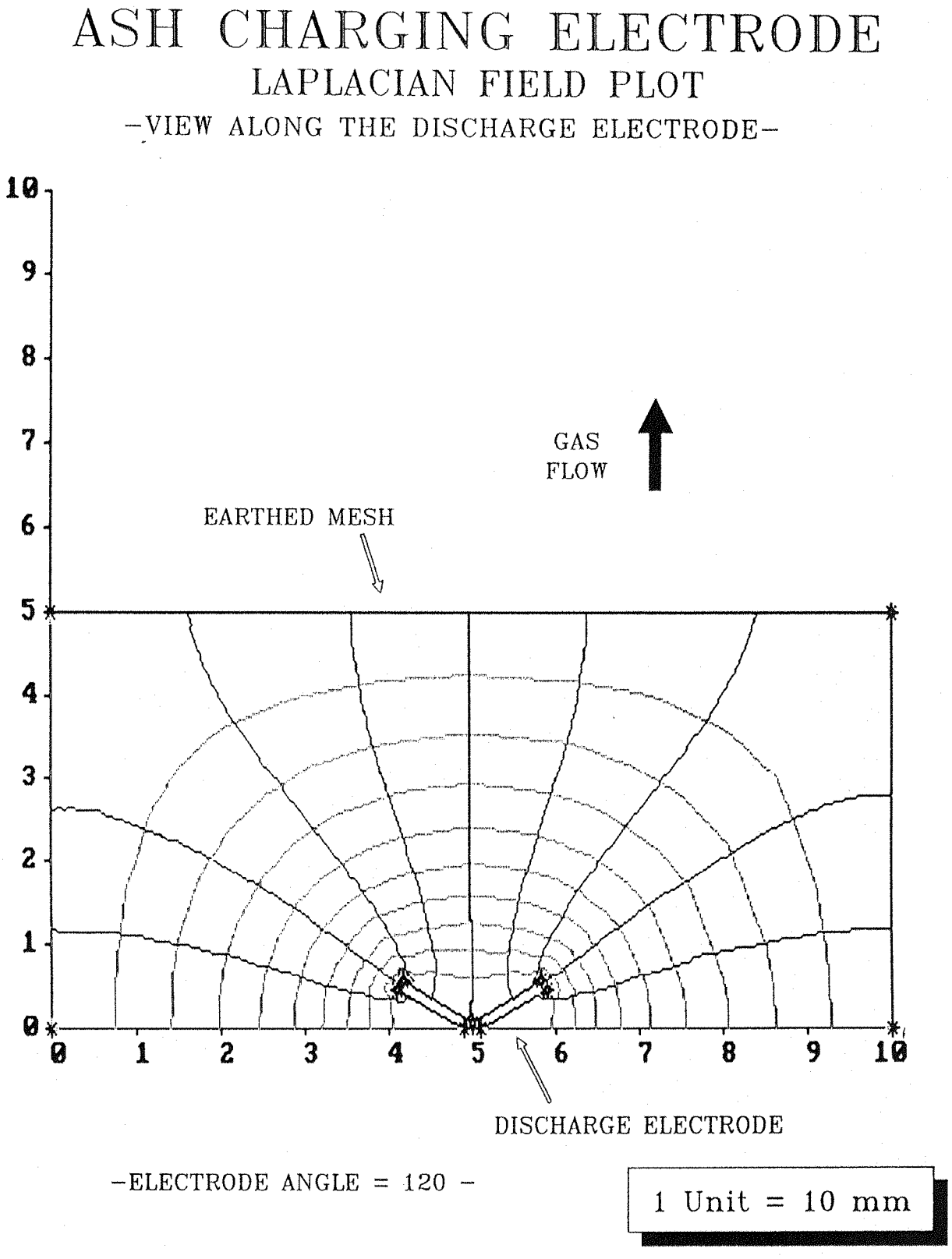

FIGURE 7.3.7 **TAS FIELD ANALYSIS PLOT SHOWING THE DISCHARGE ELECTRODE BENT TO AN ANGLE OF 120°**

Figures (7.3.5), (7.3.6) and (7.3.7) illustrate the Laplacian field line distributions that were generated with the discharge electrode bent to angles of 60^{O}, 90^{O} and 120^{O} respectively. All three of these arrangements are seen to have the desired effects of a high flux region extending across the entire width of the charging unit, while avoiding excessive ion-winds in opposition to the ash laden gas flow. It was felt that with the discharge electrode bent to an angle of 60^{O} the two corona generating ends of the electrode would become too close and the corona on one side may act to extinguish the corona on the other. Hence requiring greater voltages to be applied to the electrode to generate a uniform corona. The 120^{O} angle bend in the discharge electrode may have still resulted in a sufficient ion wind to deposit the very finest of the ash particles. So it was decided to set the electrodes within the bi-polar charger to 90^{O}.

7.4 CORONA DISCHARGE

7.4.1 CURRENT / VOLTAGE RELATIONSHIP

The voltage/current relationship for both of the discharge electrodes were measured in order to ensure that both were adequately going into corona and that the two had similar characteristics.

The first test was to energise each electrode in turn and measure the current drawn from the power supply as a function of the voltage applied to the electrode. This test was performed for both the positive and the negative polarities, on each electrode. The results of this test are given in Table (7.4.1) and the graph of the relationships plotted in Figure (7.4.1).

7.4.1.1 DISCHARGE RESULTS

All four of the graphs produced show the characteristic corona discharge current/voltage relationship with no current being drawn until the corona threshold voltage, after which the relationship becomes linear.

APPLIED VOLTAGE	CURRENT DRAWN			
(KV)	($A \times 10^{-3}$)			
	TOP ELECTRODE		BOTTOM ELECTRODE	
	-Ve	+Ve	-Ve	+Ve
0	0	0	0	0
2	0	0	0	0
4	0	0	0	0
6	0	0	0	0
7	0	0	0	0
8	0.01	0	0	0
9	0.025	0.015	0.030	0
10	0.065	0.045	0.065	0.030
11	-----	0.090	-----	0.080
12	0.165	0.135	0.170	0.140
14	0.270	0.255	0.290	0.275
16	0.390	0.385	0.410	0.390

TABLE 7.4.1 CORONA ELECTRODES CURRENT / VOLTAGE CHARACTERISTICS

For the bi-polar charger all four of the tests produced very similar results. All the 'turn on' voltages were between 7 KV and 9 KV, with the negative corona onset about 1 KV lower than the positive in both cases. The 'corner' was not sharp, as the discharge electrodes have many corona points, all of which do not come on at the same applied voltage. The slopes of the linear portion of the graphs plotted, were all about equal for all four of the tests and if expressed as a resistance by Ohm's law, the value of the slope is 33 MΩ.

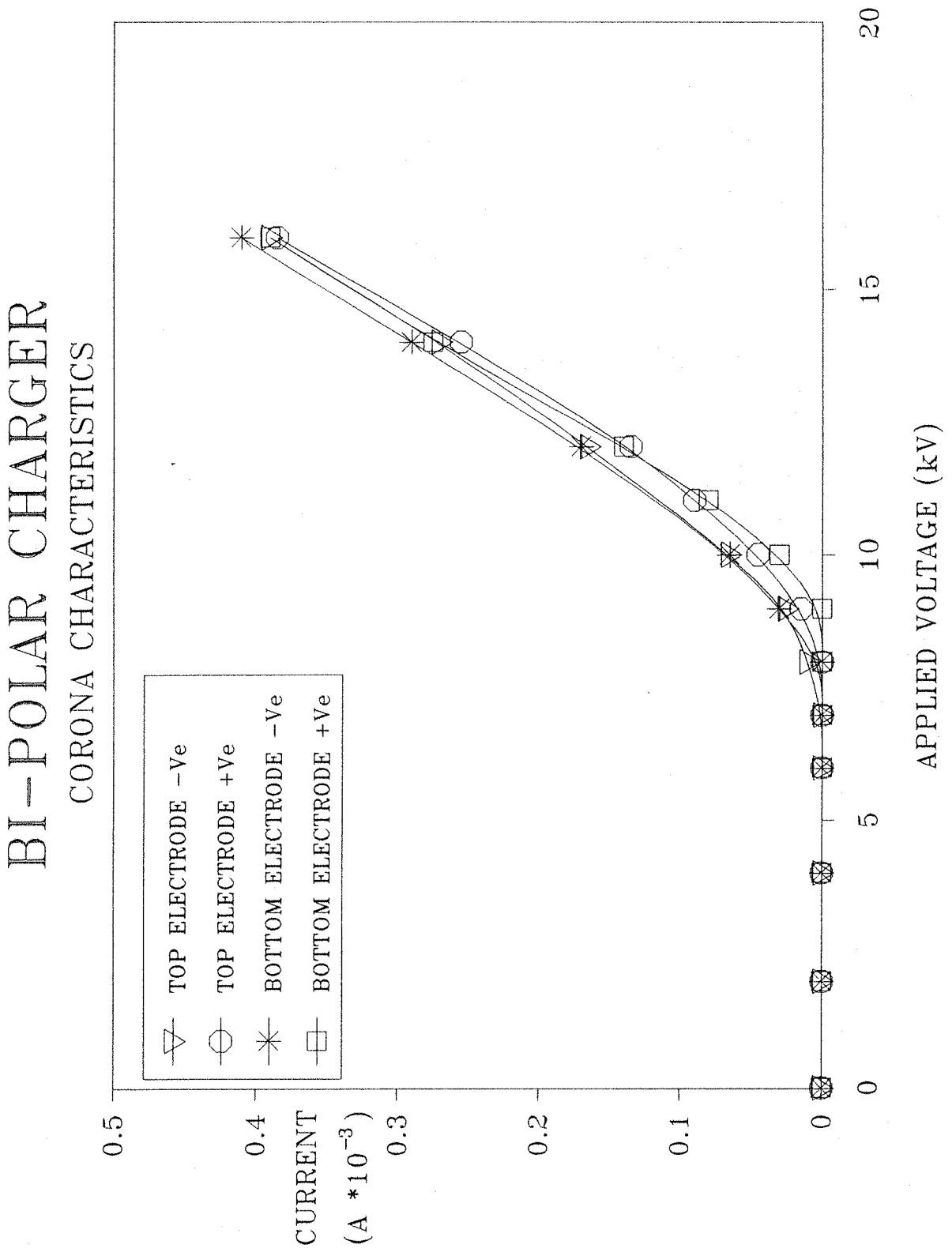

FIGURE 7.4.1 CORONA ELECTRODES CURRENT / VOLTAGE CHARACTERISTICS

As both the top and the bottom discharge electrodes produced similar characteristics for both the positive and negative potential, it was not important which was used for which potential. In fact the top electrode was set to a positive potential and the bottom to the negative.

7.4.2 ELECTRODE INTERDEPENDENCE

It was important that the no gas ions from one discharge could reach the charging zone of the opposite polarity, as these ions will then act to reduce the charge on the ash from the opposing unit. The grounded conducting meshes surrounding the discharge electrodes should have been adequate to capture all the free ions. However, this was checked by connecting each electrode in turn to an ammeter and recording the ionic current arriving at the electrode while the opposite charging unit was energised into corona. In both cases a very small amount of charge was registered as reaching the electrode, although this could have simply been capacitive linking between the two units. The actual level of current recorded was insignificant when compared to the level of the corona current.

7.4.3 EFFECT ON CORONA OF ASH LOAD

The entire system was turned on and allowed to run for some minutes, this was to allow for any deposition of the ash onto the discharge electrodes to occur. The voltage current relationship for each of the electrodes was then re-measured while the ash load was still running in order to determine the effects an ash load and dirty discharge electrodes were having on the bi-polar chargers ability to generate the required corona current. The results of these tests are given in Table (7.4.2) and the graph of the data is plotted in Figure (7.4.2).

7.4.3.1 DISCHARGE RESULTS WITH ASH LOAD

The graphs plotted in Figure (7.4.2), show that the ash load and the deposition of the ash onto the discharge electrodes had only a very small effect on the voltage/current relationship of the discharge electrodes.

APPLIED VOLTAGE	CURRENT DRAWN			
(KV)	($A \times 10^{-3}$)			
	TOP ELECTRODE +Ve		BOTTOM ELECTRODE -Ve	
	CLEAN	WITH ASH	CLEAN	WITH ASH
0	0	0	0	0
2	0	0	0	0
4	0	0	0	0
6	0	0	0	0
7	0	0.005	0	0.005
8	0	0.025	0	0.015
9	0.015	0.055	0.030	0.045
10	0.045	0.105	0.065	0.085
11	0.090	0.140	-----	0.115
12	0.135	-----	0.170	-----
14	0.255	0.225	0.290	0.215
16	0.385	-----	0.410	-----

TABLE 7.4.2 CORONA ELECTRODES
CURRENT / VOLTAGE CHARACTERISTICS
WITH AND WITHOUT THE ASH LOAD

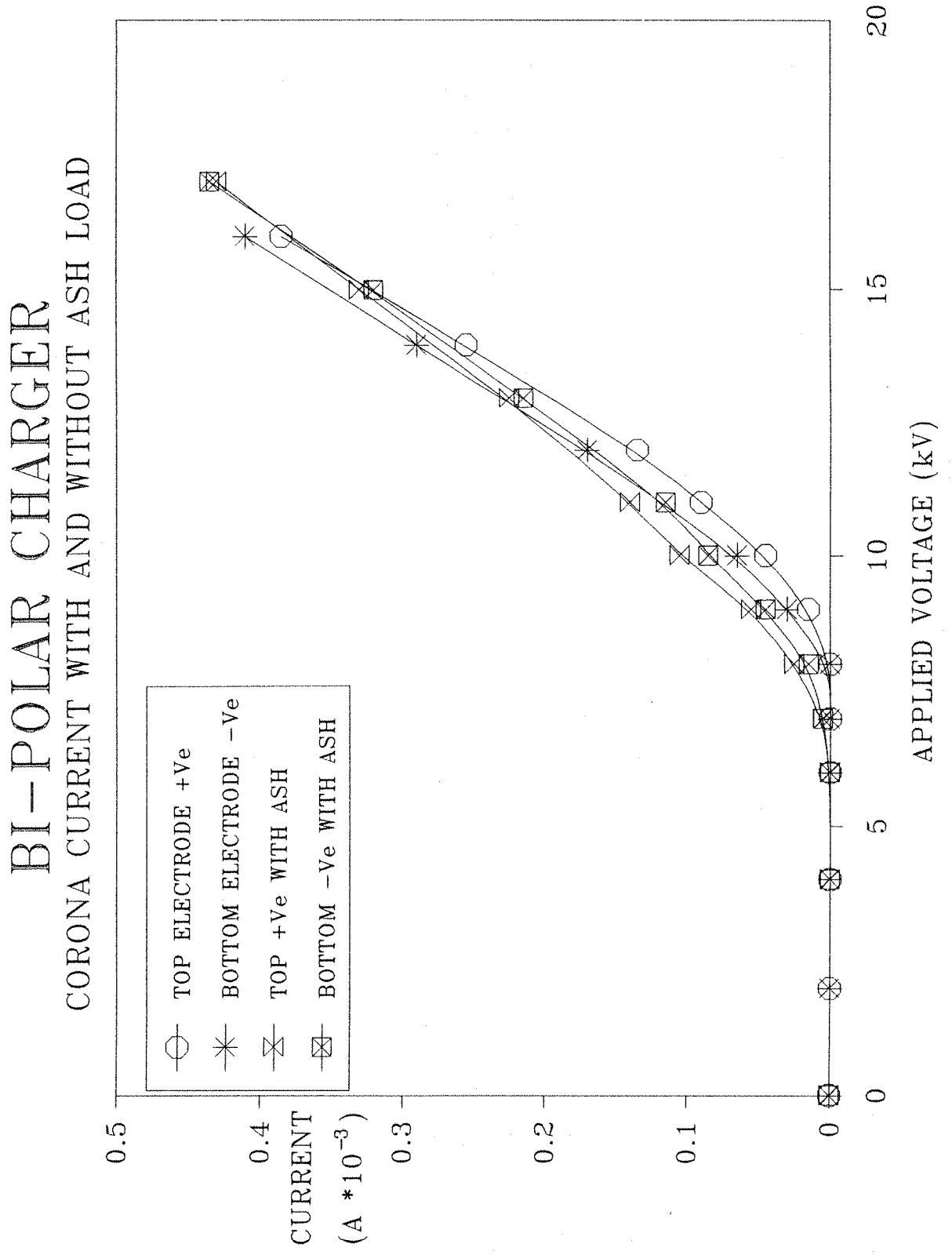

FIGURE 7.4.2 CORONA ELECTRODES CURRENT / VOLTAGE CHARACTERISTICS SHOWING THE EFFECTS OF THE ASH LOAD

At the lower voltages, just greater than the on-set voltage of the corona, the current measured with the ash load is marginally greater than without the ash being present. This could have been due to the gas ions generated by the corona becoming attached to the ash particle and being carried away down stream in the gas flow. Hence reducing the quenching effect the space charge produced by the ion flux has on the corona.

At higher potentials the slope of the linear portion of the corona curve was found to be less when the ash load was turned on. This is equivalent to a greater resistance and would be due to the build up of insulating ash particles on the corona points.

7.4.4 THE CORONA

Plate (7.4.1) shows a photograph of the bi-polar charger taken in a darkroom using a long exposure. The top electrode is the positive corona and the bottom electrode is the negative corona. In both cases the corona current was set to 3×10^{-3} Amps.

The differences seen in the photograph are due to the different reactions occurring within the corona region, as were detailed in Chapter three. The positive corona was found to be far less stable than the negative corona and was heard to make a great deal more noise than the negative. The increased light emitted from the positive corona was due to a greater number of collisions resulting in the emission of a quantum of light. In both cases the light emitted was a purple colour, this colour is dependent on the electron energy band structure of the gas molecules being ionized within the corona.

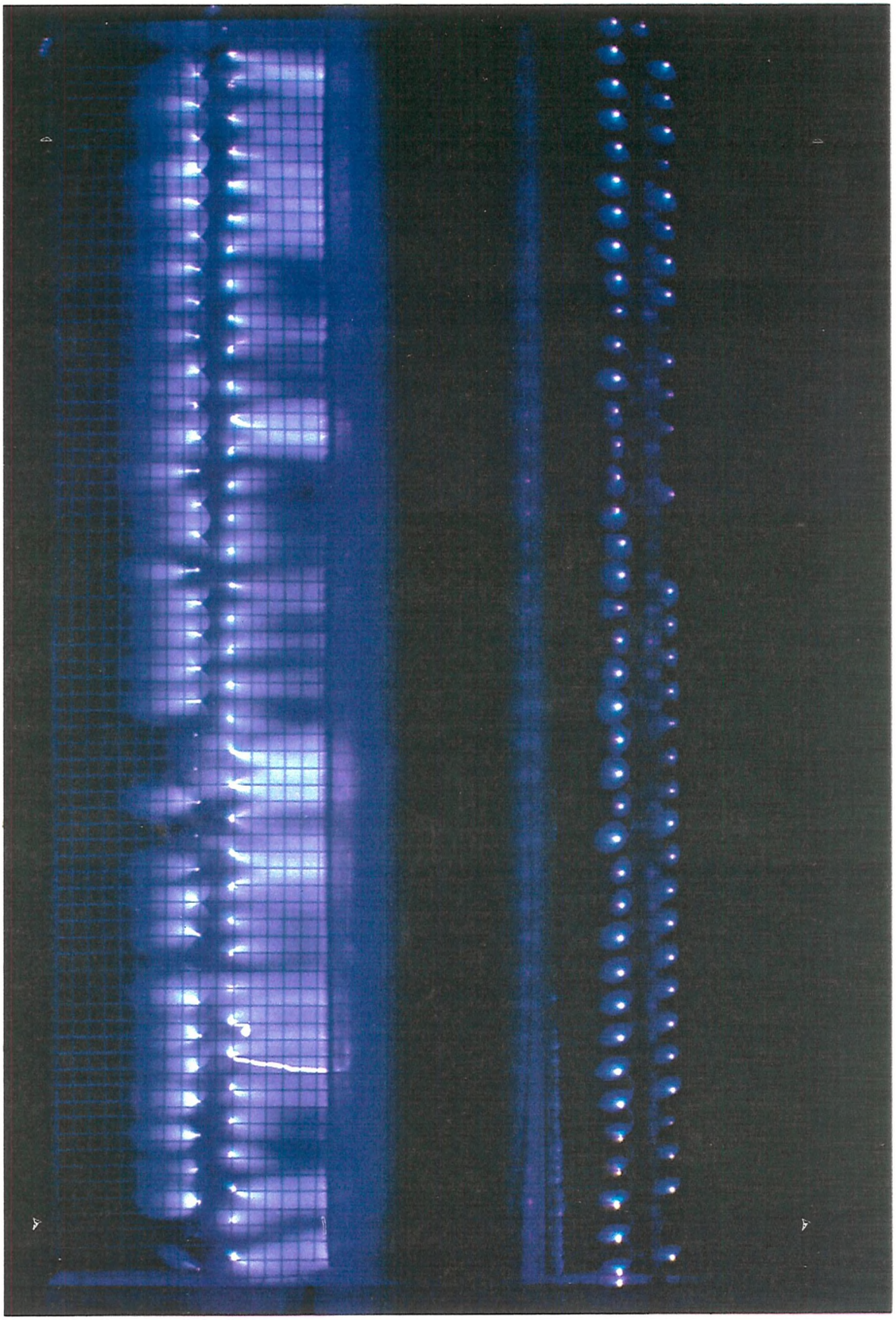

PLATE 7.4.1 BI-POLAR CHARGER IN CORONA

7.5 CHARGE TO MASS RATIO

7.5.1 THEORETICAL CALCULATIONS

In Chapter three the relationship between the theoretical maximum charge that can be deposited onto a particle through the corona charging process, and its radius was discussed. This maximum charge level was defined by the Pauthenier equation as:

$$q_{max} = 4\pi\ \varepsilon_o\ a^2\ p\ E \qquad \textbf{Equation (7.5.1)}$$

$$also\ p = \frac{3\ \varepsilon_r}{(\varepsilon_r + 2)} \qquad \textbf{Equation (7.5.2)}$$

Where:
- q_{max} = The maximum charge for the particle.
- E = The applied field strength.
- a = The particle radius.
- ε_o = The permittivity of free space.
- ε_r = The relative permittivity.

The maximum charge that can be generated on the particle is thus proportional to the square of the particle diameter. Hence the Pauthenier equation can be solved for the ash samples, as their particle size distributions are known.

Firstly we must calculate the relative permittivity 'ε_r', in order to be able to calculate 'p', the conductivity component of equation (7.5.1). This can be found by solving equation (7.5.3), where the values of the time constant 'τ' and ash resistivity 'ρ', found in Chapter five, can be substituted for these values.

$$\tau = \varepsilon_o \, \varepsilon_r \, \rho \qquad \textbf{Equation (7.5.3)}$$

Where:
- τ = The ash sample time constant.
- ε_o = The permittivity of free space.
- ε_r = The relative permittivity.
- ρ = The resistivity of the sample.

Rearranging equation (7.5.3) and substituting in the time constant and values of the resistivity for the ash gives:

$$\varepsilon_r = \frac{\tau}{\varepsilon_o \, \rho} \qquad \textbf{Equation (7.5.4)}$$

$$= \frac{(35 \times 60)}{8.854\times10^{-12} \times 77.8\times10^{+12}}$$

So:

$$\varepsilon_r = 3.05$$

Now substituting 'ε_r' into equation (7.5.2), gives the parameter 'p' as:

$$p = \frac{3 \times 3.05}{(3.05 + 2)}$$

So:

$$p = 1.81$$

Taking the average mass median diameter from the seven newer ash samples of 18.2 μm, measured with the Malvern laser particle analyzer, and assuming typical precipitator charging field strengths of 5×10^5 V/m, the Pauthenier equation (7.5.1) can now be solved, giving:

$$q_{max} = 3.34\times10^{-14}\ Coulombs$$

The charge to mass ratio can then be found by dividing this value of charge by the mass of the median particle. The mass of the particle is found through the relationship:

$$m = \rho \frac{4}{3} \pi a^3 \qquad \textbf{Equation (7.5.5)}$$

Where: m = The mass of the particle.
ρ = The density of the particle.
a = The particle radius.

Assuming that, for the ash samples:

$$\rho = 1.0\ g/cm^3$$
$$= 1000\ Kg/m^3$$

Then the mass of the particle is:

$$m = 2.53\times10^{-11}\ Kg$$

Hence the maximum charge to mass ratio is:

$$\frac{Q}{M} = \frac{3.34\times10^{-14}}{2.53\times10^{-11}}$$

So

$$\underline{\mathbf{Q/M = 1.32\times10^{-3}\ C/Kg}}$$

However, this maximum charge to mass ratio has been calculated from the average mass median diameters of the measured ash samples and takes no account of the distribution of the sizes of the particles within the sample. i.e. no account is taken of the span of the distribution.

The smallest particles contribute a greater charge by mass than the larger particles, which contribute the majority of the mass to the sample.

With such a wide distribution as that found within the samples of ash the error on the calculated value of the charge to mass ratio is unknown and could be quite large.

To get a better picture of the maximum charge and charge to mass ratio for the ash distributions, the results can be calculated for all the size bands of the Malvern particle size analyzer and then by multiplying this value by the proportion of the sample within that size band to determine a charge to mass ratio distribution of the sample. The maximum charge level and charge to mass ratio for the sample can then be found as the total of the contributions from each band.

The mid size value of each of the measuring bands of the Malvern particle size analyzer and the maximum charge and maximum charge to mass ratio was found for each result using the equations (7.5.1) to (7.5.5). The percentage of the volume distribution of the 'New Ash' sample within each of the size bands was then multiplied by the results from the Pauthenier calculations and then divided by 100 to get a per unit result.

The results of these calculations are given in Table (7.5.1) for the maximum charge and Table (7.5.2) for the maximum charge to mass ratio. The data calculated is also represented graphically in Figures (7.5.1) and (7.5.2) respectively.

SIZE BAND CENTRE VALUE	PERCENT OF ASH IN BAND	PAUTHENIER LIMIT MAXIMUM CHARGE FOR PARTICLE SIZE	PER UNIT MAXIMUM CHARGE CONTRIBUTION
(μm)	(%)	(Coulombs)	(Coulombs)
1.30	0.2	1.70×10^{-16}	3.40×10^{-19}
1.50	0.2	2.26×10^{-16}	4.52×10^{-19}
1.75	0.4	3.08×10^{-16}	1.23×10^{-18}
2.05	0.9	4.24×10^{-16}	3.82×10^{-18}
2.40	1.1	5.79×10^{-16}	6.37×10^{-18}
2.80	2.5	7.89×10^{-16}	1.97×10^{-17}
3.20	3.3	1.03×10^{-15}	3.40×10^{-17}
3.70	3.8	1.38×10^{-15}	5.24×10^{-17}
4.30	4.0	1.86×10^{-15}	7.44×10^{-17}
4.95	4.0	2.46×10^{-15}	9.84×10^{-17}
5.75	3.9	3.33×10^{-15}	1.30×10^{-16}
6.70	3.8	4.53×10^{-15}	1.72×10^{-16}
7.75	3.7	6.05×10^{-15}	2.24×10^{-16}
8.95	3.6	8.07×10^{-15}	2.91×10^{-16}
10.35	3.6	1.07×10^{-14}	3.85×10^{-16}
12.00	3.7	1.45×10^{-14}	5.37×10^{-16}
13.95	3.2	1.95×10^{-14}	6.24×10^{-16}

TABLE 7.5.1 PAUTHENIER LIMIT CHARGE FOR THE ASH SIZE DISTRIBUTION

SIZE BAND CENTRE VALUE	PERCENT OF ASH IN BAND	PAUTHENIER LIMIT MAXIMUM CHARGE FOR PARTICLE SIZE	PER UNIT MAXIMUM CHARGE CONTRIBUTION
(μm)	(%)	(Coulombs)	(Coulombs)
16.20	3.0	2.64×10^{-14}	7.92×10^{-16}
18.75	3.2	3.55×10^{-14}	1.14×10^{-15}
21.70	3.5	4.74×10^{-14}	1.66×10^{-15}
25.15	3.4	6.37×10^{-14}	2.17×10^{-15}
29.15	3.3	8.56×10^{-14}	2.82×10^{-15}
33.80	3.4	1.15×10^{-13}	3.91×10^{-15}
39.20	3.6	1.55×10^{-13}	5.58×10^{-15}
44.45	4.1	2.14×10^{-13}	8.77×10^{-15}
52.70	4.9	2.81×10^{-13}	1.38×10^{-14}
61.10	5.6	3.76×10^{-13}	2.11×10^{-14}
70.80	5.7	5.05×10^{-13}	2.88×10^{-14}
82.05	5.0	6.79×10^{-13}	3.40×10^{-14}
95.10	3.6	9.10×10^{-13}	3.28×10^{-14}

TABLE 7.5.1 (CONT.) PAUTHENIER LIMIT CHARGE FOR THE ASH SIZE DISTRIBUTION

SIZE BAND CENTRE VALUE	PARTICLE MASS	PERCENT OF ASH IN BAND	PAUTHENIER LIMIT MAXIMUM CHARGE TO MASS RATIO FOR PARTICLE SIZE	PER UNIT MAXIMUM CHARGE TO MASS RATIO CONTRIBUTION
(μm)	(Kg)	(%)	(Coulombs)/(Kilogram)	(Coulombs)/(Kilogram)
1.30	9.20×10^{-14}	0.2	1.85×10^{-2}	3.70×10^{-5}
1.50	1.42×10^{-14}	0.2	1.60×10^{-2}	3.20×10^{-5}
1.75	2.25×10^{-14}	0.4	1.36×10^{-2}	5.44×10^{-5}
2.05	3.60×10^{-14}	0.9	1.18×10^{-2}	1.06×10^{-4}
2.40	5.80×10^{-14}	1.1	9.99×10^{-3}	1.10×10^{-4}
2.80	9.16×10^{-14}	2.5	8.59×10^{-3}	2.15×10^{-4}
3.20	1.37×10^{-13}	3.3	7.50×10^{-3}	2.48×10^{-4}
3.70	2.12×10^{-13}	3.8	6.51×10^{-3}	2.47×10^{-4}
4.30	3.33×10^{-13}	4.0	5.56×10^{-3}	2.22×10^{-4}
4.95	5.08×10^{-13}	4.0	4.84×10^{-3}	1.79×10^{-4}
5.75	7.96×10^{-13}	3.9	4.18×10^{-3}	1.63×10^{-4}
6.70	1.26×10^{-12}	3.8	3.59×10^{-3}	1.36×10^{-4}
7.75	1.95×10^{-12}	3.7	3.11×10^{-3}	1.15×10^{-4}
8.95	3.00×10^{-12}	3.6	2.69×10^{-3}	9.68×10^{-5}
10.35	4.64×10^{-12}	3.6	2.32×10^{-3}	8.35×10^{-5}
12.00	7.24×10^{-12}	3.7	2.00×10^{-3}	7.40×10^{-5}

TABLE 7.5.2 PAUTHENIER CHARGE TO MASS RATIO LIMIT FOR THE ASH SIZE DISTRIBUTION

SIZE BAND CENTRE VALUE	PARTICLE MASS	PERCENT OF ASH IN BAND	PAUTHENIER LIMIT MAXIMUM CHARGE TO MASS RATIO FOR PARTICLE SIZE	PER UNIT MAXIMUM CHARGE TO MASS RATIO CONTRIBUTION
(μm)	(Kg)	(%)	$\frac{\text{(Coulombs)}}{\text{(Kilogram)}}$	$\frac{\text{(Coulombs)}}{\text{(Kilogram)}}$
13.95	1.14×10^{-11}	3.2	1.72×10^{-3}	5.50×10^{-5}
16.20	1.78×10^{-11}	3.0	1.49×10^{-3}	4.47×10^{-5}
18.75	2.76×10^{-11}	3.2	1.28×10^{-3}	4.09×10^{-5}
21.70	4.28×10^{-11}	3.5	1.11×10^{-3}	3.89×10^{-5}
25.15	6.68×10^{-11}	3.4	9.54×10^{-4}	3.24×10^{-5}
29.15	1.04×10^{-10}	3.3	8.23×10^{-4}	2.72×10^{-5}
33.80	1.62×10^{-10}	3.4	7.10×10^{-4}	2.41×10^{-5}
39.20	2.52×10^{-10}	3.6	6.10×10^{-4}	2.20×10^{-5}
44.45	3.93×10^{-10}	4.1	5.29×10^{-4}	2.12×10^{-5}
52.70	6.12×10^{-10}	4.9	4.57×10^{-4}	2.24×10^{-5}
61.10	9.52×10^{-10}	5.6	3.95×10^{-4}	2.21×10^{-5}
70.80	1.49×10^{-9}	5.7	3.39×10^{-4}	1.93×10^{-5}
82.05	2.31×10^{-9}	5.0	2.93×10^{-4}	1.47×10^{-5}
95.10	3.60×10^{-9}	3.6	2.52×10^{-4}	9.07×10^{-6}

TABLE 7.5.2 (CONT) PAUTHENIER CHARGE TO MASS RATIO LIMIT FOR THE ASH SIZE DISTRIBUTION

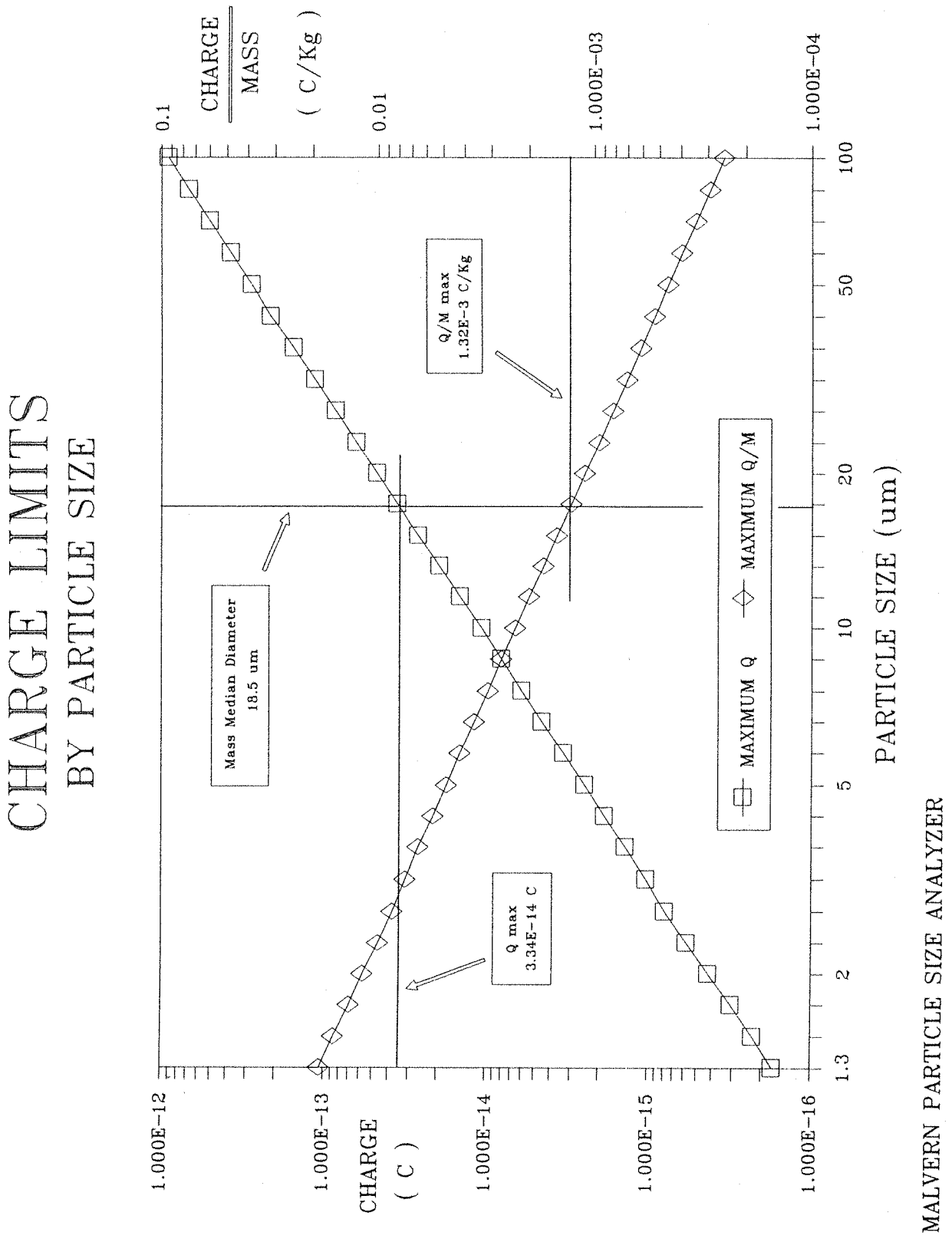

FIGURE 7.5.1 CHARGE LIMITS AS A FUNCTION OF PARTICLE SIZE

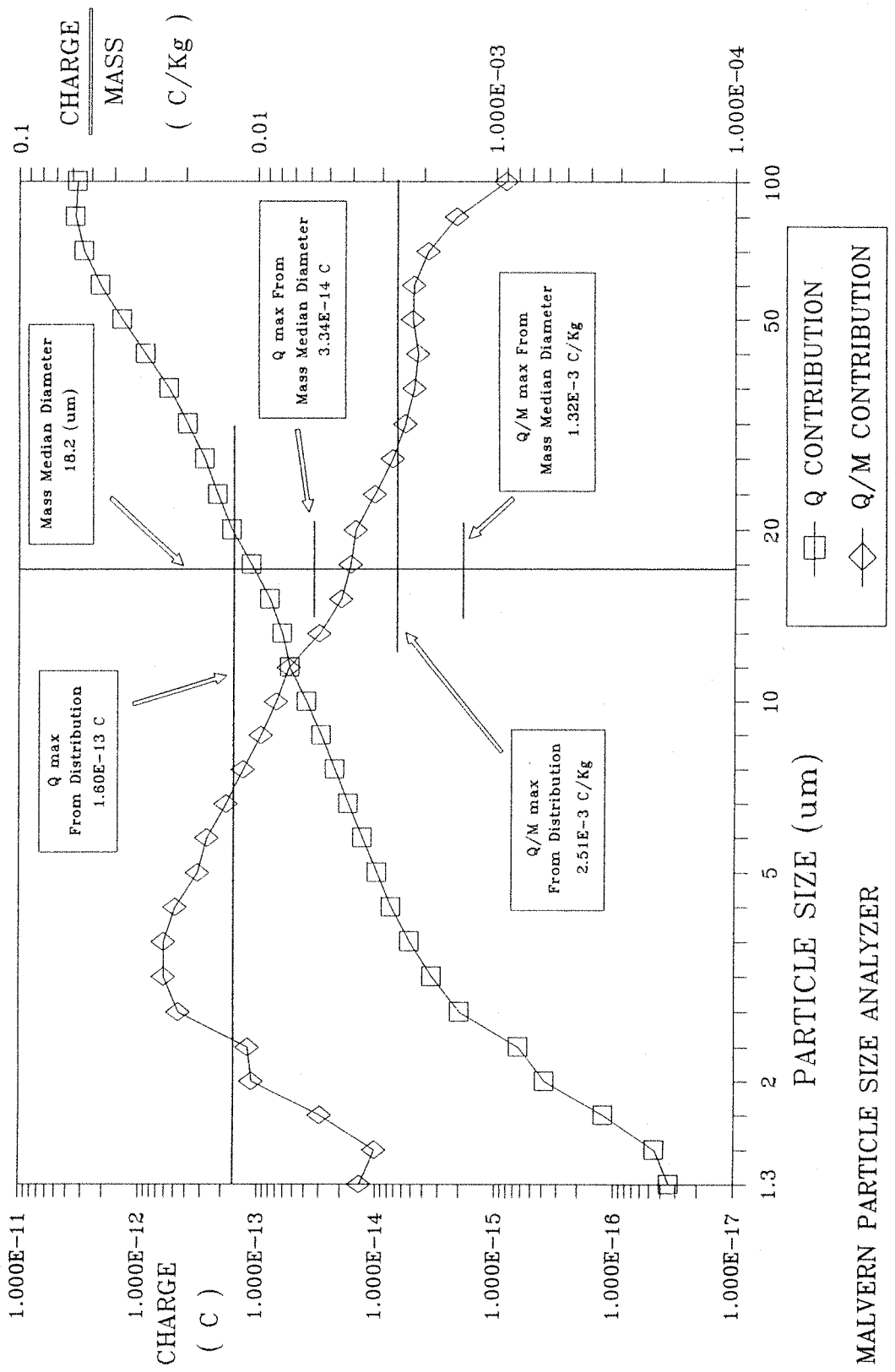

FIGURE 7.5.2 CHARGE LEVELS FOR THE ASH SIZE DISTRIBUTION

7.5.2 SUMMARY OF THE CALCULATED VALUES

The Pauthenier limit charge and the maximum charge to mass ratio for the measured distribution can be calculated from the calculated data in Tables (7.5.1) and (7.5.2). These values along with the values calculated from the mass median diameter of the measured distribution are given in Table (7.5.3).

	PAUTHENIER LIMIT MAXIMUM CHARGE	PAUTHENIER LIMIT CHARGE TO MASS RATIO
	COULOMBS	$\frac{\text{COULOMBS}}{\text{KILOGRAMS}}$
CALCULATED FROM THE MASS MEAN DIAMETER	3.34×10^{-14}	1.32×10^{-3}
CALCULATED FROM THE SIZE BAND CONTRIBUTION OF THE PARTICLE SIZE DISTRIBUTION	1.60×10^{-13}	2.51×10^{-3}

TABLE 7.5.3 SUMMARY OF CALCULATED CHARGE LIMITS

These two different calculated results underline the fact that care is required when calculating the theoretical charge limits as the charge is very dependent on the particle size. This is especially true for poly-disperse distributions, where the values of the Pauthenier charge limit calculated from the mass median diameter are far from the value calculated considering the whole range of particle sizes that exist within the sample.

7.5.3 MEASUREMENTS OF CHARGE TO MASS RATIO

The continuous flow Faraday cup, as described in Chapter four, was placed at the far down stream end of the test duct and the charge to mass ratio that could be imparted to the ash by the bi-polar charger was measured using the method also detailed in Chapter four. For these tests alone both of the charging units within the bi-polar charger were energized to the same polarity. This was to ensure that all the ash within the test duct had to pass through a region of high flux. The tests were repeated three times in order to ensure that the obtained result was representative of the sample.

The corona point in the powder feed gun was left un-energized, so that the true charging characteristics of the ash could be determined from these results. However, this corona point was energized for all the subsequent tests.

The results of these tests are given in two Tables, (7.5.4A) for the results when both of the charging unit were energized in a positive polarity and (7.5.4B) when the charging units were energized negatively. A graph was plotted of the average charge to mass ratio of the three tests as a function of the corona current, this can be seen in Figure (7.5.3).

7.5.4 CHARGE TO MASS RATIO MEASUREMENT RESULTS

The graph drawn in Figure (7.5.3) is very much as was expected, producing the characteristic 'S' shape. The point where the line cuts the zero corona current axis shows the natural charge that was present on the ash generated by its transportation through the powder feed system as the tribo charge cancelling corona was not turned on for these tests.

CORONA CURRENT	ASH CHARGE	ASH MASS	CHARGE TO MASS RATIO
AMPS	COULOMBS	KILOGRAMS	$\frac{\text{COULOMBS}}{\text{KILOGRAM}}$
$+0.5\times10^{-3}$	$+18.0\times10^{-7}$	34.65×10^{-5}	$+5.195\times10^{-3}$
$+0.5\times10^{-3}$	$+16.0\times10^{-7}$	33.68×10^{-5}	$+4.751\times10^{-3}$
$+0.5\times10^{-3}$	$+8.9\times10^{-7}$	19.34×10^{-5}	$+4.601\times10^{-3}$
		AVERAGE	$+4.849\times10^{-3}$
$+0.3\times10^{-3}$	$+10.0\times10^{-7}$	24.54×10^{-5}	$+4.075\times10^{-3}$
$+0.3\times10^{-3}$	$+8.5\times10^{-7}$	20.24×10^{-5}	$+4.257\times10^{-3}$
$+0.3\times10^{-3}$	$+8.4\times10^{-7}$	21.72×10^{-5}	$+3.867\times10^{-3}$
		AVERAGE	$+4.066\times10^{-3}$
$+0.1\times10^{-3}$	$+8.0\times10^{-7}$	28.73×10^{-5}	$+2.785\times10^{-3}$
$+0.1\times10^{-3}$	$+7.4\times10^{-7}$	25.00×10^{-5}	$+2.960\times10^{-3}$
$+0.1\times10^{-3}$	$+7.8\times10^{-7}$	24.33×10^{-5}	$+3.206\times10^{-3}$
		AVERAGE	$+2.984\times10^{-3}$
0.0	-0.93×10^{-7}	13.13×10^{-5}	$+0.708\times10^{-3}$
0.0	-0.80×10^{-7}	13.37×10^{-5}	$+0.598\times10^{-3}$
0.0	-0.94×10^{-7}	15.00×10^{-5}	$+0.627\times10^{-3}$
		AVERAGE	$+0.644\times10^{-3}$

TABLE 7.5.4A POSITIVE CHARGE TO MASS RATIO

CORONA CURRENT	ASH CHARGE	ASH MASS	CHARGE TO MASS RATIO
AMPS	COULOMBS	KILOGRAMS	$\frac{\text{COULOMBS}}{\text{KILOGRAM}}$
-0.5×10^{-3}	-8.4×10^{-7}	8.75×10^{-5}	-4.480×10^{-3}
-0.5×10^{-3}	-7.9×10^{-7}	13.97×10^{-5}	-5.655×10^{-3}
-0.5×10^{-3}	-8.8×10^{-7}	6.55×10^{-5}	-5.317×10^{-3}
		AVERAGE	-5.151×10^{-3}
-0.3×10^{-3}	-6.1×10^{-7}	16.38×10^{-5}	-3.724×10^{-3}
-0.3×10^{-3}	-5.4×10^{-7}	14.63×10^{-5}	-3.691×10^{-3}
-0.3×10^{-3}	-8.4×10^{-7}	19.89×10^{-5}	-4.274×10^{-3}
		AVERAGE	-3.896×10^{-3}
-0.1×10^{-3}	-4.5×10^{-7}	15.45×10^{-5}	-2.913×10^{-3}
-0.1×10^{-3}	-4.1×10^{-7}	14.24×10^{-5}	-2.879×10^{-3}
-0.1×10^{-3}	-4.2×10^{-7}	13.68×10^{-5}	-3.070×10^{-3}
		AVERAGE	-2.954×10^{-3}
0.0	-0.74×10^{-7}	11.10×10^{-5}	-0.667×10^{-3}
0.0	-0.71×10^{-7}	12.46×10^{-5}	-0.569×10^{-3}
0.0	-0.62×10^{-7}	9.07×10^{-5}	-0.684×10^{-3}
		AVERAGE	-0.640×10^{-3}

TABLE 7.5.4B NEGATIVE CHARGE TO MASS RATIO

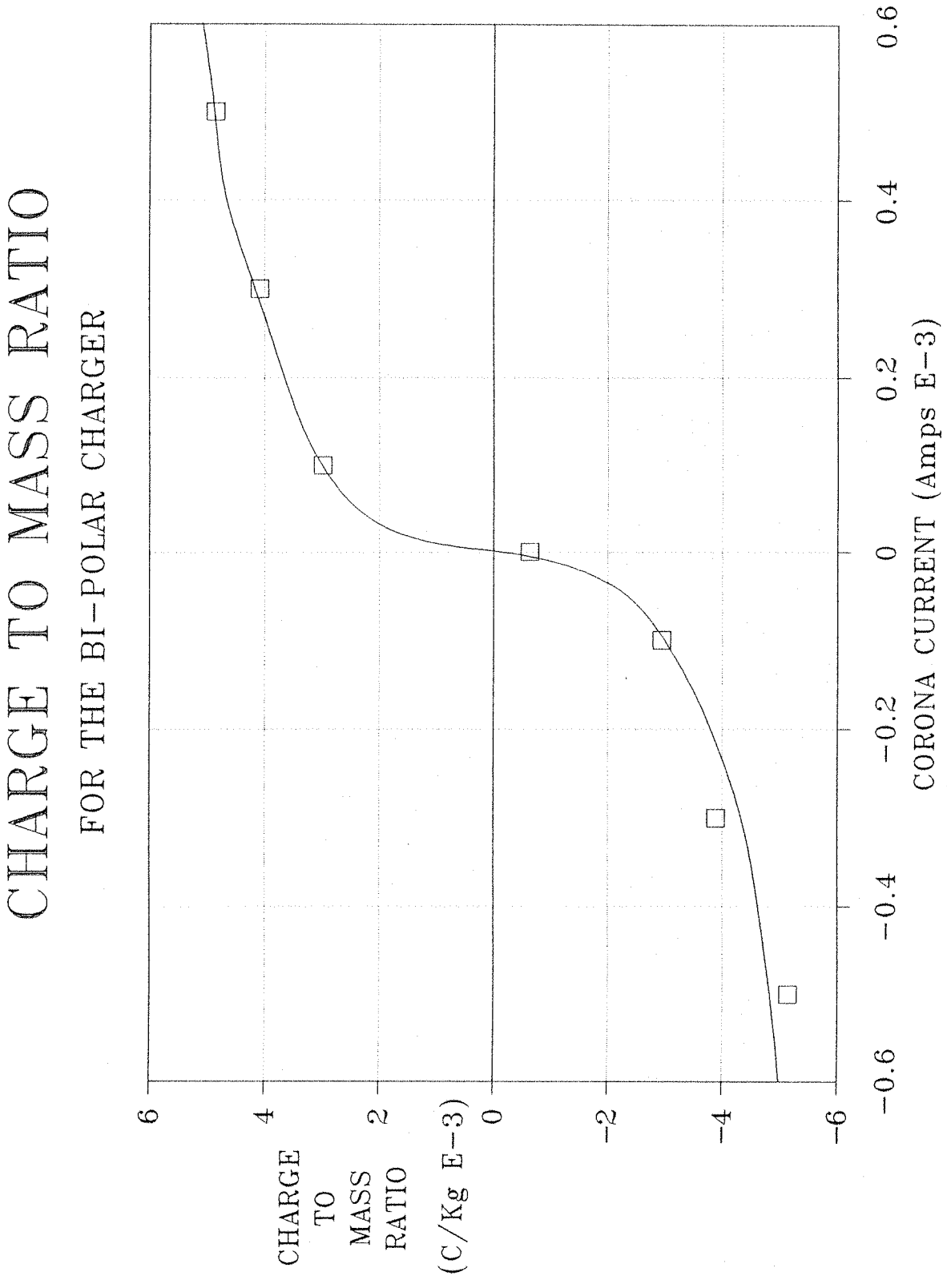

FIGURE 7.5.3 MEASURED CHARGE TO MASS RATIO RESULTS

The extremities of the curve are beginning to flatten off, towards + or - 5×10^{-3} C/Kg, indicating that the limit charge for the particle size distribution that can be applied by a corona discharge had been reached. Although the actual value of the charge to mass ratio is of the same order of magnitude as the calculated value for the distribution, it is however about twice the actual value. There are many possible mechanisms that could be responsible for this high recorded value of charge to mass ratio but the actual cause was probably a combination of them all. First, it has been shown that the largest particles within the distribution have a tendency to 'drop-out' of the air flow under the influence of gravity. This results in a particle size distribution consisting of finer particles than the original distribution and hence, by Pauthenier, the captured distribution will have a higher charge to mass ratio than the original distribution. Secondly, the continuous flow Faraday cup may have been bombarded by charged ash particles on its outer surface which then lose their charge to the electrometer but subsequently drop off the cup or become re-entrained into the gas stream prior to having their mass included in the calculations. Thirdly, there may be a greater number of free ions able to penetrate the grounded meshes surrounding the discharge electrodes and the Faraday cup than had been expected, especially if these ions are carried from the electrodes to the cup within the ash laden air stream and were not detected when the electrodes were energized alone.

The fact that a greater charge to mass ratio than had been expected was recorded was not of great importance. The tests prove that the bi-polar charging system is able to fully charge the ash, this is shown by the fact that the charge to mass ratio levels off with ever increasing corona current and hence increasing the power input into the system or producing a more efficient charging system would not increase the charge deposited onto the ash.

7.5.5 BI-POLAR CHARGING

Both of the charging units within the bi-polar charger were energised to opposite polarities at the same time and the charge to mass ratio of the ash was again measured. A zero reading of current arriving at the Faraday cup was

achievable by adjusting the two corona currents to the discharge electrodes, indicating that equal proportions of negatively charged and positively charged ash is generated within the duct.

It should be pointed out that a zero current reading on the Faraday cup with both sections of the bi-polar charger oppositely energized does not however indicate that agglomerates between the oppositely charged particles have been formed but only that equal proportions of negatively charged and positively charged ash particles have arrived at the cup, either as agglomerates or as single particles.

7.6 AGGLOMERATION DUCT AIR FLOW PATTERNS

Now that the bi-polar charger had been installed into the test duct and the gas flow disrupted by the central cylinder between the two charging units, in order to asses the degree of turbulence that had been created by the large central cylinder, it was necessary to again measure the gas flow rates within the duct.

These measurements were made using the hot-wire anemometer and the methods described in Chapter four. The test duct with the charger in place still has the same two planes of symmetry, allowing the measurements to be made in only one quarter of the duct in order to be able to assess the gas flow within the entire duct.

The gas flow vectors produced are shown in Figure (7.6.1) for the measurements made along the central plane and Figure (7.6.2) for the measurements made 5 cm in from the edge of the duct.

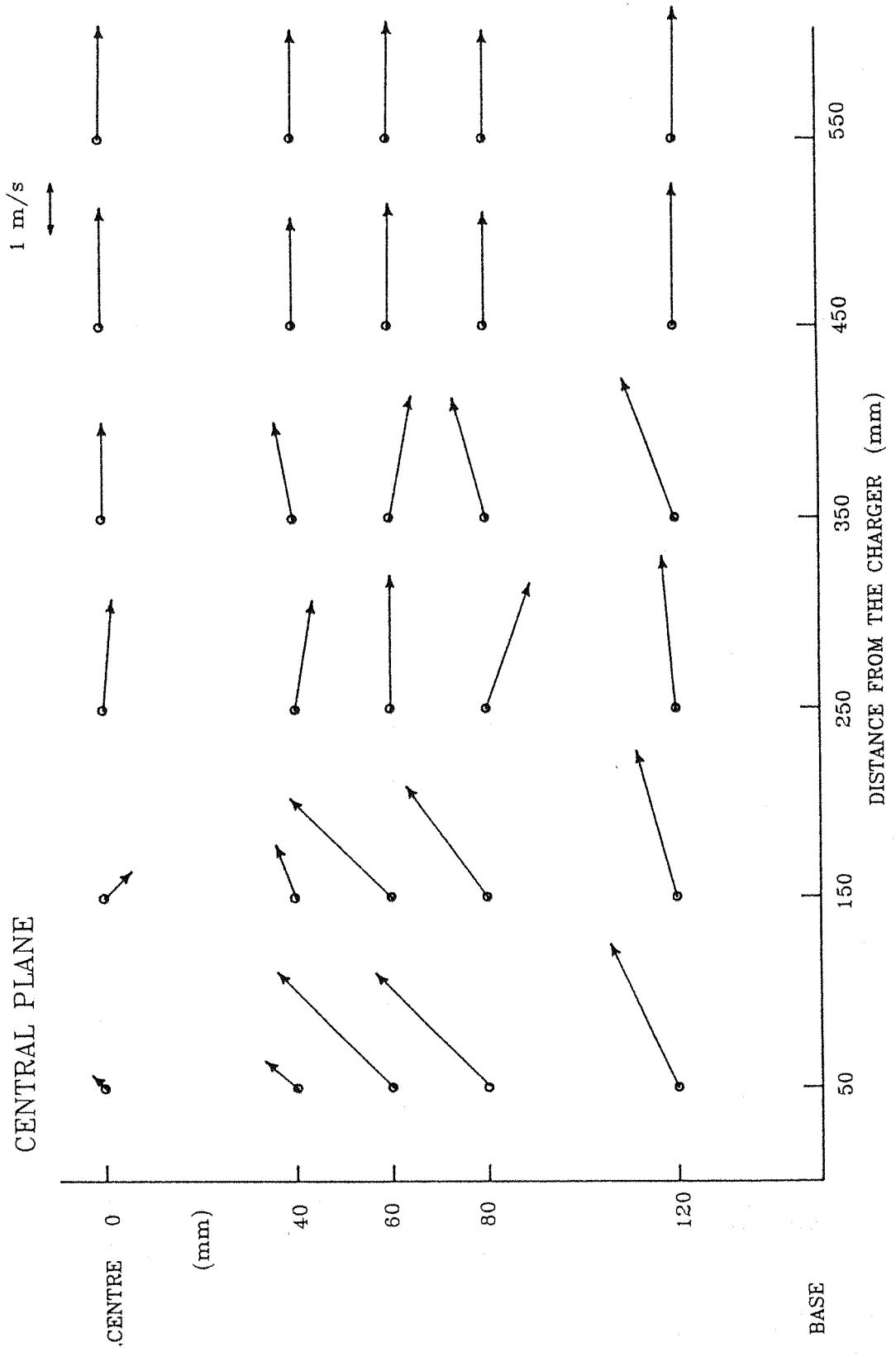

FIGURE 7.6.1 POST CHARGING GAS FLOW PATTERN AT THE CENTRE OF THE DUCT

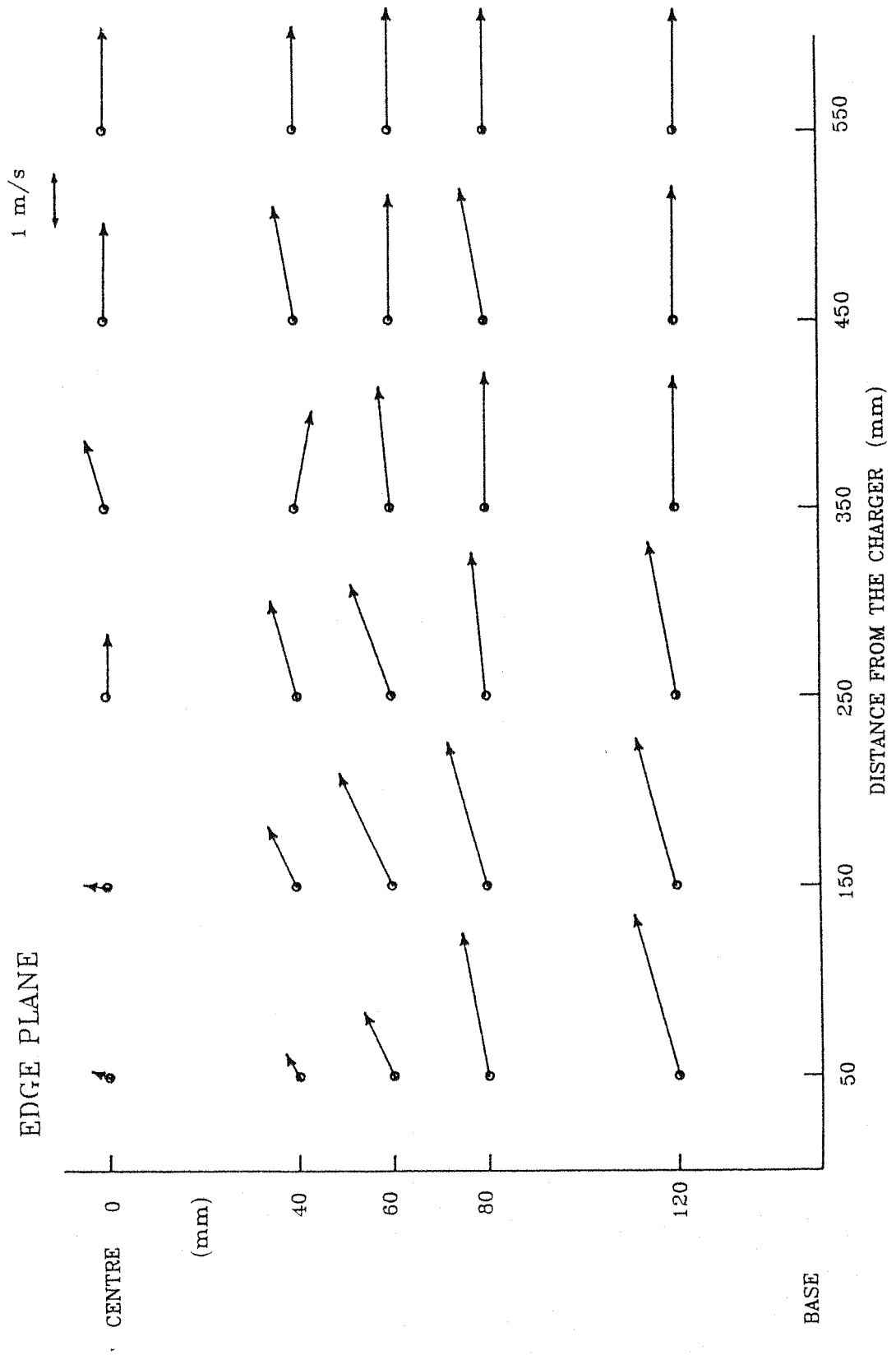

FIGURE 7.6.2 POST CHARGING GAS FLOW PATTERN 5 cm FROM THE EDGE OF THE DUCT

These results are, as before, shown as a series of arrows. The base of the arrow representing the sample point, the length of the arrow being proportional to the air velocity measured and the direction of the arrow indicating the direction of the gas flow.

It is important to remember that a short arrow may be the result of rapidly changing direction of the gas flow, with a small average in one direction, as describer in Chapter four. This is particularly prevalent in areas of high turbulence.

For all of these tests only the air supply and extraction was turned on and not the ash load, as the solid ash particles would block the anemometer.

7.6.1 GAS FLOW RESULTS

Both of the gas flow patterns produced from the central plane and from the edge of the duct now show a region of extreme turbulence immediately after the bi-polar charger, extending some 200 mm down the test duct. Large eddies could be seen in the region just down stream of the central cylinder. These eddies seem to form close to the cylinder and then spiral off down stream. For this reason the time average measurements of the gas flow produce the characteristic short arrow pointing in the direction of the net gas flow, depicting gross changes in the gas flow direction.

It is within this area of great turbulence that the intense mixing of the two oppositely charged gas streams will occur. The two streams must be mixed to such an extent that particles of opposite polarity become close enough to one another to be able to become attracted towards one another by the mechanisms of their mutual electrostatic attraction, as discused in Chapter three.

After this region of great turbulence the velocity profile of the flow pattern is seen to settle into the characteristic velocity profile of a turbulent flow. This more settled flow should induce less shear stresses on the particles, this is

should be beneficial as it is in this region that the oppositely charged particles must migrate towards one another and form electrostatic agglomerates.

CHAPTER EIGHT

AGGLOMERATION MEASUREMENTS

8.1 PARALLEL PLATES

The parallel plates were located at the far down stream end of the test rig in a vertical orientation, as can be seen in Plate (8.1.1). One of the plates was connected to ground through an electrometer, while the other was connected to a high voltage power supply, which could be grounded or energized to either a positive or negative potential. The agglomeration rig was then run in various modes, i.e. with or without the bi-polar charger energized or with only one of the charging units energized.

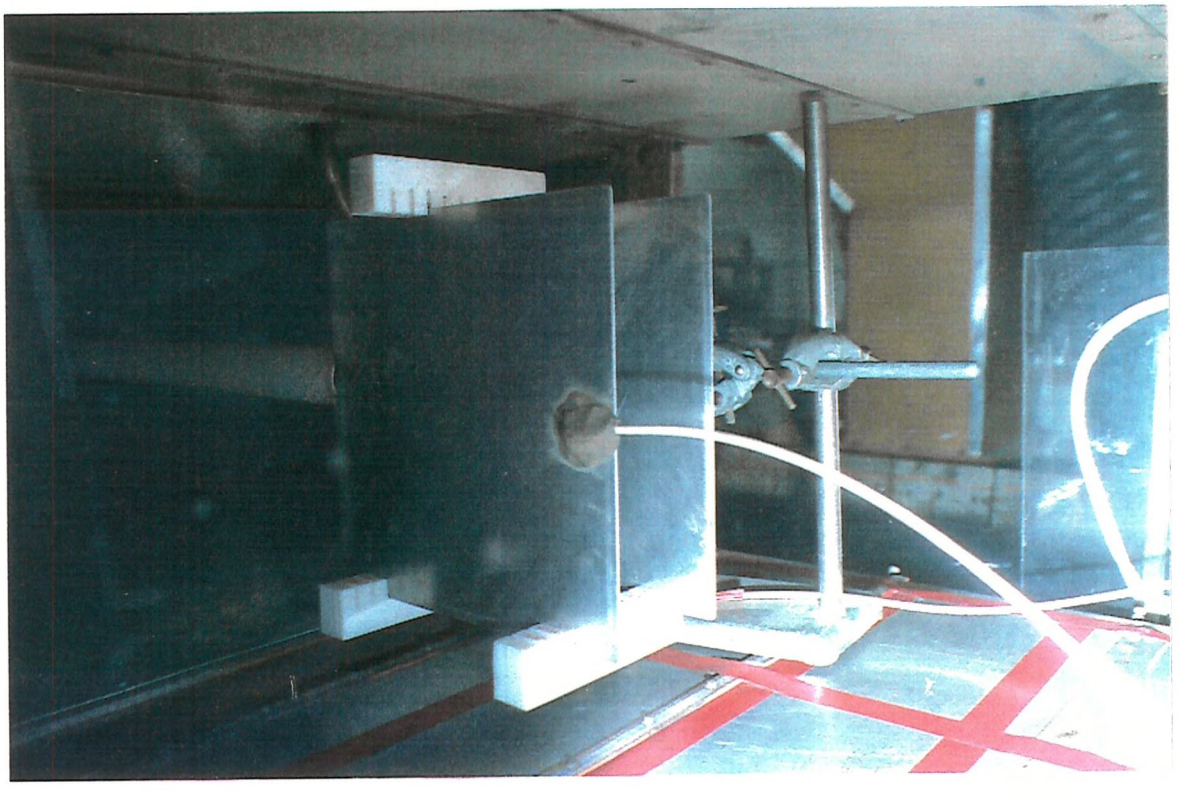

PLATE 8.1.1 PARALLEL PLATES

As the charged ash cloud passed between the parallel plates, particles will be precipitated in the deposition field onto one or the other of the plates, depending on the polarity of their charge. Positively charged particles will migrate to the negative plate and negatively charged particles will migrate to the positive plate. The particles will then become attached to the plate where they adhere due to the electrostatic force of attraction between the charge on the plate and the opposite charge on the particle. The particles will not lose their charge to the plates, as their resistivity is large and the time constant of the charge loss by conduction long, as was shown in Chapter three. The particles will even remain adhered to the plate after the power to the plates has been turned off. This is due to the electrostatic adhesion force between the charged particles and their image charge induced onto the surface of the plate. The charge of the ash deposited on the collection plate could be recorded on the electrometer and the mass of the ash determined by weighing the plate before and after the test.

In the energized state the potential on the charged plate was set to +or- 20kV. The separation between the two plates was set to 5cm for all the tests. These settings were chosen to produce an electric field as large as possible between the plates in order to optimise the deposition of the charged ash particles, while at the same time not allowing the plates to discharge to one another through a spark discharge or by going into corona. The tests were repeated several times and the results obtained normalized for a one minute test period.

8.1.1 CHARGE TO MASS RATIO RESULTS

All the charge to mass ratio results calculated from these tests were higher than might have otherwise been expected from the distribution of particle sizes previously measured. This can be attributed to the following reasons:

First, the ash particles may collide with the collection plate; transfer part of their charge and then be re-entrained into the air stream, hence not having their mass included in the calculations.

Secondly, the larger particles have been shown to 'drop out' of the air stream under the influence of gravity. Hence the particle size distribution of the

ash between the two plates consists of finer particles than the original sample. Therefore, the Pauthenier limit charge to mass ratio of the distribution will be greater than that of the original sample.

Thirdly, the parallel plates will preferentially capture the particles with the greatest charge, as the force of attraction between the plate and the particle is proportional to the charge on the particle, as was shown in Chapter three from Coulomb's law.

8.1.2 ASH DEPOSITION WITH BOTH PLATES GROUNDED

In this case there is no electric field between the two plates. Both plates will act as simple earthed surfaces onto which the ash particles can become attached by the electrostatic force of attraction to their own image charge. The collector plate was earthed through an electrometer.

The test rig was run in its various modes of operation and the mass of ash deposited on the collector plate for the normalized one minute test period recorded along with the charge on that ash. The results of these tests are given in Table (8.1.1). Bar charts were also plotted of the mass of ash deposited on the collector plate, and the charge to mass ratio of that ash for the normalised test period. These bar charts are shown in Figure (8.1.1).

8.1.2.1 PARALLEL PLATES GROUNDED, BI-POLAR CHARGER UN-ENERGIZED

Considering first the case where both the charging units of the bi-polar charger were un-energised. The ash deposited onto the collecting plate was found to have a positive charge, with a charge to mass ratio of about 4×10^{-3} C/Kg. However, the actual mass of ash caught in the one minute period was very small. This result indicates that the net charge to mass ratio on the majority of the ash sample was low and hence evades capture by the parallel plate arrangement, even though a small number of particles were found within the total sample with a considerable positive charge.

BOTH PLATES GROUNDED	BI-POLAR CHARGER STATUS			
	OFF	POSITIVE SECTION ON	NEGATIVE SECTION ON	BOTH SECTIONS ON
CHARGE (C)	$+1.4\times10^{-7}$	$+6.7\times10^{-7}$	-9.3×10^{-7}	-4.6×10^{-7}
MASS (g)	0.03	0.14	0.18	0.13
Q/M (C/Kg)	$+4.67\times10^{-3}$	$+4.79\times10^{-3}$	-5.17×10^{-3}	-3.54×10^{-3}
CHARGE (C)	$+1.9\times10^{-7}$	$+8.9\times10^{-7}$	-9.8×10^{-7}	-----
MASS (g)	0.06	0.21	0.23	-----
Q/M (C/Kg)	$+3.17\times10^{-3}$	$+4.24\times10^{-3}$	-4.26×10^{-3}	-----
CHARGE (C)	$+0.9\times10^{-7}$	$+9.1\times10^{-7}$	-9.4×10^{-7}	-4.7×10^{-7}
MASS (g)	0.02	0.16	0.21	0.14
Q/M (C/Kg)	$+4.50\times10^{-3}$	$+5.69\times10^{-3}$	-4.48×10^{-3}	-3.36×10^{-3}
AVERAGE CHARGE (C)	$+1.4\times10^{-7}$	$+8.2\times10^{-7}$	-9.5×10^{-7}	-4.7×10^{-7}
AVERAGE MASS (g)	0.04	0.17	0.21	0.13
AVERAGE Q/M (C/Kg)	$+4.11\times10^{-3}$	$+4.91\times10^{-3}$	-4.64×10^{-3}	-3.45×10^{-3}

TABLE 8.1.1 THE CHARGE AND MASS OF THE ASH CAPTURED WITH BOTH PLATES GROUNDED

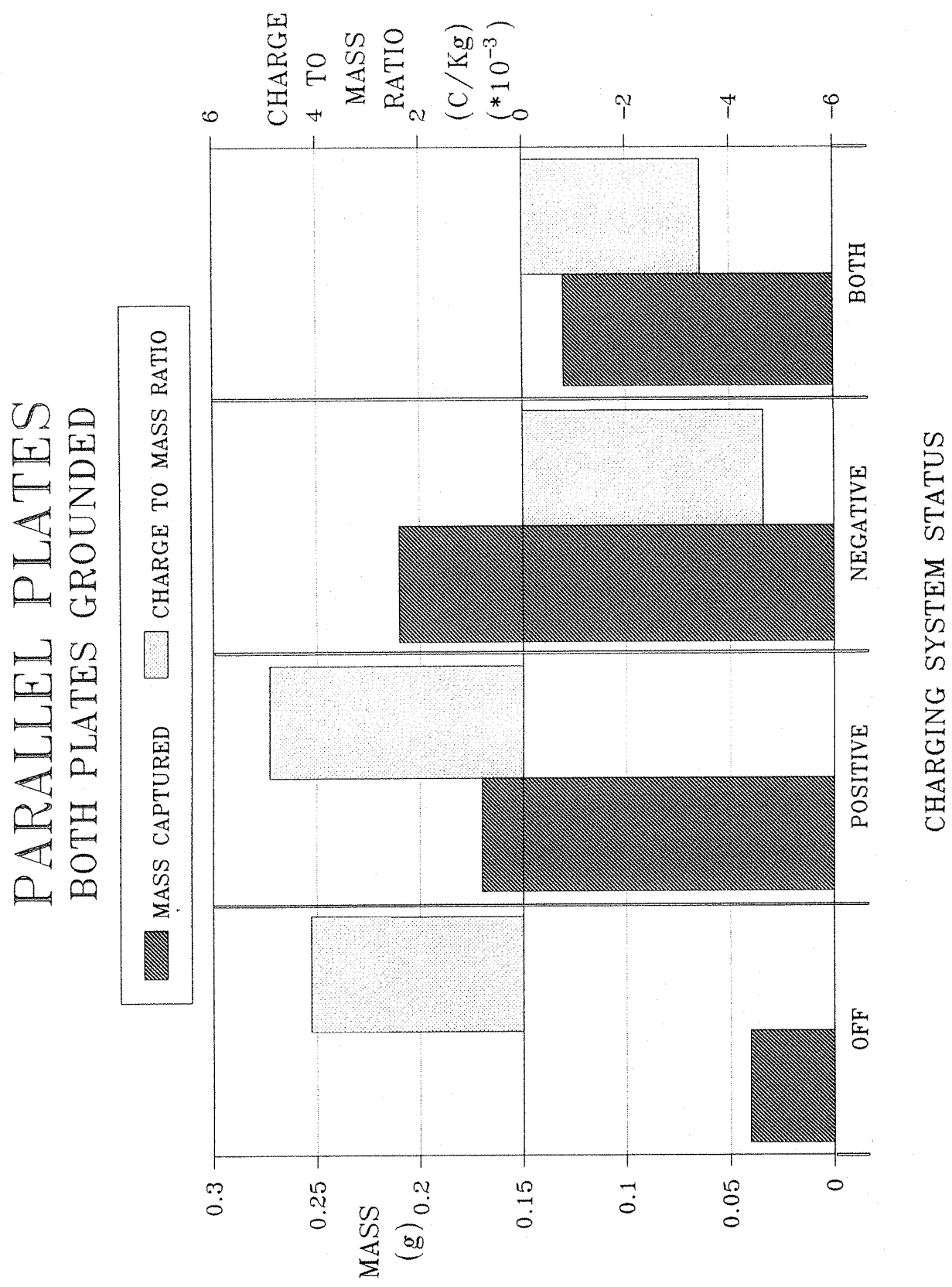

FIGURE 8.1.1 ASH DEPOSITION ON THE COLLECTING PLATE, BOTH PLATES GROUNDED

8.1.2.2 PARALLEL PLATES GROUNDED, POSITIVE SECTION OF BI-POLAR CHARGER ENERGIZED

These tests were performed with only the positive section of the bi-polar charger energised, the negative section remained un-energised. In this case the ash within the test duct would have a net positive charge, with half charged positively and half remaining uncharged. Four times the mass of ash was found to be captured on the collector plate than when both of the charging electrodes were un-energised. Also, as was to be expected, the polarity of the charge of the captured ash was found to be positive and the charge to mass ratio indicateD that the ash captured was highly charged. This result was much as expected, as there now exists a higher proportion of maximally charged positive particles within the distribution.

8.1.2.3 PARALLEL PLATES GROUNDED, NEGATIVE SECTION OF BI-POLAR CHARGER ENERGIZED

The previous set of tests were repeated, but in this case with only the negative section of the bi-polar charger energized. The positive section remained un-energized. The results of these tests were found to be exactly the same as the previous tests when only the positive section of the bi-polar charger was energized; except that the charge on the ash in this case was negative.

The previous two sets of tests have shown that the bi-polar charger generates two approximately equal ash clouds, charged maximally and to opposite polarities.

8.1.2.4 PARALLEL PLATES GROUNDED, BOTH SECTIONS OF THE BI-POLAR CHARGER ENERGIZED

This group of tests were performed with both sections of the bi-polar charger energized. In this case a smaller proportion of ash was deposited onto the collecting plate than had been found when only a single charging electrode was energized. Also the charge to mass ratio of the deposited ash was less than had been recorded in all the previous tests of this series with both of the plates

un-energized. The polarity of the charge on the captured ash was found to be negative.

As the parallel plate arrangement will only capture charged particles, the reduced mass of the deposited ash would indicate that the particles passing through the parallel plates were less charged than in the previous tests. This reduction in charge could be due to the particles discharging to one another or could be due to two or more oppositely charged particles coming together to form an agglomerate, with a reduced net charge. The particles are unlikely to discharge one another as the time constant 'τ' of this process was shown to be large in comparison to the time the particles will spend within the test rig. The net negative charge that had been recorded simply indicated that there were more negatively charged particles within the test duct than positively charged particles. This could be due to many factors and is confirmed by the increased mass of ash captured when only the negatively charged electrode was energized, compared to the mass of the ash captured when only the positive electrode was energized.

The reduced charge to mass ratio measured may have been due to one of two processes: First, both positively and negatively charged particles will alight onto the surface of the plate where their opposing charges will cancel one another. Thus the observed result shows that a greater number of negative particles than positive particles have been deposited onto the plate. Secondly, the reduced charge to mass ratio may have been due to more agglomerates with a net negative charge being formed than agglomerates with a net positive charge, as there were more negatively charged particles available within the ash cloud to form agglomerates than positively charged particles.

8.1.3 ENERGIZED PLATE AT A POSITIVE POTENTIAL

For this series of tests the energized plate was connected to the high voltage power supply which was set to a potential of +20kV. Thus, a strong electric deposition field was set up between the two plates. This field will act to drive the positively charged particles that pass between the plates towards the collection plate, and conversely the negatively charged particles towards the positively charged plate. There is no electric force on the un-charged particles.

The current being supplied to the energized plate was monitored at all times, as any loss of charge through corona or spark breakdown in the collected ash layer would cause free ions to be ejected into the electric field region. These free ions will then either act to charge any ash particle with which they collide, or will migrate to the collecting plate and produce an overly large reading of charge on the electrometer. Equally, the rate of charge arrival at the collector plate required careful monitoring, as an electrical discharge from this plate was just as likely.

The results of this series of tests are tabulated in Table (8.1.2) and the bar charts of the mass of the captured ash and charge to mass ratio for the normalized one minute period are plotted in Figure (8.1.2).

8.1.3.1 ENERGIZED PLATE AT A POSITIVE POTENTIAL, BI-POLAR CHARGER UN-ENERGIZED

The first group of tests in this series were performed with both sections of the bi-polar charger un-energized. As expected, the ash deposited onto the collector plate had a positive charge, with a charge to mass ratio typical of that so far seen in these tests. However, the amount of ash deposited was significantly greater than that seen when the plates were un-energized. This was due to the increased force of deposition produced by the intense electric field between the plates. Hence a greater proportion of the positively charged ash was captured from the air stream and the charge to mass ratio of the deposit remained un-altered.

8.1.3.2 ENERGIZED PLATE AT A POSITIVE POTENTIAL, POSITIVE SECTION OF BI-POLAR CHARGER ENERGIZED

When only the positive section of the bi-polar charger was energized, significantly more of the ash was captured on the collection plate than when the charger was un-energized. This was as expected as there would be a far greater number of positively charged particles within the air stream. However, the charge to mass ratio, although still positive, was seen to be less than was recorded when the plates were un-energized. This would imply that with the

ENERGISED PLATE +20KV	BI-POLAR CHARGER STATUS			
	OFF	POSITIVE SECTION ON	NEGATIVE SECTION ON	BOTH SECTIONS ON
CHARGE (C)	$+7.3\times10^{-7}$	$+10.3\times10^{-7}$	$+5.77\times10^{-7}$	$+7.23\times10^{-7}$
MASS (g)	0.12	0.30	0.18	0.16
Q/M (C/Kg)	$+6.08\times10^{-3}$	$+3.43\times10^{-3}$	$+3.20\times10^{-3}$	$+4.52\times10^{-3}$
CHARGE (C)	$+5.80\times10^{-7}$	$+7.17\times10^{-7}$	$+6.70\times10^{-7}$	$+6.40\times10^{-7}$
MASS (g)	0.18	0.24	0.12	0.21
Q/M (C/Kg)	$+3.22\times10^{-3}$	$+2.99\times10^{-3}$	$+5.58\times10^{-3}$	$+3.05\times10^{-3}$
CHARGE (C)	$+5.80\times10^{-7}$	$+8.63\times10^{-7}$	$+6.03\times10^{-7}$	$+6.97\times10^{-7}$
MASS (g)	0.18	0.28	0.10	0.16
Q/M (C/Kg)	$+3.22\times10^{-3}$	$+3.08\times10^{-3}$	$+6.03\times10^{-3}$	$+4.35\times10^{-3}$
AVERAGE CHARGE (C)	$+6.30\times10^{-7}$	$+8.70\times10^{-7}$	$+6.17\times10^{-7}$	$+6.87\times10^{-7}$
AVERAGE MASS (g)	0.16	0.27	0.13	0.18
AVERAGE Q/M (C/Kg)	$+4.17\times10^{-3}$	$+3.17\times10^{-3}$	$+4.94\times10^{-3}$	$+3.97\times10^{-3}$

TABLE 8.1.2 THE CHARGE AND MASS OF THE ASH CAPTURED WITH THE ENERGISED PLATE AT +20KV

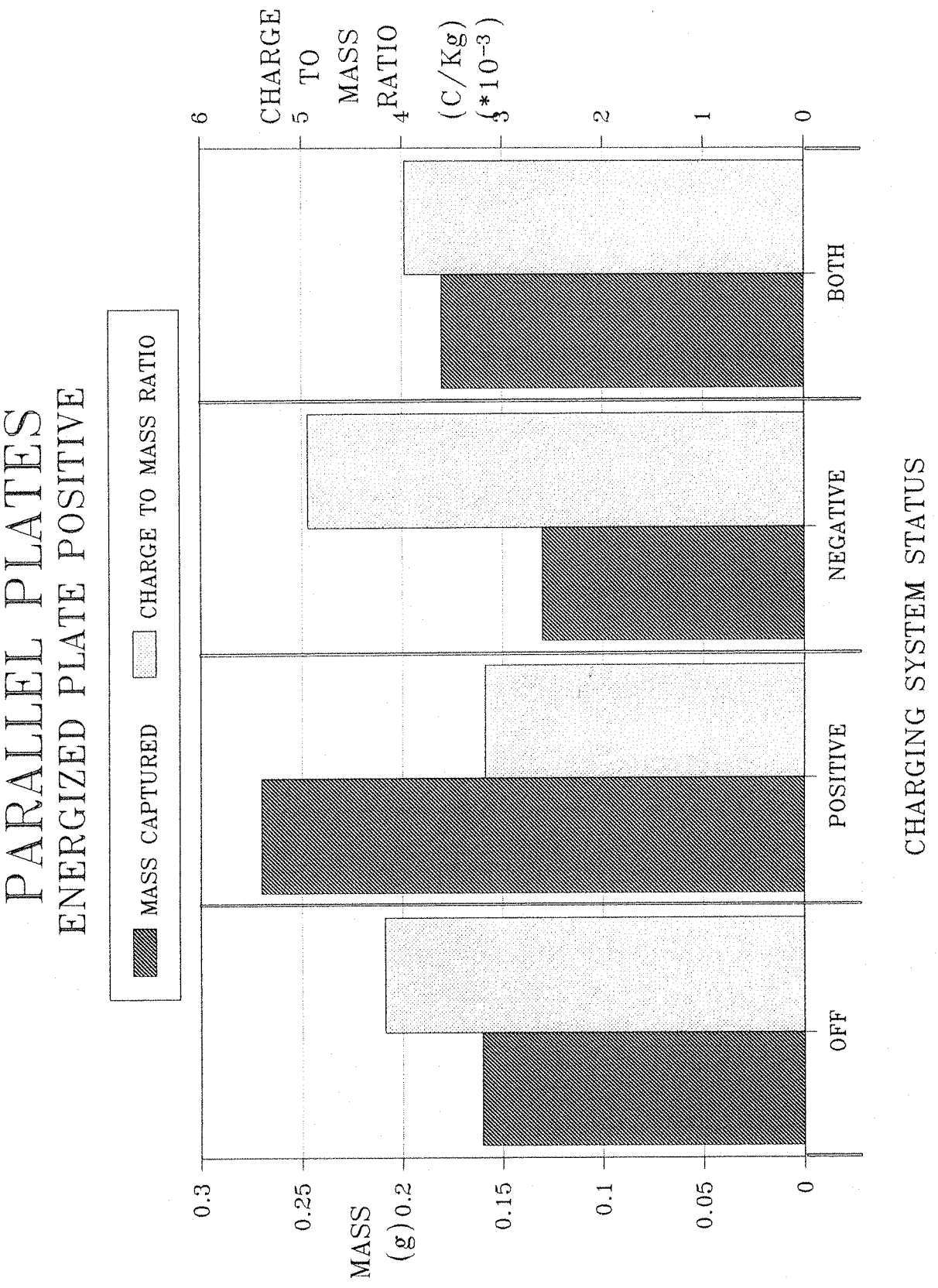

FIGURE 8.1.2 ASH DEPOSITION ON THE COLLECTING PLATE, ENERGISED PLATE AT A POSITIVE POTENTIAL

opposing plate energized the range of charge levels on the particles that can be captured had been increased. This would be expected as the force of deposition applied to all the charged particles will be greater when the electric field is applied.

8.1.3.3 ENERGIZED PLATE AT A POSITIVE POTENTIAL, NEGATIVE SECTION OF BI-POLAR CHARGER ENERGIZED

These tests were performed with only the negative section of the bi-polar charger energized. In this case it was expected that the ash deposited on the collector plate would consist of only the ash that had passed through the un-energized section of the bi-polar charger. The remainder of the ash would have been charged negatively, and would be attracted towards the positive energized plate. The result was therefore expected to be similar to the result seen in the first set of tests in this series, when neither of the charging electrodes were energized. In fact the mass of the ash captured was less than had been seen previously which was consistent with the supposition, because in this case half the available ash has been charged negatively. However, the charge to mass ratio, which was still positive, was greater than had been seen earlier. This increased charge to mass ratio value may be due to the size distribution of the ash changing prior to reaching the parallel plates. This apparent change in the particle size distribution is possible as the positive charging section of the bi-polar charger is above the negative section. So the larger particles with a lower potential Pauthenier charge to mass ratio limit would preferentially pass through the negative charger. While conversely, the finer particles with the higher potential Pauthenier charge to mass ratio limit would have passed through the positive section, towards the top of the test duct. So in fact, the finer particles would have passed through the un-energized positive charging section of the bi-polar charger. This would result in the natural charge to mass ratio of the captured ash being greater than would have been recorded had the particle size distribution of the un-charged sample been consistent with the original ash sample particle size distribution.

8.1.3.4 ENERGIZED PLATE AT A POSITIVE POTENTIAL, BOTH SECTIONS OF THE BI-POLAR CHARGER ENERGIZED

The final set of tests within this series, with the energized plate at a positive potential, was to run the system with both of the charging units of the bi-polar charger energized at opposite polarities. The charge to mass ratio of the captured ash was again found to be positive, with a value of about average for these tests. However, the actual mass of ash caught was significantly less than had been captured when only the positive charging electrode had been energised. This indicates that there are less free positively charged particles available for deposition. So, as was seen in the previous series of tests with both plates grounded, the un-captured positive particles must be in some way attached to particles of the opposite polarity to produce an agglomerate with a reduced net charge and an increased mass.

8.1.4 ENERGIZED PLATE AT A NEGATIVE POTENTIAL

In this, the final series of tests using the parallel plates, the energized plate was connected to the high voltage power supply at a negative potential of -20kV. These tests were similar to the tests of the previous series, where the energised plate was connected to a positive potential.

With a negative potential on the energized plate, the negatively charged particles will be repelled from the plate and deposited onto the collector plate, while conversely the positively charged particles will be attracted towards the energized plate. All the precautions that were required for the tests when the energized plate was at a positive potential, to ensure the prevention of any electrical discharges from either plate, were also applied for these tests.

The results of this series of tests were tabulated and bar charts of the mass of ash captured and the charge to mass ratio of that ash plotted for the normalized one minute test period. The results are shown in Table (8.1.3) and the bar charts plotted in Figure (8.1.3).

ENERGISED PLATE -20KV	BI-POLAR CHARGER STATUS			
	OFF	POSITIVE SECTION ON	NEGATIVE SECTION ON	BOTH SECTIONS ON
CHARGE (C)	-3.1×10^{-7}	-0.42×10^{-7}	-14.6×10^{-7}	-9.9×10^{-7}
MASS (g)	0.09	0.10	0.32	0.19
Q/M (C/Kg)	-3.44×10^{-3}	-0.42×10^{-3}	-4.56×10^{-3}	-5.21×10^{-3}
CHARGE (C)	-3.4×10^{-7}	-0.38×10^{-7}	-13.2×10^{-7}	-10.0×10^{-7}
MASS (g)	0.10	0.11	0.26	0.26
Q/M (C/Kg)	-3.40×10^{-3}	-0.35×10^{-3}	-5.08×10^{-3}	-3.85×10^{-3}
CHARGE (C)	-2.5×10^{-7}	-0.72×10^{-7}	-14.4×10^{-7}	-11.4×10^{-7}
MASS (g)	0.07	0.13	0.30	0.24
Q/M (C/Kg)	-3.57×10^{-3}	-0.55×10^{-3}	-4.80×10^{-3}	-4.75×10^{-3}
AVERAGE CHARGE (C)	-3.0×10^{-7}	-0.51×10^{-7}	-14.1×10^{-7}	-10.4×10^{-7}
AVERAGE MASS (g)	0.09	0.11	0.29	0.23
AVERAGE Q/M (C/Kg)	-3.47×10^{-3}	-0.44×10^{-3}	-4.81×10^{-3}	-4.60×10^{-3}

TABLE 8.1.3 THE CHARGE AND MASS OF THE ASH CAPTURED WITH THE ENERGISED PLATE AT -20KV

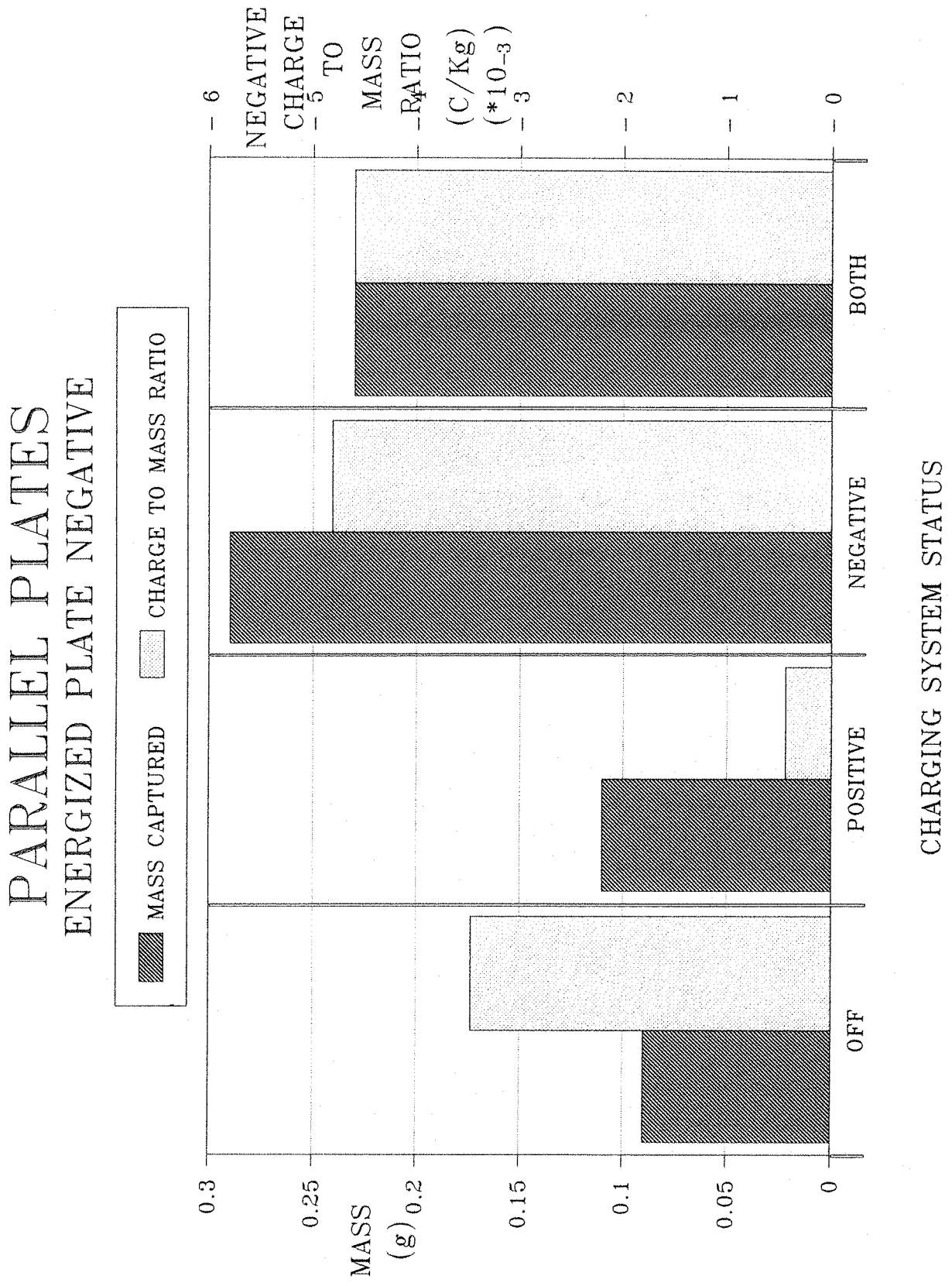

FIGURE 8.1.3 ASH DEPOSITION ON THE COLLECTING PLATE, ENERGISED PLATE AT A NEGATIVE POTENTIAL

8.1.4.1 ENERGIZED PLATE AT A NEGATIVE POTENTIAL, BI-POLAR CHARGER UN-ENERGIZED

The first set of tests in this series were with both of the charging units of the bi-polar charger un-energized. This produced a result much as expected, a low mass of negatively charged ash captured with a charge to mass ratio typical for these tests. The mass of captured ash was low as the majority of the ash within the duct was either uncharged, or had a natural positive charge. This predominantly positive natural charge on the ash has confirmed by the results of the previous two series of tests. However, as the charge to mass ratio of the captured ash was about typical, then the small amount of negatively charged particles that were caught were highly charged.

8.1.4.2 ENERGIZED PLATE AT A NEGATIVE POTENTIAL, POSITIVE SECTION OF BI-POLAR CHARGER ENERGIZED

These tests were made with only the positive section of the bi-polar charger energized. A moderate proportion of ash was captured with a very low charge to mass ratio. This low value of charge to mass ratio was the result of several mechanisms. The ash that had passed through the positive section of the bi-polar charger would be collected on the negatively energized plate, as this ash had a positive charge. So all the ash that had been deposited on the collector plate had to have passed through the un-energized negative section of the bi-polar charger; the bottom half of the charger. Since this ash consisted of predominantly the larger particles which had a lower potential Pauthenier charge to mass ratio limit, then a lower than average charge to mass ratio would be recorded. Also, it has been seen from the previous tests that the ash had a natural positive charge and so the number of naturally occurring particles within the ash cloud with a negative charge would be low.

8.1.4.3 ENERGIZED PLATE AT A NEGATIVE POTENTIAL, NEGATIVE SECTION OF BI-POLAR CHARGER ENERGIZED

In the third set of tests the negative section of the bi-polar charger was energized while the positive section remained un-energized. In this case the

amount of negatively charged ash that was deposited onto the collection plate was found to be very large, as was the charge to mass ratio of the ash. This result was much as expected as the negative charging section of the bi-polar charger had already proved itself capable of imparting a large charge on the ash.

8.1.4.4 ENERGIZED PLATE AT A NEGATIVE POTENTIAL, BOTH SECTIONS OF THE BI-POLAR CHARGER ENERGIZED

The final set of results from this series of tests were made with both the positive and negative sections of the bi-polar charger energized. The results showed only a slight reduction in the mass of ash captured compared to the mass captured when only the negative charging stage was energized. Also, the captured ash was seen to have a very large negative charge to mass ratio. This would seem to indicate that there had been some particle agglomeration, although there still remained a very large number of particles within the gas stream that had a significant negative charge. This excess of negatively charged particles was also seen in the previous series of tests, when both of the charging units were energized.

8.2 AGGLOMERATE SIZE MEASUREMENTS

The optical ash sampling tube, as described in Chapter four, was attached to the downstream end of the agglomeration test duct. Its inlet orifice was aligned with the end of the test duct just prior to the extraction system. The Malvern Particle Size Analyzer was then positioned beyond the far downstream end of the agglomeration test duct and carefully aligned so that its laser beam passed through the sampling tube at the measuring zone. It was important to ensure that the laser beam was not obscured by the sampling tube, even when diffracted by the ash particles being measured. This experimental arrangement was described in greater detail in Chapter four. The Malvern particle size analyzer can be seen in position with the optical sampling tube in Plate (4.5.1). In this location the optical sampling system could be used to measure the dynamic particle size distribution of the ash taken directly from the rig. This allowed for comparisons to be made between the particle size distributions

recorded when the bi-polar charger was energized or un-energized.

8.2.1 MEASUREMENTS

Measurements of the particle size distribution of the ash obtained using this optical system were very poor. The obscuration values of the measurements were found to be very low, indicating that there was not enough ash being measured by the particle size analyzer for the results to be statistically significant. This meant that, in order to obtain statistically significant results, long sample periods were required. However, it was also found that during the measurement, the finest of the particles within the ash cloud would deposit onto the glass windows of the sample tube. This deposition was found to bias the measured distribution more and more towards the fine particle sizes as the measurement proceeded. Many attempts were made to try to eliminate this problem, the most successful of which was to use 'O' ring seals on the glass windows which were punctured with many pin holes. These pin holes allowed enough air to flow in from the windows to oppose the flow of the ash particles out towards the windows, without generating too much turbulence within the measuring zone. Also, if too much air was drawn in from the windows the amount of ash being drawn from the test rig was then found to reduce. This would cause the sampling rate to cease being isokinetic, which would cause turbulence at the orifice of the sampling tube which in turn could break any agglomerated ash particles that may have been formed.

Even with the pin holes in the 'O' rings, the amount of ash deposited onto the glass windows was still found to be significant, as the sampling periods had to be very long to compensate for the low obscuration. For this reason all the results obtained were made by averaging many actual measurements together. All the measurements were made over a two second interval, after allowing the sampling system to run for a period of only one second in order to stabilize the air flow through the sampling tube. If the sampling system was turned off after this three second test period, and a particle size measurement made, then the resultant distribution would be that of the ash deposited on the glass windows. The obscuration value of this measurement was found to be low in comparison to the obscuration during the actual measurement of the sample, indicating that the ash deposited on the windows was not too significant on the measured

particle size result. The windows then required cleaning before the next measurement could be made.

8.2.2 DYNAMIC MEASUREMENTS OF THE PARTICLE SIZE DISTRIBUTION OF THE UN-CHARGED ASH

The first measurements with the optical sampling system were made with the bipolar charger un-energized. This produced a particle size distribution of the un-processed ash being extracted from the rig. Assuming that there were no preferential losses, then this distribution should be the same as the size distribution of the ash within the rig, which should be the same as the input particle size distribution from the powder feed gun. However, as seen in Chapter six, the larger particles within the distribution preferentially fall out of the gas flow. This will result in the particle size distribution of the ash being sampled from the end of the test rig consisting of finer particle than the input particle size distribution from the powder feed gun.

The results were obtained, as described above, by averaging several particle size measurements. The parameters of this averaged distribution are given in Table (8.2.1), along with those from the dry fed 'New Ash' sample, the dry fed 'Old Ash' sample and the dry fed 'Drop Out' sample. The measured histograms of these distributions were also plotted and are shown in Figure (8.2.1).

8.2.2.1 OBSERVATIONS

It can be seen from the tabulated data that even though the newer ash samples supplied by C.E.R.L. were used for all these tests. The measured dynamic particle size distribution produced a result with a mass median diameter far less than had been found for all these newer ash samples, but very close to that of the 'Old Ash' sample. In fact this measured particle size distribution should be the difference between the dry fed 'New Ash' distribution and the dry fed 'Drop Out' sample. As the Drop Out sample had been shown to consist of mostly the un-burnt part of the original sample, then this measured distribution must consist of mainly the ash particles. Hence, its similarity to the 'Old Ash'

sample which contained no un-burnt fuel particles.

SAMPLE NAME	MASS MEDIAN DIAMETER	90% POINT	10% POINT	SPAN
	(μm)	(μm)	(μm)	----
NEW ASH	17.9	76.0	3.7	4.0
OLD ASH	7.9	19.5	3.7	2.0
DROP OUT	52.3	91.0	13.2	1.5
SAMPLED	6.7	21.5	3.0	2.8

TABLE 8.2.1 PARTICLE SIZE PARAMETERS

The fact that the larger particles were absent from this measured distribution is beneficial, as greater significance is placed on the finer particle size ranges within the distribution. These fine particles being the particles in which we are interested. However, any quantitative results of the effects of agglomeration would have to consider the entire input particle size distribution and not just the sampled output.

From the graph in Figure (8.2.1) it can be seen that nearly all of the second peak of the original dry fed distribution is absent from the dynamically measured distribution. This confirms that nearly all the un-burnt fuel has been removed from the ash cloud prior to reaching the end of the test duct. As was stated above, the loss of these un-burnt fuel particles is beneficial. However, if there has also been a considerable loss of the large ash particles from the ash cloud, then it would not be easy to determine whether or not the finer particles had become attached to the larger particles during the agglomeration process. The graph also shows that the amount of very fine particles within the distribution was almost the same as for the dry fed sample, indicating that the

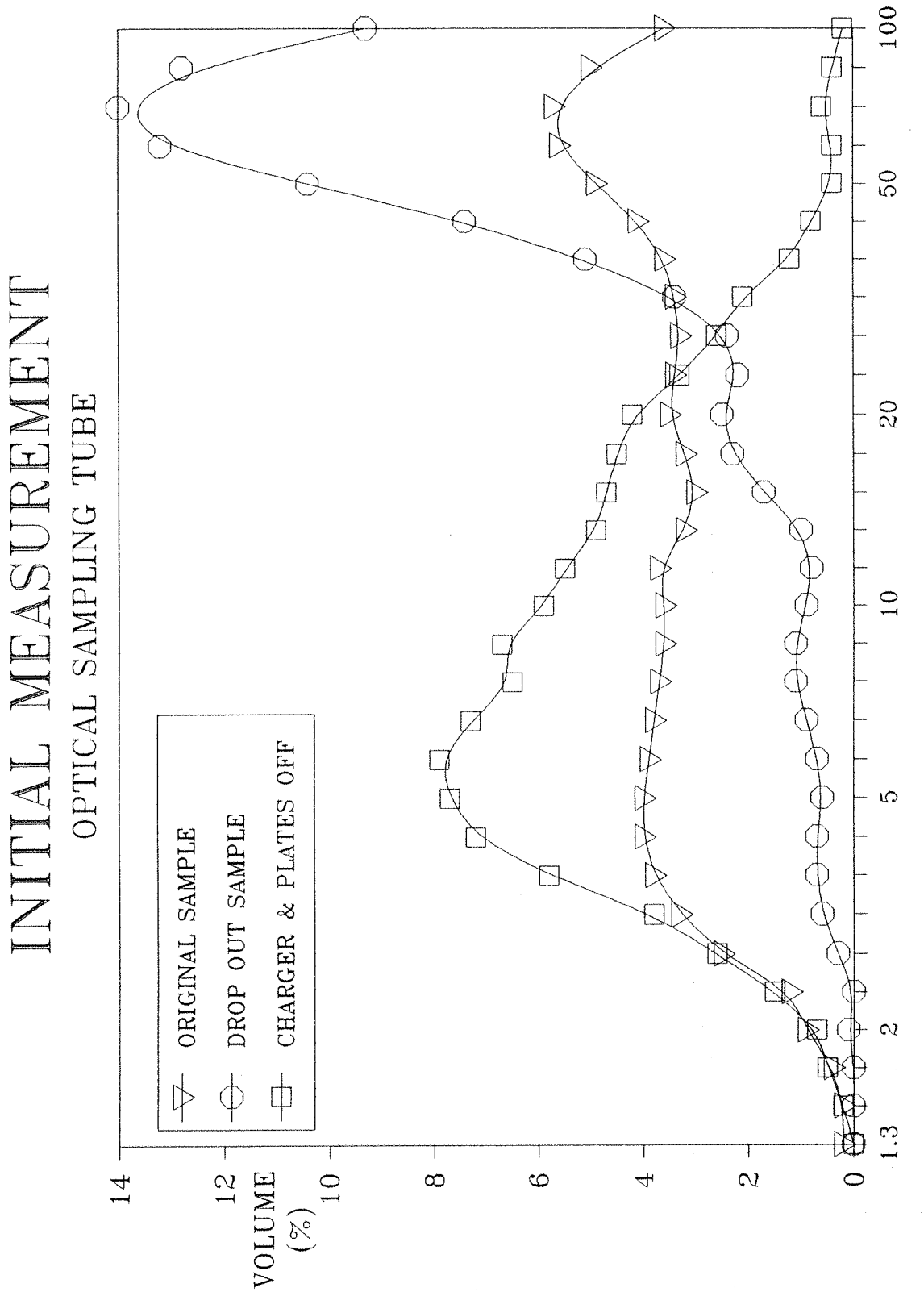

FIGURE 8.2.1 OPTICALLY SAMPLED ASH
BI-POLAR CHARGING SYSTEM UN-ENERGIZED

build up of these fine particles on the glass windows of the sampling system neither depleted the sample of them nor biased the resulting measurement towards them.

8.2.3 DYNAMIC MEASUREMENTS OF THE PARTICLE SIZE DISTRIBUTION WITH THE BI-POLAR CHARGER ENERGIZED

In this case a dynamic particle size measurement was made of the ash with both sections of the bi-polar charger energized to opposite polarities. The results were obtained, as before, by averaging several actual measurements. The average parameters of this distribution are given in Table (8.2.2), along with those from the previous test with the bi-polar charger un-energized. The two averaged histograms were also plotted in Figure (8.2.2).

BI-POLAR CHARGER STATUS	MASS MEDIAN DIAMETER	90% POINT	10% POINT	SPAN
	(μm)	(μm)	(μm)	----
OFF	6.7	21.5	3.0	2.8
ON	6.9	19.0	3.1	2.3

TABLE 8.2.2 PARTICLE SIZE PARAMETERS

8.2.3.1 OBSERVATIONS

The measured parameters for the agglomerated case show an increase in the mass median diameter of only 3% and also a 3% increase in the particle size below which 10% of the volume of the ash lies. Although these results seem to indicate that there possibly had been a small amount of particle agglomeration,

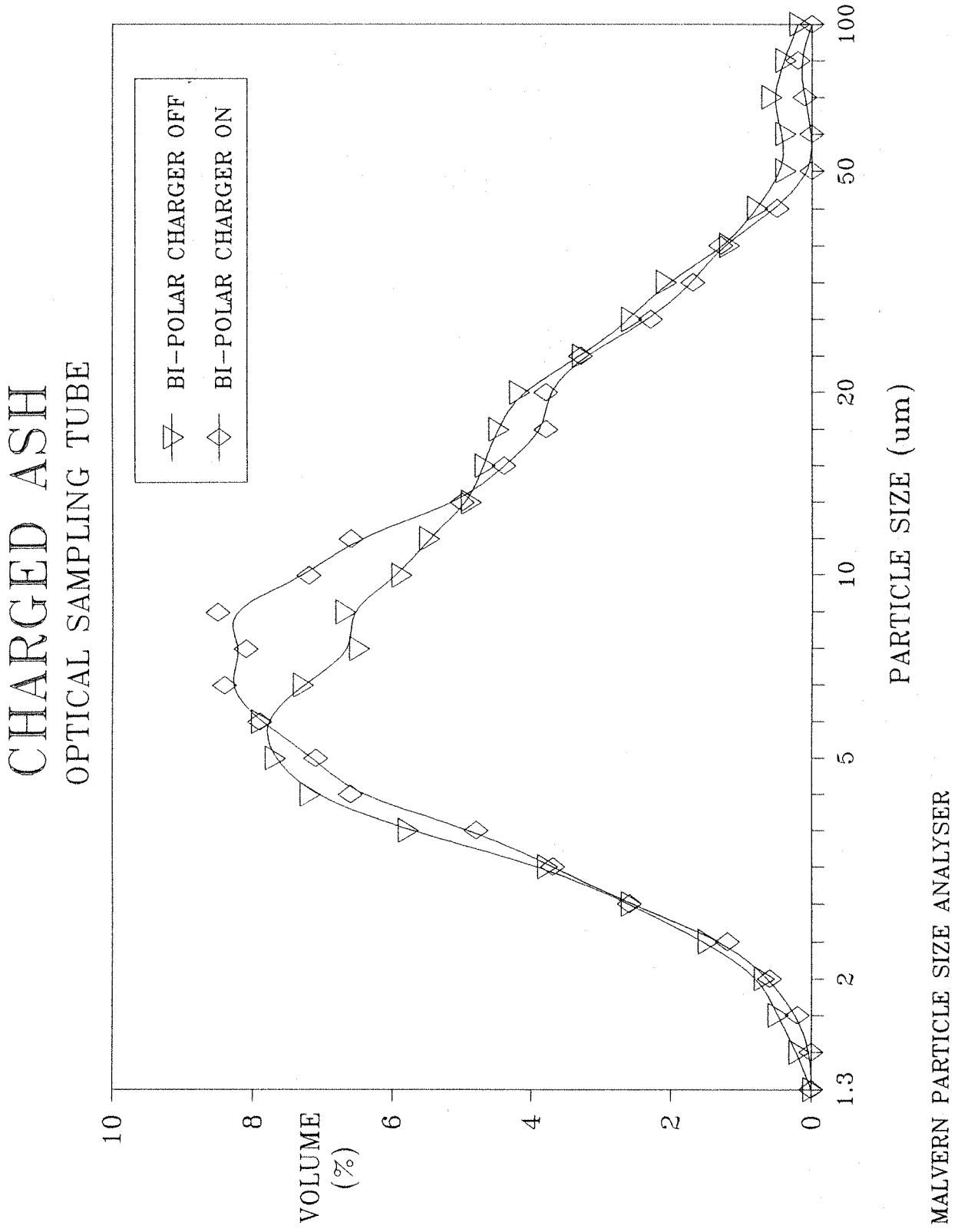

FIGURE 8.2.2 OPTICALLY SAMPLED ASH
BI-POLAR CHARGING SYSTEM ENERGIZED

they are hardly significant and are at the limits of the resolution of the Malvern instrument.

From the histograms plotted in Figure (8.2.2) it can be seen that the two distributions are almost identical. Even though the measurement made with the charger energized seems to have biased the result away from the fines, this result is not significant; especially considering the variation in the actual measured samples being averaged to produce the result. This variation was in fact greater than the 3% difference between the two figures shown here. However, averaging many more measurements both with and without the bipolar charger may in fact show that there is a general increase in the particle size distribution of the ash within the rig, and that the reduction of the number of fine particles seen here is a true indication of electrostatic agglomeration.

8.3 DYNAMIC MEASUREMENTS OF THE PARTICLE SIZE DISTRIBUTION WITH THE BI-POLAR CHARGER AND THE PARALLEL PLATES ENERGIZED.

The parallel plates, described earlier in this chapter, were now relocated in their original position at the far downstream end of the test duct; just up stream of the inlet orifice of the optical sampling tube, as can be seen in Figure (4.7.1) and Plate (6.3.1).

For these tests both of the plates were energized to 10kV, one positive and the other negative. The separation between the plates was again set to 5cm. In this mode it has been shown that a large proportion of the charged particles that pass between the plates are removed from the ash cloud; thus, leaving an increased proportion of un-charged particles to be sampled by the optical system. The presence of these un-charged particles could be due to one of three effects: First, the particles may never have been charged by the bi-polar charger. Secondly, the particles may have been charged but subsequently lose their charge through conduction. Thirdly, the un-charged particles may in fact be agglomerated particles with a net charge close to zero. It has been shown earlier in this report that the bi-polar charger is very efficient at charging all of the ash particles that pass through it, so it is unlikely that the un-charged particles were

never charged. It is also unlikely that the particles have discharged as the time constant for this process has been shown to be long compared to the time the particles will stay within the test rig. So any particles that are sampled by the optical sampling tube are more than likely to be agglomerates.

The bi-polar charger was fully energized for all these tests.

Again the results were obtained by averaging together many actual measurements of particle size. However, in this case the obscuration of the laser beam was found to be even lower than for the previous tests, indicating that even less ash was now entering the sampling system. The averaged parameters of this measured distribution along with the averaged parameters of the distribution found when the bi-polar charger was un-energized and the plates absent from the rig, are given in Table (8.3.1). The histograms of these two distributions are also plotted in Figure (8.3.1).

BI-POLAR CHARGER	MASS MEDIAN DIAMETER	90% POINT	10% POINT	SPAN
	(μm)	(μm)	(μm)	----
OFF	6.7	21.5	3.0	2.8
ON	9.0	17.1	4.2	1.4

n.b. For the measurement with the bi-polar charger energized, the parallel plates were also energized and in position within the test duct.

TABLE 8.3.1 PARTICLE SIZE PARAMETERS

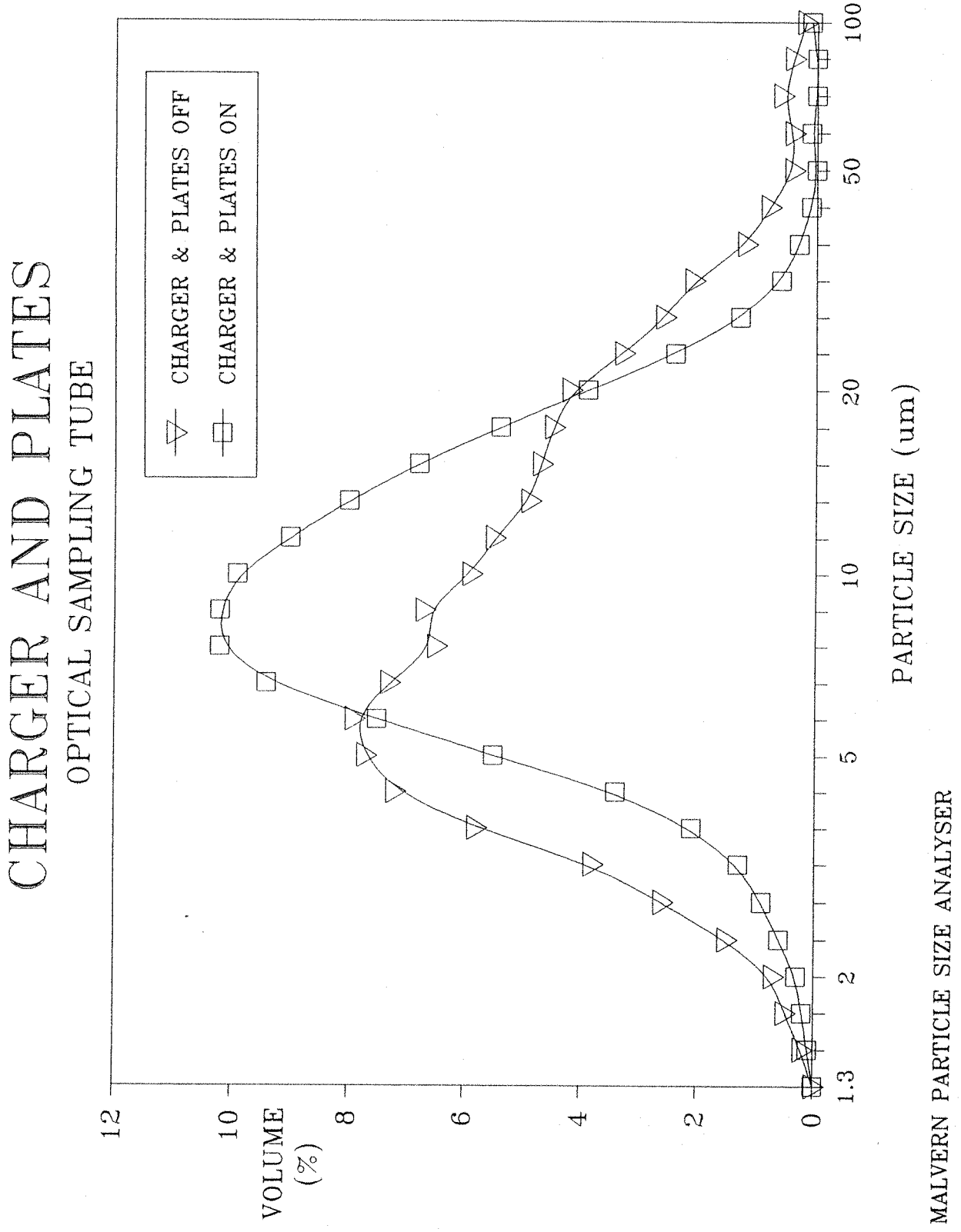

FIGURE 8.3.1 OPTICALLY SAMPLED ASH WITH AND WITHOUT BI-POLAR CHARGING

8.3.1 OBSERVATIONS

In this case there is a very great difference between the two results. First, from the histogram plot in Figure (8.3.1) it can be seen that the shape of the graph generated from the measurements with the bi-polar charger on and the plates energized, is much smoother than all the histograms produced of particle size so far. This is probably just the effect of having to average together so many actual measurements in order to get the plot.

From the table of averaged data, Table (8.3.1), it can be seen that there has been an increase in the mass mean diameter of 34%, with a 40% increase in the particle size below which 10% of the volume of the sample lies. This result shows that the loss of fines must be through some form of agglomeration, as they would not have been preferentially precipitated out of the ash cloud by the parallel plates. The results also shows a reduction in the size under which 90% of the volume of the sample lies, with an associated reduction in the span of the distribution. This loss of large particles was not expected from the agglomeration process, and must be due to their being precipitated out of the ash cloud by the parallel plates. This is quite likely, as these particles are easily captured by electrostatic precipitation. However, there could be a number of fine charged particles agglomerated to oppositely charged larger particle, but still leaving the large particle with a significant net charge to cause its precipitation within the electric field between the parallel plates.

By looking again at the histogram plot in Figure (8.3.1), it can be seen that there has not just been an increase in the size below which 10% of the volume of the sample lies, but almost all of the very fine particles (sub 2μm) are absent from the distribution.

CHAPTER NINE

9.1 CONCLUSIONS

It has been shown that the cleaning of industrial gasses, in order to remove solid particles, is of considerable economic and environmental importance. Particulate matter must be removed from gas supplies used in chemical processes and from the air supplied to clean rooms, especially in the case of semiconductor wafer fabrication, where a single sub-micron dust particle can completely destroy a silicon device. Also, it may be that the cost of the particles warrant the cost of their capture for re-cycling purposes. However, the main consideration of this study was the capture and removal of solid particles from flue gasses being vented into the atmosphere; in particular fly-ash emissions from coal burning power stations.

It has been shown, based on figures for the U.S.A., that up to 47.9% of solid airborne pollution emanates from heating and power generation. These particulate materials are an environmental hazard in themselves but moreover, it is the chemical compounds adsorbed onto the surfaces of these particles that pose the greater environmental threat. In fact the same survey of U.S. air quality reports that 74.9% of all sulphur dioxide emissions come from heat and power generation. The effects of this pollution is to increase the acidity of the precipitation in the fall out areas. This acidity can then have a considerable effect on the animal and plant life living in these areas, and may even result in their death. However, most biological systems have quite considerable resistance to increased acidity. Soil in fact has buffer systems that can cope with acidity levels of up to 2.4pH. However, these buffer systems can result in the build up of ions of elements such as aluminium, which when dissolved in the general water supply can be poisonous.

By studying global acid rain fall maps in conjunction with net weather flow maps, it is possible to pinpoint areas suffering from excessive acidic precipitation and then trace back to the source of the pollution. Such a chart is shown in the first chapter of this thesis, which shows the U.K. and northern Europe as producers of air pollution resulting in acidic precipitation over Scandinavia, contributing to the U.K. earning the un-prestigious title of "the dirty man of Europe".

Many different types of gas cleaning systems have been reviewed in this thesis, from the simplest gravitational settlement chambers through to the most complex electrostatic precipitation systems. Some of these gas cleaning systems can boast very high particle removal efficiencies, especially those relying on more than one capture mechanism. In fact figures up to 60 to 70% are claimed for some of the commercially available mechanical devices and up to 98% is not uncommon for electrostatic precipitation. However, these figures are usually based on the volume or mass of captured particles and do not consider the number or size of the particles captured. In fact the very finest particles can evade capture from all the gas cleaning systems considered. Ironically, it is these fine particles that are of the greatest concern as regards to air pollution, as they are able to drift up to great heights within the atmosphere and be carried great distances. Also the very fine particles have a greater surface area per unit volume than the larger particles. It is on the surfaces of the particles that many of the pollutants become adsorbed.

The aim of this research was to investigate a mechanism for the capture of these very fine particles. The intended mechanism was that of electrostatic agglomeration. The particles are split into two streams and then charged to opposing polarities, the two streams of particles are then recombined in such a way as to encourage the particles to form an electrostatic bond to one another. This should increase the average particle size of the distribution to within the capture particle size range of existing capture systems. Electrostatic agglomeration was chosen, as electrostatic precipitation is the favoured mechanism of particle capture within the fossil fuel power generation industries.

The method of charging considered in this study was that of corona. Corona charging was chosen as, historically, no other method of exhaust gas particle charging has been found to be satisfactory. Also, the process of corona

charging is less dependent on the ambient conditions than other mechanisms, although, it is the least power efficient of all the processes available.

It has been shown that if a particle can be charged to a large proportion of its Pauthenier limit charge, then an electrostatic bond between two such oppositely charged particles may result. This bond can have a strength several orders of magnitude greater than the force on the particles due to gravity. It is however important to remember that the bond between two agglomerated particles need not only be strong enough to withstand the shear forces that may be present within the agglomerater, but also strong enough to withstand any forces incurred in the subsequent capture processes.

The measurement of the physical parameters of the ash and all the mechanisms involved in the process were considered in some detail. Some of these parameters are fairly well defined and quite straight forward to measure, such as the particle resistivity and the gas flow rates. However, many of the parameters important to assessing the agglomeration process, were not so easy to measure and required the fabrication of special measuring systems. These included a continuous flow Faraday cup, which allowed isokinetic sampling of the ash from within the test rig in order to determine the on-line charge to mass ratio. Another important measurement was the dynamic measurement of the particle size distribution. This measurement could be used as an indication of the degree of particle agglomeration that had occurred. This required the fabrication of a system that could extract particles from any point within the rig and feed them through the measuring zone of the Malvern particle size analyzer. It was of particular importance that this system exerted the minimum of shear forces on the particles being sampled, as these forces could act to break any agglomerates that may have been formed.

Extensive work has been carried out on characterising the ash particles, so that the theoretical considerations could be applied to the ash system, allowing predictions of the particle behaviour to be made. Examinations of particle size, shape, conductivity and charge decay rate were made. The results of which showed that the ash being considered in this study was surprisingly spherical in shape, allowing confidence in the theoretical considerations as no correction for shape, other than spherical, had been applied. Also the high resistivity of the ash particles confirmed their suitability for corona charging, as

the rate of charge accumulation and maximum charge achievable, given by Pauthenier, has only a factor of three difference between an insulating particle and a conducting particle. The very high field strength within a corona coupled with the expected time the particle will remain within this high field should produce a very highly charged particle. Once out of this high field region the high resistivity and hence long charge decay rate would indicate that the particle will not quickly discharge.

The extensive analysis of the ash in this manner has brought to attention the very large amount of un-burnt fuel particles found within the ash samples. This fuel was probably the result of inefficient burners at the power station from which the sample was collected. Although it is a consideration that may effect the performance of an electrostatic agglomerater the un-burnt fuel was not of prime importance in this study.

While preparing samples for separation tests, where a sample of the ash is dispersed in water to form a suspension, it was noted that if a magnetic stirrer was used, a small proportion of the ash remained attached to the magnet. Further examinations of this magnetic property of the ash were performed which showed the magnetic material to be ferro-magnetic. However, a great deal of further investigation is required to determine whether this interesting property of the ash is in any way beneficial in the cleaning of the gas or in the reclamation of un-burnt fuel.

A test rig was developed which allowed the simulation of how an industrial scale unit might function. This rig had to have several attributes, including an extraction system, an input system, a charging zone and an agglomeration zone.

The input stage of the test rig had to produce an evenly dispersed ash cloud, whose instantaneous particle size distribution at any position across the width of the duct was constant to that of the initial ash sample. The ash load had also to be variable and controllable and had to have a net charge of zero. This generated ash cloud then had to be introduced into the test duct as straight and as even as possible, and any large eddies within the flow had to be removed. These requirements for the input system were satisfied by using an electrostatic powder coating spray gun to generate the ash cloud and spraying the ash into

a one metre long input duct, connected to the test duct by a flow straightener. The input duct allowed the ash to become evenly dispersed through the width of the duct before entering the test duct. The flow straightener removed the large eddies from the ash-laden air flow, although the gas flow mode on entering the test duct would still be 'turbulent', as opposed to 'laminar'.

The actual test duct was a one metre long box section duct with sides measuring 300mm by 500mm. The 300mm sides were constructed from clear acrylic sheet, which allowed for the examination of the ash flow within the rig. It was within this one metre section of the duct that the charging, mixing and agglomeration processes would occur.

The velocity of the ash laden air stream was controlled by the extraction system, an induced draft fan driven by a d.c. motor with variable speed control. Typical gas velocity and ash load values for electrostatic precipitaters were sought from C.E.R.L. and these rates used as target values in order to mimic the envisaged industrial conditions as closely as possible. However, it must be remembered that the test duct was only a fraction of the size of an envisaged industrial unit.

In the initial testing of the agglomeration rig it was found that a considerable proportion of the ash had 'fallen out' of the gas stream and was seen to accumulate on the base of the test duct. A sample of this ash was collected and fed through the dry powder feeder and a particle size distribution measurement made with the Malvern system. It was found that this ash sample consisted of the largest particles from within the original distribution, as would be expected as they are less well entrained within the air stream. Examinations of this sample under the optical microscope revealed that the sample was almost entirely made up of the un-burnt fuel particles.

The first part of the agglomeration process was to split the ash laden gas stream into two separate streams and then charge one half positively and the other half negatively. These two streams then have to be recombined and mixed in such a way as to promote agglomeration with oppositely charged particles. Several Corona charging systems were designed to perform these tasks, although, only one proved effective and was further developed. A two dimensional field calculating package was used to optimise the design of the

charging stages.

The discharge electrodes must impart the maximum possible charge onto the ash particles, without causing an ion wind in opposition to the ash flow. Should there be an ion wind in opposition to the gas flow, then the ash particles could be slowed to the point where they will be deposited onto the grounded parts of the charger. This deposited ash layer could then produce back ionization which would discharge the ash. The deposited layer may also act to quench the corona, as the electric field across the charged ash layer will reduce the field at the corona points. This will further reduce the efficiency with which any ash passing through the charger will be charged.

The final design of the bi-polar charger consisted of two double edged saw tooth electrodes measuring 500mm long, each with 76 corona points. These discharge electrodes were folded along their length at an angle of 60°, and located in the charger so that the saw tooth edges pointed down stream. The bend angle of 60° was chosen as the field simulation results indicated that this angle would produce the optimum flux, with little or no ion wind in opposition to the ash flow. Each of these electrodes were surrounded by a metallic box section mesh, measuring 500mm long by 100mm wide and 100mm tall. The mesh, constructed from wire with a spacing of 5mm, was grounded so as to act as the intensifying electrode for the corona discharge. These two charging units were separated by a large central cylinder, measuring 500mm long and 100mm in diameter. This cylinder functioned as a flow splitter, as well as producing a great deal of turbulence down stream of the charger to promote the mixing of the two ash streams.

Subsequent testing of the charger using the continuous flow Faraday cup, proved it was capable of imparting a considerable charge onto the ash, even after long periods of use.

A pair of parallel plates were used as a simple electrostatic precipitator. It was intended, that by capturing ash particles by electrostatic precipitation over a fixed period of time, and measuring the mass and the charge of this captured ash, that evidence of agglomeration could be found. The parallel plates were used to asses the degree of particle charging from each stage of the bipolar charger in turn. The results of these tests could then be used in comparison with

the results obtained when the charger was fully energised to determine if charged particles had been used to form agglomerates.

It was found that both sections of the bi-polar charger were able to impart a large charge onto the ash. However, it was also found that the larger particles were passing through the bottom half of the charger (the negative half). These particles, due to their increased mass, have a lower Pauthenier limit charge and hence slightly lower charge to mass ratios were measured from the negative section of the charger.

The use of the parallel plates demonstrated that there had been some degree of particle agglomeration, although how much was unclear. The results indicated that the bi-polar charger was able to impart very large charges onto the ash particles. However, the results also indicated that the mixing/agglomeration stage of the test rig was not able to thoroughly mix all the particles, as large amounts of highly charged particles were still found within the ash cloud after the agglomeration stage. It must be remembered, however, that it is both possible and likely that agglomerates will form with a net charge other than zero. For this reason, a more exact measure of particle agglomeration was required.

The optical sampling system developed in this study was used in conjunction with the Malvern particle size analyzer in order to determine if the agglomeration process had been successful in producing a shift in the particle size distribution of the ash. This sampling system did not, however, operate as well as was hoped. The ash concentrations within the measuring zone of the laser system were found to be very low, resulting in statistically poor results unless long sampling periods were used. Long sampling periods, however, resulted in the build up of the finer ash particles on the laser windows. These ash deposits were then found to bias the measurements. Many attempts were made to reduce these particle deposits, although none were entirely satisfactory as they either further reduced the volume concentration of the ash within the measuring zone, or added too much air turbulence to the system, which could have broken any agglomerates that may have been formed.

Initially the measurements made with the optical sampling system were not very encouraging, and did not show a great deal of agglomeration.

Consequently the optical system was used in conjunction with the parallel plates, which had proved capable of removing almost all the charged particles from the ash cloud. It was hoped that the charged particles would be the un-agglomerated particles, thus leaving only the agglomerates to pass through the optical sampling tube. However, this assumption may not be totally valid, as agglomerates can form with very high charge levels, especially in the case of a fine particle becoming attached to a large particle. In which case, the mass of the agglomerate will be only slightly greater than the mass of the large particle, and the net charge will be only slightly less than the original charge of the large particle. So agglomerates of this form are highly charged and may well be removed from the ash cloud by the parallel plates.

When the parallel plates were energized, the volume concentration of the ash within the laser beam was found to be even lower than before, as so much ash was being removed from the ash cloud before it entered the particle sizing system.

The actual particle size measurements now showed significant changes from the original distribution, including the almost total loss of particles below 2μm along with an increase in the mass median diameter of 34%. This indicated that there had been a great deal of agglomeration. The loss of fines cannot be due to their being precipitated out by the parallel plates, as their electrical mobility would be too low. So their absence from the measurement must be due to them forming agglomerates with larger particles and, either being precipitated by the parallel plates, or if the agglomerate had a net charge close to zero, being measured as a single larger particle by the Malvern particle sizer.

The effects of the agglomeration process and the precipitation process cannot be separated in these results. Measurement of the particle size distribution with the parallel plates energized but without the bipolar charger, could not be performed, as the particles passing between the plates would not be charged.

9.2 FUTURE RESEARCH

9.2.1 MEASUREMENTS (OPTICAL)

A better optical system is required for the dynamic measurements of the particle size distribution. The system developed in this study either had not enough ash passing through it or too much ash depositing onto the laser windows. This made measurements very complex and time consuming, resulting in doubt as to the validity of the results.

The system developed was based on the Malvern particle sizer, which assumes the particles being measured to be spherical and gives no indication of the particle shape. This is fine for the ash particles alone, which have been shown to be spheres, but the agglomerates are expected to be irregular in shape and may even be chains. A particle sizing system that creates images of the particles being measured may give a more accurate indication of the extent to which agglomeration has occurred.

9.2.2 MEASUREMENTS (MIXING)

The degree of particle mixing has been very difficult to assess, as it is unclear whether all the charged particles are forming agglomerates. At present, the best indication of the degree of mixing that has occurred is gained from the charge to mass ratio of the ash with and without the agglomerator energized. However, agglomerates will form with a net charge other than zero, making it difficult to assess the degree of agglomeration.

9.2.3 AGGLOMERATION CAPTURE

Once it can be demonstrated that agglomerates can be produced through electrostatic attraction, then the next stage would be to consider the bonding strength of these agglomerates. It was originally intended that these agglomerated fly-ash particles be removed from the gas flow by an electrostatic precipitator located down stream from the agglomerator. However, it is not

known what effect the charging stage of the precipitator might have on the agglomerates, as the electrostatic bonding force may well be modified by the new net charge. Also, it is not known how much mechanical shear stress the agglomerates can withstand without breaking up.

9.2.4 ASH CONDITIONING

The surface condition of the ash particles is very important to the electrostatic processes, as the surface resistance of particles will affect the rate of charge relaxation by conduction, and also the maximum charge level achieved. The charge imparted to the particle will lie on its surface, so some form of charge accepting species must exist on this surface.

It is well known that the surface properties of ash change quite rapidly after removal from hot flue gasses. On cooling, the chemical composition of the surface of the ash particle will change and water vapour from the atmosphere will be adsorbed onto the surface. This results in a low resistance path for current flow.

For these reasons it may be beneficial to treat the ash being used in the experimental investigations. Heating the ash and conditioning its surface before passing it through the test rig may prove beneficial, as the ash will now have physical properties close to those of the fresh ash exhusted from the power station burners.

9.2.5 FUNDAMENTAL INVESTIGATION

It may also be beneficial to undertake some more fundamental investigation into the behaviour of fly-ash and fly-ash agglomerates. i.e. measuring the bond strength under very carefully controlled conditions. This may aid with the optimization of the charging and agglomeration stages. The degree of particle mixing required to move particles to sufficiently close proximity for an electrostatic attraction to become dominant is also not clearly understood, and may also be an area worthy of future research.

REFERENCES

1.1 SABERT OGLSSBY, Jr. & GRADY B. NICHOLS:
-Electrostatic Precipitation:
-Marcel Dekker, Inc.

1.2 DONOVAN R.P, YAMAMOTO T, CLATON A.C. & ENSOR D.S. (1987):
-Dependence of particle deposition velocity on silicon wafer surface temperature:
-Electrochem soc. Fall meeting.

1.3 HASHISH ADEL:
-The influence of electrostatic charge on the deposition of therapeutic charged aerosols and airborne pollutant particles within the human respiratory system:
-A thesis submitted for the degree of doctor of philosophy:
-University of Southampton.

1.4 WELLBURN ALAN (1988):
-Air pollution and acid rain:
-Longman Scientific & Technical.

1.5 The Watt committee on energy:
-U.K.

1.6 WHELPDALE D.M:
-W.H.O. Centre on surface and ground water:
-Plenum Press.

1.7 WRIGHT (1977):
-SNSF report:
-TN 34/77, pp71.

1.8 ALABASTER & LLOYD (1980):
-Water Quality Criteria for freshwater fish:
-pp21-45:
-Butterworths.

1.9 THE TIMES, (JUNE 30 1858):

1.10 TAFFE PETER, (Dec 1988):
-The big clean up:
-pp620-631:
-Engineering.

2.1 STRAUSS W. (1966):
-Industrial gas cleaning:
-Pergamon press.

2.2 STAIRMAND C.J (1970):
-Filtration and separation:

2.3 STRAUSS W. & MAINWARING S.J. (1984):
-Air pollution:
-Edward Arnold.

2.4 ROGERS E.M.:
-Physics for the inquiring mind:
-Oxford University Press.

2.5 GILBERT W.:
-De magnete:
-English translation by S.P. Thompson:
-24-25 London 1900.

2.6 CHARLES DE COULOMB:
-Memoires de l'academie royale des sciences:
-1785-1789.

2.7 HOLFIELD M.:
-Archive fur die Gesammte Naturlehre:
-2, 205.
-1824.

2.8 LODGE O,J.:
-Nature:
-28, 297:
-1883.

2.9 COTTRELL F.G.:
-J. Ind. Eng. Chem.:
-3, 542-550:
-1911.

2.10 COTTRELL F.G.:
-J. Eng. Mining:
-101, 385-392:
-1916.

2.11 COTTRELL F.G.:
-U.S. Patent 895,729.
-1908.

3.1 TOWNSEND J.S.:
-Electricity in gasses:
-Oxford Univ. press:
-1915.

3.2 LEOB L.B.:
-Electrical Coronas:
-Univ. of California press:
-1965.

also

-Fundamental processes of electrical discharge in gases:
-Wiley, New York.

3.3 VON ENGEL A.:
-Ionized Gases:
-Clarendon press, Oxford:
-1955.

3.4 GOLDMAN M.N. & OSKAM H.J.:
-Gaseous electronics:
-New York academic press:
-1978.

3.5 HAMMOND P. ROMERO-FUSTER M.C. & ROBERTSON S.A.:
-Fast numerical method for calculation of electric and magnetic fields based on potential flux duality:
-Proc. IEE A, 1985, 132, (2) pp 84-94.

3.6 PATHENIER. M. & MOREAU-HANOT. M.:
-J. Phys. 3, 59, 0,:
-1932.

3.7 HIGNETT E.T.:
-Particle charge magnitudes in electrostatic precipitation:
-Proc. IEE 114, 1325-8:
-1967.

3.8 WHITE H.J.:
-Industrial electrostatic precipitation:
-Addison-Wesley:
-1963.

3.9 FUCHS N.A.:
-The mechanics of aerosols:
-Pergamon press, Oxford, 1964.

3.10 HINDS W.C.;

-Aerosol technology:
-John Wiley press, 1982.

3.11 RUSSEL A.:
-Coefficients of capacity and the mutual attraction and repulsion of two electrified spherical conductors when close together:
-Proc. R. Soc. A82 524-31:
-1909.

3.12 BRADLEY R.S.:
-Cohesion between surfaces and the surface energy of solids:
-Phil. Mag. 13, 853-62:
-1932.

3.13 LIFSHITZ E.M.:
-The theory of attractive forces between solids:
-Sov. Phys. JETP 2 78-83:
-1956.

3.14 KRUPPH H.:
-Particle adhesion, theory and experiment:
-Colloids and interface sci. 1, 111-239:
-1967.

3.15 ZIMON A.D., DOVNAR N.I., BELKINA G.A. & NOZDRINA G.V.:
-Research in surface forces:
-(Izd Nauka 330):
-1964.

4.1 SYKULSKI J.K:
-Computer package for calculating electric and magnetic fields exploiting dual energy bounds:
-IEE proc. Vol. 135, Pt.A, No.3, March 1988.

4.2 SWITHENBANK J., BEER J.M., TAYLOR D.S., ABBOT D., & McCREATH G.C.:

-A laser diagnostic technique for the measurement of droplet and particle size distributions:
-Progress in astronautics and Aeronautics 53 421-437:
-1977.

5.1 BICKELHAUPT R.E. (1974):
-J. Air Pollut. Contr. Assoc.:
-24 251-255.

6.1 COVENTRY P:
-An investigation of the fundamental processes in electrostatic precipitators:
-A thesis submitted for the degree of doctor of philosophy:
-University of Southampton.

7.1 -T.A.S.
-A computer package for calculating electric and magnetic fields.
-University of Southampton.